Spin Dynamics in Organic Semiconductors

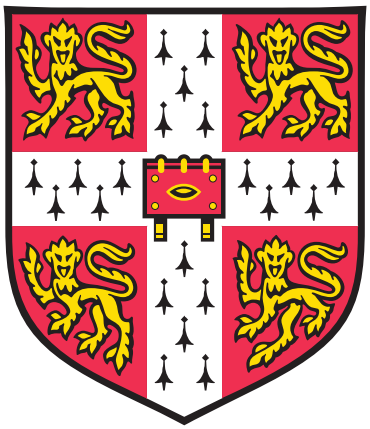

Sam Schott
Trinity Hall
University of Cambridge

A thesis submitted for the degree of
Doctor of Philosophy

September 20, 2018

Sam Schott

Abstract: Spin Dynamics in Organic Semiconductors

Organic semiconductors exhibit exceptionally long spin lifetimes, and recent observations of the inverse spin hall effect as well as micrometer spin diffusion lengths in conjugated polymers have spiked interest in employing such carbon-based materials in spintronics applications.

The charge transport and photophysics of organic semiconductors have been intensely studied for optoelectronic applications, revealing subtle relationships between molecular geometry, morphology and physical properties. Similar structure-property relationships remain mostly unknown for spin dynamics, where the charge carrier spins couple to their environment through hyperfine (HFI) and spin-orbit interactions (SOC). HFIs provide a pathway for spin relaxation while SOC plays a dual role in such materials: it couples the spin to its angular momentum and therefore enables both spin-to-charge conversion and spin relaxation. Understanding the molecular SOC, and finding a means to tune its strength, therefore is fundamentally important for materials design and selection. However, quantifying SOC strengths indirectly through spin relaxation effects has proven difficult due to competing relaxation mechanisms.

We initially present a systematic study of the g-tensor shift in molecular semiconductors and establish it as a probe for the SOC strength in a series of high mobility molecular semiconductors. The results demonstrate a rich variability of molecular g-shifts with the effective SOC, depending on subtle aspects of molecular composition and structure. We then correlate the above g-shifts to spin-lattice relaxation times over four orders of magnitude, from 200 µs to 0.15 µs, for isolated molecules in solution and relate our findings to the spin relaxation mechanisms that are likely to be relevant in solid state systems.

Isolated molecules provide an ideal model system to investigate a spin's interactions with its environment but device applications commonly employ thin films. The second half of this thesis investigates polaron spin lifetimes in field effect transistors with high-mobility conjugated polymers as active layers. We use field-induced electron spin resonance measurements to demonstrate that spin relaxation is governed by the charges' hopping motion at low temperatures while Elliott-Yafet-like relaxation due to short-range, rapid spin density dynamics likely dominates high temperature spin lifetimes. Such a microscopic relaxation mechanism is highly sensitive to the local conformation of polymer backbones and we show its dependence on the degree of crystallinity in a polymer film.

Acknowledgments

This thesis outlines the results of my work from October 2014 to September 2018 in the Optoelectronics Group at the Cavendish Laboratory, University of Cambridge. Most of the following work would have been impossible to carry out without the academic and personal support of colleagues and friends, and the close collaborations with other groups throughout Europe.

First and foremost, I would like to thank Prof. Henning Sirringhaus for guiding and supporting me throughout the PhD. His attention to detail and willingness to help with both the conceptional and experimental challenges of daily lab work have been invaluable. Henning granted me both the freedom to pursue my own interests and ideas, from the choice of research topic to the opportunity to work on side projects, and the necessary advice and encouragement if needed.

I also owe my gratitude to the Winton Program for the Physics of Sustainability for generous financial support, and for bringing together researchers and professionals across multiple sustainability-related fields. Likewise, I am grateful to the EPSRC for travel and tuition funding and to the ERC for the opportunity to work within a European Synergy Grant. It has been a joy to closely collaborate with groups from the UK, Germany and Czech Republic – on a level that would have been impossible with national research funding.

My thanks go especially to Prof. Jairo Sinova, Dr. Erik McNellis and the Sinova-group at the Johannes Gutenberg University, Mainz, for their insights into the fundamental physics of spin-orbit coupling and spin relaxation as well as fruitful collaborations and discussions.

Furthermore, large parts of this work have been enriched by simulations carried out by Dr. David Beljonne, Dr. Vincent Lemaur and Dr. Yoann Olivier at University of Mons as well as Dr. Denis Andrienko and Dr. Anton Melnyk at the Max Planck Institute for Polymer Research in Mainz.

I would also like to thank the members of the Polymer Materials group at Imperial College, especially Prof. Ian McCulloch, Cameron Jellett and Mark Little, as well as Prof. Kazuo Takimiya at Tohoku University for synthesizing and providing us with the large variety of materials studied in this thesis. My thanks also go to Prof. Chris McNeill and Dr. Xuechen Jiao for GIWAXS measurements presented in this thesis.

The work on molecular spin-orbit coupling has been started during a one month research stay at Nagoya University at the group of Prof. Shin-ichi Kuroda and

Dr. Hisaaki Tanaka and I am indebted to both for introducing me to electron spin resonance (ESR) techniques, answering my many questions and discussing the measurement results. Their hospitality has also provided me with a unique and wonderful exposure to Japanese culture.

I thank the members of Henning's group – especially the spintronics team – for many insightful discussions and fruitful collaborations. Special thanks go to Dr. Riccardo Di Pietro, Martin Statz, and Dr. Mark Nikolka for their pioneering work on charge transport in p(NDI2O–T2) and IDTBT and their collaboration for field induced ESR measurements. I am grateful to Dr. Deepak Venkateshvaran, Angela Wittmann, and Dr. Keehoon Kang for discussions on the spin and device physics of organic semiconductors as well as collaborations on doped polymer films and organic thermoelectrics. I would further like to thank Tudor Thomas for Raman and photoluminecense measurements as well as Remington Carey for Raman measurements, support with the field-induced ESR studies, his help in maintaining the ESR setup and his time for proofreading this thesis.

I am grateful to Radoslav Chakalov for essential help with sample fabrication and continued care of the cleanroom and Roger Beadle for his creative and ingenious designs of custom sample holders and chucks and his help in troubleshooting and fixing equipment malfunctions.

Furthermore, I would like to thank all who have made my time in Cambridge thoroughly enjoyable: Keehoon Kang for being an excellent desk neighbor, listing to my rants about politics and research and being a cheerful presence in our office, Leah Weiss for excellent discussions on spin physics from an entirely different perspective, Heather Goodwin, Chloe Francis and Robin Lamboll for exposing me to Scottish and English culture in this otherwise very international environment, Ture Hinrichsen for a healthy dose of hipster culture and liberal, left-wing politics, and Sebastian Concha for pulling me away from physics to play squash, go sailing and to enjoy the luxuries of life that can be found outside of the lab.

I thank Julia Wang for bringing warmth and happiness into my life, exposing me to children's literature, feminism and equality, and for supporting me during the stressful period of writing up.

I feel deeply grateful to my parents for raising me in a stimulating and supporting environment. Nothing should be taken for granted.

Declaration

This thesis is a result of my own work and includes nothing which is the outcome of work done in collaboration except where specifically indicated in the text and bibliography.

It is not substantially the same as any that I have submitted, or, is being concurrently submitted for a degree or diploma or other qualification at the University of Cambridge or any other University or similar institution except as declared in the Preface and specified in the text. I further state that no substantial part of my dissertation has already been submitted, or, is being concurrently submitted for any such degree, diploma or other qualification at the University of Cambridge or any other University or similar institution except as declared in the Preface and specified in the text.

The number of words in this report including appendices does not exceed 60,000.

January 16, 2019, Sam Schott

Laß die Moleküle rasen,
was sie auch zusammenknobeln!
Laß das Tüfteln, laß das Hobeln,
heilig halte die Ekstasen!

Christian Morgenstern

Contents

Chapter 1

Introduction

Organic semiconductors (OSCs) exhibit fundamentally different electronic structures than their inorganic counterparts. Charge transport takes place in an energetically disordered landscape where electrons are localized on a few molecules or to a polymer backbone. This results in thermally activated hopping transport and reduced mobilities, typically below $10\,\mathrm{cm^2\,V^{-1}\,s^{-1}}$. However, their unique properties such as the formation of bound singlet and triplet excitations, their tunability by chemical engineering, and their mechanical flexibility provide both intriguing physics and enable novel applications in light emitting diodes[1], solar cells[2,3], and flexible large area electronics[4].

OSCs also exhibit exceptionally long spin lifetimes of 10 ns to 10 µs, owed to their carbon- and hydrogen-based composition, and are therefore attractive for applications where charge carrier spins are used to store, transmit, and process information. Together with the recent observations of the inverse spin hall effect[5,6] and micrometer spin diffusion lengths in conjugated polymers[7], this has spiked interest in the field of organic spintronics beyond spin valves[8].

The charge transport and photophysics of OSCs have been intensely studied for optoelectronic applications, revealing subtle relationships between molecular geometry, morphology and physical properties. Similar structure-property relationships remain mostly unknown for spin dynamics, where charge carrier spins couple to their environment through hyperfine (HFI) and spin-orbit interactions (SOC). The former is dominated by hydrogen atoms in OSCs which are σ-bonded to the conjugated system; the latter is a relativistic effect which accounts for the magnetic field that a fast electron in an electrostatic potential experiences in its rest frame. It typically remains weak in OSCs due to their light elemental composition.

Both couplings provide pathways for spin relaxation but SOC plays a unique role in enabling the spin-Hall effect (SHE) and its inverse (ISHE)[9–12] which have become standard tools for the electrical creation and detection of spin currents.

Organic spintronics therefore fundamentally requires a means to measure and tune the molecular SOC from weak coupling strengths for spin transport to strong coupling for spin-to-charge conversion.

The first experimental chapter will establish the polaron g-factor, as determined by electron spin resonance (ESR), as a measure for the effective SOC in a series of small molecules of varying dimensions, side-chain configurations, and elemental compositions. The investigated series is structurally derived from the molecular semiconductors C8-BTBT and C10-DNTT which are established as high mobility materials with signs of coherent charge transport[13]. By combining ESR measurements of HFI splittings, g-shifts, and spin lifetimes with DFT calculations, carried out by the Jairo Sinova group at the University of Mainz, we show how the g-factors strongly depend on the spin density at heavier atoms in the molecule and can shift by orders of magnitude with changes to the molecular geometry.

This initial study is carried out on dispersed molecules in solution, or in the gas phase in the case of DFT calculations, and therefore suppresses more complex intermolecular effects. Device applications however require thin films and the second part of this thesis is concerned with investigating the spin dynamics of polarons in field effect transistors. Such field-induced ESR (FI-ESR) measurements allow us to probe charge transport and spin relaxation in the same device, as a function of carrier concentration and temperature. We compare a series of high-mobility conjugated polymers with varying degrees of crystallinity and establish relationships between the thin film morphology, charge motion and spin relaxation times. The results show that low temperature spin dynamics are governed by charge hopping while high temperature relaxation is dominated by much faster, short-range spin density displacements that are likely driven by low frequency vibrational modes.

But first, we will give an introduction to the electronic structure and charge transport physics of OSCs, as well as the dynamic and static interactions of a spin with its environment and the basic principles of ESR measurements.

Chapter 2

Charge transport in organic semiconductors

Optoelectronic properties of conjugated organic molecules somewhat resemble those of inorganic semiconductors: akin to the band structure in covalently bonded crystals, the energy difference between the highest occupied molecular orbital (HOMO) and the lowest unoccupied molecular orbital (LUMO) acts as a band gap and hole or electron transport can occur in the respective HOMO or LUMO bands. This band-like structure originates from the delocalized π-electron system that is intrinsic to extended conjugated carbon-carbon bonds. The following chapter will review the electronic structure of conjugated polymers and discuss the nature of charge transport in such materials.

2.1 Electronic structure of organic semiconductors

Hybridization of carbon orbitals

In its ground state, carbon only has two unpaired electrons in 2p orbitals and its ability to form up to four bonds with neighboring atoms stems from the energetically favorable hybridization of its atomic orbitals. In the case of conjugated carbon bonds, three hybrid orbitals are formed as linear combinations of one $2s$ and two $2p$ orbitals. These three sp^2 orbitals are evenly spaced in the plane perpendicular to the remaining $2p_z$ orbital. In a carbon-carbon double bond, the two overlapping sp^2 orbitals combine with the same phase to form a σ-bond where electrons are highly localized between atoms and the two out-of-plane p_z orbitals form a π-bond with more delocalized electrons. If the orbitals are combined with opposite phases to form anti-bonding σ^* or π^* orbitals, the resulting states lie at higher energies and are unoccupied in the ground state. This hybridization is depicted for the example of ethylene in Fig. 2.1.

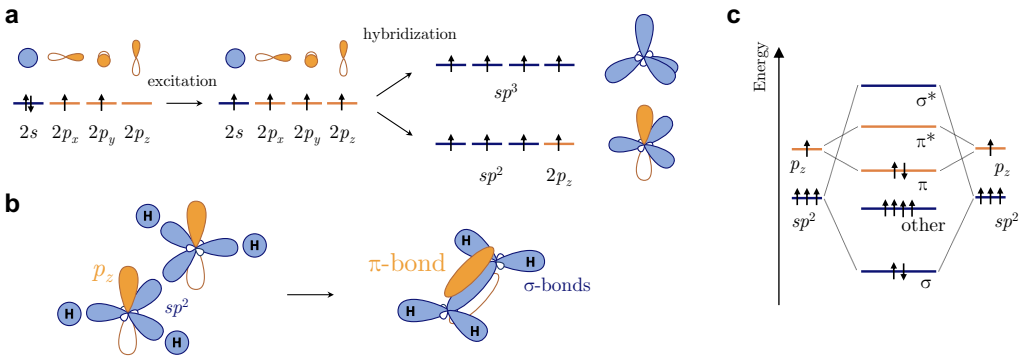

Figure 2.1: (**a**) Possible sp^3 or sp^2 hybridizations of carbon orbitals from the ground state. (**b**) Formation of σ and π bonds from sp^2 and p_z orbitals, respectively, on the example of ethylene. (**c**) Energy levels in ethylene. The anti-bonding π^* and σ^* orbitals remain unoccupied in the ground state. 'other' orbitals denote σ-bonds with hydrogen atoms.

Formation of a band structure

In a chain of conjugated carbon bonds, electrons in π-bonds become delocalized over the whole chain. With increasing chain length, the number of possible linear combinations of p_z orbitals increases until they are sufficiently closely spaced to approach a band structure. The almost-continuous band of bonding and anti-bonding orbitals is half filled (anti-bonding orbitals remain unoccupied) and we would expect an accordingly high conductivity. This is visualized in Fig. 2.2 with the transition from ethane to polyacetylene.

However, spontaneous dimerization lowers the energy of the carbon-conjugated system and causes the appearance of a band gap around the Fermi level between bonding and anti-bonding orbitals[14]. This Peierls transition is responsible for the semiconducting properties exhibited by many organic materials. Note that neglecting σ orbitals and considering only π-electrons for charge or spin transport corresponds to a frozen angular moment approximation where both the orbital angular momentum and spin-orbit coupling are quenched[15]. We will see that this approximation needs to be relaxed to accurately describe the interactions of a charge carrier spin with its environment[16].

Owed to the discrete nature of energy levels in organic materials, organic semiconductors have band widths E_B on the order of 0.1 eV, and possibly exceeding 1 eV for molecular crystals, compared to their inorganic counterparts with $E_\mathrm{B} =$ 1–10 eV[17]. Estimating the minimum trap residence time from the Heisenberg uncertainty principle as $\Delta t \approx \hbar/E_\mathrm{B}$ gives intrinsic trapping times on the order of 10 fs which, in practice, will be prolonged by effects of energetic disorder and the reorganization of the nuclei's positions in a molecule to accommodate the additional charge.

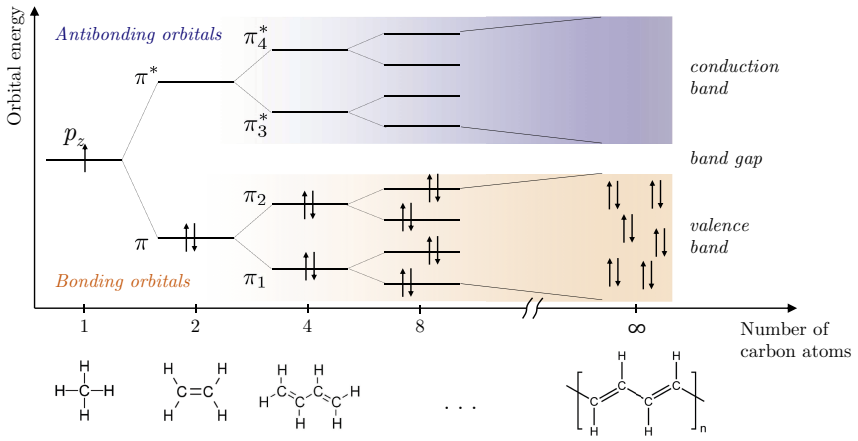

Figure 2.2: Conduction and valence bands in polyacetylene. With an increasing conjugation length the gap between the HOMO and LUMO levels decreases to ~1.5 eV. The energy levels in the HOMO band are linear combinations of predominantly bonding orbitals while the LUMO band is composed of predominantly anti-bonding orbitals.

2.2 Polaronic charge transport in organics

The band-like structure caused by π-electron delocalization could hypothetically extend over the whole polymer backbone or over the bulk of a molecular single crystal. However, strong electron-phonon coupling, reduced effective conjugation lengths caused by spatial disorder, and defects or impurities in organic films result in much more localized states.

A charge carrier introduced onto a molecule causes the surrounding atoms to reorganize, thereby screening the charge and lowering its energy with respect to the HOMO/LUMO levels[18]. Such localized charges with respective lattice distortions behave like quasi particles and are termed polarons.[1] Evidence of the polaronic nature of charge carriers includes for instance the appearance of additional optical transitions below the absorption edge of a neutral molecule when charges are introduced to the latter. This can be observed in charge modulation spectroscopy by monitoring the change in absorption while increasing the charge carrier density in an operational field effect transistor[19]. A polaron hopping from one site to another also requires the molecular configurations of those sites to reorganize, resulting in thermally activated charge transport where the charge carrier mobility increases with higher temperatures. This stands in strong contrast to inorganic semiconductors with fully delocalized bands where charge transport is limited mostly by electron-phonon scattering and higher temperatures result in lower mobilities.

[1] The conventional jargon describes a charge localized by both static disorder and electron-phonon interactions as a polaron.

A model Hamiltonian

However, the polaronic nature of charge transport and its characteristic temperature dependence is usually masked by the stronger effects of energetic disorder in organic films[20] that localize the wave-functions. We distinguish between diagonal disorder, the variation of energies ϵ_i across different sites in the film, and off-diagonal disorder, the variation of electronic couplings (transfer integrals) J_{ij} between sites, for example due to different spatial separations or orientations of those sites. A similar distinction is made for the electron-phonon coupling: it is separated into diagonal terms $g_{i,q}$ which modulate the on-site energies (polaronic coupling) and off-diagonal couplings $g_{ij,q}$ which modulate the transfer integrals (Peierls-type coupling). The system can then be described by a model Hamiltonian of electrons coupled to harmonic bath: the Holstein-Peierls Hamiltonian

$$\begin{aligned}\mathcal{H}^{\text{tot}} &= \mathcal{H}^{\text{el}} + \mathcal{H}^{\text{el-ph}} + \mathcal{H}^{\text{ph}} \\ &= \sum_i \epsilon_i \left|i\right\rangle \left\langle i\right| + \sum_{i\neq j} J_{ij} \left|i\right\rangle \left\langle j\right| + \sum_i \sum_q \hbar\omega_q g_{i,q}(b_q^\dagger + b_q) \left|i\right\rangle \left\langle i\right| \\ &\quad + \sum_{i\neq j} \sum_q \hbar\omega_q g_{ij,q}(b_q^\dagger + b_q) \left|i\right\rangle \left\langle j\right| + \sum_q \hbar\omega_q (b_q^\dagger b_q + \frac{1}{2})\end{aligned} \tag{2.1}$$

where $b_q^\dagger$ (b_q) are the creation (annihilation) operators for a phonon with frequency ω_q. The electron-phonon couplings $g_{ij,q}$ are split into diagonal (local) parts $g_{i,q}$ and off-diagonal (non-local) parts $g_{ij,q}$.

The above Hamiltonian is written in the basis set of wave-functions $|i\rangle$ localized on 'sites' such as individual molecules or monomers of a polymer chain and one can see that transition rates between the latter will increase with larger couplings J_{ij} and smaller energy differences $\Delta\epsilon_{ij}$. Both are closely linked to the thin film morphology: torsion in polymer chains results in varying effective conjugation lengths and different electronic coupling strengths are caused by different relative orientations and positions of conjugated segments. Reducing π-π stacking distances and thus increasing transfer integrals, reducing backbone torsion by chemical engineering or increasing polymer crystallinity are methods that have been shown to improve charge carrier mobilities. An insightful discussion of how morphology influences charge transport can be found in a review by Sirringhaus[4].

The polaron transformation

The model Hamiltonian from Eq. (2.1) without non-local electron-phonon couplings ($g_{ij,q} = 0$) is known as the Holstein Hamiltonian[21] and forms the basis of most charge transport theories for organic semiconductors. A concise overview of such models, with a focus on small molecules, is given by Fratini in ref.[22].

Most treatments proceed by transforming Eq. (2.1) to a "polaron basis" where the electron-phonon couplings are incorporated in dressed electronic couplings, the so-called polaron or Lang-Firsov transformation[21,23]. Carrying out this transformation with $S = \sum_{i,q} g_{i,q} |i\rangle \langle i| (b_q - b_q^\dagger)$ gives[24–26]

$$\tilde{\mathcal{H}} = e^{S^\dagger} \mathcal{H} e^S = \sum_i (\epsilon_i - \lambda_i) |i\rangle \langle i| + \sum_{i \neq j} J_{ij} \hat{\kappa}_{ij} |i\rangle \langle j| + \sum_q \hbar\omega_q (b_q^\dagger b_q + \frac{1}{2}) . \quad (2.2)$$

This representation captures two fundamental effects of charge transport in organics. First, the site energies are offset by reorganization energies $\lambda_i = \sum_q g_{i,q}^2 \omega_q$ due to polaron formation. Second, the electronic couplings J_{ij} are dressed by bath displacement operators

$$\hat{\kappa}_{ij} = e^{-\sum_q g_{i,q}(b_q - b_q^\dagger)} e^{\sum_q g_{j,q}(b_q - b_q^\dagger)} . \quad (2.3)$$

Following ref.[25], we separate the dressed coupling terms into their thermal average $J_{ij} \langle \hat{\kappa}_{ij} \rangle$ and fluctuations around it $\hat{V}_{ij} = J_{ij}(\hat{\kappa}_{ij} - \langle \hat{\kappa}_{ij} \rangle)$. The former do not include any phonon operators and are added back to the electron Hamiltonian while the latter are taken as the new electron-phonon couplings such that $\tilde{\mathcal{H}} = \tilde{\mathcal{H}}^{\text{el}} + \tilde{\mathcal{H}}^{\text{el-ph}} + \tilde{\mathcal{H}}^{\text{ph}}$:

$$\begin{aligned} \tilde{\mathcal{H}}^{\text{el}} &= \sum_i (\epsilon_i - \lambda_i) |i\rangle \langle i| + \sum_{i \neq j} J_{ij} \langle \hat{\kappa}_{ij} \rangle |i\rangle \langle j| \\ \tilde{\mathcal{H}}^{\text{el-ph}} &= \sum_{i \neq j} J_{ij} (\hat{\kappa}_{ij} - \langle \hat{\kappa}_{ij} \rangle) |i\rangle \langle j| = \sum_{i \neq j} \hat{V}_{ij} |i\rangle \langle j| \\ \tilde{\mathcal{H}}^{\text{ph}} &= \mathcal{H}^{\text{ph}} . \end{aligned} \quad (2.4)$$

The transfer integrals are therefore renormalized by a Frank-Condon factor that describes the overlap of phonon wave-functions between polaronic states on sites i and j:

$$\langle \hat{\kappa}_{ij} \rangle = e^{-\frac{1}{2} \sum_q (g_{i,q} - g_{j,q})^2 \coth(\omega_q / 2k_B T)} . \quad (2.5)$$

In this description, $\tilde{\mathcal{H}}^{\text{el}}$ only contains operators that act on electron degrees of freedom but nevertheless introduces a temperature and electron-phonon coupling dependence of the transfer integrals. The impact of increasing temperature or electron-phonon couplings is solely to reduce the renormalized transfer integrals $J_{ij} \langle \hat{\kappa}_{ij} \rangle$ and therefore narrow the polaron bands. Such Anderson localization is a fully coherent effect which localizes the charge carriers to fewer monomers or molecules.

An eigenstate of $\tilde{\mathcal{H}}^{\mathrm{el}}$ can be expressed as a linear combination of single-site wave-functions $|\psi_k\rangle = \sum_i c_{ik} |i\rangle$ and can be delocalized over several sites. Without coupling to a bath, such eigenstates do not evolve over time because $\tilde{\mathcal{H}}^{\mathrm{el}}$ is diagonal in the basis $|\psi_k\rangle$[27].

Calculations of these eigenstates $|\psi_\mu\rangle$ have been carried out for example by Troisi and coworkers for a toy polymer chain model (including polaronic effects)[28] and for a full morphology of the semi-crystalline polymer pBTTT (neglecting polaronic effects)[27]. Both results show that states close to the band gap are strongly localized while eigenstates higher in energy can extend over many repeat units and π-stacks (see Fig. 2.3). This would permit longer-range hopping and more efficient charge transport, which, as extended states become more accessible, could introduce an intrinsic dependence of the charge carrier mobility on the carrier concentration and the temperature.

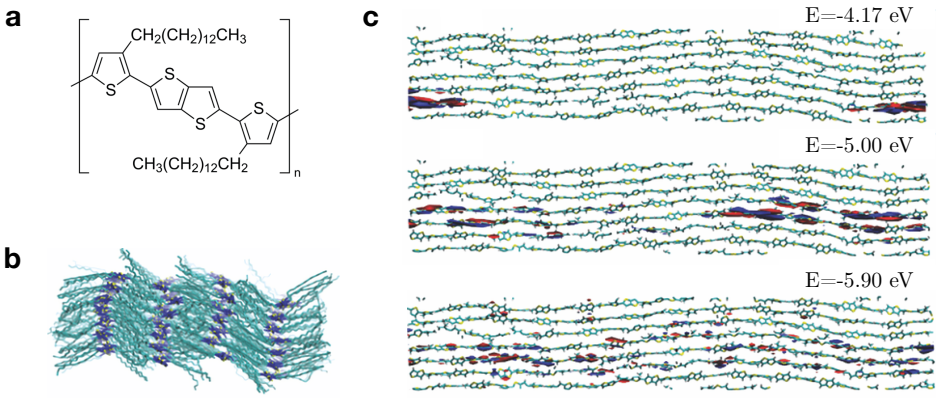

Figure 2.3: (**a**) Chemical structure of pBTTT. (**b**) A semi-crystalline pBTTT morphology from molecular dynamics simulations, shown in the plane perpendicular to the extension of polymer chains. (**c**) The same morphology viewed in the π-π stacking plane, showing the charge densities of eigenstates of $\mathcal{H}^{\mathrm{el}}$ at different energies. States closer to the band edge of $-4.7\,\mathrm{eV}$ tend to be more localized. Figures have been reproduced from ref.[27].

Incoherent hopping between sites

The Hamiltonian from Eq. (2.1) or its formulation in the polaron basis from Eq. (2.4) can generally be used to describe both band transport and strongly localized systems since we have so far made no assumptions about the amount of energetic disorder, the magnitude of the electron-phonon coupling, or the phonon frequencies. Any perturbative treatment of transition rates between electronic states and therefore of charge transport must make such assumptions.

If the electronic couplings J_{ij} are weak or electron-phonon interactions are sufficiently strong such that $J_{ij} \langle \hat{\kappa}_{ij} \rangle$ becomes small, one can treat charge transport

in terms of transition rates between states $|i\rangle$ and $|j\rangle$ localized on single sites (which can be extended to include multiple monomers if necessary). Fermi's golden rule then gives the incoherent hopping rate between such states.

To arrive at a more tractable expression, the small fluctuations $\hat{V}_{ij}$ are often dropped since the bulk of the electron-phonon coupling has already been incorporated in the renormalized transfer integrals $J_{ij}\,\langle\hat{\kappa}_{ij}\rangle$. This corresponds to the Condon approximation that the effects of the electron-bath coupling can be replaced by their thermal average. Furthermore, for sufficiently high temperatures $\hbar\omega_q \ll k_\mathrm{B}T$, the phonon populations can be treated classically. It is in this limit where the Marcus hopping rate, originally established for chemical reactions and biological electron-transfer processes[29], holds[25,30]:

$$k_{ij} \propto \frac{J_{ij}^2}{\sqrt{\lambda_{ij} k_\mathrm{B} T}} \exp\left(-\frac{(\lambda_{ij} + \Delta\epsilon_{ij})^2}{4\lambda_{ij} k_\mathrm{B} T}\right). \tag{2.6}$$

The Marcus rate is proportional to the renormalized transfer integral and a thermally activated exponential factor, accounting for the energy difference between the initial and final states $\Delta\epsilon_{ij} = \epsilon_j - \epsilon_i$ and the energy of polaronic reorganization during the transition $\lambda_{ij} = \lambda_i + \lambda_j$ which have to be provided by the bath. This captures the experimentally observed thermal activation of charge transport in organics, and the Marcus rate therefore has found widespread use in modeling charge carrier mobilities in organics.

A generalized Marcus rate

Unfortunately, the strong assumptions necessary to arrive at the Marcus rate expression often break down. Most prominently, the classical treatment of the bath is often invalid in semiconducting polymers where for instance the stretching modes of carbon-carbon bonds lie between 1200–1600 cm^{-1} and are still in the vibrational ground state at room temperature, in contrast to a classical oscillator. Deviations become more pronounced as $T \to 0$ where experiments show small but finite charge carrier mobilities while Eq. (2.6) predicts vanishing hopping rates. A generalized version of the Marcus rate which remains valid at low temperatures can be derived with a quantum mechanical treatment of the bath and gives, for an Ohmic spectral density of phonons[31]:

$$k_{ij} = \frac{J_{ij}^2}{\hbar^2\omega_\mathrm{c}} \left(\frac{\hbar\omega_\mathrm{c}}{2\pi k_\mathrm{B} T}\right)^{1-2\alpha} \left|\Gamma\left(\alpha + i\frac{\epsilon_{ij}}{2\pi k_\mathrm{B} T}\right)\right|^2 \Gamma(2\alpha)^{-1} \exp\left(\frac{\epsilon_{ij}}{2\pi k_\mathrm{B}} - \frac{|\epsilon_{ij}|}{\hbar\omega_\mathrm{c}}\right). \tag{2.7}$$

Here, ω_c is the cut-off frequency of the spectral density, $\alpha = \lambda_{ij}/2\omega_c$ is the Kondo parameter describing the coupling strength between charge and bath and Γ is the complex gamma function.

One can predict the expected charge currents under application of a voltage by offsetting the site energies ϵ_i according to the electric potential and summing over forward and backward hopping contributions such that

$$I \sim (k_{\text{forward}} - k_{\text{backward}})e = (k(\epsilon_{ij}) - k(\epsilon_{ji}))e\,. \tag{2.8}$$

Asadi et al. have carried out such calculations and arrived at an analytical expression for $I(T)$ that can be successfully fitted to the charge currents observed for several polymers at high carrier concentrations[32]. Notably, independent measurements by other groups have shown the same scaling but have been interpreted for instance with a Luttinger liquid[33] or quasi-1D variable range hopping model[34].

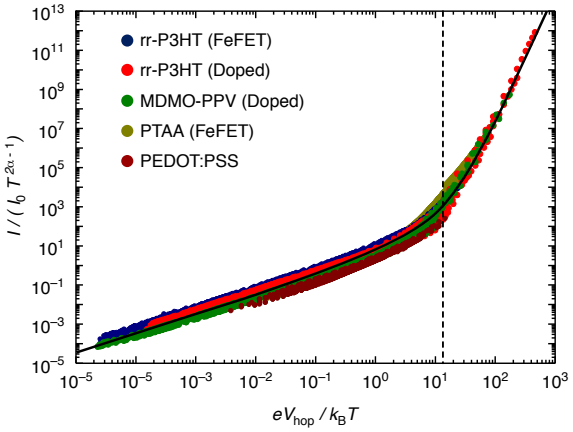

Figure 2.4: Universal scaling of the current-voltage characteristics of different semiconducting polymers, reproduced from[32] and fitted to the expected charge currents from ref. Eq. (2.7) (solid line). The crossover to the classical Marcus rate regime occurs when the potential energy for a single hop exceeds the thermal energy $eV_{\text{hop}} \gg k_B T$ (dashed line).

Hopping between eigenstates

If the couplings $J_{ij}\,\langle\hat{\kappa}_{ij}\rangle$ become too large, charge transport between two sites becomes coherent and Fermi-golden-rule treatments break down. This can occur for polymers if structural disorder such as backbone torsion is small, or for close π-π stacking where the polaron is delocalized in two dimensions across several π-stacks. The latter occurs for example in the polymer p3HT where the charge-induced optical absorption spectrum shows transitions which are dipole-forbidden for isolated chains[35]. The former limit may be approached in the donor-acceptor

co-polymer IDTBT where minimal backbone torsion allows for nearly disorder-free charge transport despite the more amorphous morphology[36].

Within the polaron Hamiltonian of Eq. (2.4), this can be dealt with by adjusting the definition of a 'site' to the typical spread of the wave-function. Nevertheless, Marcus or other golden-rule-based rate expressions can only be applied if those sites are sufficiently weakly coupled and finding such a diabatic basis set can be challenging. The most natural approach is to find the eigenstates with $\tilde{\mathcal{H}}^{\mathrm{el}} |\psi_\mu\rangle = E_\mu |\psi_\mu\rangle$ where $\tilde{\mathcal{H}}^{\mathrm{el}}$ is diagonal and all electronic couplings vanish. As shown in Fig. 2.3, this accounts for the localization of charges specific to the morphology.

Any time evolution and therefore transitions between such eigenstates is now given by the fluctuations $\hat{V}_{ij}$ of the electron-phonon couplings around their thermal equilibria which have been previously neglected. Those fluctuations are often small and, if the bath relaxation time is short, hopping rates can again be found by perturbation theories such as Fermi's golden rule[30] or a more general a Redfield equation approach for the density matrix[25]. A similar Redfield approach will be presented for the spin density matrix in Chapter 4.

Naturally, hopping distances will be different for every pair of eigenstates, depending on their localization lengths, and charge transport will be dominated by states that afford long-distance displacements of the charge carrier, as is shown in Fig. 2.5 for polaron hopping along a single polymer chain by Troisi et al.[37].

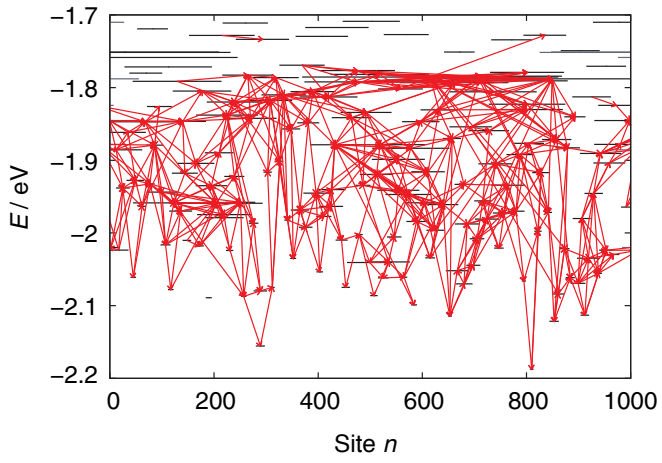

Figure 2.5: Energy levels along a model polymer chain of 1000 monomers with energetic disorder, reproduced from ref.[37]. Horizontal segments represent eigenstates of $\tilde{\mathcal{H}}^{\mathrm{el}}$ extended over multiple monomers. Red arrows represent "particle currents": the transitions rates between states multiplied by their populations.

Macroscopic charge transport

Experimentally, one does not measure transition rates but rather charge currents upon application of a voltage. For a uniform sample, the current directly follows from the hopping rates as in Eq. (2.8). If the state populations obey Boltzmann statistics, the charge carrier mobility can be calculated from the Einstein relation $\mu = eD/k_\mathrm{B}T$ and reads

$$\mu = \frac{e\overline{R_{ij}}^2}{k_\mathrm{B}T}\overline{k_{ij}} \tag{2.9}$$

where R_{ij} is the hopping distance between states i and j and the overline denotes an ensemble average over the whole sample.[1]

[1] For a classical diffusion process, the diffusion constant $D = \Delta x^2/\Delta t$ depends on the root mean square step size $\Delta x = \overline{R_{ij}}$ and the time per step $\Delta t = 1/\overline{k_{ij}}$.

However, many polymer films exhibit additional morphological disorder on the mesoscopic level, such as the formation of small crystalline segments separated by more amorphous regions as depicted in Fig. 2.6. Macroscopic expressions for the current and charge mobility then follow from path optimization and modeling of the energy differences between sites[38]. Notably, Vissenberg and Matters as well as Brondijk et al. have successfully predicted the thermally activated temperature dependence of charge transport in a range of polymers by percolation transport in a Gaussian density of states[39–41].

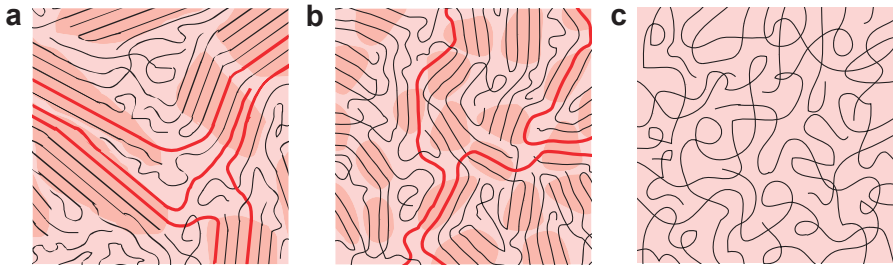

Figure 2.6: Polymer chains which connect crystallites (depicted in red) afford efficient charge transport through disordered regions. This is schematically shown for (**a**) a semi-crystalline polymer film, (**b**) a morphology of disordered aggregates, and (**c**) an entirely amorphous film. Figure reproduced from ref.[42].

Transient localization

The vast majority of models for charge hopping between either sites or eigenstates relies on the assumption that fluctuations of the electronic couplings away from their thermal average $J_{ij}\,\langle\hat{\kappa}_{ij}\rangle$ are small. This is mostly owed to neglecting the non-local electron-phonon coupling in Eq. (2.1) which directly modulates the transfer integrals. As a result, the prevailing intuition in the field understands charge transport in terms of incoherent hops between well-defined states which remain static over time.

There is often no *a priori* justification for this assumption, apart from the failure of perturbative treatments if the fluctuations are on the same order as the couplings themselves. Physically, this manifests itself in the spread of wave-functions changing dynamically, on timescales defined by the lattice vibrations. Such effects were first reported for small molecules where even in highly pure single crystals, thermal fluctuations of molecular positions and orientations strongly scatter the charge carriers. This "transient localization" scenario[22,43] was invoked to explain the coexistence of both signatures of coherent charge transport (such as the Hall effect[44]) and hopping transport (such as thermally activated mobilities at low temperatures[45]) in molecular crystals. It also reproduces the characteristic far-infrared peak observed in the optical conductivity of such materials[46].

Indirect experimental evidence was also provided by Illig et al. who showed that alkylation of molecules suppresses specific translational modes, as seen in the diffuse scattering patterns in transmission electron microscopy, and is correlated to an increase of the macroscopic charge carrier mobility of such molecules[47].

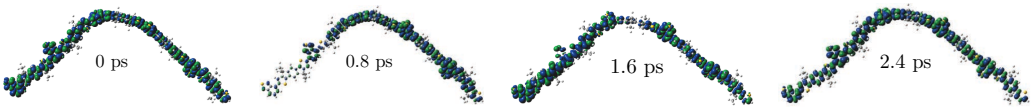

Figure 2.7: Plots of the charge density on one IDT-BT chain consisting of five monomers with snapshots every 0.8 ps. Simulations where performed by Vincent Lemaur and David Beljonne (private communication).

Similar work on polymeric semiconductors is still in its infancy and many vibrations tend to be stiffer compared to molecular crystals and therefore have smaller amplitudes. Nevertheless, there still exist low frequency vibrations such as torsional modes of carbon-carbon bonds along the polymer backbone (around 5–100 cm^{-1}) that can potentially cause large fluctuations of transfer integrals and dynamically localize a charge's wave-function. An example of such dynamics in the polymer indacenodithiophene-co-benzothiadiazole (IDT-BT) is shown in Fig. 2.7 where the charge density distribution is predicted to fluctuate on the picosecond timescale across five monomers. Contrary to molecular crystals however, it is yet unclear how strongly the macroscopic charge mobilities are affected by such intra-chain dynamics and if similar inter-chain effects can be observed.

Chapter 3

Introduction to electron spin resonance

Electron spin resonance (ESR) measures the resonant absorption of microwaves into Zeeman-split energy levels of electron spins[48]. As such, ESR can detect charge carriers in semiconductors or conductors, paired charges in triplet states and unpaired localized charges in lattices. Since the energy levels of a spin system strongly depend on the interaction of spins with their static or fluctuating electromagnetic environment, the frequency dependence and intensity of resonance spectra can be a powerful probe of spin and polaron dynamics in organic systems.

The following chapter will introduce the reader to the basic concepts of spin resonance and the most relevant interactions of a spin with its environment in an organic semiconductor. We will first introduce the Pauli spin Hamiltonian and later discuss its components as they become relevant. Section 3.1 starts with the spin-Zeeman interaction and introduces the phenomenon of spin resonance for a model isolated spin. Section 3.2 expands this to an ensemble of spins with a phenomenological rate-equation approach. Section 3.3 derives expressions for the number of spins in a semiconductor contributing to the ESR signal - and therefore the magnetic susceptibility - depending on the shape of the density of states. Sections 3.4 and 3.5 discuss the coupling of a spin to its environment through the spin-orbit and hyperfine interactions and finally, Chapter 4 will demonstrate how and when such couplings lead to spin relaxation by investigating the time evolution of the spin density matrix coupled to a bath.

The Pauli spin Hamiltonian

In many applications of organic semiconductors in optoelectronics or spintronics, charge densities are sufficiently low to ignore multi-electron interactions such as dipolar and exchange coupling between charge carriers. The energy of a single electron in an electromagnetic field is then described by the single-particle Dirac equation[49] and contributions of the molecular environment (such as nuclei and screening influences of non-conduction electrons) are accounted for through the

electric and magnetic fields:

$$\mathbf{B} = \boldsymbol{\nabla} \times \mathbf{A}\,, \quad \mathbf{E} = -\boldsymbol{\nabla} V - \frac{\partial \mathbf{A}}{\partial t}\,. \tag{3.1}$$

$\mathbf{A}$ and V are the magnetic and electric potentials, respectively. While this approximation fails to provide the accuracy of many-body quantum chemical calculations, it is the most instructive for an introduction to spin phenomena. A more complete treatment starting with the Breit-Pauli equation can be found for instance in the PhD thesis of Manninen[50].

One arrives at a more convenient Hamiltonian for velocities much smaller than the speed of light $v \ll c$ by decoupling the Dirac equation into separate differential equations for components of the spinor that are large and small with v/c.

Foldy and Wouthuysen[51] found a unitary transformation that block-diagonalizes the four-component Dirac Hamiltonian and used it to decouple the two components to successively higher orders of c^{-1}. They derive the Pauli Hamiltonian with contributions up to the order of c^{-2}:

$$\begin{aligned}\mathcal{H} = \underbrace{\frac{1}{2m}(\mathbf{p} - e\mathbf{A})^2 + eV}_{\text{classical}} - \underbrace{\frac{e\hbar}{2m}\vec{\sigma}\cdot\mathbf{B}}_{\text{spin-Zeeman } \mathcal{H}_{\mathrm{SZ}}} + \underbrace{\frac{e}{4m^2c^2}\vec{\sigma}\cdot(\boldsymbol{\nabla} V \times (\mathbf{p} - e\mathbf{A}))}_{\text{spin-orbit coupling } \mathcal{H}_{\mathrm{SO}}} \\ + \underbrace{\frac{e}{8m^2c^2}\nabla^2\mathbf{V}}_{\text{Darwin correction } \mathcal{H}_{\mathrm{D}}} - \underbrace{\frac{1}{8m^3c^2}\left((\mathbf{p} - e\mathbf{A})^2 - e\vec{\sigma}\cdot\mathbf{B}\right)^2}_{\substack{\text{mass velocity, Zeeman kinetic energy} \\ \text{and other corrections}}}\,.\end{aligned} \tag{3.2}$$

Here, e and m are the electron charge and mass, respectively, $\hbar = h/2\pi$ is the reduced Planck constant and $\vec{\sigma} = (\sigma_x, \sigma_y, \sigma_z)$ is a vector of Pauli matrices. $\mathbf{p} = -i\hbar\boldsymbol{\nabla}$ is the momentum operator and the spin operator follows as $\mathbf{S} = \frac{1}{2}\vec{\sigma}$.

The first two terms on the right hand side are the classical Hamiltonian of a charged particle in an electromagnetic field. Expanding $(\mathbf{p} - e\mathbf{A})^2$ and assuming a homogeneous magnetic field $\mathbf{A} = \mathbf{B} \times \mathbf{r}$ yields

$$\mathcal{H}_{\text{classical}} = \underbrace{\frac{p^2}{2m} + eV}_{\mathcal{H}_{\mathrm{S}}} + \underbrace{\frac{e}{2m}\mathbf{L}\cdot\mathbf{B}}_{\substack{\text{orbital Zeeman} \\ \text{energy } \mathcal{H}_{\mathrm{OZ}}}} + \underbrace{\frac{e^2}{2m}\mathbf{A}^2}_{\text{diamagnetism}} \tag{3.3}$$

with the angular momentum operator $\mathbf{L} = \mathbf{r} \times \mathbf{p}$. In our case, the first term $\mathcal{H}_{\mathrm{S}}$ describes an electron in the potential V set by the nuclei of a π-conjugated molecule and for this chapter we will assume that $\mathcal{H}_{\mathrm{S}}$ has already been diagonalized and a basis set of molecular orbital functions is known.

The second term $\mathcal{H}_{\mathrm{OZ}}$ is the Zeeman energy of the orbital magnetic moment in an external field. In π-conjugated systems the low spatial symmetry results in non-degenerate molecular orbitals (excluding spin)[52] and the orbital angular momentum is quenched in the first order.[1] We would therefore expect no contribution from $\mathcal{H}_{\mathrm{OZ}}$ but will revise this assumption later when including terms that mix orbital states.

The last term is the diamagnetic energy which is independent of spin and only shifts the ground state levels without splitting them. It therefore does not contribute to any spin related phenomena.

[1] This can be seen by a simple argument: Because the angular momentum operator is Hermitian, its diagonal matrix elements $\langle\varphi|\mathbf{L}|\varphi\rangle$ have to be real. But since the wave-function $|\varphi\rangle$ of a non-degenerate state can always be chosen to be real and $\mathbf{L}$ itself is purely imaginary, its diagonal matrix elements are both real and imaginary and thus zero.

The dominant energy contribution in the Pauli Hamiltonian comes from the spin-Zeeman term $\mathcal{H}_{\mathrm{SZ}}$ that lifts the spin-degeneracy in an external magnetic field. It is the only non-relativistic correction from the Dirac equation and naturally introduces the magnetic moment of an electron. Written in terms of the spin operator $\mathbf{S} = \frac{1}{2}\vec{\sigma}$ and with the Bohr magneton $\mu_{\mathrm{B}} = e\hbar/2m$ or the gyromagnetic ratio $\gamma_{\mathrm{e}} = g_{\mathrm{e}}\mu_{\mathrm{B}}/\hbar$, the spin-Zeeman term reads:

$$\mathcal{H}_{\mathrm{SZ}} = g_{\mathrm{e}}\mu_{\mathrm{B}}\mathbf{S}\cdot\mathbf{B} = \hbar\gamma_{\mathrm{e}}\mathbf{S}\cdot\mathbf{B}\,. \tag{3.4}$$

Here, g_{e} is the free electron g-factor which is predicted to be $g_{\mathrm{e}} = 2$ by the Dirac equation. The measured electron g-factor of a free electron is slightly larger due to radiative corrections (correctly predicted by quantum electrodynamics)[53] and is experimentally known to 12 significant digits[54]:

$$g_{\mathrm{e}} = 2.0023193043617(15)\,. \tag{3.5}$$

Other terms from the Pauli Hamiltonian will be successively introduced and treated as perturbations when we discuss their effects on the ESR spectrum. We will then arrive at an effective spin-Hamiltonian by integrating over the spatial degrees of freedom in the g-tensor and hyperfine coupling tensor.

3.1 Rabi oscillations and spin resonance

A spin in an external field

In the absence of spin-orbit coupling or other magnetic interactions, the orbital and spin parts of the wave-functions are independent $|\psi\rangle = |\varphi\rangle\,|m_S\rangle$ and the energy shift introduced by $\mathcal{H}_{\mathrm{SZ}}$ only depends on the electron spin. For a static external field along the z-axis $B_0\mathbf{e}_z$, the eigenstates of $\hbar\gamma_{\mathrm{e}}B_0S_z\,|m_S\rangle = E\,|m_S\rangle$ are $m_S \pm 1/2$

and the resulting energies are

$$E_\pm = \langle\psi|\mathcal{H}_{\mathrm{SZ}}|\psi\rangle = \hbar\gamma_\mathrm{e} B_0 \langle m_S|S_z|m_S\rangle \langle\varphi|\varphi\rangle = \pm\frac{1}{2}\hbar\gamma_\mathrm{e} B_0 \,. \tag{3.6}$$

Typical ESR experiments employ a magnetic field of around 350 mT, giving a total splitting between the levels which corresponds to microwave frequencies of 9–10 GHz for X-band ESR spectrometers

$$\Delta E = \hbar\gamma_\mathrm{e} B_0 \approx 40\,\mu\mathrm{eV}\,. \tag{3.7}$$

Since $\mathcal{H}_{\mathrm{SZ}}$ does not yet include any time dependence such as a microwave drive, the time evolution of an eigenstate is given by

$$|m_S(t)\rangle = |m_S\rangle\, e^{-iE_\pm t/\hbar} = |m_S\rangle\, e^{\mp\pm i\omega_\mathrm{L} t/2} \tag{3.8}$$

where we have introduced the Larmor frequency $\omega_\mathrm{L} = \gamma_\mathrm{e} B_0$. A prepared eigenstate will therefore accumulate a phase over time but no transitions will occur.

Note that it takes a time $4\pi/\omega_\mathrm{L}$ for the wave-function to return to its initial state but it only takes $2\pi/\omega_\mathrm{L}$ for the expectation value $\langle S(t)\rangle$ to do so. This can be observed in the quantum interference of spin wave-functions and forms for example the basis of the spin hall effect in a network of hopping triads[55].

Equations of motion

The time evolution of the spin operator $\mathbf{S}(t)$ in the Heisenberg representation is determined by the equation of motion

$$i\hbar\frac{\mathrm{d}}{\mathrm{d}t}\mathbf{S}(t) = [\mathbf{S}(t), \mathcal{H}] \tag{3.9}$$

where $[\,\cdot\,,\,\cdot\,]$ denotes the commutator. For a single spin with only the spin-Zeeman interaction, we can solve Eq. (3.9) exactly without the need to fall back to perturbation theory. Inserting the spin-Zeeman Hamiltonian $\mathcal{H} = \hbar\gamma_\mathrm{e}\mathbf{S}\cdot\mathbf{B}$ and using the commutator rules for angular momentum operators gives the same differential equation for the spin operator and its expectation value:

$$\frac{\mathrm{d}}{\mathrm{d}t}\mathbf{S}(t) = \gamma_\mathrm{e}\mathbf{B}\times\mathbf{S}(t) \tag{3.10}$$

$$\Rightarrow\frac{\mathrm{d}}{\mathrm{d}t}\langle\mathbf{S}(t)\rangle = \gamma_\mathrm{e}\mathbf{B}\times\langle\mathbf{S}(t)\rangle\,. \tag{3.11}$$

For a constant field $\mathbf{B}_0 = B_0\mathbf{e}_z$ this has the well-known solution of the spin precessing around $\mathbf{B}_0$ with the Larmor frequency $\omega_\mathrm{L} = \gamma_\mathrm{e} B_0$ while its z-component

remains constant. Anticipating such a precession, it is convenient to express the spin in terms of ladder operators $S^{\pm} = S_x \pm iS_y$ and we get

$$\langle S^{\pm}(t)\rangle = \langle S^{\pm}(0)\rangle\, e^{\pm i\omega_{\mathrm{L}}t},\ \langle S_z(t)\rangle = \langle S_z(0)\rangle\ . \tag{3.12}$$

Rabi oscillations

We now add an oscillating (microwave) field $\mathbf{B}_{\mathrm{mw}} = B_{\mathrm{mw}}(\mathbf{e}_x \cos\omega t + \mathbf{e}_y \sin\omega t)$ which is circularly polarized in the plane normal to $\mathbf{e}_z$. The calculations again simplify when expressing the microwave field in terms of circular components

$$B^{\pm}_{\mathrm{mw}} = B^{x}_{\mathrm{mw}} \pm iB^{y}_{\mathrm{mw}} = B_{\mathrm{mw}} e^{\pm i\omega t}\,. \tag{3.13}$$

Equation (3.10) can then be solved by switching to the rotating frame of the microwave field; the steps are outlined in most ESR or NMR textbooks such as ref.[56]. We are interested in the expectation value of S_z which is related to the probability of finding the spin in the state $+1/2$ or $-1/2$. For a spin initially aligned with the static field $\mathbf{B}_0$ such that $\langle S_z(0)\rangle = +1/2$, the solution is given by

$$\begin{aligned}\langle S_z(t)\rangle &= \frac{1}{2} - \frac{(\gamma_{\mathrm{e}}B_{\mathrm{mw}})^2}{(\gamma_{\mathrm{e}}B_{\mathrm{mw}})^2 + (\omega_{\mathrm{L}}-\omega)^2}\sin^2\left(\frac{1}{2}t\sqrt{(\gamma_{\mathrm{e}}B_{\mathrm{mw}})^2 + (\omega_{\mathrm{L}}-\omega)^2}\right)\\ &= \frac{1}{2} - \underbrace{\sin^2\theta\sin^2\left(\frac{1}{2}t\sqrt{\omega_1^2 + (\omega_{\mathrm{L}}-\omega)^2}\right)}_{p_-(t)}\\ \text{with}\quad \sin^2\theta &= \frac{\omega_1^2}{\omega_1^2 + (\omega_{\mathrm{L}}-\omega)^2}\,,\ \omega_1 = \gamma_{\mathrm{e}}B_{\mathrm{mw}}\,.\end{aligned} \tag{3.14}$$

This is the famous formula describing Rabi oscillations between two spin states. The term $p_-(t)$ can be identified as the probability of finding the spin in the state $m_S = -1/2$ and the factor $\sin^2\theta$ describes by how much the spin vector is tilted away from its initial direction parallel to $\mathbf{B}_0$.

Equation (3.14) can be intuitively understood in the rotating frame of the microwaves in which the spin sees a static field with magnitude $B^2_{\mathrm{eff}} = B^2_{\mathrm{mw}} + (B_0 - \omega/\gamma_{\mathrm{e}})^2$ tilted away from the z-axis by the angle θ. The spin precesses around this field with the frequency $\gamma_{\mathrm{e}}B_{\mathrm{eff}} = \sqrt{(\gamma_{\mathrm{e}}B_{\mathrm{mw}})^2 + (\omega_{\mathrm{L}}-\omega)^2}$, describing a cone as shown in Fig. 3.1. When the microwave frequency matches ω_{L}, the cone opens up to its maximum and the expectation value of S_z oscillates with the Rabi frequency $\omega_1 = \gamma_{\mathrm{e}}B_{\mathrm{mw}}$ between $\pm 1/2$. On resonance, Eq. (3.14) simplifies to:

$$\langle S_z(t)\rangle = \frac{1}{2}\cos\omega_1 t\,. \tag{3.15}$$

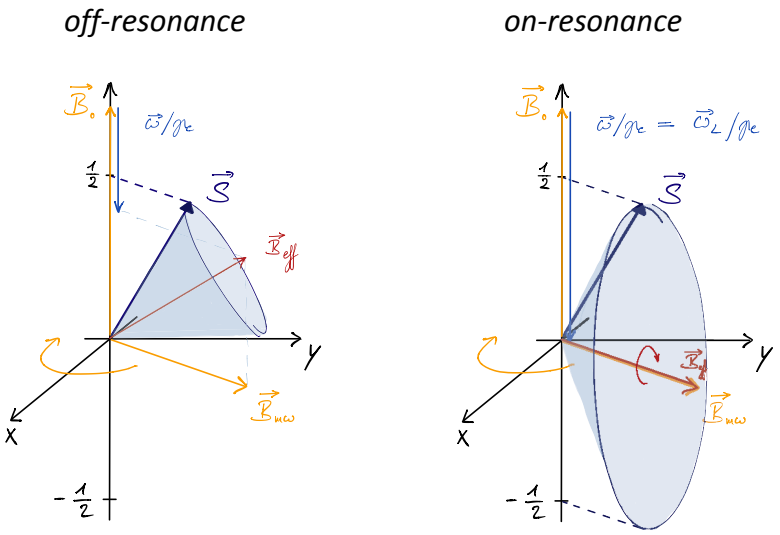

Figure 3.1: Schematic of a spin's precession around a constant effective $\mathbf{B}_{\text{eff}}$ in the rotating frame of the microwaves, off resonance and on resonance.

Off-resonance, the frequency increases and the magnitude of the oscillation drops off sharply for small microwave fields. This becomes evident when plotting the time-averaged transition probability $\overline{p_-(t)}$ as a function of $\omega - \omega_{\text{L}}$ as shown in Fig. 3.2. The rate of microwave-induced transitions $\frac{\mathrm{d}}{\mathrm{d}t}p_-(t)$ is itself an oscillating function, contrary to what is observed in an actual solid state system:

$$\frac{\mathrm{d}p_-(t)}{\mathrm{d}t} = \frac{\omega_1^2 \sin\left(t\sqrt{\omega_1^2 + (\omega - \omega_{\text{L}}^2)}\right)}{2\sqrt{\omega_1^2 + (\omega - \omega_{\text{L}})^2}} \xrightarrow{\omega=\omega_{\text{L}}} \frac{1}{2}\omega_1 \sin(t\omega_1)\,. \tag{3.16}$$

A spin ensemble: towards a constant transition rate

Considering the above exact derivations, how is it possible to then arrive at a constant rate of microwave absorption as seen experimentally? A typical solid state system consists of an ensemble of spins coupled to a bath at a finite temperature. This coupling drives the system back to thermal equilibrium after a perturbation by microwaves. The characteristic timescales for the decay of coherences and the return of populations to their equilibrium values are denoted T_1 and T_2, respectively. The relationship between the properties of the bath and the relaxation times will be derived explicitly in Chapter 4.

For now, the above means that we only need to be concerned with the microwave induced transition rate for times $t < T_1, T_2$ before the populations are "reset" by the bath. Further, the finite coherence time causes a broadening of energy levels $\rho(\Delta E)$ and therefore a distribution of frequencies $g(\omega') = \hbar\rho(\hbar\omega')$ around a central value ω_{L} and normalized through $\int g(\omega')\mathrm{d}\omega' = 1$.

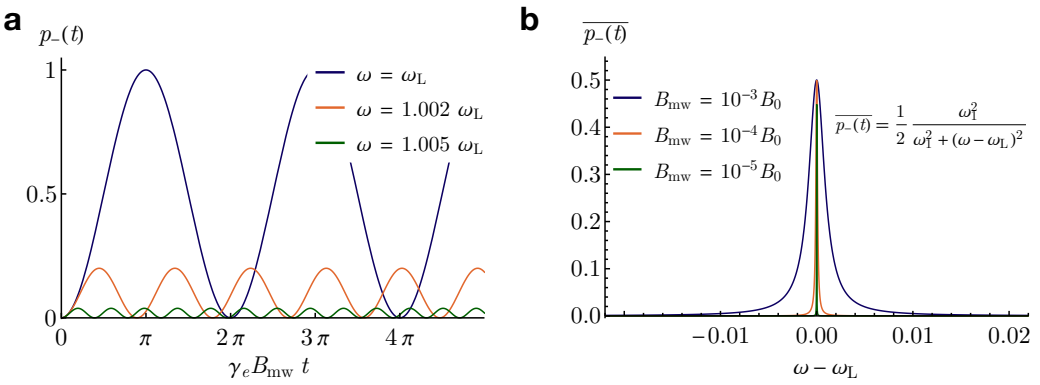

Figure 3.2: (**a**) Time dependence of the transition probability $p_-(t)$ for the $m_S = -1/2$ state, on resonance (blue line) and for different offsets from resonance, plotted for a microwave field of $B_{\mathrm{mw}} = 10^{-3} B_0$. (**b**) Time averaged transition probability $\overline{p_-(t)}$ as a function of resonance offset for different microwave field amplitudes.

We account for this broadening by writing the total transition probability as an integral over the individual probabilities, weighted by $g(\omega)$:

$$P(t) = \int_{-\infty}^{\infty} \frac{\omega_1^2}{\omega_1^2 + (\omega' - \omega)^2} \sin^2\left(\frac{1}{2} t \sqrt{\omega_1^2 + (\omega' - \omega)^2}\right) g(\omega') \mathrm{d}\omega' \tag{3.17}$$

$$= \int_{-\infty}^{\infty} p_-(\omega', t) g(\omega') \mathrm{d}\omega' \,. \tag{3.18}$$

p_- is a sharply peaked function around $\omega - \omega' = 0$ and falls off rapidly if t is sufficiently large and $\omega_1 t \lesssim 1$ is sufficiently small. We can then take $g(\omega')$ as practically constant over the range where the integrand is non-zero and replace $p_-(\omega', t)$ with $\omega_1^2 \pi \frac{t}{2} \delta(\omega' - \omega)$. The total transition probability and the resulting rate V_{mw} are then given by

$$P(t) = \frac{\pi}{2} \omega_1^2 g(\omega) t \tag{3.19}$$

$$V_{\mathrm{mw}} = \frac{\mathrm{d}}{\mathrm{d}t} P(t) = \frac{\pi}{2} \omega_1^2 g(\omega) \,. \tag{3.20}$$

The same result is obtained by treating the microwave field as a small perturbation and applying Fermi's famous golden rule yields

$$\begin{aligned} V_{\mathrm{mw}} &= \frac{2\pi}{\hbar} \left| \langle m_S | \, \hbar \gamma_{\mathrm{e}} \mathbf{S} \cdot \mathbf{B}_{\mathrm{mw}} \left| m'_S \right\rangle \right|^2 \frac{g(\omega)}{\hbar} \\ &= 2\pi \gamma_{\mathrm{e}}^2 \left| \langle m_S | \, (S^+ B_{\mathrm{mw}}^+ + S^- B_{\mathrm{mw}}^-)/2 \left| m'_S \right\rangle \right|^2 g(\omega) \\ &= \frac{\pi}{2} \gamma_{\mathrm{e}}^2 B_{\mathrm{mw}}^2 g(\omega) \,. \end{aligned} \tag{3.21}$$

It also clearly shows the selection rule for microwave induced transitions of $\Delta m_S = \pm 1$, which also holds for $S > 1/2$ where the spin states split into more than two levels. Incidentally, the derivation of Fermi's golden rule follows very much the same approximations and holds under similar conditions as Eq. (3.20).

Consistent with the observed exponential decay of coherence after turning off the microwave excitation, one typically assumes $g(\omega)$ to take the shape of a normalized Lorentz function with a width that is inversely proportional to the coherence time $1/T_2$:

$$g(\omega) = \frac{T_2/\pi}{1 + T_2^2(\omega_\mathrm{L} - \omega)^2}\,. \tag{3.22}$$

The resonance lineshape observed in ESR measurements will therefore be Lorentzian. It will not only depend on the rate from Eq. (3.20) but also on the populations of the energy levels in interaction with the bath.

3.2 A rate-equation approach to ESR

In lieu of a full density matrix treatment we will briefly discuss the effects a spin system in thermal equilibrium with a bath in terms of an intuitive rate-equation approach, following standard ESR or NMR textbooks such as Pake[57] and Slichter[48]. This is less rigorous but helps the reader develop a physical "feel" for ESR measurements.

In the absence of microwave radiation, the Zeeman splitting will result in a higher thermal population of the lower energy state with spins parallel to the external field. Macroscopically, this corresponds to a magnetization of the sample parallel to the field direction - materials with unpaired spins are therefore

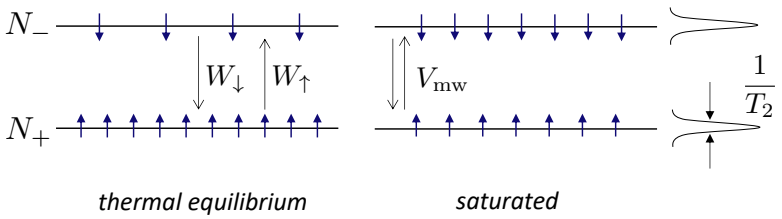

Figure 3.3: Populations of spin-up and down levels in thermal equilibrium and under microwave radiation. If the induced transition rate increases to $V > W_\mathrm{e}$, the populations will equalize and a further increase in MW power will not increase the MW absorption.

paramagnetic. Microscopically, the population difference is determined by the transition rates $W_\downarrow$ and $W_\uparrow$ from coupling to a lattice (see Fig. 3.3), for instance through interactions with nuclear magnetic moments or spin-orbit coupling. After a perturbation, the populations will again return to thermal equilibrium with the spin-lattice relaxation rate $1/T_1 = W_\downarrow + W_\uparrow$ which macroscopically describes the decay of the longitudinal magnetization.

A microwave magnetic field $\mathbf{B}_{\mathrm{mw}}$ will induce additional transitions with a rate of V_{mw} for both stimulated absorptions and emissions.[1] This pushes the system out of thermal equilibrium and towards an equal population of both levels. The changes in the population difference $n = N_+ - N_-$ are thus governed by the rate-equation

$$\frac{\mathrm{d}n}{\mathrm{d}t} = \frac{1}{T_1}(n_0 - n) - 2nV_{\mathrm{mw}} \tag{3.23}$$

[1] Unlike the induced absorption and emission of phonons, the rates $V_\uparrow$ and $V_\downarrow$ are practically equal due to the high photon density of the microwave field.

where n_0 is the population difference in thermal equilibrium. For a constant microwave power, the steady state solution of Eq. (3.23) determines a new quasi equilibrium with $n_{\mathrm{ss}} = n_0/(1 + 2T_1V_{\mathrm{mw}})$ and the rate of energy absorption is proportional to this population difference: $P(\omega) = n_{\mathrm{ss}}V_{\mathrm{mw}}\hbar\omega$.

Inserting the microwave-induced transition rate V_{mw} calculated in the previous section yields the overall power absorption rate

$$P(\omega) = \frac{n_0}{2}\frac{\hbar\omega\gamma_{\mathrm{e}}^2 B_{\mathrm{mw}}^2 T_2}{1 + T_2^2(\omega_{\mathrm{L}} - \omega)^2 + \gamma_{\mathrm{e}}^2 T_1 T_2 B_{\mathrm{mw}}^2}\,. \tag{3.24}$$

This absorption of microwaves is typically detected by a Schottky diode where the detector current varies with the square root of the power. The ESR signal for an external field B_0 is therefore proportional to B_{mw} instead of B_{mw}^2:

$$S(B_0) \propto \chi_0 \frac{\omega B_{\mathrm{mw}} T_2}{1 + T_2^2(\gamma_{\mathrm{e}}B_0 - \omega)^2 + \gamma_{\mathrm{e}}^2 T_1 T_2 B_{\mathrm{mw}}^2}\,. \tag{3.25}$$

Here we have replaced the equilibrium population difference n_0 with the resulting magnetic susceptibility (see Section 3.3):

$$\chi_0 = \mu_0 \frac{g_{\mathrm{e}}\mu_{\mathrm{B}}}{2}\frac{n_0}{B}\,. \tag{3.26}$$

Spin lifetimes and the lineshape

Equation (3.25) gives a Lorentzian resonance line centered at ω_{L} with a width determined by the spin lifetimes. Typical ESR experiments are conducted in a cavity setup where the frequency ω is fixed and instead the external magnetic field B is swept. Resonance occurs when the Zeeman splitting matches the fixed

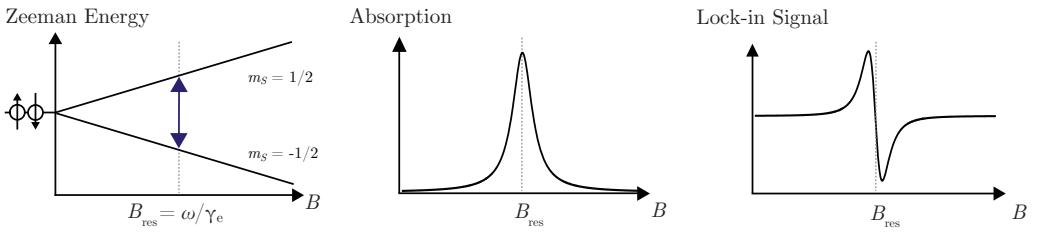

Figure 3.4: ESR spectrometers operate at a fixed frequency, determined by the cavity dimensions, and sweep the external magnetic field. This field is typically modulated at 100 kHz and the resulting ESR signal is detected by a lock-in amplifier. It resembles the derivative of the absorption curve from Eq. (3.25) with respect to B.

frequency at $B_{\mathrm{res}} = \omega/\gamma_{\mathrm{e}} = \hbar\omega/g_{\mathrm{e}}\mu_{\mathrm{B}}$. The half width at half maximum of the Lorentzian, with respect to the field, then reads

$$\Delta B_{1/2} = \frac{1}{\gamma_{\mathrm{e}} T_2}\sqrt{1+\gamma_{\mathrm{e}}^2 B_{\mathrm{mw}}^2 T_1 T_2}\,. \tag{3.27}$$

One can see that the linewidth scales inversely with the coherence time for small microwave powers ($\gamma_{\mathrm{e}}^2 B_{\mathrm{mw}}^2 T_1 T_2 \ll 1$) and broadens under increasing power. This occurs when the rate of MW-induced transitions increases to a point where it reduces the lifetime of the spin states and causes broadening in addition to the intrinsic width $\propto 1/T_2$.

The total area beneath the absorption curve scales linearly with B_{mw} and the magnetic susceptibility of the sample for small B_{mw} and can be used to "count" the total number of spins after careful calibration of the spectrometer. Integration of Eq. (3.25) with respect to B gives

$$A(B_{\mathrm{mw}}) \propto \chi_0 \frac{\pi}{\gamma_{\mathrm{e}}} \frac{B_{\mathrm{mw}}}{\sqrt{1+\gamma_{\mathrm{e}}^2 T_1 T_2 B_{\mathrm{mw}}^2}}\,. \tag{3.28}$$

The area eventually saturates to $A(B_{\mathrm{mw}}) \to \chi_0/\gamma_{\mathrm{e}}^2\sqrt{T_1 T_2}$ for high microwave powers when the population difference vanishes. In principle this allows us to determine the product of lifetimes $T_1 T_2$, as will be outlined in Section 5.2. Another consequence of the saturating area together with the broadening linewidth is a decreasing peak amplitude of the Lorentzian which makes it more difficult to detect saturated ESR resonances.

If the lineshape of the ESR spectrum is the intrinsic lineshape governed by spin relaxation, the two relaxation times T_1 and T_2 can be readily determined from the width and power saturation behavior of the ESR spectrum.

Bloch equations

It is worth noting that while the spin-lattice relaxation time T_1 describes the decay of the magnetization component M_z parallel to $\mathbf{B}$, the lifetime T_2 originates from dynamic changes in the Larmor frequency. Decoherence therefore results in the decay of the magnetization components $M_{x,y,}$ perpendicular to $\mathbf{B}$. Unlike M_z, the net magnetizations M_x and M_y are zero in thermal equilibrium but will be finite under coherent microwave excitation.

Those decay processes can be written macroscopically as Bloch equations which track the time evolution of $\mathbf{M}(t)$ and are often used to describe spin resonance experiments. Their solution is outlined in standard ESR or NMR textbooks[48,56] and gives the same result as Eq. (3.24) for the absorbed microwave power.

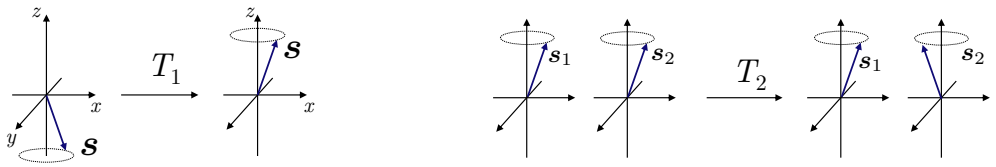

$$\frac{dM_z}{dt} = \gamma(\boldsymbol{B} \times \boldsymbol{M})_z - \frac{M_z - M_0}{T_1} \qquad \frac{dM_{x,y}}{dt} = \gamma(\boldsymbol{B} \times \boldsymbol{M})_{x,y} - \frac{M_{x,y}}{T_2}$$

Longitudinal relaxation *Transverse relaxation*

Figure 3.5: Schematic of longitudinal and transverse spin relaxation of the ensemble magnetization. The two processes can be described phenomenologically by Bloch equations which capture the precession and exponential decay of the magnetization.

3.3 Magnetic susceptibility

We have seen in the previous section that the total area of the ESR absorption curve scales linearly with the population difference of spin states in thermal equilibrium. This population difference creates a macroscopic magnetization of the sample, according to the magnetic moment $g_e\mu_B/2$ associated which each spin, and the magnetic susceptibility χ_0 is therefore given as:

$$\chi_0 = \mu_0 \frac{M_0}{B_0} = \mu_0 \frac{g_e \mu_B}{2} \frac{N_+ - N_-}{B_0} \,. \tag{3.29}$$

If the spins belong to charge carriers within the density of states (DOS) of a semiconductor, as will be the case for large parts of this work, this population difference will not only depend on the field B_0 but also on the shape of the DOS. In this section, we will derive expressions for χ_0 in both the low occupation (Boltzmann) and high occupation (degenerate) limits.

For semiconductors and metals in an external magnetic field, the populations N_+ and N_- depend on the density of states $\rho(E)$ and the Fermi level E_F. The former is split for spin-up and spin-down charge carriers by the Zeeman energy $\Delta E = g_\mathrm{e}\mu_\mathrm{B}B$, as illustrated in Fig. 3.6, and the populations are given by

$$N_\pm = \frac{1}{2}\int_{-\infty}^{\infty} f(E - E_\mathrm{F})\rho(E \pm \Delta E/2)\mathrm{d}E \tag{3.30}$$

where $f(E) = 1/(1+\mathrm{e}^{\beta E})$ is the Fermi-Dirac distribution function and $\beta = (k_\mathrm{B}T)^{-1}$ is the thermal energy.

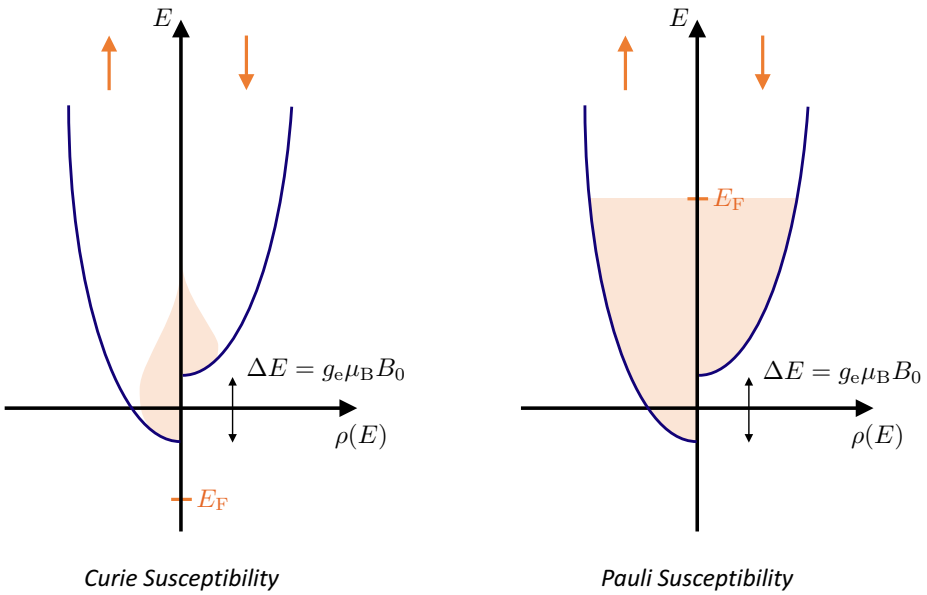

Figure 3.6: Density of states for spins parallel and perpendicular to an external magnetic field. Shaded areas indicate the occupation of states for the Fermi level E_F below or above the band edge. This figure is adapted from[52].

The Curie susceptibility

For convenience, we set the band edge to zero so that $\rho(E < 0) = 0$. If the carrier concentration is sufficiently low so that the Fermi level is far away from the band edge ($E_\mathrm{F} \ll k_\mathrm{B}T$), the Fermi-Dirac distribution can be approximated by its exponential tail and we can apply Maxwell-Boltzmann statistics: $f(E) \approx \exp(-\beta E)$. Depending on the shape of the DOS, this will be the case for most narrow-band organic semiconductors with only field-induced charges. Equation (3.30) then reads

for the lower energy state

$$\begin{aligned} N_+ &= \frac{1}{2}\int_{-\infty}^{\infty} \mathrm{e}^{-\beta(E-E_\mathrm{F})}\rho(E+\Delta E/2)\mathrm{d}E \;\; \mid E \to E' - \Delta E/2 \\ &= \frac{1}{2}\int_{-\infty}^{\infty} \mathrm{e}^{-\beta(E'-\Delta E/2-E_\mathrm{F})}\rho(E')\mathrm{d}E' \,. \end{aligned}$$

The population of the higher energy state N_- is obtained by substituting $\Delta E/2 \to -\Delta E/2$. We then get for the population difference $n_0 = N_+ - N_-$:

$$\begin{aligned} n_0 &= \frac{1}{2}\underbrace{\left(\mathrm{e}^{\beta\Delta E/2} - \mathrm{e}^{-\beta\Delta E/2}\right)}_{2\sinh(\beta\Delta E/2)} \cdot \underbrace{\int_{-\infty}^{\infty} \mathrm{e}^{-\beta(E-E_\mathrm{F})}\rho(E)\mathrm{d}E}_{\text{total number of charges } N} \\ &\simeq \beta\frac{\Delta E}{2}N = \frac{g_\mathrm{e}\mu_\mathrm{B}B}{2k_\mathrm{B}T}N \,. \end{aligned} \tag{3.31}$$

The last line of Eq. (3.31) requires the so-called high-temperature approximation $\Delta E/2 \ll k_\mathrm{B}T$ which remains valid down to 5 K for typical fields of ∼0.4 T in X-band ESR measurements.

As one might expect, the population difference is proportional to the total number of charges $N = N_+ + N_-$ and scales inversely with temperature as there is less thermal energy to populate the higher energy level. This gives the Curie susceptibility which can be generalized for spins $S > 1/2$:

$$\chi_0^\mathrm{Curie} = \mu_0\frac{Ng_\mathrm{e}^2\mu_\mathrm{B}^2}{4k_\mathrm{B}T} = \frac{\mu_0\mu_\mathrm{B}^2g_\mathrm{e}^2}{3k_\mathrm{B}T}NS(S+1)\,. \tag{3.32}$$

An alternative derivation of Eq. (3.32) treats all spins as independent from the start can be found in standard solid state physics textbooks such as Kittel[52].

The Pauli susceptibility

The opposite case of a highly doped semiconductor with the Fermi level well above the band edge ($E_\mathrm{F} \gg k_\mathrm{B}T$) can again be treated without exact knowledge of the shape of $\rho(E)$. We follow the derivation by Kittel[52] and approximate the Fermi-Dirac distribution by a step function which is unity below the Fermi level and zero above: $f(E - E_\mathrm{F}) = \Theta(E_\mathrm{F} - E)$ where Θ is the Heaviside distribution. The state populations from Eq. (3.30) then become

$$N_\pm = \frac{1}{2}\int_{\mp\Delta E/2}^{E_\mathrm{F}} \rho(E \pm \Delta E/2)\mathrm{d}E \simeq \frac{1}{2}\int_0^{E_\mathrm{F}} \rho(E)\mathrm{d}E \pm \frac{1}{2}\frac{\Delta E}{2}\rho(E_\mathrm{F})\,. \tag{3.33}$$

The population difference $n_0 = \rho(E_\mathrm{F})\Delta E/2$ therefore does not depend on temperature and the magnetic susceptibility reads

$$\chi_0^{\mathrm{Pauli}} = \mu_0 \frac{g_\mathrm{e}^2 \mu_\mathrm{B}^2}{4} \rho(E_\mathrm{F})\,. \tag{3.34}$$

This Pauli susceptibility can be understood intuitively by noting that in the high occupancy limit, only charge carriers within $k_\mathrm{B}T$ of the Fermi level will be able to reorient their magnetic moment when an external field is applied (see Fig. 3.6). For charges below the E_F, the Pauli exclusion principle will prevent such a spin flip since all neighboring states are already occupied. χ_0 is therefore proportional to the density of states at the Fermi level.

Transitions between the two regimes of a Curie- and a Pauli-like temperature dependence can occur for example as a function of temperature or carrier concentration. The former takes place because, when lowering the temperature, E_F moves to higher energies if a constant carrier concentration is maintained. One would then expect $\chi_0(T)$ to flatten out instead of diverging for $T \to 0$. In such an intermediate regime of $E_\mathrm{F} \sim k_\mathrm{B}T$ the exact shape of course depends on $\rho(E)$ and must be modeled separately for each case.

It is worth noting that the above results are in principle valid for both organic and inorganic semiconductors, independent of the localization of states and the nature of charge transport, provided that the DOS itself is independent of the number of charges. This however may not be the case for strong Coulomb interactions in more localised systems[58].

3.4 Hyperfine interactions

We will now expand our treatment by successively including further terms of the Pauli Hamiltonian. In addition to the external magnetic field, electrons experience fields caused by nuclei with finite magnetic moments. Hydrogen with a nuclear spin of $I = 1/2$ is among the most frequent of such nuclei in organic materials. Such hyperfine interactions (HFI) cause the splitting of energy levels and resonance lines and can be exploited to probe the spin density distribution in a molecule or polymer chain. In this section, we will explore the relationship between spin densities and the resulting ESR lineshape.

The hyperfine interaction Hamiltonian

Nuclear magnetic moments are incorporated into the Hamiltonian as an additional non-isotropic magnetic field with the vector potential

$$\mathbf{A}_\mathrm{N} = \frac{\mu_0}{4\pi} \sum_n g_\mathrm{N} \mu_\mathrm{N} \frac{\mathbf{I}_n \times \mathbf{r}_n}{r_n^3} \,. \tag{3.35}$$

The summation ranges over all nuclei in the molecule, μ_0 is the vacuum permeability, g_N and μ_N are the nuclear g-factor and magneton, respectively, and $\mathbf{r}_n = \mathbf{r} - \mathbf{R}_n$ denotes the position of the unpaired spin relative to the n-th nucleus. Inserting the nuclear fields $\mathbf{B}_\mathrm{N} = \boldsymbol{\nabla} \times \mathbf{A}_\mathrm{N}$ into the spin-Zeeman operator $\mathcal{H}_\mathrm{SZ}$ yields two terms, the Fermi contact and the dipolar interaction[50]:

$$\mathcal{H}_\mathrm{FC} = \frac{2\mu_0}{3} \hbar \gamma_\mathrm{e} \sum_n g_\mathrm{N} \mu_\mathrm{N} \delta(\mathbf{r}_n) \mathbf{S} \cdot \mathbf{I}_n \tag{3.36}$$

$$\mathcal{H}_\mathrm{DP} = \frac{\mu_0}{4\pi} \hbar \gamma_\mathrm{e} \sum_n g_\mathrm{N} \mu_\mathrm{N} \mathbf{S} \cdot \frac{3\mathbf{r}_n \mathbf{r}_n^\intercal - \mathbb{1} r_n^2}{r_n^5} \cdot \mathbf{I}_n \,. \tag{3.37}$$

The Fermi contact interaction gives an isotropic contribution proportional to the charge density at the nuclear core and the dipolar interaction leads to an anisotropic hyperfine coupling that depends on the orbital shape via $\mathbf{r}_n$. For an electron in the state $|\psi\rangle$, the spin Hamiltonian can be written as

$$\begin{aligned} \mathcal{H} &= \hbar \gamma_\mathrm{e} \mathbf{S} \cdot \mathbf{B} + \sum_n a_n \mathbf{S} \cdot \mathbf{I}_n + \sum_n \mathbf{S} \cdot \mathbf{T}_n \cdot \mathbf{I}_n \,, \\ a_n &= \frac{\mu_0}{4\pi} \frac{8\pi}{3} \hbar \gamma_\mathrm{e} g_\mathrm{N} \mu_\mathrm{N} \langle \delta(\mathbf{r}_n) \rangle_\psi \,, \\ \mathbf{T}_n &= \frac{\mu_0}{4\pi} \hbar \gamma_\mathrm{e} g_\mathrm{N} \mu_\mathrm{N} \left\langle \frac{3\mathbf{r}_n \mathbf{r}_n^\intercal - \mathbb{1} r_n^2}{r_n^5} \right\rangle_\psi \,. \end{aligned} \tag{3.38}$$

$\mathbf{T}_n$ is a symmetric 3×3 matrix that vanishes for s-orbitals and gives small corrections for not rotationally symmetric orbitals[59]. In the case of rapid isotropic molecular motion, such as for molecules in a solution, this anisotropic part averages to zero and we are left with the Fermi contact part only.

The observation of isotropic hyperfine interactions in organic semiconductors on the order of $a_n/\hbar\gamma_\mathrm{e} \sim 0.1$–$1\,\mathrm{mT}$ demonstrates that charges do not reside in pure π-orbital states which are linear combinations of p_z orbitals and therefore have zero spin density at the atomic cores. The finite spin densities at the nuclei are a result of mixing between σ- and π-orbitals, for instance through spin-orbit or exchange couplings[60,61]. A modern approach for calculating hyperfine constants has been developed by Neese[60].

Because the spin polarization of the hydrogen's s-orbital is often dominated by a local, atomic exchange mechanism with the unpaired π-electron, there remains an approximate empirical proportionality to the unpaired spin density at the adjacent carbon atom ρ_{C}^{π}[59,61–63]:

$$a_n/\hbar\gamma_{\mathrm{e}} \approx Q\rho_{\mathrm{C}}^{\pi} \quad \text{with } Q = -(2.5 \pm 0.1)\,\mathrm{mT}\,. \tag{3.39}$$

Accordingly, the hyperfine constant for a spin localized on a single C-H unit is $a_0^H \approx 2.5\,\mathrm{mT}$. Provided it is possible to resolve the splitting of ESR lines, one can estimate the distribution of spin-densities in a molecule by comparison with more accurate quantum chemical calculations.

HFI splitting of resonance lines

For an isotropic system with $S = 1/2$, the spin Hamiltonian with hyperfine interactions Eq. (3.38) can be diagonalized analytically and energy states are given by the well-known Breit-Rabi formula[64]. At small magnetic fields, the spin states are mixed and must be described as a triplet with total spin $F = S + I = 1$ and $m_F = -1, 0, +1$. For magnetic fields around 350 mT, the spin-Zeeman interaction becomes much larger than the HFI and nuclear and electron spins can be considered to be independent such that $|m_S, m_I\rangle = |m_S\rangle\,|m_I\rangle$. The Hamiltonian then is already diagonal with each spin state m_S split into $(2I_n + 1)$ sub levels. The selection rules for transitions between those states are $\Delta m_S = \pm 1$ and $\Delta m_I = 0$ where $I = \sum_n I_n$ is the sum of nuclear spins. This means that the microwaves can flip electron but not nuclear spins. The spectrum will split accordingly into $(2I_n + 1)$ resonance lines per nucleus with distances of $a_n/\hbar\gamma_{\mathrm{e}}$. This situation is depicted in Fig. 3.7b for two spin 1/2 nuclei with equivalent HFI couplings.

Unresolved splittings

The hyperfine structure cannot be resolved if the splitting between lines is smaller than the linewidth $1/\gamma_{\mathrm{e}}T_2$ and the resulting spectrum is said to be inhomogeneously broadened. This is often the case for the solid state where the wave-function is delocalized over several molecules, or even for polymers in solution. For a large number of nuclei and an ensemble of molecules, the lineshape will converge to a Gaussian envelop of unresolved lines[65]. The width of this Gaussian is proportional to the average hyperfine constant and scales with the square root of the number of nuclei $\sqrt{N}$ contributing to the splitting[65,66]. If the wave-function is spread over N nuclei the average hyperfine constant becomes $\overline{a}/N$ and the half width at half maximum can be approximated by[66]

$$\Delta B_{1/2} = \frac{\overline{a}}{N}\sqrt{N} = \overline{a}/\sqrt{N}\,. \tag{3.40}$$

This allows us to estimate the localization of wave-functions, even if individual splitting cannot be resolved.

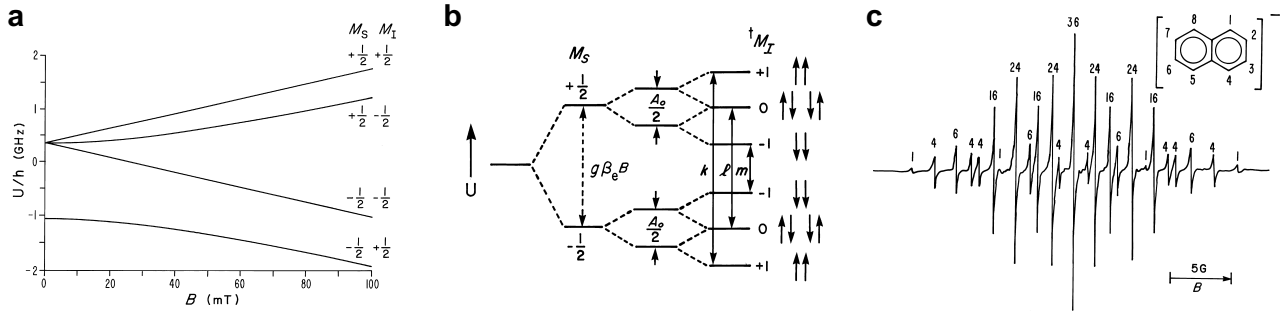

Figure 3.7: (**a**) Breit-Rabi diagram for a $S = 1/2$ spin coupled to a single nucleus with $I = 1/2$. At $B = 0$ the eigenstates show zero field splitting, revealing the triplet character of the coupled electron and nuclear spins. At higher fields, they become practically independent and can be described as product states $|m_S, m_I\rangle = |m_S\rangle\,|m_I\rangle$. (**b**) Energy levels and transitions for a system with one $S = 1/2$ spin and two equivalent nuclei with $I_n = 1/2$. When the hyperfine couplings are the same for both nuclei, the $m_I = 0$ states become doubly degenerate and the respective resonance line will double in intensity. (**c**) Derivative ESR spectrum of a naphthalene anion radical in solution. The numbers above each line are the degeneracies of the corresponding nuclear-spin states. Figures reproduced from[59].

3.5 Spin-orbit coupling and the g-tensor

We have so far only considered the spin-Zeeman term of the Pauli Hamiltonian and the interaction of an unpaired spin with surrounding nuclear spins. But for the Fermi contact interaction, we have already seen that terms coupling the orbital motion of an electron to its spin cannot be neglected. The same holds for spin-orbit coupling (SOC), where considering only π electrons corresponds to a frozen angular momentum approximation and a complete quenching of SOC[15].

In the case of a conjugated π-electron system, spin-up states of the π-orbital will be mixed with spin-down states of the σ-orbital and vice versa.[1] This spin admixture depends both on the energy separation Δ between π and σ orbitals and on the magnitude of the electrostatic potential. Incorporation of heavier atoms such as selenium (Se) into molecules will significantly increase the spin-orbit coupling strength and spin-admixture.

π-orbital spins thus acquire a finite angular momentum which couples to the external field through $\mathcal{H}_{\mathrm{OZ}} = \mu_{\mathrm{B}}\mathbf{L}\cdot\mathbf{B}$ in addition to the spin-Zeeman energy and therefore causes a shift of resonance positions. The effective spin Hamiltonian can

[1] Even though SOC mixes up and down spins, Kramer's theorem requires the new quasi spin states to still be degenerate at zero magnetic field. In the case of $S > 1/2$ however, SOC does lead to zero field splitting.

be written as

$$\mathcal{H} = \mu_\mathrm{B} \mathbf{S} \cdot \mathbf{g} \cdot \mathbf{B} \,. \tag{3.41}$$

where we have replaced the isotropic free electron g-factor with a 3×3 tensor $\mathbf{g}$ that depends on the electronic state $|\psi\rangle$. The above notation implies the following definition of the $\mathbf{g}$-tensor

$$\mathbf{g} \coloneqq \frac{1}{\mu_\mathrm{B}} \frac{\partial^2 \langle \mathcal{H} \rangle}{\partial \mathbf{S} \partial \mathbf{B}} \,. \tag{3.42}$$

We will see that there are three major corrections to the g-factor, with the first two arising from the interplay of spin-orbit and orbital-Zeeman couplings and the last one being a relativistic mass correction:

$$\mathbf{g} = g_\mathrm{e} \mathbb{1} + \Delta \mathbf{g}^{\mathrm{OZ/SO}} + \Delta \mathbf{g}^{\mathrm{GC}} + \Delta \mathbf{g}^{\mathrm{RMC}} \,. \tag{3.43}$$

Spin-orbit and orbital Zeeman corrections

In the derivation of the g-factor corrections, we follow Neese[67] and Stone[68] by considering only the leading contributions from the Pauli Hamiltonian that depend on $\mathbf{S}$ and $\mathbf{B}$. To include all molecular orbitals, we need to consider a many-electron system and the SOC term sums over all electrons:

$$\mathcal{H}_\mathrm{SO} = \frac{e}{2m^2c^2} \sum_i \mathbf{s}_i \cdot (\boldsymbol{\nabla} V \times (\mathbf{p}_i - e\mathbf{A})) \,. \tag{3.44}$$

Here, $\mathbf{s}_i$ and $\mathbf{p}_i$ are the spin and momentum operators for the i-th electron, respectively. The total molecular field is given by the sum over radial electric fields from individual nuclei $\mathbf{E} \propto \sum_n \xi_n(\mathbf{r}_n)\mathbf{r}_n$. Inserting this into Eq. (3.44) and dropping the magnetic potential $\mathbf{A}$ gives the following spin-orbit and orbital Zeeman energies:

$$\mathcal{H}_\mathrm{SO} + \mathcal{H}_\mathrm{OZ} = \sum_{i,n} \xi_n(\mathbf{r}_{i,n}) \mathbf{s}_i \cdot \mathbf{l}_{i,n} + \mu_\mathrm{B} \sum_i \mathbf{l}_i \cdot \mathbf{B} \tag{3.45}$$

where $\mathbf{l}_{i,n} = \mathbf{p}_i \times \mathbf{r}_{i,n}$ and $\mathbf{r}_{i,n} = \mathbf{r}_i - \mathbf{R}_n$ are the angular momentum and position of the i-th electron relative to the n-th nucleus, respectively. A perturbation treatment of $\mathcal{H}_\mathrm{SO} + \mathcal{H}_\mathrm{OZ}$ yields an energy correction with cross-over terms that are linear in both magnetic field and spin. The resulting shift of the resonance position is obtained by taking the partial derivative and gives[68]

$$\Delta g_{r,s}^{\mathrm{OZ/SO}} = 2 \sum_{\mu \neq \nu} \frac{\langle \psi_\mu | \, l^r \, | \psi_\nu \rangle \, \langle \psi_\nu | \sum_n \xi_n(\mathbf{r}_n) l^s \, | \psi_\mu \rangle}{E_\mu - E_\nu} \,. \tag{3.46}$$

In the above equation, $r, s = x, y, z$ are the spatial coordinates and $\mathbf{l}$ is the angular momentum operator of the unpaired electron. Equations (3.45) and (3.46) show

that heavier nuclei with larger electrostatic potentials will lead to both increased spin-orbit coupling and larger g-shifts.

The gauge correction

When a magnetic field is applied, the simplified SOC operator from Eq. (3.45) is no longer gauge invariant but depends on the choice of origin for the coordinate system. This results from dropping the magnetic potential in the derivation. Fortunately, the additional term from retaining $\mathbf{A}$ depends linearly on both the magnetic field and spin and its contribution to the g-tensor follows directly from taking the partial derivatives in Eq. (3.42). Since it restores the gauge invariance, it is commonly referred to as gauge correction $\Delta\mathbf{g}^{\mathrm{GC}}$.

The relativistic mass correction

The last contribution accounted for by Neese arises from the fifth term in Pauli Hamiltonian Eq. (3.2). It is a relativistic correction to the kinetic energy proportional to the spin-Zeeman interaction:

$$\mathcal{H}_{\text{Z-KE}} = -g_{\mathrm{e}}\frac{e}{8m^3c^2}\sum_i p_i^2 \mathbf{s}_i \cdot \mathbf{B}\,. \tag{3.47}$$

The contribution of $\mathcal{H}_{\text{Z-KE}}$ is termed relativistic mass correction and can be immediately written down as[67]

$$\Delta\mathbf{g}^{\mathrm{RMC}} = -g_{\mathrm{e}}\frac{e}{8m^3c^2}\left(\sum_{\mu,\nu}\rho^s_{\mu\nu}\left\langle\varphi_\mu\right| p^2 \left|\varphi_\nu\right\rangle\right)\mathbb{1} \tag{3.48}$$

Implications for organics

For organic semiconductors, the relativistic mass and gauge corrections are both much smaller than $\Delta\mathbf{g}^{\mathrm{OZ/SO}}$ and easier to calculate. The OZ/SO correction can be quite large and can be used to probe the strength of SOC by monitoring the g-shift in ESR spectra. Z. Yu points out in his discussion of SOC in organics[16] that the g-shift is only sensitive to spin-admixture between different orbitals while

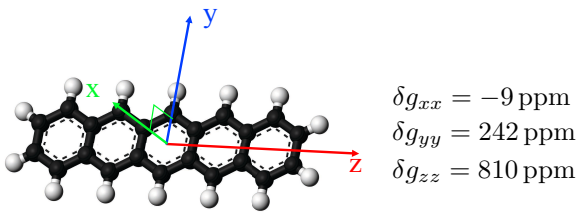

Figure 3.8: Sketch of the g-tensor principle axes for a pentacene cation and simulated principle values. Calculations were performed by Erik McNellis (Johannes Gutenberg-Universität Mainz) following the Neese method presented in this report.

SOC also mixes spins within the same orbital[16] and therefore may underestimate the SOC strength. Nevertheless, we will attempt to do the above in Chapter 6.

The SOC corrections to the g-factor depend of course on the orientation of the magnetic field relative to the orbital and are thus anisotropic. But it can always be diagonalized and its principle axes are commonly perpendicular to the molecular plane (g_x) and in-plane along the short (g_y) and the long axes (g_z) of the molecule. The planar geometry intrinsic to organic semiconductors built of aromatic rings typically leads to a larger angular momentum in the yz-plane such that $\delta g_{xx} < \delta g_{yy} < \delta g_{zz}$, as shown in Fig. 3.8.

Although deviations from the g-factor are only on the order of 100–1000 ppm for organic materials[16,67,69], the resulting shifts of resonance lines are still around $1\,\mathrm{mT} = 10\,\mathrm{G}$ and thus often larger than the linewidth. By combining angle resolved measurements with g-tensor simulations, it is for example possible to determine the orientation of molecules in a solid.

Chapter 4

Spin relaxation and lineshapes

In the previous chapter, we have seen how the effective Hamiltonian for an unpaired spin follows from the Pauli Hamiltonian with relativistic corrections as

$$\mathcal{H}_{\text{spin}} = \mu_{\text{B}} \mathbf{B} \cdot \mathbf{g} \cdot \mathbf{S} + \sum_n a_n \mathbf{S} \cdot \mathbf{I}_n + \sum_n \mathbf{S} \cdot \mathbf{T}_n \cdot \mathbf{I}_n \tag{4.1}$$

where the couplings to the spin's environment are encoded in the g- and hyperfine tensors. By itself, this static Hamiltonian would produce a spectrum of perfectly sharp resonance lines. When accounting for exponential spin relaxation, we showed that these resonances acquire a finite linewidth and saturate under large microwave fields. So far this treatment has been phenomenological (Section 3.2), disregarding the underlying relaxation mechanisms. In this chapter, we will give an introduction to spin relaxation processes with an emphasis on spin-bath couplings, which are relevant for organic semiconductors.

Spin-bath interactions can be fully treated with quantum mechanics by including the bath Hamiltonian $\mathcal{H}_{\text{B}}$ and an interaction term $\mathcal{H}_{\text{I}}$ containing both spin and bath operators

$$\mathcal{H} = \mathcal{H}_{\text{S}} + \mathcal{H}_{\text{I}} + \mathcal{H}_{\text{B}} \tag{4.2}$$

or semi-classically by including the effects of the bath as a time-dependent term $\mathcal{H}_{\text{I}}(t)$. In either case, the interactions can be understood in terms of fluctuating magnetic fields that couple to the spin's magnetic moments. These can be effective fields, such as from spin-orbit coupling, or real fields, from nuclear spins or other nearby electronic spins.

Established relaxation mechanisms

Established literature distinguishes between three different relaxation mechanisms, mediated by either hyperfine interactions or spin-orbit coupling, that become relevant for organic semiconductors with incoherent charge transport.

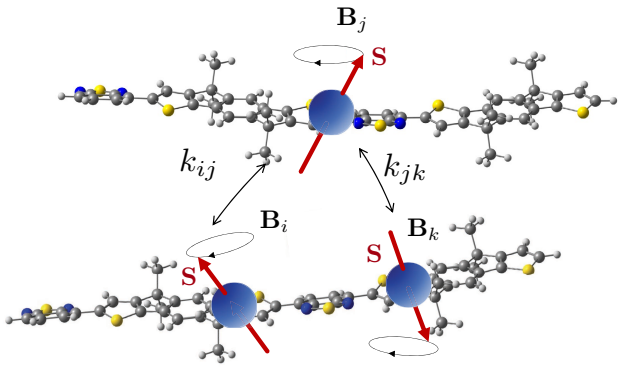

Figure 4.1: Sketch of a charge carrier hopping between sites with different local magnetic fields. In addition to the dynamic changes in Larmor frequency, there is a small but finite spin-flip probability associated with every hop.

The first one is intra-site relaxation (ISR), caused by the modulation of SOC and HFI fields by vibrational modes while the charge carrier is localized at a site. Because of the small Zeeman splitting energy of $\sim 40\,\mu\text{eV}$ and the high frequencies of intra-molecular vibrations starting at $\sim 1\,\text{meV}$, intra-site relaxation typically requires two-vibron Raman-like processes and is therefore expected to be weaker than competing mechanisms.

The second mechanism, motional relaxation (MR), describes the effects of a charge's hopping motion as it moves through an environment with hyperfine interactions and different local g-tensors. The latter originate for instance from a distribution of molecular orientations in the sample. This creates fluctuating magnetic fields in the rest frame of the spin. Motional narrowing is akin to Dyakonov-Perel spin relaxation for charge carriers in a band structure where the spin experiences varying $\mathbf{k}$-dependent spin-orbit fields between two momentum scattering events[70].

Finally, we have seen in Section 2.2 that an incoherent hopping event itself is a phonon-induced process, caused by rapidly fluctuating electric couplings which modulate the spin-orbit fields accordingly (see Section 3.5). This source of spin relaxation closely resembles the established Elliott-Yafet (EY) relaxation mechanism for inorganics where fluctuating spin-orbit fields during momentum scattering events cause spin relaxation[71,72].

Only a few theoretical studies have examined spin relaxation in organic semiconductors[73–77] and disentangling the above processes experimentally can be challenging: both intra-site and Elliott-Yafet type relaxation rates increase with temperature as more vibrational modes become populated and hopping rates increase, and both spin-orbit or hyperfine fields contribute to motional and intra-site

relaxation. Further, there are various studies that report both spin-lattice relaxation and coherence times in organic semiconductors over a significant temperature range[78,79]. So far, only motional relaxation has been unambiguously identified due its unique property of showing longer spin lifetimes if the charge motion becomes sufficiently fast[80]. Additionally, many molecular crystals[44] and some semiconducting polymers[81] show signs of at least locally coherent charge dynamics that would require an entirely new description of spin relaxation within a dynamic localization scenario.

The spin density matrix

Before discussing the above relaxation mechanisms, we will introduce a general density matrix formalism for spin-bath coupling. Compared to perturbative rate-equations such as Fermi's golden rule, this has the advantages of capturing the dynamics of both populations (diagonal elements of the density matrix) and coherences (off-diagonal elements) simultaneously. Once the time dependence of the spin density matrix σ is known, the expectation value of any operator, such as the ensemble spin polarization $\mathbf{S} = \sum_a \mathbf{S}_a$, will follow by taking the trace:

$$\langle \mathbf{S} \rangle = \mathrm{Tr}(\sigma \mathbf{S})\,. \tag{4.3}$$

We will see that coupling to a bath causes the matrix elements of σ to decay to their thermal equilibrium values, given by the canonical distribution

$$\sigma_{\mathrm{eq}} = e^{-\beta \mathcal{H}_{\mathrm{S}}}/\mathcal{Z} \tag{4.4}$$

where $\mathcal{Z} = \mathrm{Tr}\big(e^{-\beta \mathcal{H}_{\mathrm{S}}}\big)$ is the partition function and $\beta = (k_{\mathrm{B}}T)^{-1}$ is the Boltzmann factor. The decay processes for diagonal and off-diagonal elements are called spin-lattice relaxation and decoherence, respectively, and their characteristic timescales are denoted T_1 and T_2. Note that σ_{eq} is diagonal in the eigenbasis of $\mathcal{H}_{\mathrm{S}}$. Coherences between the energy eigenstates are therefore fully destroyed in thermal equilibrium and only appear when exciting the system, for example with microwaves. A brief introduction to the density matrix is given in Appendix A.

Spin dynamics and the lineshape

Since we aim to probe spin dynamics through microwave resonance measurements, the relationship between the time evolution of $\mathbf{S}$ and the observed ESR lineshape is central to this thesis. It can be derived by treating the microwave field $\mathbf{B}_{\mathrm{mw}}$ as a small perturbation and expressing the absorption rate by Fermi's rule as in Section 3.1. With the energy levels $\mathcal{H}\,|n\rangle = E_n\,|n\rangle$ and accounting for the

populations of states, the absorbed microwave power per unit time reads

$$P(\omega) = \hbar\omega \sum_{m,n} (\sigma_{nn} - \sigma_{mm}) \frac{2\pi}{\hbar^2} |\langle m| \hbar\gamma_e \mathbf{S} \cdot \mathbf{B}_{mw} |n\rangle|^2 \delta(\omega - (E_m - E_n)/\hbar) \,. \quad (4.5)$$

The thermal equilibrium populations are given by Eq. (4.4) as $\sigma_{nn} = e^{-\beta E_n}/\mathcal{Z}$. By replacing the delta function with its integral representation and recasting the population difference as

$$\sigma_{nn} - \sigma_{mm} = (e^{-\beta E_n} - e^{-\beta E_m})/\mathcal{Z} = (1 - e^{-\beta\hbar\omega}) e^{-\beta E_n}/\mathcal{Z}$$

we can write Eq. (4.5) as the Fourier transform of a trace:

$$\begin{aligned} P(\omega) &= \frac{1 - e^{-\beta\hbar\omega}}{\mathcal{Z}} \hbar\omega \sum_{m,n} e^{-\beta E_n} \frac{2\pi}{\hbar^2} |\langle m| \hbar\gamma_e \mathbf{S} \cdot \mathbf{B}_{mw} |n\rangle|^2 \frac{1}{2\pi} \int_{-\infty}^{\infty} e^{-i(\omega - (E_m - E_n)/\hbar)t} \mathrm{d}t \\ &= \frac{1 - e^{-\beta\hbar\omega}}{\mathcal{Z}} \hbar\omega\gamma_e^2 B_{mw}^2 \int_{-\infty}^{\infty} \sum_{m,n} \langle n| e^{-\beta E_n} S^+ |m\rangle \langle m| e^{itE_m/\hbar} S^- e^{-itE_n/\hbar} |n\rangle e^{-i\omega t} \mathrm{d}t \\ &= (1 - e^{-\beta\hbar\omega}) \hbar\omega\gamma_e^2 B_{mw}^2 \int_{-\infty}^{\infty} \frac{\mathrm{Tr}\left(e^{-\beta\mathcal{H}} S^+(0) S^-(t)\right)}{\mathcal{Z}} e^{-i\omega t} \mathrm{d}t \\ &= (1 - e^{-\beta\hbar\omega}) \hbar\omega\gamma_e^2 B_{mw}^2 \int_{-\infty}^{\infty} \left\langle S^+(0) S^-(t) \right\rangle_{eq} e^{-i\omega t} \mathrm{d}t \,. \end{aligned}$$

In the high temperature approximation $\beta\hbar\omega \ll 1$ we have $(1 - e^{-\beta\hbar\omega}) \approx 1$ and the above equation becomes

$$P(\omega) = \hbar\omega\gamma_e^2 B_{mw}^2 \int_{-\infty}^{\infty} \left\langle S^+(0) S^-(t) \right\rangle_{eq} e^{-i\omega t} \mathrm{d}t \,. \quad (4.6)$$

The ESR lineshape is therefore proportional to the Fourier transform of a correlation function $G(t) \coloneqq \langle S^+(0) S^-(t) \rangle_{eq}$ which describes the transverse relaxation of spins. A more rigorous derivation of Eq. (4.6) does not rely on Fermi's golden rule but starts from linear response theory[82]. One can then go the opposite route and show the validity of Eq. (4.5), as done for example by Kubo[82,83].

The physical meaning of Eq. (4.6) becomes intuitive when noting that $G(t)$ describes the dephasing of the spin ensemble and $P(\omega)$ essentially gives the distribution of Larmor frequencies. Those two quantities are naturally related by a Fourier transformation.

Fourier-transform spin resonance

This has significant practical consequences which form the basis for Fourier transform ESR: the shape of a resonance line can be determined by preparing a coherent transverse spin polarization and tracking its decay over time[84].

The principle is depicted in Fig. 4.2: In thermal equilibrium the spin polarization is aligned with the external magnetic field along the z-axis. When applying a pulse of resonant microwaves with a duration of $t_{\frac{\pi}{2}} = \gamma_e B_{mw}/4$, the spins perform a quarter of a Rabi oscillation and are tilted into the xy-plane. The created transverse magnetization will precess around $\mathbf{B}_0$ and eventually decay. This free induction decay (FID) can be detected by the voltage that it induces in detector coils around the cavity. It gives a signal which oscillates at one or multiple Larmor frequencies with a decaying amplitude. By Fourier transforming the signal, one can recover the continuous wave (cw-)ESR lineshape $P(\omega)$ from a single time domain measurement.

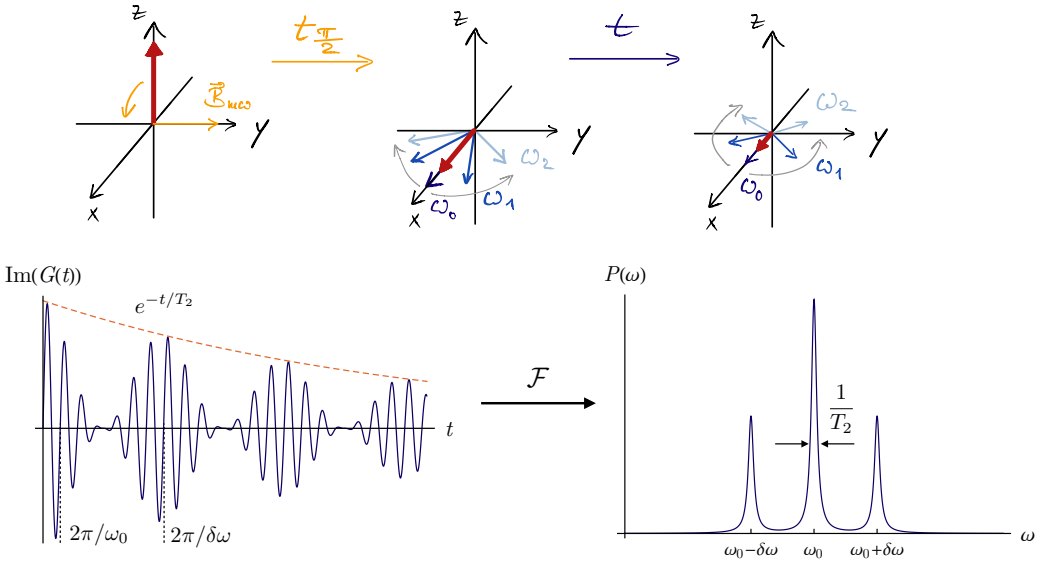

Figure 4.2: Illustration of an out-of-phase $\pi/2$ pulse tilting spins into the xy-plane followed by a free induction decay, shown in the rotating frame of microwaves. The red arrow denotes the ensemble spin while blue arrows represent individual spin packets. The corresponding cw-ESR spectrum is a convolution of δ-peaks with a lineshape function. The peak positions are determined by oscillations of $G(t)$, i.e., the Larmor frequencies, and the lineshape is the Fourier transform of the envelope decay function.

4.1 Spin bath coupling: a semi-classical model

The most rigorous approach treats both the spins and the lattice quantum-mechanically but for sufficiently high temperatures it gives the same results as a semi-classical treatment where a thermal equilibrium is introduced phenomenologically[85]. We follow the easier route of separating the spin Hamiltonian into a main time-independent part $\mathcal{H}_S$ and a smaller semi classical spin-bath interaction

term $\mathcal{H}_\mathrm{I}(t)$:

$$\mathcal{H} = \mathcal{H}_\mathrm{S} + \mathcal{H}_\mathrm{I}(t)\,. \tag{4.7}$$

We assume that $\mathcal{H}_\mathrm{S}$ results only in discrete levels, such as the Hamiltonian $\mathcal{H}_\mathrm{spin}$ in Eq. (4.1) and transitions between the eigenstates are induced by $\mathcal{H}_\mathrm{I}(t)$.

Our starting point is the von-Neumann equation for the density matrix. It is convenient to separate the time evolution caused by $\mathcal{H}_\mathrm{S}$ and continue in the interaction representation with

$$\tilde{\sigma}(t) = e^{i\mathcal{H}_\mathrm{S}t/\hbar}\sigma(t)e^{-i\mathcal{H}_\mathrm{S}t/\hbar}\,, \quad \tilde{\mathcal{H}}_\mathrm{I}(t) = e^{i\mathcal{H}_\mathrm{S}t/\hbar}\mathcal{H}_\mathrm{I}(t)e^{-i\mathcal{H}_\mathrm{S}t/\hbar}\,. \tag{4.8}$$

The above typically corresponds to a transformation into the rotation frame of the spins in an external field. $\tilde{\sigma}$ then follows the von-Neumann equation in the interaction representation:

$$\frac{\mathrm{d}\tilde{\sigma}}{\mathrm{d}t} = -i\hbar^{-1}[\tilde{\mathcal{H}}_\mathrm{I}(t), \tilde{\sigma}]\,. \tag{4.9}$$

Timescales of spin-bath coupling

The best approach to find the dynamics of a spin ensemble depends on the characteristic timescale τ_c of fluctuations in $\mathcal{H}_\mathrm{I}$ compared to their amplitude ($\delta\omega$ in frequency units). One can generally distinguish between three regimes, shown in Fig. 4.3 on the example of a nitroxide radical in solution: (1) rapid fluctuations (2) slow fluctuations, and (3) the rigid limit.

In the rapid limit the timescale of fluctuations in $\mathcal{H}_\mathrm{I}$ is quick compared to the maximum difference of precession frequencies $\delta\omega$ caused by $\mathcal{H}_\mathrm{I}$: $\tau_\mathrm{c}\delta\omega \ll 1$. The time variations can therefore never manifest themselves as a shift of resonance frequencies (energy levels) and $\mathcal{H}_\mathrm{I}(t)$ only causes a broadening of ESR lines (spin relaxation). In this limit spin relaxation takes place exponentially and Redfield derived analytical expressions for this broadening through perturbation theory, as shown in Section 4.3.

In the rigid limit of no spin-bath interactions, $\mathcal{H}_\mathrm{I} = 0$, there simply is no decoherence or spin-lattice relaxation. Nevertheless, hyperfine interactions or a distribution in g-tensors from different local environments can cause a static distribution of precession frequencies. If one creates an aligned and in-phase spin polarization at $t = 0$ it will macroscopically dephase over time. This can be modeled by diagonalizing $\mathcal{H}_\mathrm{S}$ analytically or numerically for a given magnetic field and then tracking the time evolution of an initially aligned ensemble of spins (see Section 4.2).

In the intermediate regime with slow fluctuations ($\tau_\mathrm{c}\delta\omega \gtrsim 1$) the time-dependent term $\mathcal{H}_\mathrm{I}$ causes both a broadening and a shift of energy levels in a non-trivial

and unintuitive way. One has to solve the stochastic Liouville equation for the density matrix numerically to obtain spin dynamics and relaxation is generally non-exponential. This becomes more tractable if one can separate $\mathcal{H}_\mathrm{I}$ into rapidly and slowly fluctuating components and only numerically solve for the latter. The obtained spectrum can then be convoluted with the analytical linewidths given by the Redfield theory.

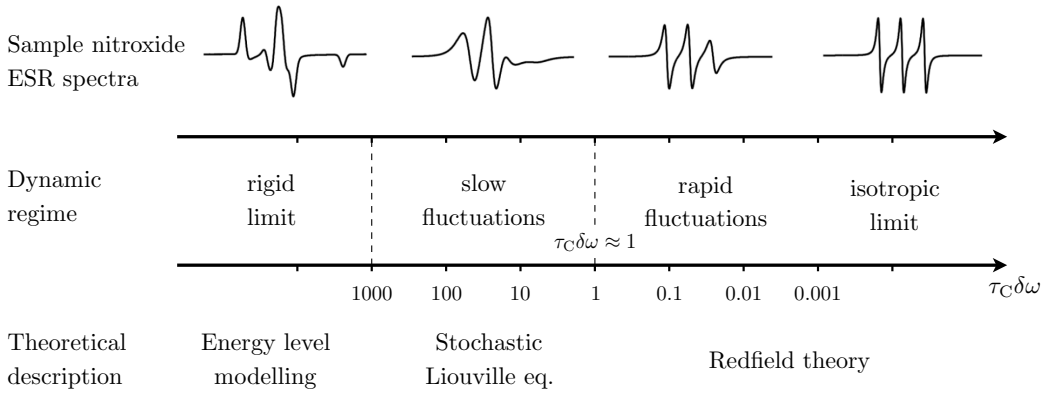

Figure 4.3: Schematic representation of the timescales of fluctuations in $\mathcal{H}_\mathrm{I}(t)$ on the example of a nitroxide radical in solution. The tumbling motion of molecules in solution causes the anisotropic parts of the spin Hamiltonian from Eq. (4.1) to average out with time. In the case of rapid motion, they only contribute to the linewidth and the resonance positions are determined purely by the isotropic HFIs and g-factor. If the solution becomes more viscous and the tumbling motion slows down, the ESR spectrum clearly becomes anisotropic. In the rigid limit of a frozen solution, the full anisotropic HFI interactions and g-tensors are revealed: the spectrum becomes the ensemble average over all molecular orientations in solution. The figure has been adapted from[86].

4.2 The static limit

Assume that the static Hamiltonian $\mathcal{H}_\mathrm{S}$ gives rise to a distribution of energy levels, e.g., through hyperfine interactions, or that the spin ensemble is characterized by a distribution of different Hamiltonians $\mathcal{H}_\mathrm{S}$, such as from different spatial orientations of molecules or from inhomogeneities in the external field. In either case, the result will be a distribution of precession frequencies around a center ω_L.

As an instructive example, let us take this distribution to be Gaussian with a width of $\delta\omega$, as will be the case for hyperfine interactions with a sufficiently large number of nuclei (see Section 3.4):

$$p(\omega_a) = \frac{1}{\sqrt{2\pi\delta\omega^2}} e^{-\omega_a^2/2\delta\omega^2} . \tag{4.10}$$

As usual, we take the external field to be along the z-axis and the time evolution of the individual spins is given by

$$\left\langle S_a^{\pm}(t)\right\rangle = \left\langle S_a^{\pm}(0)\right\rangle e^{\pm i\omega_{\mathrm{L}}t} e^{\pm i\omega_a t}\,. \tag{4.11}$$

If all spins in the ensemble are aligned at $t = 0$, the total spin will be the sum of individual spins:

$$\begin{aligned}\left\langle S^{\pm}(t)\right\rangle &= \left\langle S^{\pm}(0)\right\rangle e^{\pm i\omega_{\mathrm{L}}t} \int_{-\infty}^{\infty} e^{\pm i\omega_a t} p(\omega_a)\mathrm{d}\omega_a \\ &= \left\langle S^{\pm}(0)\right\rangle e^{\pm i\omega_{\mathrm{L}}t} e^{-\delta\omega^2 t^2/2}\,.\end{aligned} \tag{4.12}$$

Because all fields are independent of time, there is no exchange of energy with the lattice and therefore no longitudinal relaxation. In general, the phase decay is not exponential but takes the shape of the Fourier transform of the resonance frequency distribution $P(\omega)$. For our example this is again a Gaussian with the characteristic lifetime of $\delta\omega^{-1}$.

Reversible dephasing and spin-echos

This type of phase decay is also called T_2^* relaxation. It is not a decoherence process since the individual spins retain their phase memory. Figure 4.4 shows how it can be fully reversed with a so-called π pulse.

Let us again assume a fully in-phase spin ensemble at $t = 0$. After a time t_1 the individual spin packets will have fanned out according to their different precession frequencies, with the slower spins trailing behind the faster ones; the ensemble spin has decayed from its initial value. When applying a pulse of resonant microwaves with a duration of $t_\pi = \gamma_{\mathrm{e}} B_{\mathrm{mw}}/2$, the spins perform half a Rabi precession around B_{mw}. The in-plane components $S_{\pm}(t)$ will be in-plane again but with reversed order, the slowest being first and quickest being last. They will catch up with each other and the initial spin polarization will be recovered at $t = 2t_1$. This 'Hahn echo' is exploited in pulsed ESR to remove all inhomogeneous broadening effects.

4.3 Rapid motion: Bloch-Wagness-Redfield theory

In the limit of rapid motion $\tau_{\mathrm{c}}\delta\omega \ll 1$, we can apply the Bloch-Wagness-Redfield theory[85] to determine the time evolution of the density matrix and spin polarization. This will allow us to relate the relaxation times directly to the vibrational spectrum of the spin-bath coupling. This summary will generally follow the presentations of the Redfield theory by Slichter[48], Goldman[87] and Abragam[56].

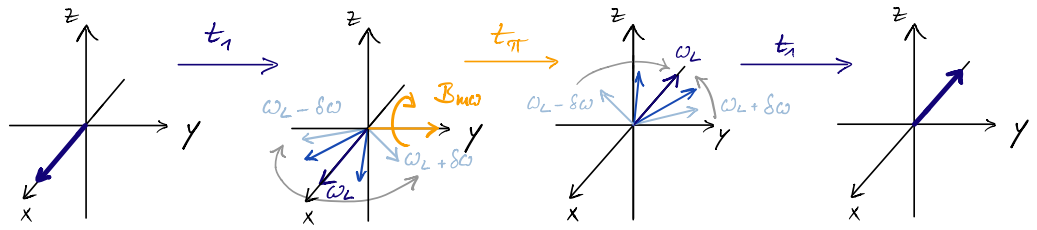

Figure 4.4: Illustration of an out-of-phase π-pulse to refocus a dephasing spin ensemble, shown in the rotating frame of ω_L. The duration t_π depends on the magnitude of B_mw.

We start again with the Hamiltonian $\mathcal{H} = \mathcal{H}_\mathrm{S} + \mathcal{H}_\mathrm{I}(t)$ and assume that the field fluctuations are due to a stochastic and ergodic process such that the temporal and ensemble averages of $\mathcal{H}_\mathrm{I}$ both vanish:

$$\int_0^\infty \mathcal{H}_\mathrm{I}(t)\mathrm{d}t = 0,\ \overline{\mathcal{H}_\mathrm{I}(t)} = 0\,. \tag{4.13}$$

An ac microwave drive for example would have a vanishing time average but a finite ensemble average and therefore violates those assumptions.

Our starting point is the von-Neumann equation in the interaction representation. Following the standard method of time-dependent perturbation theory, but for the density matrix, we integrate, resubstitute and differentiate Eq. (4.9). After taking the ensemble average over the whole system, one arrives at

$$\frac{\mathrm{d}}{\mathrm{d}t}\overline{\tilde{\sigma}(t)} = -\frac{i}{\hbar}\overline{[\tilde{\mathcal{H}}_\mathrm{I}(t), \tilde{\sigma}(0)]} - \frac{1}{\hbar^2}\int_0^t \overline{[\tilde{\mathcal{H}}_\mathrm{I}(t), [\tilde{\mathcal{H}}_\mathrm{I}(t-\tau), \tilde{\sigma}(t-\tau)]]}\mathrm{d}\tau \tag{4.14}$$

where the first term on the right-hand side vanishes due to $\overline{\mathcal{H}_\mathrm{I}(t)} = 0$. This expression is still rigorous but non-Markovian, i.e., the change in the density matrix at time t depends on all states at all previous times, making analytical or numerical solutions intractable.

Assumptions

The first central assumption of the Redfield theory is that the correlations between $\tilde{\mathcal{H}}_\mathrm{I}(t)$ and $\tilde{\mathcal{H}}_\mathrm{I}(t-\tau)$ vanish after a small characteristic time τ_c and we can extend the upper integration limit to infinity.

The second assumption is that the time evolution of $\tilde{\sigma}(t)$ is slow on timescales of τ_c. We can then replace $\tilde{\sigma}(t-\tau)$ on the right hand side of Eq. (4.14) by $\tilde{\sigma}(t)$, the so-called Markov approximation. From Eq. (4.14), one can estimate that $\tau_\mathrm{c}\overline{|\mathcal{H}_\mathrm{I}|}/\hbar \ll 1$ must be fulfilled[56]. This corresponds to our previous definition of rapid field fluctuations. With the above modifications Eq. (4.14) now reads

$$\frac{\mathrm{d}}{\mathrm{d}t}\overline{\tilde{\sigma}(t)} = -\frac{1}{\hbar^2}\int_0^\infty \overline{[\tilde{\mathcal{H}}_\mathrm{I}(t), [\tilde{\mathcal{H}}_\mathrm{I}(t-\tau), \tilde{\sigma}(t)]]}\mathrm{d}\tau \tag{4.15}$$

which is also called the Redfield equation for the density matrix.

Towards a Markovian master equation

We continue by expanding $\mathcal{H}_\mathrm{I}(t)$ as a linear combination of operators V_α acting on spin coordinates only and complex valued coefficients $F_\alpha(t)$ such that

$$\mathcal{H}_\mathrm{I}(t) = \sum_\alpha F_\alpha(t) V_\alpha \,. \tag{4.16}$$

The operators can always be chosen such that $[\mathcal{H}_0, V_\alpha] = \hbar\omega_\alpha V_\alpha$[87]. This particular choice is not necessary but convenient since it gives in the interaction representation $\tilde{V}_\alpha(t) = e^{i\omega_\alpha t} V_\alpha$. Using this decomposition and performing the ensemble average for the Hamiltonian and density matrix independently,[1] we arrive at the master equation for the time evolution of the density matrix[48,56,85]:

$$\frac{\mathrm{d}}{\mathrm{d}t}\overline{\tilde{\sigma}(t)} = -\frac{1}{2\hbar^2}\sum_{\alpha,\beta}[V_\alpha, [V_\beta^\dagger, \overline{\tilde{\sigma}(t)}]] e^{i(\omega_\alpha-\omega_\beta)t}\int_{-\infty}^{\infty}\overline{F_\alpha(t)F_\beta^*(t-\tau)}e^{i\omega_\beta\tau}\mathrm{d}\tau \,. \tag{4.17}$$

[1] For sufficiently long times, the local density matrices $\tilde{\sigma}$ will have experienced random perturbations for many times τ_c so that the correlations between $\tilde{\sigma}$ and $\tilde{\mathcal{H}}_\mathrm{I}(t)\tilde{\mathcal{H}}_\mathrm{I}(t-\tau)$ become negligible.

The transition rates between elements of the density matrix therefore are directly related to the spectral densities of the field fluctuations

$$J_{\alpha\beta}(\omega) \coloneqq \int_{-\infty}^{\infty}\overline{F_\alpha(t)F_\beta^*(t-\tau)}e^{i\omega\tau}\mathrm{d}\tau \,. \tag{4.18}$$

The time evolution of the density matrix is therefore given by a set of linear differential equations which in principle one can always solve.

A quantum mechanical treatment

Because we did not include the bath coordinates explicitly in the Hamiltonian, Eq. (4.17) predicts the relaxation of the density matrix towards an equal population of all states. Phenomenologically, we can correct for this by replacing $\tilde{\sigma}(t)$ with $\tilde{\sigma}(t)-\tilde{\sigma}_\mathrm{eq}$ where $\tilde{\sigma}_\mathrm{eq}$ is the thermal equilibrium density matrix $\tilde{\sigma}_\mathrm{eq} = \sigma_\mathrm{eq} = e^{-\beta\mathcal{H}_\mathrm{S}}/\mathcal{Z}$. We can thus modify Eq. (4.17) as follows:

$$\frac{\mathrm{d}}{\mathrm{d}t}\tilde{\sigma}(t) = -\frac{1}{2\hbar^2}\sum_{\alpha,\beta}[V_\alpha, [V_\beta^\dagger, \tilde{\sigma}(t)-\tilde{\sigma}_\mathrm{eq}]] J_{\alpha\beta}(\omega_\beta) e^{i(\omega_\alpha-\omega_\beta)t} \,. \tag{4.19}$$

A more rigorous treatment would explicitly include the bath coordinates in the model Hamiltonian. In addition to the above substitution, this will result in replacing the fluctuating couplings $F_\alpha(t)$ with operators containing the bath coordinates. Their time evolution is determined by the bath Hamiltonian as

$\hat{F}_\alpha(t) = e^{i\beta\mathcal{H}_\mathrm{B}t}\hat{F}_\alpha e^{-i\beta\mathcal{H}_\mathrm{B}}$ and the spectral densities will be replaced by[85]

$$\begin{aligned} J_{\alpha\beta}(\omega) &= \int_{-\infty}^{\infty} \overline{\hat{F}_\alpha(t)\hat{F}_\beta^\dagger(t-\tau)} e^{i\omega\tau}\mathrm{d}\tau \\ &= \frac{1}{\mathrm{Tr}(e^{-\beta\mathcal{H}_\mathrm{B}})}\int_{-\infty}^{\infty}\sum_{q,q'} \langle q|\,\hat{F}_\alpha\,|q'\rangle\,\langle q'|\,\hat{F}_\beta^\dagger\,|q\rangle\, e^{-\beta\hbar E_q} e^{i(\omega-(E_q-E_{q'})/\hbar)\tau}\mathrm{d}\tau\,. \end{aligned} \tag{4.20}$$

The temperature of the bath therefore naturally enters into the spectral density, as do the eigenstates and energies of the bath $\mathcal{H}_\mathrm{B}\,|q\rangle = E_q\,|q\rangle$. Equation (4.20) requires that a transition between spin states with energy difference $\hbar\omega$ must be accompanied by transitions in the bath with matching energies.

Once the time evolution of $\tilde{\sigma}(t)$ is known, one can deduce equations of motion for the expectation value of an operator Q in the rotating frame by multiplying Eq. (4.19) with Q and taking the trace $\langle Q\rangle_r = \mathrm{Tr}(\tilde{\sigma}(t)Q)$.

Application of the Redfield theory

The above derivations were shown in some detail because they involve several assumptions and approximations. To understand them means to understand the regime where the Redfield theory can be applied. The next steps are of a more practical nature and we will therefore skip most of the calculations. They can be found for example in Abragam's "Principles of Nuclear Magnetism"[56].

We will briefly demonstrate how the Redfield theory applies to spins that are coupled to a fluctuating magnetic field through the model Hamiltonian

$$\mathcal{H}_\mathrm{I}(t) = \hbar\gamma_\mathrm{e}\sum_{q=x,y,z} B_q(t)S_q \tag{4.21}$$

and choose the spin-Zeeman interaction $\mathcal{H}_\mathrm{SZ} = \hbar\gamma_\mathrm{e}B_0S_z$ as the unperturbed Hamilton. Of course, the same formalism can be applied to different scenarios such as dipolar couplings between spins. Following Eq. (4.21), we conveniently expand $\mathcal{H}_\mathrm{I}$ in terms of the operators $S^\pm$ and S_z such that the fluctuating fields are given by

$$F_{1,2}(t) = \frac{\hbar\gamma_\mathrm{e}}{2}(B_x(t) \pm iB_y(t)),\;\; F_3(t) = \hbar\gamma_\mathrm{e}B_z(t)\,. \tag{4.22}$$

For simplicity, we assume that fluctuations in different spatial directions are uncorrelated such that $\overline{B_q(t)B_{q'}(t-\tau)} = 0$ for $q \neq q'$. This will hold for example if for any value of B_q, the values $|B_{q'}|$ and $-|B_{q'}|$ occur with equal probability.

We can now find the time evolution of the ensemble-averaged spin operators. The calculations are straightforward but cumbersome. After converting the results back to the Schrödinger picture, they finally give differential equations resembling

the Bloch equations (for convenience, we will continue with the convention of omitting the overlines when an ensemble average is clearly implied):

$$\begin{aligned}\frac{\mathrm{d}}{\mathrm{d}t}\left\langle S^{\pm}(t)\right\rangle &= \mp i\gamma_{\mathrm{e}}B_0\left\langle S^{\pm}(t)\right\rangle - \frac{1}{\hbar^2}\left(\frac{J_{xx}(\omega_{\mathrm{L}})+J_{yy}(\omega_{\mathrm{L}})}{2}+J_{zz}(0)\right)\left\langle S^{\pm}(t)\right\rangle \\ \frac{\mathrm{d}}{\mathrm{d}t}\left\langle S_z(t)\right\rangle &= -\frac{1}{\hbar^2}\left(J_{xx}(\omega_{\mathrm{L}})+J_{yy}(\omega_{\mathrm{L}})\right)\left(\left\langle S_z(t)\right\rangle - \left\langle S_z\right\rangle_{\mathrm{eq}}\right)\end{aligned} \tag{4.23}$$

The functions $J_{qq'}(\omega)$ are the spectral densities of the magnetic field fluctuations:

$$J_{qq'}(\omega) = (\hbar\gamma_{\mathrm{e}})^2\int_{-\infty}^{\infty}\overline{B_q(t)B_{q'}(t-\tau)}e^{i\omega\tau}\mathrm{d}\tau\,. \tag{4.24}$$

Equation (4.23) shows that spin relaxation is indeed an exponential process if it is caused by a rapidly fluctuating coupling to a bath, and we can immediately give the resulting lifetimes:

$$\frac{1}{T_1} = \frac{1}{\hbar^2}\left(J_{xx}(\omega_{\mathrm{L}})+J_{yy}(\omega_{\mathrm{L}})\right) \tag{4.25}$$

$$\frac{1}{T_2} = \frac{1}{\hbar^2}\left(\frac{J_{xx}(\omega_{\mathrm{L}})+J_{yy}(\omega_{\mathrm{L}})}{2}+J_{zz}(0)\right)\,. \tag{4.26}$$

The above results can be understood intuitively: Transitions between spin-up and spin-down states are induced by magnetic field fluctuations perpendicular to B_0 that match the Larmor frequency - as is the case for microwave resonance. The spin-lattice relaxation time T_1 thus depends on the spectral density of those fluctuations at ω_{L}.

T_2 relaxation on the other hand does not require the exchange of energy with a bath and consequently depends on the spectral density at zero frequency $J_{zz}(0)$. In addition, spin flips will also cause a decay of the transverse magnetization but are only half as effective. The two contributions are often separated such that

$$\frac{1}{T_2} = \frac{1}{2T_1}+\frac{1}{T_2'} \quad \text{with} \quad \frac{1}{T_2'} = \gamma_{\mathrm{e}}^2 J_{zz}(0) \tag{4.27}$$

where T_2' is the pure dephasing contribution to decoherence.

An exponential decay of correlations

For many practical applications, the correlations decay roughly exponentially over time. We can write this as $\overline{B_q(t)B_{q'}(t-\tau)} = \delta_{qq'}\overline{B_q^2}\, e^{-|\tau|/\tau_c}$ and get Lorentzian spectral densities:

$$J_{qq}(\omega) = (\hbar\gamma_e)^2\overline{B_q^2}\frac{\tau_c}{1+\omega^2\tau_c^2}\,. \tag{4.28}$$

τ_c is the characteristic decay time of the correlations that was implied in the derivation of the Redfield theory. The resulting formulas for the relaxation times are often used for practical calculations and read

$$\frac{1}{T_1} = \gamma_e^2(\overline{B_x^2}+\overline{B_y^2})\frac{\tau_c}{1+\omega_L^2\tau_c^2} \tag{4.29}$$

$$\frac{1}{T_2} = \gamma_e^2\frac{1}{2}(\overline{B_x^2}+\overline{B_y^2})\frac{\tau_c}{1+\omega_L^2\tau_c^2} + \gamma_e^2\overline{B_z^2}\;\tau_c\,. \tag{4.30}$$

The dependence of the relaxation times on τ_c is plotted in Fig. 4.5b. As anticipated, spin-lattice relaxation becomes most effective if the correlation time matches the Larmor frequency. For typical ESR experiments, this corresponds to timescales of $\omega_L^{-1} \simeq 15\,\mathrm{ps}$. If magnetic fields fluctuate more slowly one generally finds that $T_1 > T_2$ whereas faster fluctuations give $T_1 \simeq T_2$.

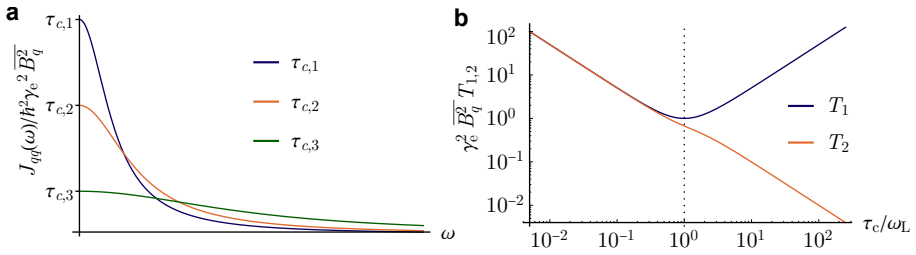

Figure 4.5: (**a**) Spectral density from Eq. (4.28) for three correlation times $\tau_{c,1} > \tau_{c,2} > \tau_{c,3}$. For small correlation times, $J_{qq}(\omega) \simeq J_{qq}(0) \propto \tau_c$ approaches a white spectrum. (**b**) Normalized spin relaxation times as a function of the bath correlation time τ_c.

4.4 Motional relaxation

For a charge carrier moving through an organic thin film, there are two major sources of fluctuating magnetic fields: First, hyperfine interactions cause a spread of resonance frequencies as discussed in Section 3.4. The most common atoms with nuclear spins in organic semiconductors are hydrogen with $I = 1/2$ and nitrogen with $I = 1$. Second, a distribution in the orientation of molecules or polymer chains

causes a spread in g-tensor orientations and therefore different local spin-orbit fields for every site.[1]

[1] Note that if all g-tensors are equally oriented, all sites exhibit the same g-shift and there will be no motional relaxation from SOC.

This leads to the characteristic temperature dependence of the ESR signal for charge carriers in organics: At very low temperatures charges move slowly and we observe a splitting of resonance lines from local fields (or a Gaussian lineshape if this splitting remains unresolved). But with higher charge carrier mobilities at increased temperatures, those fields fluctuate sufficiently fast in the reference frame of the spin so that resonances merge into a single Lorentzian line.

Redfield picture of motional narrowing

If the charge carrier motion is sufficiently fast, one can apply the Redfield formalism to describe the resulting spin dynamics. In literature it is commonly assumed that the correlation time corresponds to the inverse hopping rate between sites $\tau_c^{-1} \sim k$ and a close relation between the two is intuitive[69,80,88].

Assuming a random distribution of local fields with width δB_{rms}, the coherence time for $\gamma_e \delta B_{\mathrm{rms}} \tau_c \ll 1$ is given by Eq. (4.30):

$$\frac{1}{T_2'} = \frac{1}{\hbar^2} J_{zz}(0) = \gamma_e^2 \delta B_{\mathrm{rms}}^2 \tau_c \,. \tag{4.31}$$

Longer coherence times are therefore achieved at higher temperatures, similar to the conceptually related Dyakonow-Perel mechanism where higher temperatures lead to a faster momentum scattering rate[89]. Only the dependence on the charge carrier mobility is reversed: faster "spatial scattering" leads to increased mobilities in the hopping picture while faster momentum scattering hinders band transport.

This "motional narrowing" of the ESR spectrum has been exploited to probe charge dynamics in semi-crystalline thin films. For example, Matsui et al. have demonstrated that one can distinguish between charge motion within and between crystalline domains by exploiting the large in-plane g-factor anisotropy due to different crystallite orientations[69].

Naturally, the spin-lattice relaxation time is predicted to first show an opposite temperature dependence from Eq. (4.29): it will decrease as the hopping rate slowly approaches the Larmor frequency and increase again with $T_1 \simeq T_2$ for larger rates.

Slow motion regime

Before the onset of motional narrowing, we are firmly in the regime of the stochastic Liouville equation and numerical simulations. However in the case of a Gaussian distribution of local fields, we may still attempt a phenomenological treatment.

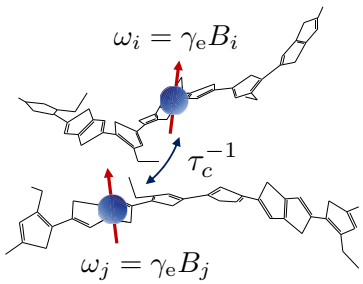

Figure 4.6: Sketch of hopping between two sites with different local magnetic fields. The spin will only experience the average field from both molecules if $\tau_c^{-1} > |\omega_i - \omega_j|$.

For sufficiently slow charge motion, the spins are almost stationary and precess around the constant fields at their respective sites. A change in Larmor frequency only occurs after hopping to the next site, and is completed on average after spending the time $t_d = (\gamma_e \delta B_{rms})^{-1}$ at the new site. In this limit, the decoherence time is proportional to the residence time at a site τ_c plus the additional time to dephase:

$$T_2' = \tau_c + \frac{1}{\gamma_e \delta B_{rms}} \tag{4.32}$$

In this toy model, motional narrowing will become effective when the spin continues on towards the next site before t_d has elapsed. We can account for this by attenuating the dephasing contribution from each site according to the reduced residence time $t_d \to t_d\,(1 + t_d/\tau_c)$. Equation (4.32) then reads

$$T_2' = \tau_c + \frac{1}{\gamma_e \delta B_{rms}} + \frac{1}{\gamma_e^2 \delta B_{rms}^2 \tau_c}\,. \tag{4.33}$$

Note that in the fast hopping regime, τ_c becomes small and the last term from Eq. (4.33) dominates. We therefore recover the behavior from the Redfield regime from Eq. (4.31).

Boehm et al. have shown that Eq. (4.33) indeed fits their results from numerical simulations of hopping in a cubic lattice of sites[90] and a similar transition has been observed by Yu et al.[76] when numerically tracking the decay of an initial spin polarization in a lattice with random hyperfine interaction fields. Notably, Yu also derives an analytical expression for HFI-induced relaxation in the slow hopping limit matching Eq. (4.32). To our knowledge, this transition is reported experimentally for the first time in this thesis.

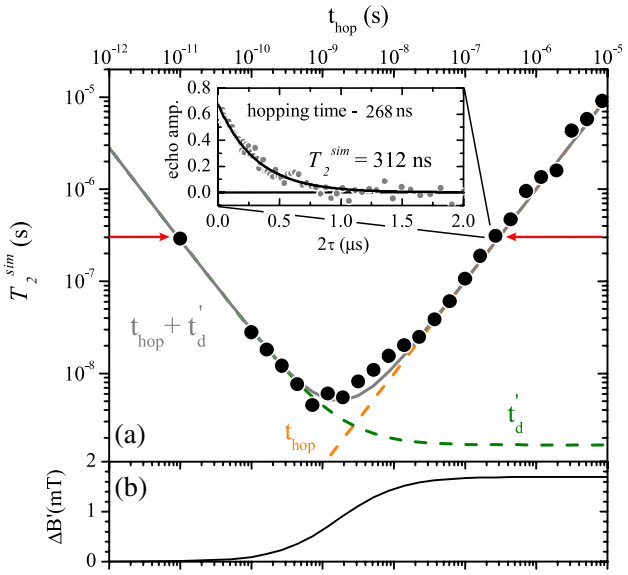

Figure 4.7: (**a**) T_2' as a function of hopping time t_{hop} at the transition to motional narrowing. The gray line represents predicted values from Eq. (4.33) and the black dots are numerical results for a cubic lattice with 125 sites. Orange and green dashed lines represent the model solutions for slow motion and motional narrowing, respectively. (**b**) Dependence of the expected ESR linewidth on t_{hop} showing the onset of motional narrowing. Figure reproduced from[90].

4.5 Elliott-Yafet relaxation

In the previous section, we have noted that spin-orbit fields can cause motional relaxation if they vary between sites. Unlike the HFI, which intrinsically causes a splitting of spin levels and therefore a distribution of precession frequencies, SOC only shifts the energy levels and therefore the resonance position. A distribution of g-factors is only observed if there is a variation of local spin Hamiltonians such as from different orientations of monomers or molecules, or different localization lengths of charges, etc.

Nevertheless, in the absence of such variations, the 'intrinsic' SOC can still cause spin relaxation because it mixes the spin-up and -down states and therefore allows for hopping events that do not conserve spin. The only theoretical description of such an Elliott-Yafet type relaxation mechanism for a hopping system has been developed by Yu in refs.[16,75]. For consistency with the previous sections, we will follow the fluctuating magnetic field approach from ref.[16] and generalize it to an arbitrary form of the spectral density $J_{qq}(\omega)$. Alternatively, one may treat the full charge and spin density matrix with a Redfield approach[75].

For a charge carrier in the eigenstate $|\psi_\mu\rangle$, the nominally up state in the presence of SOC is given by perturbation theory as[68]:

$$\begin{aligned}|\psi_\mu+\rangle = |\psi_\mu\uparrow\rangle &- \frac{1}{2}\sum_{\nu\neq\mu}\frac{\langle\psi_\nu|\sum_n \xi_n(\mathbf{r}_n) l_i^z |\psi_\mu\rangle}{E_\nu - E_\mu}|\psi_\mu\uparrow\rangle \\ &- \frac{1}{2}\sum_{\nu\neq\mu}\frac{\langle\psi_\nu|\sum_n \xi_n(\mathbf{r}_n)(l_i^x + il_i^y)|\psi_\mu\rangle}{E_\nu - E_\mu}|\psi_\mu\downarrow\rangle\end{aligned} \tag{4.34}$$

where $|\uparrow\rangle$ and $|\downarrow\rangle$ denote the states with $m_S = \pm 1/2$, respectively, and the same nomenclature as in Section 3.5 is used. We have seen in Section 3.5 that this spin admixture, together with the orbital Zeeman energy, lies at the origin of g-shifts.

In the case of organic semiconductors, the dominant contribution to spin mixing comes from the nearby σ-orbitals since the angular momentum is fully quenched in π-orbitals. One can therefore define the dimensionless spin admixture parameter as the ratio between the atomic spin-orbit coupling ξ and the energy splitting Δ between σ- and π-orbitals: $\gamma \simeq \xi/(2\Delta)$.

The coupling between two eigenstates with opposite spins $|\psi_i+\rangle$ and $|\psi_j-\rangle$ therefore does not vanish. One can write the fluctuating electron-phonon couplings $\hat{V}_{ij}$ from Section 2.2, Eq. (2.4), as the sum of a spin-conserving contribution $\hat{V}_{ij}^0$ and spin-flipping contributions:

$$\hat{V}_{ij} = \hat{V}_{ij}^0 \mathbb{1} + 2\sum\nolimits_q S_q \hat{V}_{ij}^q \tag{4.35}$$

where $q = x, y, z$. We recall that $\hat{V}_{ij}$ describe deviations from the thermal average and therefore have a vanishing temporal average. They can again be treated classically, as time-dependent couplings, or quantum-mechanically by transforming them to the interaction representation with respect to the bath. In either case, SOC leads to effective fluctuating magnetic fields $V_{ij}^q(t)$ that are only present *during* a hopping event. From Eq. (4.34), Yu explicitly calculates those couplings and finds for their amplitude, averaged over a random distribution of site orientations

$$\overline{V_x^2} = \overline{V_y^2} = \overline{V_z^2} = \frac{2}{3}\gamma^2\overline{V_0^2}\,. \tag{4.36}$$

The average spin-flip couplings therefore depend on the spin admixture γ^2 and are a fraction of the spin-conserving couplings $\overline{V_0^2}$. The exact scaling will however change with the orientational disorder in the sample.

We can proceed by calculating the relaxation times from the fields $\hbar\gamma_e\overline{B_q^2} = \overline{|V_q^2|}$ within the Redfield theory. τ_c in this case is not the inverse hopping rate but the

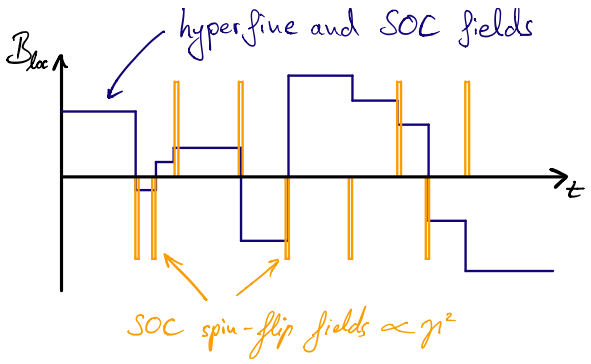

Figure 4.8: Sketch of magnetic fields experienced by a spin during a random walk between sites. Blue line indicates Dyakonov-Perel like fields that cause motional relaxation while the orange lines represent Elliott-Yafet type fields that are only present during hopping events. Figure adapted from[74].

correlation time of lattice vibrations which modulate $\hat{V}_{ij}^q(t)$ and induce a hopping event. Such vibrational modes are significantly faster than the Larmor frequency of $\sim 10\,\mathrm{GHz}$ so that their spectral density becomes the Fourier transform of a sharply peaked correlation function. It can be approximated by a white spectrum that is practically independent of frequency:

$$J_{qq}(\omega_\mathrm{L}) = \int_{-\infty}^{\infty} \overline{V_{ij}^q(t), V_{ij}^q(t-\tau)} e^{-i\omega_\mathrm{L}\tau} \mathrm{d}\tau \simeq J_{qq}(0) \tag{4.37}$$

where $J_{qq}(0) \propto \tau_\mathrm{c}$ roughly scales with the correlation time, depending on the exact shape of $J_{qq}(\omega)$. This is shown for the example of exponentially decaying correlations in Fig. 4.5a. We therefore have $T_1 \simeq T_2$ from Eqs. (4.25) and (4.26) (see also Fig. 4.5b)

$$\frac{1}{T_1} = \frac{1}{T_2} = \frac{1}{\hbar^2}(J_{xx}(0) + J_{yy}(0))\,. \tag{4.38}$$

One can then express the spin-conserving hopping rate similarly as a temporal correlation function (which gives equivalent results to Fermi's golden rule)[75]:

$$k_{ij}^0 = \frac{1}{2\hbar^2} \int_{-\infty}^{\infty} \overline{V_{ij}^0(t), V_{ij}^0(t-\tau)} e^{i\omega_{ij}\tau} \mathrm{d}\tau \tag{4.39}$$

where $\hbar\omega_{ij} = E_j - E_i$ is the energy difference between the states $|\psi_i\rangle$ and $|\psi_j\rangle$. For sufficiently rapid fluctuations $\omega_{ij} \ll \tau_\mathrm{c}^{-1}$, we can again apply the white spectrum approximation such that $k_{ij}^0(\omega_{ij}) \simeq k_{ij}^0(0) =: k^0$. Physically, this means that phonon-induced transitions rates become larger when the two states remain correlated or in-phase for a longer time $k^0 \propto \tau_\mathrm{c}$. This condition is more stringent since it requires that $\tau_\mathrm{c}^{-1} > 10\,\mathrm{THz}$ for typical energetic disorder in organics.

Under such white spectrum conditions, the spin-flip and spin-conserving rates are related by Eq. (4.36) as $J_{qq}(0) = \frac{4}{3}\gamma^2\hbar^2 k^0$. Substituting this into Eq. (4.38), one finally arrives at an expression for the spin lifetimes as a function of the hopping rate:

$$\frac{1}{T_1} = \frac{1}{T_2} = \frac{8}{3}\gamma^2 k^0 \,. \tag{4.40}$$

Note that this expression does not depend on the external magnetic field, unlike the previous Redfield expressions for motional relaxation. This is a consequence of the much shorter correlation times for lattice vibrations compared to charge motion between sites.

Similar to the established Elliott-Yafet mechanism, the above relaxation rates increase with the number of scattering events. But while increased "spatial scattering" leads to higher mobilities in hopping transport, momentum scattering inhibits charge transport in a band structure. The mobility dependence of the spin lifetimes is therefore reversed.

4.6 Intra-site relaxation

Unlike motional relaxation, intra-site site relaxation (ISR) generally requires a quantum mechanical treatment of the bath, such as with Eq. (4.20), due to the high frequency vibrational modes in organics. The electron-phonon coupling Hamiltonian does not directly cause spin relaxation but perturbs both SOC and HFI Hamiltonians which depend on the nuclear coordinates. Relaxation then involves Raman-like multi-vibron processes since the lowest frequency vibrational modes typically exceed the Zeeman splitting energy $\leq 40\,\mu\text{eV}$ for most experimental conditions. Intra-site relaxation therefore is expected to be weaker than competing mechanisms and is very sensitive to the vibrational spectrum of the specific molecular geometry and morphology.

Consequently, there are only a few papers treating intra-site relaxation in organics, such as ref.[91] which discusses SOC-mediated relaxation in endohedral N@C_{60}. Related literature can also be found for example in the context of singlet-triplet inter-system crossing of excitons[92] or spin relaxation in quantum dots[93] which are concerned with immobile spins.

Experimental work is similarly scarce, due to the difficulties in isolating ISR from Elliott-Yafet type relaxation and the expected slow relaxation rates relative to competing mechanisms.

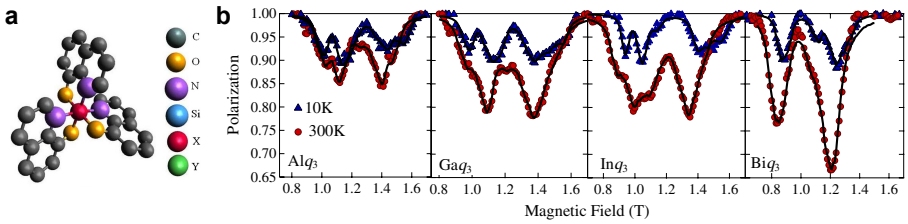

Figure 4.9: (**a**) Molecular geometry of Alq_3-based series Xq_3, where X = Al, Ga, In, Bi. (**b**) Muon spin rotation ALC resonances for the Xq_3 series of molecules at 300 K (red circles) and 10 K (blue triangles). Black curves are fits to the data to extract spin relaxation rates, which scale with the amplitude of the ALC curves. Figures reproduced from[96].

First evidence for an intra-site mechanism was found by Drew and coworkers who pioneered the use of muon spin resonance to probe electron spin relaxation in organic semiconductors[94]. In this technique, fully spin-polarized positive muons are implanted in an OSC where some of them capture an unpaired electron and form a hydrogen-like quasi particle. This "muonium" binds to a molecule where it remains localized during its lifetime of $\sim 2.2\,\mu s$[94].

Drew et al. then measure the increase of avoided level crossing (ALC) resonances of the muonium triplet state due to the relaxation of the bound electron spin. The extracted electron spin lifetimes for several small molecules show an Arrhenius-like temperature dependence with characteristic activation energies that indicate the thermal population of vibrational modes, such as 20 meV and 3 meV for 6,13-bis(triisopropylsilylethinyl) pentacene (TIPS-pentacene)[95].

To determine the type of coupling, they proceed with measurements on a series of molecules based on tris(8-hydroxyquinolinato) aluminum (Alq_3) and show a reduction of the electron spin lifetime at room temperature from 4.5 µs to 0.8 µs upon substitution of the central metal with successively heavier atoms (from aluminum, $Z = 13$ to bismuth, $Z = 83$)[96]. Their results, shown in Fig. 4.9, indicate that ISR is indeed mediated by SOC for this series of molecules, and that lifetimes remain comparatively long despite the heavy metal content (compare for example to Chapter 6).

Chapter 5

Experimental Methods

5.1 ESR setup

All ESR measurements in this thesis were carrier out on a Bruker E500 spectrometer with an X-band microwave source and Bruker's ER 4122SHQE cavity. Low temperature measurements were performed with an Oxford Instruments ESR900 helium cryostat, controlled through a MercuryiTC temperature controller. Electrical measurements and biasing of devices mounted in the ESR cavity were performed with a Keithley 2602b with dual source measurement units (SMUs). All measurements were carried out through CustomXepr, a self-developed Python software enabling the integrated control of all three instruments and the scheduling of automated measurements and temperature cycles. An introduction to CustomXepr is given in Appendix C.

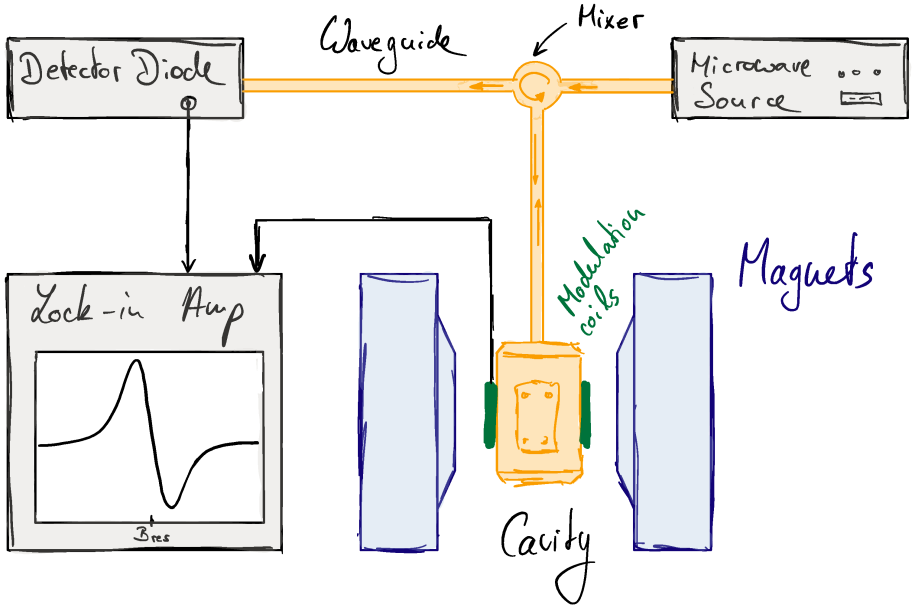

Figure 5.1: Sketch of the Bruker E500 setup.

ESR spectra are recorded as a lock-in measurement where coils attached to the cavity modulate the external magnetic field at a frequency of 100 kHz and with amplitudes between 10 µT to 2 mT. The resulting ESR signal is approximately proportional to the derivative of the absorption curve as shown in Fig. 5.1. The modulation amplitude should be set to a value smaller than the resonance linewidth to prevent distortions and artificial broadening of the spectrum. The magnetic field is determined with an accuracy of ±1 µT by using a nuclear magnetic resonance teslameter.

Cavity layout and field

The SHQE cavity with a mounted cryostat has a resonance frequency of 9.4 GHz and is designed to separate the electric and magnetic components of the microwave field, with the latter being largest at the sample area in the cavity centre (see Fig. 5.3). This gives a volume with a diameter of 5 mm and a height of 40 mm as a sample space. The samples themselves are held in quartz tubes with an inner diameter of 3.8 mm and an outer diameter of 4.5 mm, leaving a thin gap for helium flow between the sample tube and the cryostat walls while still allowing for 3.0 mm wide samples.

Since the field separation is not perfect, samples with a high dielectric constant cause additional absorption of the microwave electric field and a concurrent reduction of the total field amplitude, resulting in a loss of sensitivity. Moreover, the magnetic component falls off towards the top and bottom of the cavity and samples in those areas will give weaker signals. Section 5.3 discusses how both effects can be taken into account for quantitative measurements.

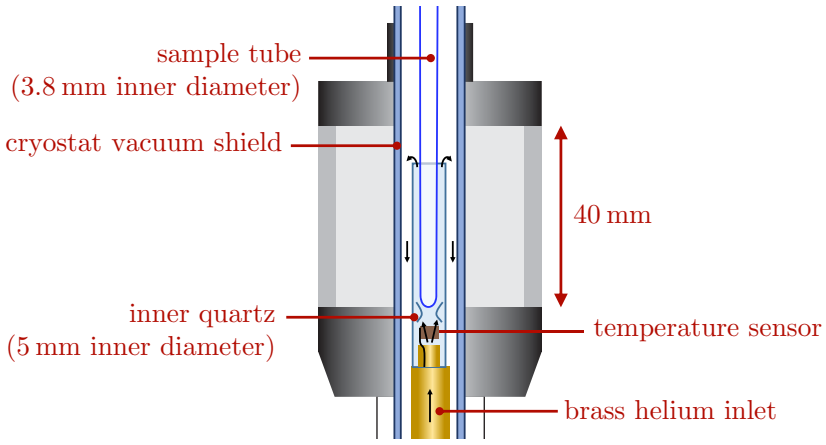

Figure 5.2: Schematic of the Oxford Instruments ESR900 helium cryostat with sample tube inside the ESR cavity. Black arrows indicate the direction of helium flow.

The reduction of the microwave field amplitude through absorption from the sample can be quantified by changes to the cavity Q-factor. It is defined as the energy stored divided by the energy dissipated per microwave cycle and scales inversely with the FWHM of the cavity resonance $\Delta\omega$ and linearly with its resonance frequency ω_{res}:

$$Q = \frac{\omega_{\text{res}}}{\Delta\omega} \tag{5.1}$$

The empty Bruker E500 SHQE cavity exhibits a Q-factor of $\sim$11,000 which is reduced to values between 4,000 - 8,000 with a loaded sample, depending on its dielectric constants.

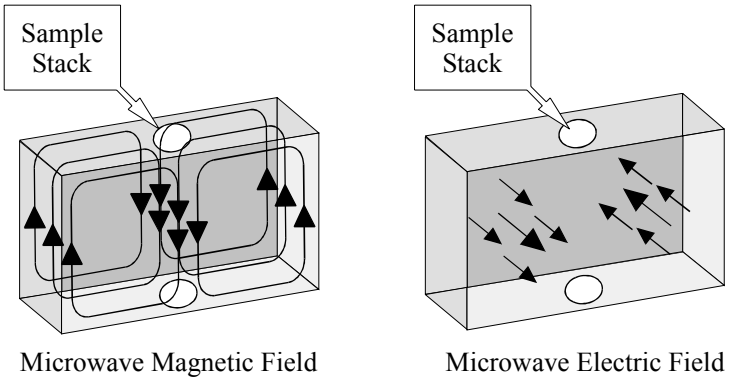

Figure 5.3: Microwave magnetic and electric fields in a ESR cavity (reproduced from Bruker E500 manual). The external magnetic field **B** is oriented in the horizontal plane.

5.2 Determination of spin lifetimes

One of the key factors that determines a material's suitability for spintronics applications is the spin lifetimes. As outlined in the previous chapter, we distinguish between the spin-lattice relaxation time T_1 which determines the lifetime of a non-equilibrium spin polarization, the spin-coherence time T_2, and the macroscopic dephasing time T_2^*. This section will show how we can, under most conditions, extract all three lifetimes from microwave-power-dependent ESR measurements. We will first discuss the best fitting procedures to determine spin lifetimes from absorption spectra and then proceed to account for effects of the field modulation and lock-in detection.

Determining T_2 from a single Lorentzian resonance.

Charges in organic semiconductors are, over a wide temperature range, sufficiently mobile for motional narrowing to average over local hyperfine and spin-orbit fields. The coherence time T_2 can therefore be extracted directly from the width of the resulting single Lorentzian resonance line if the system is not in saturation. The ESR absorption signal from Eq. (3.25) simplifies to

$$L(B, B_{\mathrm{mw}}) \propto \chi_0 \frac{\omega B_{\mathrm{mw}} T_2}{1 + \gamma_{\mathrm{e}}^2 T_2^2 (B - B_{\mathrm{res}})^2 + \gamma_{\mathrm{e}}^2 T_1 T_2 B_{\mathrm{mw}}^2} \tag{5.2}$$

$$\simeq \chi_0 \frac{\omega B_{\mathrm{mw}} T_2}{1 + \gamma_{\mathrm{e}}^2 T_2^2 (B - B_{\mathrm{res}})^2} \tag{5.3}$$

with Eq. (5.3) valid for $\gamma_{\mathrm{e}}^2 T_1 T_2 B_{\mathrm{mw}}^2 \ll 1$. A least-squares fit to an absorption signal will then give the spin-coherence time but not the spin-lattice relaxation time.

Accounting for field modulation

In continuous-wave (cw-)ESR measurements, the external magnetic field is modulated with a frequency ω_{mod} and a peak-to-peak amplitude B_{mod}

$$B(t) = B_0 + \frac{B_{\mathrm{mod}}}{2} \sin(\omega_{\mathrm{mod}} t) \tag{5.4}$$

and the signal is detected by a lock-in amplifier as a first or second harmonic of ω_{mod}. It is therefore proportional to the change in microwave absorption during a modulation cycle and a larger modulation amplitude B_{mod} will result in a stronger signal.

If the absorption curve is approximately linear in the modulation interval, e.g., if B_{mod} is much smaller than the linewidth, the first harmonic signal resembles the derivative of the absorption curve. The derivatives of Eq. (5.2) or Eq. (5.3) with respect to B are therefore commonly used to fit ESR spectra.

The required small modulation amplitudes are often impractical for field-induced ESR measurements, where the number of spins and therefore the signal intensity is very weak. To improve the of signal-to-noise ratio, we are often forced to choose values of B_{mod} that approach the smallest features in the spectrum and account for the resulting distortions in lineshape during fitting.

We follow the method outlined by Hyde et al.[97] to account for field modulation but emphasize that it is applicable to lock-in measurements in general. The full time-dependent diode current $s(B_0, B_{\mathrm{mod}}, t)$ can be expressed in terms of the Fourier transform $\tilde{S}(\beta)$ of the ESR absorption signal:

$$s(B_0, B_{\mathrm{mod}}, t) = \int_{-\infty}^{\infty} \tilde{S}(\beta) \mathrm{e}^{iB(t)\beta} \mathrm{d}\beta = \int_{-\infty}^{\infty} \tilde{S}(\beta) \mathrm{e}^{i[B_0 + (B_{\mathrm{mod}}/2)\sin(\omega_{\mathrm{mod}} t)]\beta} \mathrm{d}\beta \tag{5.5}$$

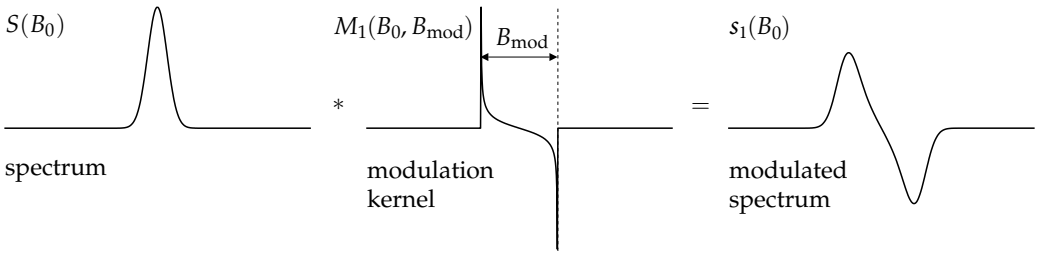

Figure 5.4: Visualization of field modulation and first harmonic detection as a convolution with a modulation kernel $M_1(B_0, B_{\mathrm{mod}})$. In this case the modulation amplitude exceeds the linewidth of the Lorentzian spectrum and the resulting modulated signal clearly deviates from a Lorentzian derivative. Figure reproduced with modifications from[86].

The exponent can be expanded as a sum of nth order Bessel functions J_n of the first kind as follows:

$$s(B_0, B_{\mathrm{mod}}, t) = \sum_{n=-\infty}^{\infty} \mathrm{e}^{in\omega_{\mathrm{mod}}t} \int_{-\infty}^{\infty} \tilde{S}(\beta) J_n\left(B_{\mathrm{mod}}\beta/2\right) \mathrm{e}^{iB_0\beta} \mathrm{d}\beta \tag{5.6}$$

First harmonic detection only measures the part of the signal which varies in time as ω_{mod}, the summands with $n = \pm 1$, and therefore gives

$$s_1(B_0, B_{\mathrm{mod}}, t) = 2i \sin(\omega_{\mathrm{mod}}t) \int_{-\infty}^{\infty} \tilde{S}(\beta) J_1\left(B_{\mathrm{mod}}\beta/2\right) \mathrm{e}^{iB_0\beta} \mathrm{d}\beta\,. \tag{5.7}$$

The time-dependence drops out during phase-sensitive detection with the lock-in amplifier. Corresponding expressions can be given for higher order harmonics (see refs.[86,97]). The above equation is implemented in MATLAB to reproduce the experimental spectra: the expected curve for specific lifetimes is Fourier transformed, multiplied with a first order Bessel function $J_1\left(B_{\mathrm{mod}}\beta/2\right)$ and transformed back before fitting to the spectrum. Since the modulation amplitude is known from the selected acquisition parameters, the resulting signal distortions are fully taken into account.

The effect of field modulation therefore can be written as a convolution of the absorption spectrum $S(B_0)$ with a modulation kernel[86]

$$M_n(B_0, B_{\mathrm{mod}}) = i^n \int_{-\infty}^{\infty} J_n\left(B_{\mathrm{mod}}\beta/2\right) \mathrm{e}^{iB_0\beta} \mathrm{d}\beta \tag{5.8}$$

so that the n-th harmonic signal (with the time dependence dropped) is given by

$$s_n(B_0, B_{\mathrm{mod}}) = M_n(B_0, B_{\mathrm{mod}}) * S(B_0)\,. \tag{5.9}$$

This makes it easy to visualize the effect of field modulation, as seen in Fig. 5.4 for the first harmonic spectrum. The modulation kernel becomes a function with two peaks separated by B_{mod}. Distortions from the derivative shape are introduced when the separation of those peaks approaches the linewidth of the spectrum.

However, if B_{mod} exceeds the spectral linewidth the true multi-photon nature of the field-modulated ESR experiment results in the appearance of side bands[98,99] which are not modeled by Eq. (5.7).

Fitting a power saturation measurement

Determining both T_1 and T_2 requires us to know the saturation behavior of the spectrum under sufficiently high microwave powers. Mathematically, this results from the fact that $S(B_0)$ is independent of T_1 in the absence of saturation. Physically, driving the system until spin-lattice relaxation is unable to maintain a population difference tells us the relaxation rate.

The common approach in literature has been to determine the integrated area of spectra for different microwave powers individually and then fit the power dependence of this area to Eq. (3.28):

$$A(B_{\mathrm{mw}}) \propto \chi_0 \frac{\pi}{\gamma_{\mathrm{e}}} \frac{B_{\mathrm{mw}}}{\sqrt{1+\gamma_{\mathrm{e}}^2 T_1 T_2 B_{\mathrm{mw}}^2}} \,. \tag{5.10}$$

This method, even though commonly applied to noisy FI-ESR spectra[78,79], has the significant disadvantage of large fitting errors for spectra at either very small or large microwave powers. This is shown for a simulated power saturation measurement in Fig. 5.5a with artificially introduced $1/f$ noise to give a signal-to-noise (S/N) ratio of 5 dB. Extracting the lifetimes from Eq. (5.10) yields a T_1 value which is under-estimated by 80 % and a deviation in T_2 of 10 % (see Fig. 5.5b). We propose instead to fit the full power saturation measurement, i.e., all spectra at once, to the expected saturation behavior from Eq. (5.2):

$$\begin{aligned} s(B_0, B_{\mathrm{mw}}) &= M_1(B_0, B_{\mathrm{mod}}) * L(B_0, B_{\mathrm{mw}}) \\ &\propto M_1(B_0, B_{\mathrm{mod}}) * \chi_0 \frac{\omega B_{\mathrm{mw}} T_2}{1+\gamma_{\mathrm{e}}^2 T_2^2 (B_0 - B_{\mathrm{res}})^2 + \gamma_{\mathrm{e}}^2 T_1 T_2 B_{\mathrm{mw}}^2} \,. \end{aligned} \tag{5.11}$$

Such a 2D surface fit uses the stronger signal from intermediate MW powers to stabilize the fit of the saturated and low power spectra. This fitted surface is shown in Fig. 5.5a and the fitted lifetimes for T_1 and T_2 deviate by only 4% and 7%, respectively, from the actual ones used to create the data set. Especially the extracted T_1 value is significantly more accurate despite the high noise level.

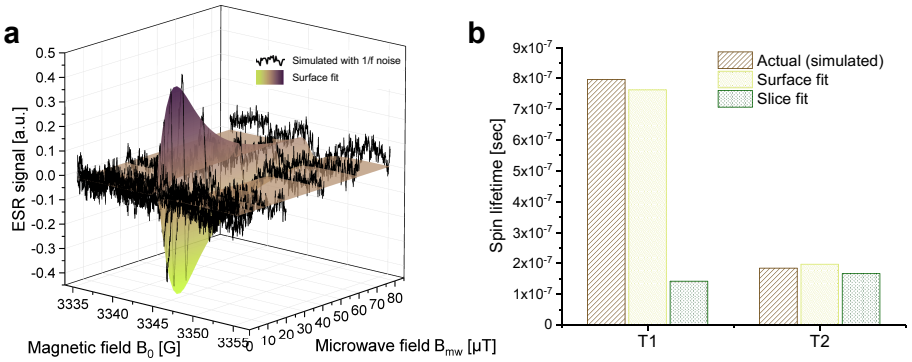

Figure 5.5: Fitting a power saturation measurement in the presence of noise. (**a**) Simulated ESR spectra for a Lorentzian resonance with lifetimes of $T_1 = 0.8\,\mu s$ and $T_2 = 0.2\,\mu s$ for increasing microwave fields. $1/f$ noise with a S/N ratio of 5 dB has been artificially added and the resulting spectra are fitted as a single 2D data set to Eq. (5.11). (**b**) Comparison of actual lifetimes used for the simulation and lifetimes extracted from the 2D surface fit and from Eq. (5.10) with integrated areas obtained from Lorentzian fits to individual spectra.

Fitting an inhomogeneous line

A single Lorentzian fit is no longer possible when the resonance line is inhomogeneously broadened, for example at sufficiently low temperatures where motional narrowing becomes ineffective. In the simplest case, an unresolved splitting from local HFI and SOC fields can be modeled as a Gaussian distribution around the center resonance B_{res} with a standard deviation of B_{rms}:

$$G(B - B_{\mathrm{res}}) = \frac{1}{\sqrt{2\pi B_{\mathrm{rms}}^2}} \exp\left(-\frac{(B - B_{\mathrm{res}})^2}{2B_{\mathrm{rms}}^2}\right) . \tag{5.12}$$

In many cases, all spin packets approximately have the same lifetimes $T_{1,2}$. This will be confirmed experimentally in Chapter 6 for small molecules in solution where we can fit the HFI-split spectra with a single linewidth for all resolved resonances. In this case every unresolved local field contributes the same Lorentzian lineshape to the overall resonance. The absorption signal becomes a convolution of a Gaussian envelope and a Lorentzian lineshape, which is a so-called Voigt function:

$$V(B_0, B_{\mathrm{mw}}) = \int_{-\infty}^{\infty} L(B' - B_0, B_{\mathrm{mw}}) G(B' - B_{\mathrm{res}}) \mathrm{d}B' . \tag{5.13}$$

Qualitatively, the effect of the Gaussian envelop will be to delay the broadening of the resonance with MW power while the integrated area still saturates with Eq. (5.10). In the limit of weak spectral diffusion, the overall power saturation behavior follows the fit function[100,101]

$$s(B_0, B_{\mathrm{mw}}) = M_1(B_0, B_{\mathrm{mod}}) * V(B_0, B_{\mathrm{mw}}) \tag{5.14}$$

with five parameters fitting parameters: the spin lifetimes $T_{1,2}$, the inhomogeneous field distribution B_{rms}, the resonance center B_{res}, and the overall magnitude of the signal, which is proportional to χ_0. Only the first three determine the lineshape and its saturation behavior, with mutually independent effects, resulting in a very robust fit.

If the envelope function of the spin packet distribution is not known or cannot be easily modeled, it will become necessary again to determine the product of spin lifetimes T_1T_2 from a fit to the integrated area of the spectra. In this case it is essential to achieve a sufficiently high S/N ratio to minimize the potentially large errors.

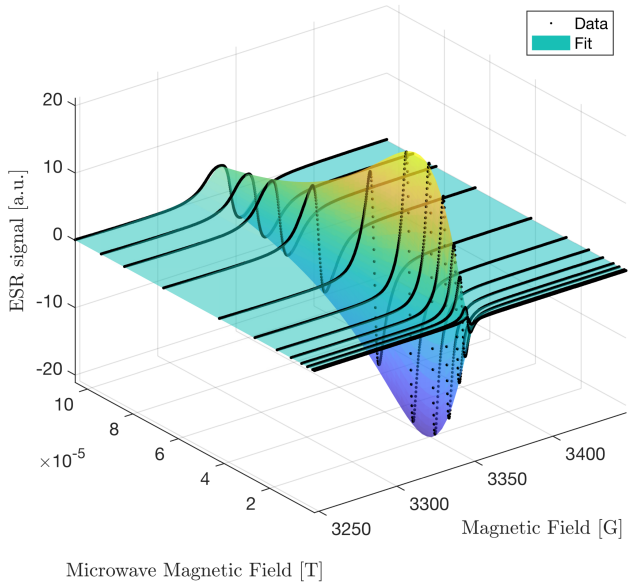

Figure 5.6: ESR spectra of the polymer pBTTT doped with the small molecule F4–TCNQ at 5 K and surface fit of the power saturation behavior to Eq. (5.11).

5.3 Microwave field in cavity

Determining the absolute number of spins or the spin-lattice relaxation time of a sample relies on the knowledge of B_{mw} over the sample volume while only the applied power P_{mw} is recorded during an experiment. The scaling of B_{mw} with $\sqrt{P_{\mathrm{mw}}}$ depends on the resonator architecture and losses inside the cavity.

In the absence of power saturation, the integrated absorption signal of a paramagnetic sample scales only with its magnetic susceptibility and the field amplitude B_{mw} at the sample position. This allows us to determine B_{mw} from the integrated

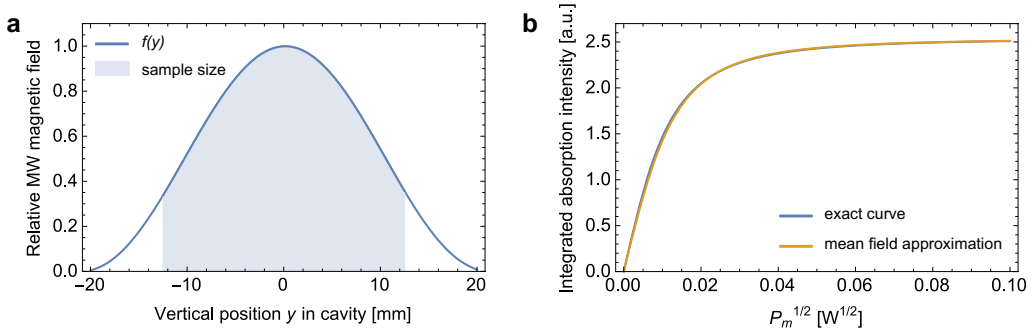

Figure 5.7: (**a**) Microwave magnetic field distribution $f(y)$ inside the Bruker ER 4122SHQE cavity. The shaded area is representative of a 25 mm long sample. (**b**) Exact power saturation curve from Eq. (5.17) taking into account the variation in signal intensity for different positions in the cavity and power saturation behavior of a sample that only sees a uniform average microwave field $\overline{B_{\mathrm{mw}}(y)}$. Shown curves are for $L = 25\,\mathrm{mm}$ since any visible difference disappears for smaller lengths.

absorption signal of a reference sample with a known susceptibility. For the center of the cavity, we find as a function of the cavity Q-value and the incident microwave power

$$B_{\mathrm{mw}}^{\mathrm{center}} = \eta \cdot \sqrt{Q P_{\mathrm{mw}}}\,, \quad \eta = 2.4069 \times 10^{-6}\,\mathrm{T\,W^{-1/2}}\,. \tag{5.15}$$

The vertical microwave magnetic field distribution $f(y)$ is given by Bruker as a 9th order polynomial and stored with each data acquisition file (Fig. 5.7a). We additionally confirmed the values by monitoring the ESR signal intensity for a point-like marker sample for different positions in the cavity. Since our samples are confined in a tube with a diameter of 3 mm around the cavity center, we only correct for the vertical field distribution by calculating the average microwave field across the sample length L and neglect any radial variations:

$$\overline{B_{\mathrm{mw}}(y)} = \frac{1}{L}\int_{-L/2}^{L/2} f(y) B_{\mathrm{mw}}^{\mathrm{center}}\,\mathrm{d}y \tag{5.16}$$

A small error is introduced when using the average field over the sample volume to fit the power saturation behavior because we neglect that parts of the sample at positions with a lower field will not only saturate later but also contribute less to the total ESR signal. In fact, the precise expression for the integrated area DI of a spectrum would be

$$\mathrm{DI}(P_{\mathrm{mw}}) = \frac{1}{V}\int_{-L/2}^{L/2} A\left(f(y) B_{\mathrm{mw}}^{\mathrm{center}}\right) \cdot f(y)\,\mathrm{d}y \text{ with } V = \int_{-L/2}^{L/2} f(y)\,\mathrm{d}y\,, \tag{5.17}$$

where A denotes the integrated absorption spectrum for a single microwave field from Eq. (3.28). Our approximation on the other hand gives

$$\mathrm{DI}(P_{\mathrm{mw}}) \approx A(\overline{B_{\mathrm{mw}}(y)}) = A(\overline{f(y)}\eta\sqrt{QP_{\mathrm{mw}}})\,. \tag{5.18}$$

However, the resulting error for our sample length of $L = 20\,\mathrm{mm}$ remains well below 1 % because the volume fraction at positions $y \neq 0$ is double that of the volume fraction at $y = 0$. A comparison of estimated and exact power saturation curves for a 25 mm long sample is shown in Fig. 5.7b; any visible differences disappear completely for sample lengths of $\sim 20\,\mathrm{mm}$.

We also neglect the (small) distortion of the microwave field due to the sample's dielectric properties, which we expect to create a systematic error $< 4\%$ in T_1 .

5.4 Field effect transistors

A common approach to investigate charge transport in organic semiconductors is through their use as active layers in field effect transistors (FETs). This allows for tuning of the carrier concentration by modulating the gate voltage, without the need to introduce dopants to the film, and provides a platform to concurrently study spin and charge dynamics. Beyond their use in research, organic FETs also enable applications for high mobility polymers such as active-matrix addressing of flexible organic light-emitting diode (OLED) displays[4]. In this section, we introduce the basic concept of FETs and Section 5.5 will present the large-area transistor architecture we developed for field-induced ESR measurements.

FETs are based on a metal-insulator-semiconductor architecture where, upon application of a gate voltage V_{G}, charges accumulate at the semiconductor-insulator interface (see Fig. 5.8). This charge accumulation layer allows a current to flow between two electrodes (source and drain) if a second voltage V_{D} is applied at the drain electrode.

When recording current-voltage characteristics, one can either apply a fixed gate voltage and sweep V_{D} (output characteristic) or fix the drain voltage and sweep V_{G} (transfer characteristic). Assuming a carrier-concentration-independent mobility, the current flowing though the channel is given by[17,102]

$$I_{\mathrm{SD}} = \frac{W}{L}\mu C_{\mathrm{i}}\left((V_{\mathrm{G}} - V_{\mathrm{th}})V_{\mathrm{D}} - \frac{1}{2}V_{\mathrm{D}}^2\right)\,. \tag{5.19}$$

Here, C_i is the dielectric capacitance per unit area and W and L are the channel width and length, respectively. V_{th} is the threshold voltage that needs to be overcome for the FET to switch "on".

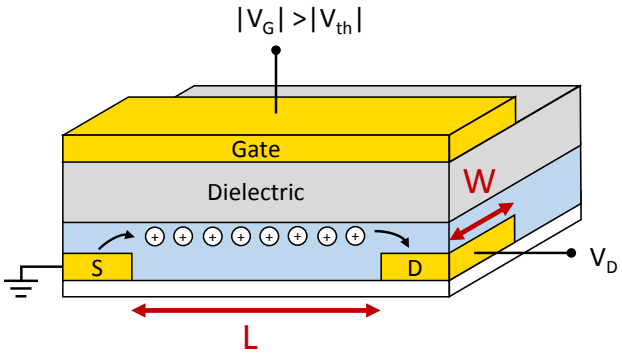

Figure 5.8: Sketch of a FET in hole accumulation mode. Upon application of a negative drain bias V_D holes are injected from the source electrode and travel to the drain electrode.

For small source-drain voltages, the above equation describes a linear increase of the current with V_G, due to the higher number of charge carriers, and with V_D, due to the higher drift velocity. As V_D approaches the gate voltage, the potential difference between gate and drain electrodes decreases and so does the carrier concentration close to the drain electrode. This pinch-off is depicted in Fig. 5.9 in the second row.

Increasing the drain voltage beyond V_G only moves this pinch-off point further into the channel and therefore does not increase the source-drain current. The FET is said to operate in the saturation regime. Eq. (5.19) remains valid by substituting $V_D \to V_G - V_{th}$:

$$I_{SD}^{sat} = \frac{W}{2L}\mu C_i (V_G - V_{th})^2 \tag{5.20}$$

Equations (5.19) and (5.20) can be used to extract the charge carrier mobilities in the linear and saturation regime, respectively. Simple differentiation gives

$$\mu_{lin} = \frac{L}{WC_iV_D}\frac{\partial I_{SD}}{\partial V_G} \qquad \text{for} \quad V_D \leq V_G - V_{th} \tag{5.21}$$

$$\mu_{sat} = \frac{2L}{WC_i}\left(\frac{\partial\sqrt{I_{SD}}}{\partial V_G}\right)^2 \qquad \text{for} \quad V_D \geq V_G - V_{th}\ . \tag{5.22}$$

We typically record two transfer curves to calculate mobilities, one at $V_D = \pm 5\,V$ and one at $V_D = \pm 60\,V$, and sweep the gate voltage up to $V_G = \pm 60\,V$. When extracting the mobility from the first curve in the interval from $\pm 40\,V$ to $\pm 60\,V$, we are well within the linear regime. For the second curve, we are in saturation only. The derivatives $\partial I_{SD}/\partial V_G$ and $\partial\sqrt{I_{SD}}/\partial V_G$ are extracted as linear fits to I_{SD} or $\sqrt{I_{SD}}$, respectively.

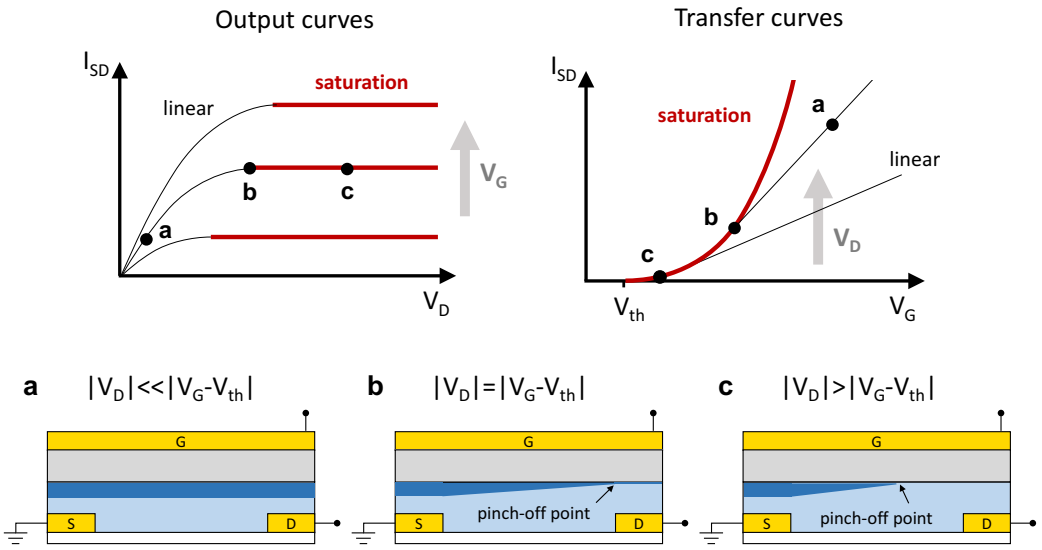

Figure 5.9: Carrier concentration in a FET channel during device operation: in the linear regime (**a**), at the onset of saturation (**b**), and well in the saturation regime (**c**). The respective points are highlighted in the output and transfer characteristics. The accumulation layer is only a few nm thick and the increasing width of the dark blue area does not indicate a thicker accumulation layer but a higher carrier concentration.

The above equations describe the FET behavior in the case of a field-independent mobility. As we have seen in Section 2.2, this must not generally be the case and transfer characteristics often deviate from the ideal FET behavior. This deviation often becomes more pronounced at low gate voltages since states in the tail of the DOS tend to be more localized. Nevertheless, Eqs. (5.21) and (5.22) still allow the extracting of an effective, gate-voltage-dependent mobility.

Even though FETs provide a convenient way to investigate charge transport in organic semiconductors, one should keep in mind that the source-drain current not only depends on the intrinsic properties of the material and its thin film morphology but also on external factors such as the dielectric-semiconductor interface (e.g., higher-k dielectrics tend to introduce more dipolar disorder in the accumulation layer) and the efficiency of charge injection at the electrodes (contact resistance)[20]. Such effects manifest themselves in different ways in the current-voltage characteristics: a high contact resistance at the source or drain electrodes for instance can be overcome by applying large gate voltages in the saturation regime but will cause an underestimation of the mobility in the linear regime[103] or dielectric-induced disorder can mask the effects of smaller intrinsic energetic disorder.

5.5 Field-induced ESR devices

Sample layout

The layout of the ESR cavity results in the microwave magnetic field B_{mw} being dominant in a narrow volume around the cavity center and requires a matching device design. We simultaneously aim to maximize the channel area in order to increase the number of spins and thus the ESR signal. Our transistor design with an active area of 2.45 mm width and 20 mm height therefore limits the device to a volume where B_{mw} is dominant over the electric component while maintaining a large total area. Such an asymmetric layout naturally poses problems for spin-coating, the method of choice for polymer thin film deposition. In addition, the large active area increases the probability of small defects and pin holes that typically result in high gate-leakage currents. Avoiding such defects imposes stringent requirements on the polymer and dielectric deposition process. It is thus preferable to manufacture multiple FETs on one large substrate and to separate them post processing.

Plastic substrates can be conveniently cut into shape after manufacturing but their high surface roughness introduces additional defects in large area FETs[78]. We instead use 0.5 mm thick and $40 \times 40\,\mathrm{mm}^2$ large high purity Vitreosil®77 fused quartz for bottom substrates with only trace amounts of paramagnetic impurities (see Table 5.1). To facilitate the separation of FETs after processing, we pre-cut 0.3 mm deep grooves into the substrate's back side with a diamond saw. A custom-designed vacuum chuck made out of polydimethylsiloxane (PDMS) with a hole pattern matching the grooves is used to hold the substrate during spin-coating.

Element	ppm
Al	15
Ca	0.5
Cr	< 0.01
Cu	< 0.01
Fe	0.1
K	0.2
Li	0.2
Mn	0.01
Na	0.1
Nd	0.01
Ti	1.3
Y	< 0.1
Zr	1.3
OH	170

Table 5.1: Concentration of trace elements in Vitreosil quartz.

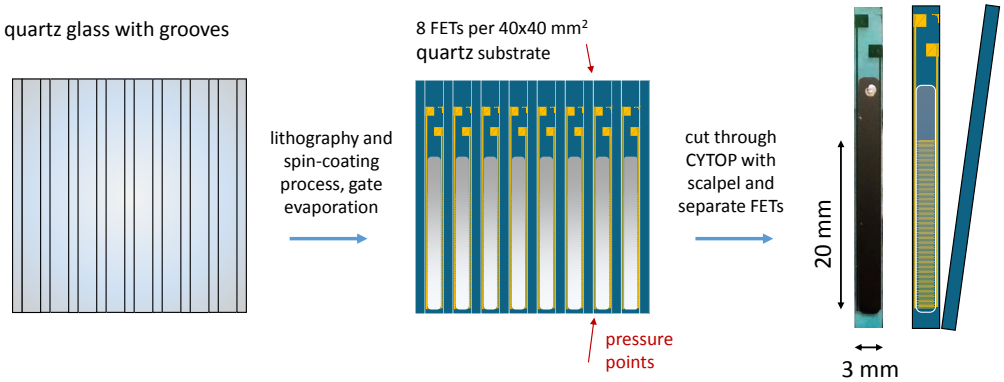

Figure 5.10: Manufacturing process of IDTBT transistors for FI-ESR on top of $40 \times 40\,\mathrm{mm}^2$ quartz slides with pre-cut grooves on the back. The photograph on the right shows a real device.

We then proceed with a standard top-gate bottom-contact FET manufacturing process on the substrates smooth top surface. We use interdigitated source and drain electrodes made out of gold with the design shown in Fig. 5.11. The channel length and width are $L = 100\,\mu m$ and $W = 243\,mm$, respectively, with $50\,\mu m$ wide electrode fingers and a total active area size of $2.45 \times 20\,mm^2$. Contact pads for electrical connections are located at the top of the sample, about 10 mm away from the active area, to be placed outside the microwave cavity.

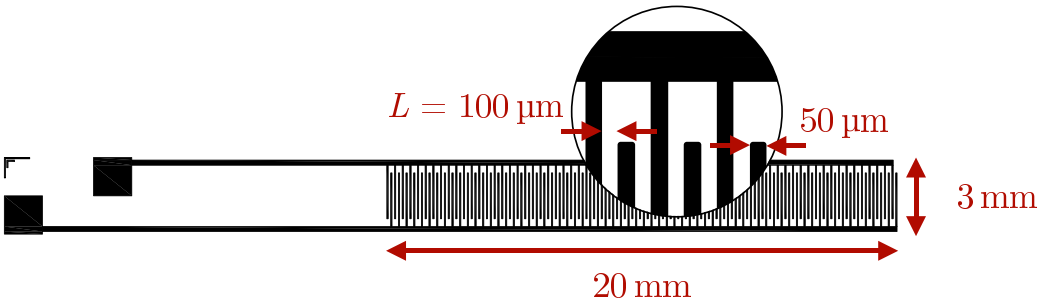

Figure 5.11: Schematic of FI-ESR source and drain electrode layout.

Fabrication steps

To achieve the required precision, the gold electrodes are evaporated onto the quartz substrate after a double layer lithographic patterning process: A layer of lift-off-resist and photo-resist subsequently are spin-coated on top of the cleaned substrates and exposed to UV-light through a photomask with the previously described electrode pattern. The double layer of resist is then developed, removing it at the exposed areas with a small undercut and effectively creating a high-precision evaporation mask on the quartz surface.

In a vacuum of 1×10^{-6} mbar we then evaporate 4 nm of chrome as an adhesion layer and 25 nm of gold for the electrodes. After lifting off the remaining photo resist in a 1-Methyl-2-pyrrolidone (NMP) bath for 2 h, we are left with patterned gold electrodes. The whole process is optimized for large area substrates with the following processing parameters:

Spin LOR 5B lift-off resist at 500 rpm for 5 sec and 2000 rmp for 45 sec, bake at 170 °C for 5 min

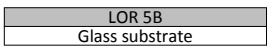

Spin S1813 photo resist at 500 rpm for 5 sec and 3000 rmp for 45 sec, bake at 110 °C for 2 min

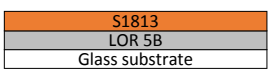

Expose with UV-light beneath photo mask for 14 sec

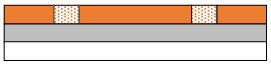

Develop in MF-319 for 60 sec, clean in deionized water, dry in N_2 and etch with O_2 plasma at 150 W for 1 min

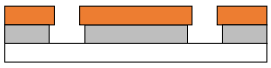

Evaporate 4 nm of chrome and 20 nm of gold at a rate of 0.5 Å sec^{-1} and a pressure $< 10^{-6}$ mbar

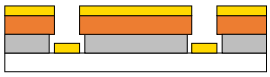

Lift-off in NMP for 2 h, rinse in acetone and IPA and etch with O_2 plasma at 300 W for 10 min

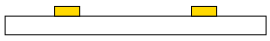

The substrates with bottom electrodes are then cleaned by sonicating them in acetone and IPA and exposing them to O_2 plasma for 10 min at 300 W. The active polymer layer and dielectric are successively spin-coated on top and annealed, with the exact deposition parameters depending on the chosen materials. Finally, a 30 nm thick aluminum electrode is deposited through shadow-mask-evaporation as a top gate, covering the entire active area. The finished devices can then be separated by applying a small amount of manual pressure to the pre-cut grooves on either side of the substrate.

Electrical contacting

The devices are mounted on top of a quartz glass carrier with copper tracks for the electrode connections as shown in Fig. 5.12 and contacted though wire bonding. This results in electrical connections which remain stable down to 5 K and over multiple temperature cycles while keeping the bulk of the electrical connections (soldering points, copper tracks) outside of the cavity. The device electrodes themselves are much thinner than the skin depth of ca. 800 nm for gold and aluminium at a microwave frequency of 9 GHz and therefore have little impact on the resonance properties of the cavity.

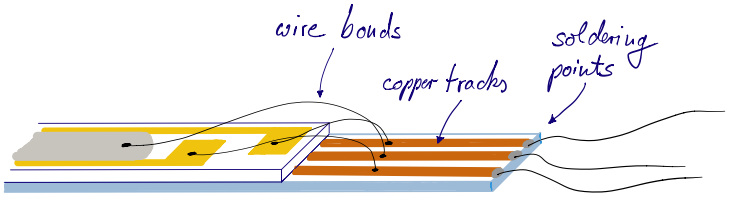

Figure 5.12: Schematic of electrical contacts to a FI-ESR device.

Chapter 6

Tuning spin-orbit coupling in small molecules

Organic semiconductors exhibit exceptionally long spin lifetimes, and the recently observed inverse spin hall effect in conjugated polymers could enable all organic spintronics devices. The control of spins and spin-to-charge conversion in organics requires understanding the molecular spin-orbit coupling (SOC), and a means to tune its strength. However, quantifying SOC strengths indirectly through spin relaxation effects has proven difficult due to competing relaxation mechanisms.

We present a systematic study of the g-tensor shift in molecular semiconductors and link it directly to the SOC strength in a series of high mobility molecular semiconductors with strong potential for future devices. The results demonstrate a rich variability of molecular g-shifts with the effective SOC, depending on subtle aspects of molecular composition and structure. We demonstrate that alkylation can have strong effects on the spin-physics with only minor alterations of the electronic properties.

We correlate the above g-shifts to spin-lattice relaxation times over four orders of magnitude, from 200 μs to 0.15 μs, for isolated molecules in solution and relate our findings to the spin relaxation mechanisms that are likely to be relevant in solid state systems.

Organic semiconductors and conductors are enabling flexible, large-area optoelectronic devices, such as organic light-emitting diodes, transistors, and solar cells. Due to their exceptionally long spin lifetimes, these carbon-based materials could also have an impact on spintronics where carrier spins play a key role in transmitting, processing and storing information[8]. The recently observed inverse spin hall effect (ISHE) in organics[5,6] – the conversion of a spin current to a transverse charge current – potentially enables fully organic spintronics devices.

Spin-orbit coupling (SOC), a relativistic effect which couples a charge's angular momentum to its spin, plays a dual role in such devices: it drives the spin-to-charge conversion and also provides a pathway for spin relaxation. Despite its fundamental importance for device applications, quantifying SOC strengths in organics based on investigating spin relaxation has proven difficult due to the competing and hard-to-distinguish contribution from hyperfine interactions (HFI)[73], which is the coupling of the charge's spin to nuclear spins. In fact, both SOC and HFI have been used separately to explain the magneto resistance[104] and spin diffusion length[105] in spin valves of the same organic material.

The comparison of spin diffusion lengths λ_S on the other hand has indeed revealed significant variations between different organic semiconductors[66,104,106], but separating effects of the charge carrier mobility and density[77] from the spin's coupling to its environment remains challenging. In addition, organic spin valve measurements can be affected by tunneling magneto resistance through pin hole defects[107] which complicates an accurate determination of λ_S.

A more direct probe of SOC is the voltage generated by spin-to-charge conversion (ISHE voltage). However, such measurements often only provide the product of λ_S and the spin Hall angle[6] and are prone to artifacts[108]. A systematic quantitative study of SOC strengths has therefore been hindered by the difficulty in isolating the effect of SOC on spin lifetimes, diffusion lengths or inverse spin hall voltages.

In this work we show that the g-factor (the isotropic part of a spin's coupling to an external magnetic field) of an unpaired spin from a charged molecule can be used as a measure of the effective SOC, over a wide range of SOC strengths. By effective SOC, we mean the overlap between the orbital and spin angular momentum distributions, which respectively depend on the molecular composition and geometry, and the spin density in the charged molecule. Shifts of the g-factor from its free electron value (Δg) arise from SOC and orbital Zeeman terms in

the Hamiltonian and are easily accessible by electron spin resonance (ESR). This provides a method to quickly and unambiguously determine the effective SOC over a wide range of light molecules without relying on indirect measurements. Our results demonstrate a remarkably rich variability - and therefore, potential for purposeful tuning - of molecular g-factors with subtle aspects of the molecular structure and composition.

In the second part of this chapter, we correlate the above g-shifts to spin-lattice relaxation times determined by power saturation ESR measurements and demonstrate a change in spin lifetimes over four orders of magnitude, from 200 µs to 0.15 µs, with increasing Δg. This suggests that the change in g-factor can be indeed attributed to an increase in SOC and a corresponding reduction of the spin-lattice relaxation time.

While our simulations and measurements were all performed on isolated molecules, we argue that the gained information will be valuable to understand bulk systems, which in these systems are strongly influenced by the single molecule properties.

We compare a set of 32 fused-ring molecular semiconductors with systematically varying geometries and atomic substitutions, most of which are based on central thiophene or selenophene moieties that are commonly found in high-mobility organic semiconductors. Many of the chosen molecules such as 2,7-dioctyl[1]benzothieno[3,2-b][1]benzothiophene (C8-BTBT), 2,9-didecyl-dinaphtho[2,3-b:2',3'-f]thieno[3,2-b]thiophene (C10-DNTT) or rubrene are widely studied and perform exceptionally well in organic thin film transistors with hole mobilities of 5–10 $\mathrm{cm^2\,V^{-1}\,s^{-1}}$ and signs of coherent charge transport such as a metallic Hall effect[13] and a band-like temperature dependence of the mobility[109]. Since high charge carrier mobilities are expected to improve spin diffusion lengths[8] and the spin Hall angle is predicted to increase with reduced energetic disorder[55], such systems are natural candidates for spintronics applications. Hence, the chosen series of molecules offers a unique opportunity to systematically study the strength of SOC and its effect on spin lifetimes.

All ESR measurements were performed on radical cations in solution. To quantitatively understand these measurements we performed density functional theory (DFT) calculations on positively charged molecules in the gas phase. This enables us to calculate spin density distributions with an accuracy that is not achievable for bulk systems and to experimentally resolve the HFI splitting of resonance lines. The latter acts as a probe of the spin density at nuclear coordinates throughout

the molecule and provides an experimental method to validate the spin density calculations. Large parts of this chapter have been published in Nature Communications[110].

6.1 Experimental g-shifts in organic molecules

Sample preparation and measurement conditions

In order to achieve controllable experimental conditions with spin densities that can be reasonably compared to DFT calculations, we performed all ESR experiments on highly dilute solutions of radical cations in dichloromethane (DCM). The chosen cation concentrations below $0.5 \times 10^{-3}\,\mathrm{mol\,L^{-1}}$ prevent interactions between spins on different molecules. The neutral molecules were oxidized in solution by adding aluminum chloride ($AlCl_3$), a strong oxidizing agent which is sufficiently soluble in DCM, and the successful p-type doping was confirmed by optical spectroscopy (Fig. 6.1a,b)[45]. All ESR spectra were recorded on a Bruker E500 X-band spectrometer with a Bruker ER 4122SHQE cavity at frequencies of 9.4–9.7 GHz and at low microwave powers of 0.006–0.06 mW to prevent power saturation effects and the concurrent linewidth broadening as shown in Fig. 6.7c.

The external magnetic field was modulated at 100 kHz and the spectra were recorded in lock-in measurements. As a consequence, passage effects can distort the signal shape if the spin packets cannot relax between modulation cycles. This is avoided by choosing a sufficiently small modulation amplitude B_{mod} or frequency ω_{mod} so that $\omega_{\mathrm{mod}} B_{\mathrm{mod}} \ll 1/\gamma_e T_1 T_2$ and the spin system remains continually in thermal equilibrium[111].

The solutions of molecules in dichloromethane were prepared in a nitrogen glove box and sealed in sample tubes prior to the measurement. To minimize the perturbation of the microwave field inside the cavity, the solution was confined to a capillary tube with an inner diameter of 1 mm at the cavity center where the magnetic field is largest (Fig. 6.7a). This allows us to perform the measurements at high quality factors of $Q \approx 8000 - 10000$ (the ratio between the power stored and the power dissipated per microwave cycle).

The molecules were doped by adding $AlCl_3$ and most solutions remained stable for > 12 h (confirmed by both ESR and optical spectroscopy). Acquiring a full series of spectra with varying microwave powers took at most 1.5 h. After 24 h we could observe a noticeable reduction in the number of cations but no spectral changes that would indicate a reaction of $AlCl_3$ with the molecules. The only exception to this are C8-BTBT and C8-BSBS which exhibit the emergence of a secondary

spectrum with a smaller g-factor but partially overlapping with the organic radical signal. The new species are likely to be chlorinated versions of the molecules. We therefore conducted all C8-BTBT and C8-BSBS measurements immediately after adding $AlCl_3$ and before any spectral changes took place.

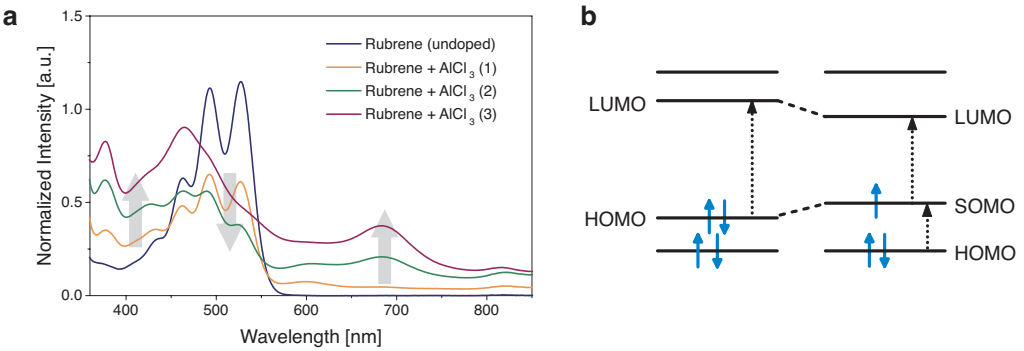

Figure 6.1: (**a**) Optical absorption spectra of a $0.5 \times 10^{-3}\,\mathrm{mol\,L^{-1}}$ solution of rubrene in DCM with increasing amounts of $AlCl_3$ (molar ratio in brackets). We observe the expected bleaching of the transition between the highest occupied molecular orbital (HOMO) and the lowest unoccupied molecular orbital (LUMO) together with the emergence of charge-induced transitions in the sub band gap regime from the HOMO to the singly occupied molecular orbital (SOMO). The gray arrows emphasize the increase of charge-induced absorption and the decrease of the neutral molecule absorption peaks with higher doping levels. (**b**) A schematic of energy levels with possible optical transitions for a neutral and positively charged molecule. The shifts of the HOMO and LUMO energy levels reflects the reorganization of the molecular geometry to accommodate the charge.

Selected molecular structures

The experimentally investigated molecular structures and their measured and calculated isotropic g-shifts g_{exp} and g_{theo} are summarized in Table 6.1; the corresponding ESR spectra are shown in Fig. 6.3. The series begins with the pure hydrocarbons rubrene and pentacene that are expected to show very weak SOC. The remaining set of molecules is based on the BTBT structure which incorporates heavier sulfur atoms in two central thiophene units. For maximum consistency and rigor, theoretical calculations were performed on a set of systematic variations of this structure, including extending it with a single set of phenyl rings to form dinaphtho[2,3-b:2',3'-f]thieno[3,2-b]thiophene (DNTT), or two sets to form dinanthra[2,3-b:2',3'-f]thieno[3,2-b]thiophene (DATT), adding a set of outer thiophene rings (dibenzothiopheno-thieno-thiophene, DTBTBT) in a curved (C-DTBTBT) or linear (L-DTBTBT) geometry, and substituting the sulfur in all of these with selenium (BSBS, DNSS, DSBSBS etc.) for a total of 10 distinct geometries.

Each of these structures was additionally examined with insulating alkyl chains attached to the outer phenyl or thiophene units (C8-BSBS, C10-DNTT etc.) and with the same side chains shifted one position closer to the closest central sulfur atom (labeled C8*s*-BTBT etc., see Fig. 6.4 for the labeling of side chain positions), in total adding up to 32 distinct molecules. Table 6.2 provides a complete list of all molecular names, structures and the corresponding acronyms.

From those 32 molecules, our experimental data is limited to the 11 molecules shown in Table 6.1 that were physically available. While those molecules have alkyl chain lengths between C8 and C12, all calculations were performed with C8 chains. Tests showed the alkyl chain influence to be well converged at this length, meaning that the theoretical results are comparable to experimental measurements at chains equal to or longer than 8 methylene units.

Results

ESR measures the resonant absorption of microwaves between Zeeman split energy levels in an external magnetic field $\mathbf{B}$. The rapid motion of molecules in a solution causes an averaging over the anisotropic terms in the spin Hamiltonian so that the resulting resonances arise from

$$\mathcal{H}_{\text{spin}}^{\text{iso}} = g\mu_{\text{B}}\mathbf{S}\cdot\mathbf{B} + \sum_n a_n \mathbf{S}\cdot\mathbf{I}_n \tag{6.1}$$

where the isotropic hyperfine interaction (HFI) couplings a_n for the nuclear spin $\mathbf{I}_n$ are proportional to the spin density at the nth nucleus. As a result, we observe symmetric spectra where the isotropic g-factor $g = \hbar\omega/\mu_{\text{B}}B_0$ is directly given by the microwave frequency ω and the resonance center B_0 ($2\pi\hbar$, Planck's constant). The isotropic HFI additionally causes a splitting of resonances proportional to a_n.

Some of the g-factor changes follow expected trends. As expected for holes in the highest occupied molecular orbital (HOMO) level with a strong coupling to lower lying σ-orbitals, all g-factors show positive shifts relative to the free electron value $g_{\text{e}} \approx 2.002319$. The light-element molecules pentacene and rubrene show g-factors close to g_{e} and we see an increase of the g-shift by almost one order of magnitude for BTBT or DNTT with the inclusion of heavier sulfur atoms.

Consistently, the next significant jump to $\sim 10^4$ ppm takes place for BSBS and DNSS when replacing sulfur by selenium, reflecting the stronger SOC of selenium. On the other hand, there is only a minuscule decrease in Δg, on the order of 100 ppm, with the addition of phenyl rings on either side of the molecule (BTBT $\rightarrow$ DNTT or BSBS $\rightarrow$ DNSS).

Acronym	Chemical name	Structure	Δg_{exp} [ppm]	Δg_{theo} [ppm]
Rubrene	Rubrene	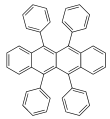	309	372
Pentacene	Pentacene	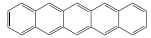	311	348
BTBT	[1]Benzothieno[3,2-b][1]benzothiophene	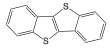	2,141	2,008
C8-BTBT	2,7-Dioctyl[1]benzothieno[3,2-b][1]benzothiophene	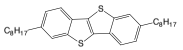	1,087	809
DNTT	Dinaphtho[2,3-b:2',3'-f]thieno[3,2-b]thiophene	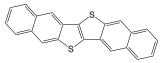	1,959	1,990
C10-DNTT	2,9-Didecyldinaphtho[2,3-b:2',3'-f]thieno[3,2-b]thiophene	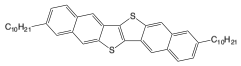	1,657	1,646
C-C12-DTBTBT	2,8-Didodecyldibenzothiopheno[7,6-b:7',6'-f]thieno[3,2-b]thiophene	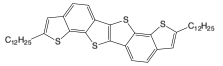	354	420
L-C12-DTBTBT	2,8-Didodecyldibenzothiopheno[6,5-b:6',5'-f]thieno[3,2-b]thiophene	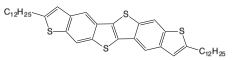	3514	4,180
BSBS	[1]Benzoseleno[3,2-b][1]benzoselenophene	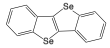	10,010	14,255
C8-BSBS	2,7-Dioctyl[1]benzoseleno[3,2-b][1]benzoselenophene	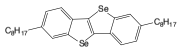	6,322	6,773
DNSS	Dinaphtho[2,3-b:2',3'-f]seleno[3,2-b]selenophene	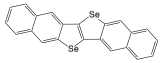	9,772	10,415

Table 6.1: Simulated and experimental molecular g-shifts. The experimental values have an uncertainty of ± 30 ppm, limited by the uncertainty of the external magnetic field of $\pm 5\,\mu$T. Due to the extremely low solubility of Pentacene, the g-shift was measured for TIPS-Pentacene with a very similar conjugated system.

Other changes are more surprising. The addition of (insulating) alkyl chains to a molecule does not introduce or remove any atoms with strong SOC from the π-conjugated system, nor should it significantly alter the electronic structure of the latter[112]. Nevertheless, the g-shift is reduced by half with the introduction of side chains for BTBT $\rightarrow$ C8-BTBT and by about one quarter for DNTT $\rightarrow$ C10-DNTT.

Hyperfine interactions as a measure of spin densities

To understand the origin of this reduction in Δg, we can exploit the isotropic HFI from the hydrogen nuclei as local probes of the spin density throughout the molecule. We determine the HFI coupling constants from the derivative ESR spectra by diagonalizing the spin Hamiltonian from Eq. (6.1) and convoluting the obtained resonance positions with a Lorentzian line to account for the finite linewidths. The resulting resonance spectrum is then fitted to the experimental ESR spectrum with the genetic algorithm of the EasySpin Toolbox[113] as shown in Figs. 6.2 and 6.3.

When fitting the spectra of molecules with attached side chains, we had to include the HFI from the first two hydrogens on each side chain in order to reproduce the spectral shape (Fig. 6.2b for C8-BTBT and Fig. 6.3). The number of hydrogens included in the fit provides clear experimental evidence for a spin density that leaks out onto the side chains and an accompanying change of the spin density distribution on the molecule.

Another striking experimental observation is the large difference in g-shifts between C-C12-DTBTBT and L-C12-DTBTBT. Both molecules are composed of exactly the same atoms and their only difference lies in the position of the outer thiophene units, either introducing a curve (C-C12-DTBTBT) or providing a more linear geometry (L-C12-DTBTBT). Even though both molecules contain four sulfur atoms, the g-shift changes from ~ 4000 ppm to ~ 400 ppm when switching from the linear to the curved isomer. This arises from the difference in spin density distributions between the two molecules, as revealed by the changing HFI splitting in the ESR spectra (Fig. 6.3), and is fully consistent with the molecular modeling discussed below.

The changes of the spin density distribution with alkylation, observed indirectly via the HFI, or the introduction of a curvature in the molecule suggest a strong dependence of the g-shift not only on the atomic composition of the molecules but also their geometries and the resulting spin densities. However, we cannot distinguish HFI couplings from different hydrogens experimentally unless they have different numbers of equivalent nuclei[113] and common sulfur or selenium

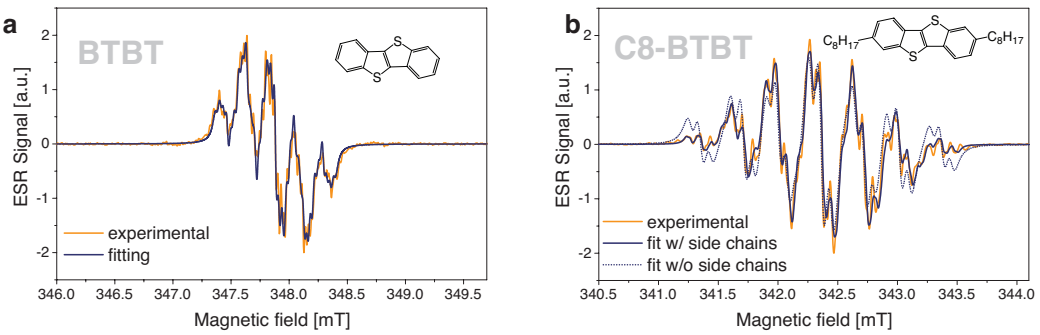

Figure 6.2: Derivative ESR spectra of (**a**) BTBT and (**b**) C8-BTBT with best fits including (solid line) or excluding (dashed line) HFI from the first two hydrogens on the side chains.

isotopes have zero nuclear spins. DFT modeling on the other hand can provide an accurate, spatially resolved picture of the spin wave-functions in the molecule.

6.2 DFT modeling of spin densities and g-shifts

In order to explain the experimental results above, and investigate the importance of the spin density distribution for Δg, we performed state-of-the-art DFT calculations of molecular g-tensors and spin densities in collaboration with the Sinova group at Johannes Gutenberg University, Mainz. We have chosen an all-electron, hybrid exchange-correlation functional DFT level of theory, which also accounts for scalar relativistic and spin-orbit coupling effects.

All density-functional theory calculations were performed using the NWChem[114] (version 6.5) and ORCA[115] (version 3.0.3) quantum chemistry software packages using an all-electron DFT method, with nuclear relativistic effects described by the zeroth-order regular approximation (ZORA[116]) using the standard point-charge approximation for the atomic nuclei. g-tensors were calculated using the method[67] developed by Neese et al. and related techniques[117] as implemented in the ORCA software package. The full computational methodology can be found in Appendix Appendix D.

In a follow-up paper by McNellis et al.[118] we expand on the first-principles theoretical model presented here, address geometric relaxation effects, elaborate on methodological aspects and extend our class of molecules.

As evident from Table 6.1, the accuracy of the theoretically predicted Δg is generally excellent, validating the quality of our methodology. The only significant

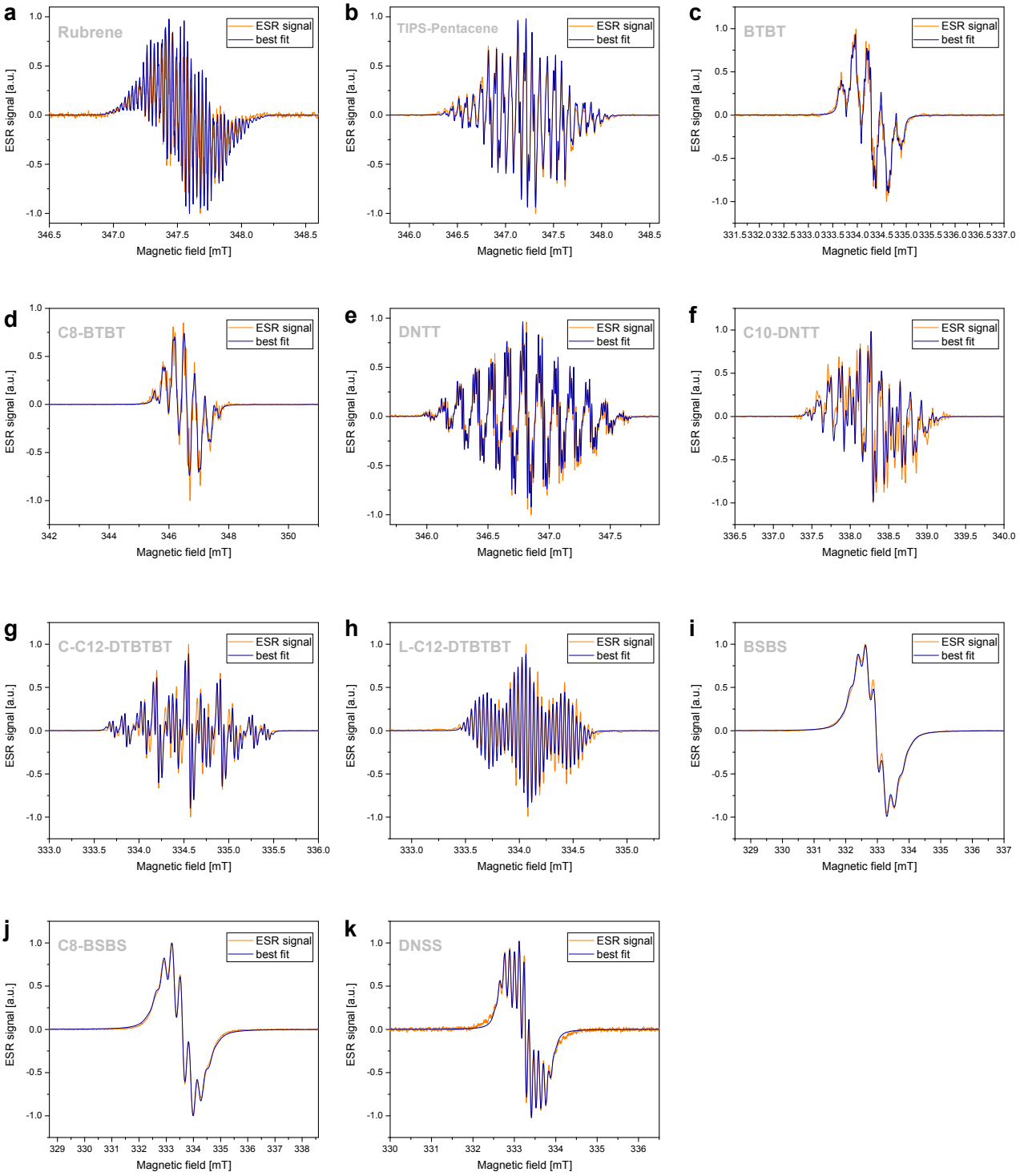

Figure 6.3: Overview of all recorded ESR spectra. Microwave powers were chosen sufficiently small to prevent any saturation of the signal (typically 0.006–0.06 mW) and the modulation amplitude was chosen smaller than the linewidth to prevent distortions of the spectrum.

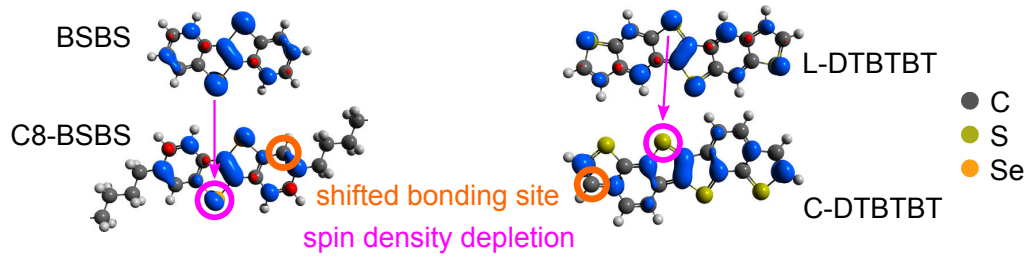

Figure 6.4: Spin isodensity contours of cationic (left) BSBS and C8-BSBS, and (right) L-DTBTBT and C-DTBTBT radicals. The C8-BSBS molecule shown has alkyl chains at the *outer* bonding site. Spin maxima and minima are shown in blue and red, respectively. The *shifted* bonding site at the phenyl rings has been labeled, and the observed spin depletion at heavy atoms highlighted. Note that only part of the alkyl chains in C8-BSBS are shown.

discrepancy is found for BSBS which will be discussed later. In each of these calculations, the spin density in the cationic radical was calculated, plotted and visualized as shown in Fig. 6.4.

In the left of this figure, the qualitative effect of alkylation at the *outer* bonding site is shown using BSBS as an example. The effect is identical for the sulfur-based analogues, and similar but weaker in DNTT, DNSS, DATT and DASS. We attribute the reduced magnitude of the effect to the weaker charge confinement in these molecules.

In essence, the significant spin maximum (blue contour) at the *outer* bonding site causes the spin density to leak onto the alkyl chain, resulting in a net spin density depletion at the heavy atoms, visible in Fig. 6.4 as a diminished contour at the heavy atom site. Moving the alkyl chain to the *shifted* bonding site, which in the base molecule shows a spin density minimum (red contour) has a negligible or weakly opposite effect on the heavy atom spin density.

In the right of Fig. 6.4, the effect of the geometry on the DTBTBT spin density is similarly shown, with the heavy atoms all but entirely depleted in the curved species. The same is observed in DSBSBS.

Comparing this visual analysis to the corresponding trends in g-shifts in Table 6.1 confirms the experimentally established picture of the spin density weight at heavy atoms, i.e., the overlap of orbital and spin angular momentum distributions, as the key quantity for understanding g-shifts in this class of molecules. To verify this qualitative analysis, we proceed to build a quantitative model of the dependence of Δg on the spin density. In the formulation of Neese[67], the molecular Δg

Acronym	Chemical name	Structure	Δg_{theo} [ppm]	$\Delta g_{theo}^{OZ/OSC}$ [ppm]
Rubrene	Rubrene		81	73
Pentacene	Pentacene		352	346
BTBT	[1]Benzothieno[3,2-b][1]benzothiophene		2,238	2,216
C8-BTBT	2,7-Dioctyl[1]benzothieno[3,2-b][1]benzothiophene	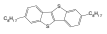	1,107	1,109
C8*s*-BTBT	3,8-Dioctyl[1]benzothieno[3,2-b][1]benzothiophene		2,828	2,812
BSBS	[1]Benzoseleno[3,2-b][1]benzoselenophene		14,255	14,129
C8-BSBS	2,7-Dioctyl[1]benzoseleno[3,2-b][1]benzoselenophene	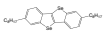	6,773	6,696
C8*s*-BSBS	3,8-Dioctyl[1]benzoseleno[3,2-b][1]benzoselenophene		16,677	16,548
DNTT	Dinaphtho[2,3-b:2',3'-f]thieno[3,2-b]thiophene		2,073	2,035
C8-DNTT	2,9-Dioctyldinaphtho[2,3-b:2',3'-f]thieno[3,2-b]thiophene	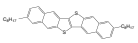	1,794	1,778
C8*s*-DNTT	3,10-Dioctyldinaphtho[2,3-b:2',3'-f]thieno[3,2-b]thiophene	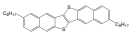	1,769	1,754
DNSS	Dinaphtho[2,3-b:2',3'-f]seleno[3,2-b]selenophene		10,414	10,289
C8-DNSS	2,9-Dioctyldinaphtho[2,3-b:2',3'-f]seleno[3,2-b]selenophene	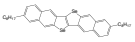	8,760	8,662
C8*s*-DNSS	3,10-Dioctyldinaphtho[2,3-b:2',3'-f]seleno[3,2-b]selenophene	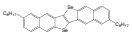	8,526	8,429
DATT	Dianthra[2,3-b:2',3'-f]thieno[3,2-b]thiophene	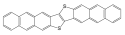	1,598	1,553
C8-DATT	2,11-Dioctyldianthra[2,3-b:2',3'-f]thieno[3,2-b]thiophene	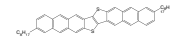	1,481	1,459
C8*s*-DATT	3,12-Dioctyldianthra[2,3-b:2',3'-f]seleno[3,2-b]selenophene	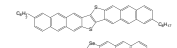	1,527	1,506
DASS	Dianthra[2,3-b:2',3'-f]seleno[3,2-b]selenophene	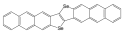	7,031	6,911
C8-DASS	2,11-Dioctyldianthra[2,3-b:2',3'-f]seleno[3,2-b]selenophene	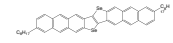	6,415	6,321
C8*s*-DASS	3,12-Dioctyldianthra[2,3-b:2',3'-f]seleno[3,2-b]selenophene	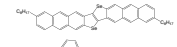	6,620	6,526
C-DTBTBT	Dibenzothiopheno[7,6-b:7',6'-f]thieno[3,2-b]thiophene		419	383
C-C8-DTBTBT	2,8-Dioctyldibenzothiopheno[7,6-b:7',6'-f]thieno[3,2-b]thiophene	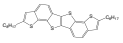	237	231
C-C8*s*-DTBTBT	3,9-Dioctyldibenzothiopheno[7,6-b:7',6'-f]thieno[3,2-b]thiophene	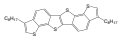	802	759
C-DSBSBS	Dibenzoselenopheno[7,6-b:7',6'-f]seleno[3,2-b]selenophene		2,498	2,395
C-C8-DSBSBS	2,8-Dioctyldibenzoselenopheno[7,6-b:7',6'-f]seleno[3,2-b]selenophene	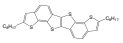	1,117	1,041
C-C8*s*-DSBSBS	3,9-Dioctyldibenzoselenopheno[7,6-b:7',6'-f]seleno[3,2-b]selenophene	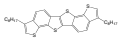	4,672	4,547
L-DTBTBT	Dibenzothiopheno[6,5-b:6',5'-f]thieno[3,2-b]thiophene	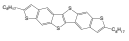	4,176	4,128
L-C8-DTBTBT	2,8-Dioctyldibenzothiopheno[6,5-b:6',5'-f]thieno[3,2-b]thiophene	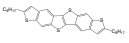	4,180	4,143
L-C8*s*-DTBTBT	3,9-Dioctyldibenzothiopheno[6,5-b:6',5'-f]thieno[3,2-b]thiophene	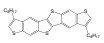	4,166	4,105
L-DSBSBS	Dibenzoselenopheno[6,5-b:6',5'-f]seleno[3,2-b]selenophene		23,265	23,082
L-C8-DSBSBS	2,8-Dioctyldibenzoselenopheno[6,5-b:6',5'-f]seleno[3,2-b]selenophene	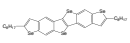	23,527	23,353
L-C8*s*-DSBSBS	3,9-Dioctyldibenzoselenopheno[6,5-b:6',5'-f]seleno[3,2-b]selenophene	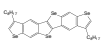	23,082	22,882

Table 6.2: Molecular g-tensor shifts calculated with DFT and the corresponding contributions from $\Delta g^{OZ/SOC}$ terms as defined in Eq. (6.2).

can be written as

$$\Delta g = \Delta g^{\mathrm{RMC}} + \Delta g^{\mathrm{GC}} + \Delta g^{\mathrm{OZ/SOC}}, \tag{6.2}$$

where Δg^{RMC} is a relativistic mass correction, Δg^{GC} is a diamagnetic gauge correction, and $\Delta g^{\mathrm{OZ/SOC}}$ is a cross-term between the orbital Zeeman and spin-orbit coupling operators corresponding to the mixed derivative of the molecular total energy with respect to the electron magnetic moment and external magnetic field[67]. The first of these terms, like other relativistic effects, is generally negligibly small in light organic molecules. The second term is in the current set of molecules also comparably small and of opposite sign, nearly canceling the first term. The g-shifts in this set are therefore virtually identical to the third term $\Delta g^{\mathrm{OZ/SOC}}$ as shown in Table 6.2.

Deviation of g-shifts for BSBS

All g-factor factors show an excellent agreement between experiment and theory apart from the values determined for BSBS which exceed the experimental value by 42 %. A systematic error in the DFT calculations is unlikely since only BSBS shows a large discrepancy. We consequently tried to eliminate error sources for the ESR measurements such as aggregation of molecules in solution, chemical impurities or reactions with the dopants.

To rule out aggregation we reduced the concentration of BSBS close to the detection limit of the setup ($0.05 \times 10^{-3}\,\mathrm{mol\,L^{-1}}$ or 4×10^{14} spins in the sample tube) and heated up the solution to 38 °C (boiling point of DCM: 39.6 °C) during the measurement. Neither resulted in any changes of the g-factor. In a control experiment, we investigated the solutions at different concentrations using diffusion-ordered nuclear magnetic resonance spectroscopy (DOSY NMR). A significant reduction of the diffusion constant of BSBS with higher concentrations would indicate the aggregation of molecules. However, such a reduction could not be observed over two orders of magnitude from $0.28 \times 10^{-3}\,\mathrm{mol\,L^{-1}}$ to $28 \times 10^{-3}\,\mathrm{mol\,L^{-1}}$ (see Appendix Appendix E for a summary of the data). Furthermore, a spread of the spin density over more than one molecule would not only shift the g-factor but also increase the number of protons causing HFI splitting, contrary to experimental evidence.

However, consistent with the difference in g-factors, we observe a difference in magnitude of HFI coupling constants between theory and experiment: BSBS shows a root mean square (rms) deviation of ~ 3 between theoretical and experimental HFI couplings compared to rms deviations < 0.8 for all other molecules. The discrepancy in g-shifts is therefore reflected by a discrepancy in the spin density distribution between theory and experiment.

The hydrogen NMR spectrum (Fig. 6.5) reveals small impurity peaks in the aliphatic region which could contribute to such a shift in spin density.

Another contribution might come from charge lifetime effects. All DFT calculations were performed in the short charge lifetime limit, i.e., for a neutral molecular geometry. The theoretically predicted g-shift of BSBS is reduced by 2500 ppm in the long charge lifetime limit which allows for relaxation to the cationic geometry. Such relaxation effects are more pronounced for selenium-containing molecules due to the larger polarizability of Se-C bonds compared to S-C bonds. Still, the short lifetime approximation successfully reproduces the C8-BSBS measurements. For an in depth discussion of charge-lifetime effects we refer to McNellis et al.[118].

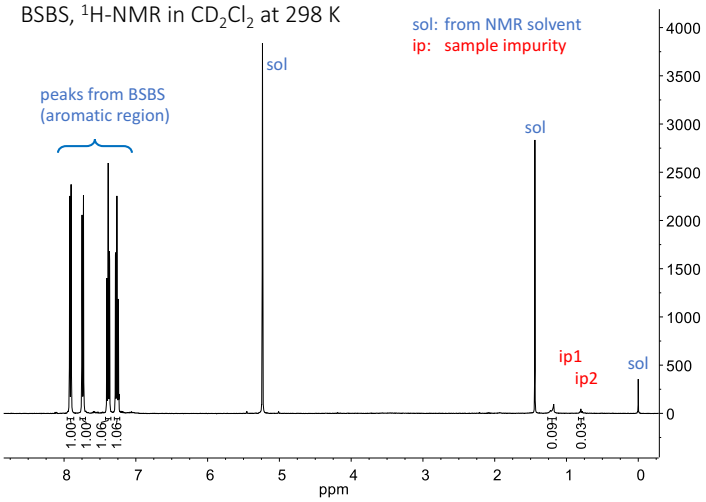

Figure 6.5: ^{1}H-NMR spectrum of BSBS dissolved in BSBS in deuterated dichloromethane (CD_2Cl_2) at a concentration of 0.02 mg mL^{-1} with small impurity peaks in the aliphatic region labeled ip1 and ip2. The spectrum was recorded on a Bruker AV-400 spectrometer at 298 K in deuterated dichloromethane and is reported in ppm relative to tetramethylsilane (TMS).

6.3 Fit of g-shifts vs atomic spins

To establish a quantitative model that relates the g-shift to the spin density distribution, we use an Ansatz with a linear dependence of $\Delta g^{\mathrm{OZ/SOC}}$ on the sum of spin densities at each type of element in the molecule:

$$\Delta g^{\mathrm{OZ/SOC}} \approx \sum_{e=1}^{N} c_e \sum_{n=1}^{N_e} \sigma_n^e. \tag{6.3}$$

Here, σ_n^e is the effective spin at atom n of element e, N_e is the number of atoms of that element in the molecule, c_e is the corresponding proportionality constant, and N is the number of different elements. σ_n^e is here treated in units of electronic spin (i.e., on the scale of $\frac{1}{2}\hbar = 1$), and therefore as dimensionless. The proportionality constants represent the net effect of the orbital angular momentum operators in $\Delta g^{\mathrm{OZ/SOC}}$. By fitting Eq. (6.3) to calculated g-shifts, we will be able to validate if $\Delta g^{\mathrm{OZ/SOC}}$ can be predicted from the local spin-densities only.

This Ansatz requires calculating atomic spin populations from the molecular spin density, in other words, finding an appropriate solution to the atoms-in-molecules problem. This mapping onto atomic spin densities was performed using the Voronoi Deformation Density (VDD) method[119] as implemented in the 'bader' program developed by Henkelman et al.[120], version 0.95a. The model then describes g-shifts as dependent on the overlap of orbital and spin angular momentum distributions, or equivalently, an effective spin-orbit coupling. We prove its validity by studying the correlation between g-shifts calculated from DFT, and shifts fitted to the same on the form of Eq. (6.3).

The fit of Eq. (6.3) is performed as follows: for each molecule, the atomic spin populations are summed up per element. Then, the proportionality constants per element c_e of Eq. (6.3) are fitted using all other molecules in the fit statistic. The molecule fitted for is thus never part of the fit statistic. Finally, the fitted value of $\Delta\mathrm{g}^{\mathrm{OZ/SOC}}$ is calculated as the scalar product between the arrays of per element atomic spin population sums and the corresponding fitted proportionality constants c_e. Since a negative c_e lacks physical meaning in this model, a non-negative multivariate linear regression method was used. As an approximate statistical test, we for each fit calculate the R^2-value according to

$$R^2 \equiv 1 - \frac{SS_{\mathrm{res}}}{SS_{\mathrm{tot}}} = 1 - \frac{\sum_i (x_i - y_i)^2}{\sum_i (x_i - \bar{x})^2} \tag{6.4}$$

where SS_{res}, SS_{tot}, x_i and y_i are the residual sum of squares, the total sum of squares, and the calculated and fitted $\Delta\mathrm{g}^{\mathrm{OZ/SOC}}$ value, respectively.

The results of this fit are shown in a correlation plot in Fig. 6.6a and the fit coefficients c_e are given in Table 6.3. As expected of a parameter representing the net effect of orbital angular momentum, c_e increases dramatically going from carbon via sulfur to selenium. The reasons for the precise magnitude of the c_e are convoluted, and we will here refrain from a detailed interpretation. It is however

Element	c_e avg.	c_e std. dev.
C	1.31×10^{-5}	9.08×10^{-6}
S	9.10×10^{-3}	6.72×10^{-5}
Se	3.47×10^{-2}	1.32×10^{-4}

Table 6.3: Average and standard deviations of the dimensionless proportionality constants c_e fitted for the $\Delta g^{OZ/SOC}$ terms of the set of molecules presented in Table 6.2.

noteworthy that the fit is relatively consistent for the heavier elements, with standard deviations below a percent of the average value. Because of its very small contributions to the $\Delta g^{OZ/SOC}$ combined with the limited precision of input data, the carbon fits are considerably less numerically consistent, resulting in a relative standard deviation of approximately 70 percent.

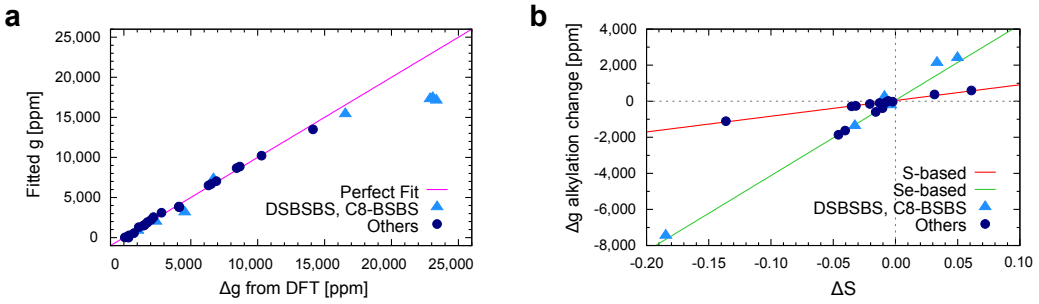

Figure 6.6: (**a**) Correlation plot of $\Delta g^{OZ/SOC}$-terms calculated using DFT vs. fitted on the form of Eq. (6.3). The outliers identified in the text are shown as light blue triangles, with the other numbers represented by dark blue circles. The magenta line $y = x$ represents a perfect fit. For brevity $\Delta g^{OZ/SOC}$ has here been relabeled Δg. (**b**) Plot of changes in $\Delta g^{OZ/SOC}$ terms as a function of change of effective heavy atom spin upon alkylation of molecules (see text). Red and green lines represent linear fits to the sulfur- and selenium-based molecules, respectively.

Using the coefficient of determination, or 'R^2-value' as a quality measure of the fit, we note that a straight fit of atomic spins to calculated $\Delta g^{OZ/SOC}$ values of the full 32 molecule set yields a fairly low R^2 of 0.960. For a strictly linear statistical hypothesis, this is unconvincing. However, the statistic is straightforwardly divided into a) 8 outliers consisting of all the Se-substituted DTBTBT molecules (i.e. {C-,L-}{C8-,C8*s*-}DSBSBS), and the alkyl-functionalized, Se-substituted BTBT molecules ({C8-,C8*s*-}BSBS), and b) the 24 molecules in the rest of the set. The outliers and the rest are shown in Fig. 6.6a as light blue triangles and darker blue circles, respectively. Excluding the outliers from the fit yields a very high R^2

of 0.996, showing that the model works well for the pure hydrocarbons, all the sulfur-based molecules, the non-functionalized BSBS molecule, and all variations of the DNSS and DASS molecules.

The reason why the Ansatz of Eq. (6.3) works better for sulfur than selenium is the non-local terms scaling with the smaller orbital angular momentum in the former. Furthermore, the dual heavy-atom structure in the DSBSBS molecules significantly complicates their electronic structure, with much larger non-local terms compared to the other, simpler molecules. The alkyl-functionalized BSBS molecules are also included in the outliers because the positive charge is much more strongly confined in BSBS than in the larger DNSS and DASS. As will be elaborated upon below, the spin density of BSBS is consequentially more strongly perturbed when chains are added, leading to stronger non-local interactions and violating the premises of the linear model.

With the range of applicability of this model thus established, we continue by applying it to studying the effect of alkyl-chain functionalization. In Fig. 6.6b, the difference in $\Delta g^{\mathrm{OZ/SOC}}$ upon alkylation has been plotted as a function of the corresponding difference ΔS in effective spin at the heavy atoms of the molecule. For clarity, the sets of outliers and the rest in Fig. 6.6a have been colored the same way. Two things stand out in Fig. 6.6b. Firstly, the relationship between the change in the spin density on the sulfur atoms and the change in g-shift upon alkylation is linear. This fact explains the, in parts, dramatic alkylation effects on g-shifts. Such large shifts occur when the alkyl chain bonds to a site where the spin density is large in the non-functionalized molecule. The spin density will then spread partly into the chain and will be reduced on the heavy atom, hence allowing for tuning of the effective spin-orbit coupling by targeted alkylation.

Secondly, the outliers of Fig. 6.6a are now a much better fit in Fig. 6.6b. This is due to some non-local terms canceling when differences are taken between alkylated and non-alkylated g-shifts. Of the outliers, C8-BSBS and C8*s*-BSBS respectively exhibit the strongest decrease and increase of spin at the heavy atoms, and are found in Fig. 6.6b at either extreme of the Se-based statistic. As explained above, this strong alkylation effect is attributed to the confinement of the electron hole in the small BSBS molecule leading to a large shift of the spin density distribution. This point is additionally reinforced by the Se-based molecules not among the outliers: for C8-DNSS and C8*s*-DNSS, the electrons are less confined to begin with and the effect of attaching an alkyl chain is therefore less pronounced.

6.4 Relationship between g-shift and spin lifetimes

In the previous section, we have argued that the g-shift can be correlated to an effective SOC over a wide range of g-factors. This series of molecules therefore presents a unique opportunity to systematically study the effect of SOC on spin lifetimes. We show in the following that the spin-lattice relaxation time T_1 indeed scales with Δg over four orders of magnitude and interpret this in the framework of the Bloch-Wagness-Redfield theory of spin relaxation.

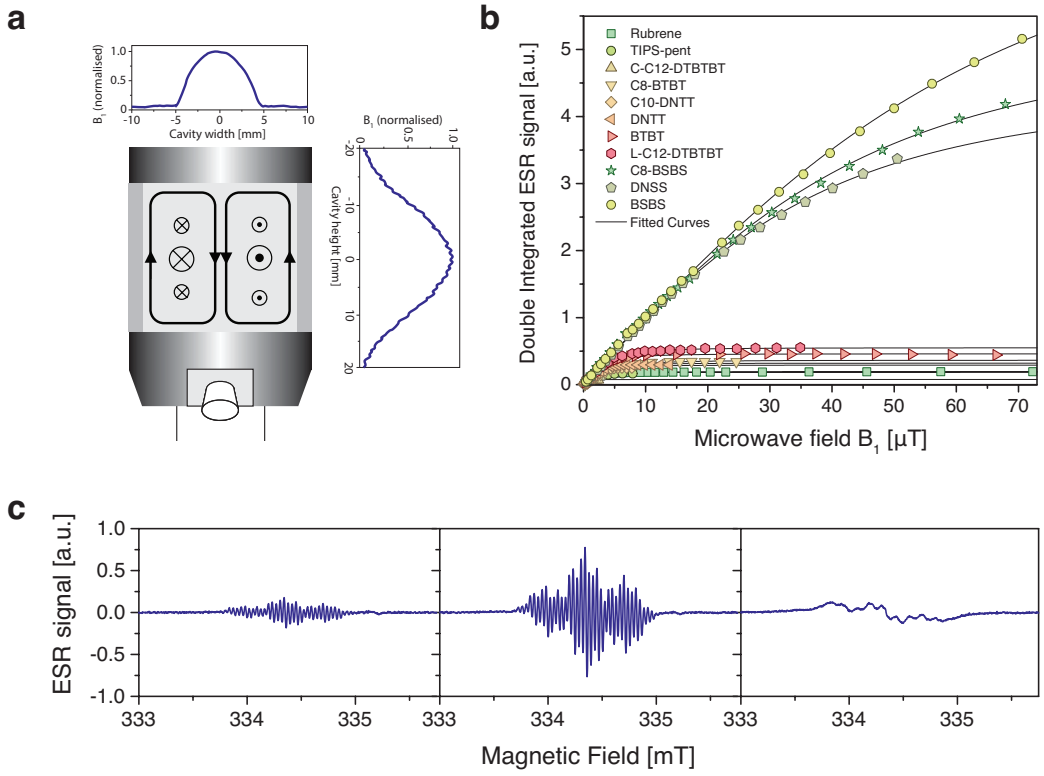

Figure 6.7: Power saturation measurement of spin lifetimes. (**a**) Schematic of the Bruker ER 4122SHQE cavity with microwave magnetic and electric fields in-plane and out-of-plane, respectively. Plot insets show the magnetic field strength across the cavity. We account for the vertical distribution of B_1 and minimize horizontal variations by confining our samples to a diameter of 1 mm. (**b**) Power saturation of the integrated ESR absorption spectra for the series of molecules with fitted curves to extract T_1 and T_2. (**c**) Evolution of derivative ESR spectrum with increasing microwave powers for the example of L-C12-DTBTBT.

The majority of reported experimental architectures in (organic) spintronics employ an external magnetic field **B** to either generate or control and manipulate

spins inside the target material. The employed fields of 10–400 mT[121,122] are on the same order or smaller than in ESR measurements. In the presence of an external field one must distinguish between longitudinal and transverse spin relaxation. The first manifests itself macroscopically as the decay of the sample magnetization parallel to **B** and requires transitions between the Zeeman split spin-up and spin-down states. This implies an exchange of energy with the spin's environment (the 'lattice') and is characterized by the spin-lattice relaxation time T_1. The decay of the transverse magnetization is characterized by the coherence time T_2. This results from spin dephasing and can occur in an energetically neutral process. A long T_2 enables the coherent manipulation of spins while a large T_1 is crucial to maintain a spin polarization along a preferred axis.

We determine the product T_1T_2 from the power saturation behavior of the ESR spectra (Fig. 6.7) and T_2 from the unsaturated linewidth, as described in Section 5.2. This requires both a sufficiently large microwave field B_{mw} and an exact knowledge of the latter over the sample volume. We therefore minimize the variation of B_{mw} by confining the sample to a capillary tube at the cavity center and account for the lateral field distribution across the sample as shown in Fig. 6.7a and described in Section 5.3.

The resulting values for T_1 reveal a strong correlation between spin-lattice relaxation times and g-shifts: we observe a change in T_1 over four orders of magnitude, from 212 µs for molecules with small g-shifts (e.g. C-C12-DTBTBT) down to 0.15 μs (BSBS, DNSS) for the largest g-shifts (Fig. 6.8a). This demonstrates the impact of tuning the g-factor beyond changing the coupling of a spin to the external magnetic field. By increasing the spin density at selenium or sulfur atoms, we increase the effective SOC for the spin and as result the transition rate between spin-up and spin-down levels increases as well.

Redfield approach to spin relaxation

The spin coherence times, T_2, are systematically smaller than T_1 and show a less pronounced dependence on Δg and a larger scatter of values. This can be understood when considering the underlying mechanism that contribute to T_2. A spin couples to its environment via magnetic fields and the exchange of energy required for spin-lattice relaxation implies that the transitions between Zeeman levels are induced by fluctuating fields. Those typically are internal HFI and SOC fields which fluctuate with lattice vibrations, the tumbling motion of molecules in a solution or (in the rest frame of the spin) due to the spatial motion of the charge carrier in a solid state system.

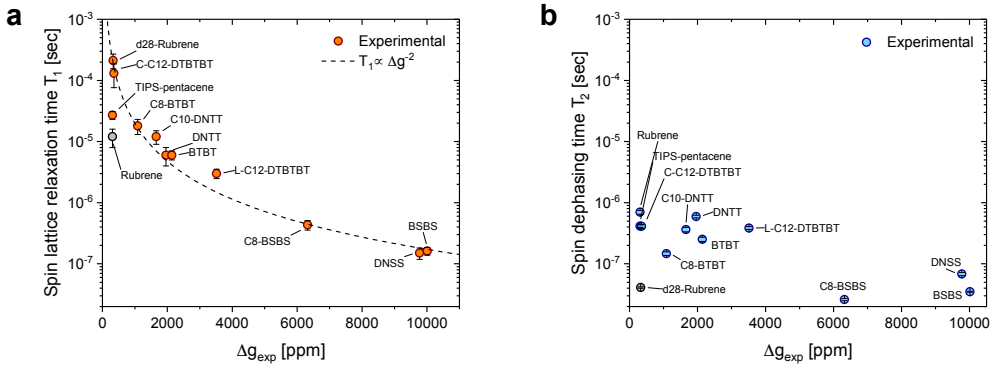

Figure 6.8: Dependence of spin relaxation times on the effective SOC. (**a**) spin-lattice relaxation time vs Δg for all measured molecules. Error bars represent 95% confidence intervals. Dashed line shows the expected proportionality $T_1 \propto (\Delta g)^{-2}$ for relaxation via SOC fields. (**b**) Spin coherence time vs Δg for all measured molecules. Error bars show the 95% confidence intervals.

In the framework of the Bloch-Wagness-Redfield theory[48,85], those fields are treated classically by adding a time-dependent perturbation $\mathcal{H}_{\text{pert}}(t) = \mathbf{S} \cdot \mathbf{F}(t)$ to the spin Hamiltonian and examining the spectral densities $k_{x,y,z}(\omega)$ of the fluctuating fields $F_{x,y,z}(t)$. The spin-lattice relaxation time then depends on the spectral density at the Larmor frequency $\omega_{\text{L}} = \gamma_e B$ while the spin coherence time includes an additional contribution from $k(0)$[48]:

$$T_1^{-1} = \frac{1}{\hbar^2}[k_x(\omega_{\text{L}}) + k_y(\omega_{\text{L}})] \tag{6.5}$$

$$T_2^{-1} = (2T_1)^{-1} + \frac{1}{\hbar^2} k_z(0) \ . \tag{6.6}$$

Equations (6.5) and (6.6) imply that $T_2 \lesssim T_1$, which is consistent with our measured values. We also see that T_2 is susceptible to static local variations such as small inhomogeneities in the external magnetic field. This effectively creates an upper bound for T_2 or equivalently a lower bound for the linewidth ($\sim 3 \times 10^{-3}$ mT) and introduces larger fluctuations between measurements, e.g., due to differences in the sample position, that do not affect T_1.

If we consider relaxation caused by SOC fields only, the fluctuations can be written as $\mathbf{F}(t) = \mu_{\text{B}} \Delta\mathbf{g}(t) \cdot \mathbf{B}$. This incorporates a time dependence from lattice vibrations or molecular tumbling. Assuming that the amplitude of the SOC fluctuations approximately scales with Δg itself, one expects that the spectral densities follow the proportionality $k_q(\omega) \propto (\Delta g)^2$ and the relaxation time to follow $T_1 \propto (\Delta g)^{-2}$.

Fig. 6.8a shows that T_1 indeed follows this proportionality with a remarkable accuracy. We conclude that spin-lattice relaxation is therefore dominated by the effective SOC at magnetic fields of $\sim 350\,\mathrm{mT}$.

Note that fluctuating HFI fields create perturbations of the form $\mathbf{F}_n(t) = \mathbf{A}_n(t)\cdot\mathbf{I}_n$ where $\mathbf{A}_n(t)$ is the coupling tensor for the nuclear spin $\mathbf{I}_n$. This expression does not depend on the external field and the HFI therefore becomes less effective at flipping the spin when the Zeeman splitting increases at higher fields. In contrast, spin-lattice relaxation by fluctuating SOC fields will remain equally effective at all external field strengths. Measurements on organic spin valves for instance are typically performed at different magnetic fields between 5–500 mT, depending on the switching field of the ferromagnetic electrodes. The effect of HFI fields on spin relaxation will therefore be suppressed to different degrees which complicates a systematic comparison of spin diffusion lengths.

Only two outliers, TIPS-pentance and rubrene, stand out for their small T_1 relative to the g-shift. Both have a large number of hydrogens attached to the conjugated system and we speculate that the HFI provides an additional relaxation pathway. Naturally, this would be most pronounced for rubrene where 28 protons contribute to the HFI. In a control experiment, we repeated the measurement on fully deuterated d28-rubrene, which strongly suppresses hyperfine interactions[66,123]. Together with a reduction of the HFI couplings by a factor of 2–3, we observe an increase of T_1 by more than an order of magnitude which brings it in line with the other molecules.

The large deviation from the $T_1 \propto (\Delta g)^{-2}$ dependency can therefore be traced back to hyperfine interactions. We can quantify their contribution by summing over SOC and HFI relaxation rates $T_1^{-1} = (T_{1,\mathrm{HFI}})^{-1} + (T_{1,\mathrm{SOC}})^{-1}$ which yields pure HFI relaxation times of $\sim 13\,\mu\mathrm{s}$ for h28-rubrene and $\sim 30\,\mu\mathrm{s}$ for TIPS-pentacene. Such an estimate is only meaningful when the deviation from $T_1 \propto (\Delta g)^{-2}$ is larger than the measurement uncertainty, i.e., when the contribution of $T_{1,\mathrm{HFI}}$ to T_1 is not negligible. We therefore cannot systematically extract HFI contributions for most of the molecules in this study but instead can identify a domain of weak SOC with $\Delta g \lesssim 500\,\mathrm{ppm}$ where, in the presence of a sufficient number of nuclear spins, hyperfine fields will significantly contribute to spin-lattice relaxation.

When excluding the outliers and assuming that both T_1 and T_2 are dominated by a single relaxation process, SOC in our case, one can find a simple expression for the spectral density $k_q(\omega) = \overline{F_q^2}\ \tau_C/(1+\omega\tau_C^2)$, where τ_c is the correlation time of field fluctuations and $\overline{F_q^2}$ is the mean square of the fluctuating field[48].

Figure 6.9a shows the dependence of both relaxation times on τ_c in this model and demonstrates that spin-lattice relaxation becomes most effective when the frequency τ_c^{-1} matches the energy difference between the Zeeman-split levels.

In a rough approximation, we can take $\overline{F_x^2} = \overline{F_y^2} = \overline{F_z^2}$ and estimate the correlation time τ_c from the ratio $T_1/T_2 = 1 + \omega_L^2\tau_c^2/2$. The resulting values are on the order of $\tau_c^{-1} = 2.5$–$50\,\mathrm{GHz}$ (Fig. 6.9b). For comparison, simulations of intra-molecular vibrational modes of DNTT predict frequencies of 6–50 THz for stretching modes along the molecule's symmetry axes, distortions of the phenyl rings and vibrations of the C-H bonds, in ascending order[124]. They exceed the Zeeman splitting by orders of magnitude and are therefore less effective at flipping the spin.

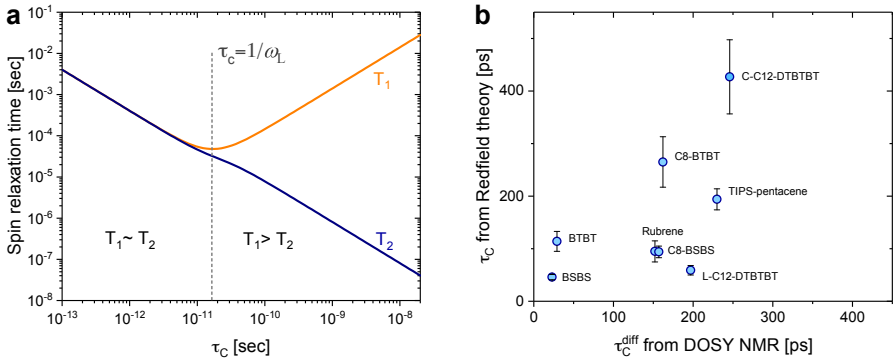

Figure 6.9: Fluctuating magnetic field approach to spin relaxation. (**a**) Dependence of T_1 and T_2 on the correlation time τ_c of field fluctuations from the Redfield theory. Model values of $\omega_L/2\pi = 9.4\,\mathrm{GHz}$ and $B_{x,y,z}^2 = 0.2\,\mathrm{mT}$ were used for the plot. (**b**) Correlation times τ_c as estimated from the Redfield theory and plotted against rotational correlation times obtained from DOSY NMR diffusion constants (when available). Error bars from 95% confidence intervals of T_1 and T_2 and error propagation.

Molecular tumbling as a source of spin relaxation

Alternatively, we consider SOC fields that are static in the molecule's rest frame but fluctuate relative to the external field (and thus the spin quantization axis) with the tumbling motion of molecules in a solution. It is possible to estimate the rotational correlation time of this tumbling motion from the diffusion constant of molecules in solution as determined by diffusion-ordered nuclear magnetic resonance spectroscopy (DOSY NMR) measurements.

DOSY NMR measurements we carried out at a concentration of $0.2\,\mathrm{mg\,mL^{-1}}$ after confirming the absence of aggregation by monitoring the diffusion constant for successively smaller concentrations (8.9–$0.089\,\mathrm{mg\,mL^{-1}}$). The DOSY NMR spectra were recorded on a Bruker AV-500 spectrometer at 298 K in deuterated dichloromethane. The diffusion experiments were performed using the Bruker

ledbpgp2s pulse sequence with a diffusion delay of 28 ms and a $\delta/2$ pulse of 1.3 ms. 24 experiments were collected with 192 scans and 32000 data points per experiment.

The translational diffusion constants D_{tr} from DOSY NMR allow us to calculate the hydrodynamic volume and Stokes radius r_{S} of the respective molecule by the Stokes-Einstein equation $D_{\mathrm{tr}} = k_{\mathrm{B}}T/(6\pi\eta r_{\mathrm{S}})$ with a viscosity of DCM at room temperature of $\eta = 4.13 \times 10^{-4}\,\mathrm{kg\,m^{-1}\,s^{-1}}$. Knowledge of the hydrodynamic volume then allows us to estimate the rotational diffusion constant $D_{\mathrm{rot}} = k_{\mathrm{B}}T/(8\pi\eta r_{\mathrm{S}}^3)$ and the corresponding rotational correlation time, i.e., the timescale for which the rotational motion of the molecule is completely randomized, which is given by[48,56]

$$\tau_{\mathrm{c}}^{\mathrm{diff}} = \frac{1}{6D_{\mathrm{rot}}} = \frac{2}{9}\left(\frac{k_{\mathrm{B}}T}{\pi\eta}\right)^2 \frac{1}{D_{\mathrm{tr}}^3}\,. \tag{6.7}$$

The solubility of DNTT and DNSS in dichloromethane was too small to record DOSY NMR spectra but the rotational correlation times $\tau_{\mathrm{c}}^{\mathrm{diff}}$ for the remaining molecules are shown in Fig. 6.9b together with τ_{c} values estimated from the spin lifetime ratios. Even though the values of τ_{c} are only rough estimates, derived under the previously discussed assumptions, we observe an approximate agreement with $\tau_{\mathrm{c}}^{\mathrm{diff}}$. It is therefore likely that the observed relaxation times are indeed a result of SOC fields which fluctuate due to the molecular rotations in solution.

6.5 Discussion

Isolated molecules, both in the gas phase and in solution, are significantly easier to model and to understand than solid thin films. They also provide us with the unique opportunity to resolve the hyperfine structure of ESR signals and to verify the spin densities from relativistic DFT modeling by comparing experimental and theoretical HFI couplings. Together with accurate measurements and predictions of the g-factor, we demonstrate the subtle dependence of SOC strengths on the molecular geometry: the inclusion of heavier atoms in the molecular structure increases SOC but the effect of such substitutions can be almost completely suppressed by the molecular geometry and the resulting spin density distribution. As a result, molecules such as C-C12-DTBTBT with four sulfur atoms exhibit SOC strengths close to pure hydrocarbons. We demonstrate an empirical linear relationship between the g-shift and the atomic spin densities where the proportionality constants depend only on the type of element and its local SOC, regardless of its molecular environment. This enables the targeted molecular design of materials

with excellent charge transport properties and suppressed or enhanced spin-orbit coupling for either spin transport or spin-to-charge conversion applications.

The mechanism of spin relaxation in solution, which is most likely dominated by molecular tumbling, cannot be directly transferred to solid systems. Nevertheless, we expect to see some parallels. Initial ESR measurements on field-induced charges in thin films reveal relaxation times that come close to the solution values and agree with pulsed ESR data from thin films at room temperature[90,125]. In the solid state, the fluctuations of SOC fields will not be provided by molecular rotations but by intermolecular phonon modes which lie at smaller frequencies than their intra-molecular counterparts or by the hopping motion of spins in the organic semiconductor. When a charge carrier hops between sites with differently oriented molecules, it will experience the change in g-tensor orientation as a fluctuating field in its rest frame. Hopping times are estimated to be in the range of 100–1000 ps[126], close to the rotational correlation times in solution, and some lower frequency intermolecular modes can reach timescales $> 10\,\mathrm{ps}$[127,128]. In the solid state, the spin densities are likely spread over multiple molecules but we expect Δg to still be a measure of the effective SOC. Since the fluctuation amplitudes will still scale with the latter, knowing the relaxation times in solution should provide a good estimate for both the coherence and spin-lattice relaxation times in thin films.

Chapter 7

Polaron spin dynamics in conjugated polymers

Polymeric semiconductors exhibit exceptionally long spin lifetimes, and recently observed micrometer spin diffusion lengths in conjugated polymers demonstrate the potential for organic spintronics devices. Weak spin-orbit and hyperfine interactions lie at the origin of their long spin lifetimes but the coupling mechanism of a spin to its environment remains elusive. For instance, spin-vibron coupling, the charges' hopping motion through a disordered local field environment, and Elliott-Yafet type spin flips at spatial scattering events can all potentially contribute to spin relaxation.

In this chapter, we present a systematic study of polaron spin lifetimes in field effect transistors with high-mobility conjugated polymers as an active layer. We demonstrate how spin relaxation is governed by the charges' hopping motion at low temperatures while Elliott-Yafet-like relaxation due to short-range coherent charge-density dynamics likely dominates high temperature spin lifetimes. Such a microscopic relaxation mechanism is highly sensitive to the local conformation of polymer backbones and we demonstrate its dependence on the degree of crystallinity in a polymer film.

Recent reports of 100–1000 nm long spin diffusion lengths[7,122] and successful spin-to-charge conversion in conjugated polymers[5,6] may lead the way towards the application of conjugated polymers in spintronics devices. Despite their low charge carrier mobilities, such carbon-based materials are of interest for spin transport due to their weak hyperfine and spin-orbit interactions and the resulting long spin lifetimes. The strength of those fundamental interactions has been recently investigated on a molecular level, showing a subtle dependence on the elemental composition and geometry of the conjugated systems[110,118,129,130].

Both spin-orbit coupling (SOC) and hyperfine interactions (HFIs) can be treated as effective magnetic fields which, when fluctuating in the rest frame of the spin, will result in spin-lattice relaxation and decoherence with the respective timescales T_1 and T_2. In organic materials, these fluctuations are closely linked to charge transport: they may be caused by the charge's hopping motion between different molecular sites, by the modulation of couplings with local vibrational modes while a charge rests at a site, or by the vibrational modes which drive an incoherent hopping event. Accordingly, theoretical treatments typically distinguish between the three types of mechanisms[74]: motional[76], intra-site[76], and Elliott-Yafet-like relaxation[16,75] (named in analogy to Elliott-Yafet spin relaxation during momentum scattering events in inorganic semiconductors).

Charge carrier and spin dynamics are therefore fundamentally related and an understanding of spin relaxation at a microscopic level may pave the way to higher performance materials for electronic and spintronics applications.

Spin transport has been historically probed along the low-mobility out-of-plane direction, for instance in organic spin valves[104,131–133], by spin pumping[121,122], or by electrically and optically detected spin resonance[134,135], and accurately determining polaron spin lifetimes in organic semiconductors has been challenging. Especially magnetoresistance measurements are prone to device related artefacts[136,137], which may explain the large variability in reported spin lifetimes of 1–1000 µs, inferred from spin diffusion lengths and charge carrier mobilities.

Field-induced ESR measurements (FI-ESR) provide a way to simultaneously probe charge transport and spin lifetimes in devices with dominantly in-plane transport and consistently show shorter lifetimes on the order of 10 ns to 10 µs. Unlike ESR measurements on doped organic films[81,138], FI-ESR does not suffer from overlapping signals of dopant counter ions and can easily distinguish between free charge carriers and background signals by modulating the applied gate voltage.

Overview

In this chapter, we compare spin dynamics in four state-of-the-art conjugated polymers with varying degrees of crystallinity: an indacenodithiophene-co-benzothiadiazole copolymer (IDTBT)[36], poly[N,N9-bis(2-octyldodecyl)-naphthalene-1,4,5,8-bis(dicarboximide)-2,6-diyl]-alt-5,59-(2,29-bithiophene) p(NDI2OD–T2)[139], poly[2,5-bis(3-tetradecylthiophen-2-yl)thieno[3,2-b]thiophene] (pBTTT), and poly[[2,5-bis(2-octadecyl)-2,3,5,6-tetrahydro-3,6-diketopyrrolo[3,4-c]pyrrole-1,4-diyl]-alt-(2-octylnonyl)-2,1,3-benzotriazole] (DPP–BTz)[140]. The respective molecular structures are shown in Fig. 7.1.

This selection includes two of the workhorse p-type and n-type polymeric semiconductors pBTTT and p(NDI2OD–T2), respectively, and two high performing, newly developed p-type copolymers with mobilities of 1–2 $\mathrm{cm^2\,V^{-1}\,s^{-1}}$: the almost amorphous IDTBT with exceptionally low energetic disorder[36] and the highly crystalline DPP–BTz[141] . Such high-mobility systems are promising candidates for spintronics applications due to their demonstrated[7,122] or potentially long spin diffusion lengths.

We correlate spin-lattice relaxation, coherence, and bulk dephasing times with in-situ electrical transport measurements and show that spin relaxation at low and intermediate temperatures of 5–150 K, depending on the polymer and processing conditions, is determined by the same hopping motion which limits the charge carrier mobility. At higher temperatures, spin dynamics become decoupled from the macroscopic mobility and are instead determined by ultrafast local motions of the charge density. For the nearly amorphous polymer IDTBT, this can be traced back to coherent intra-chain fluctuations of the charge density on picosecond timescales, while relaxation in more crystalline films is highly sensitive to the ordering of polymer backbones and is likely dominated by dynamics along the π-π stacking direction.

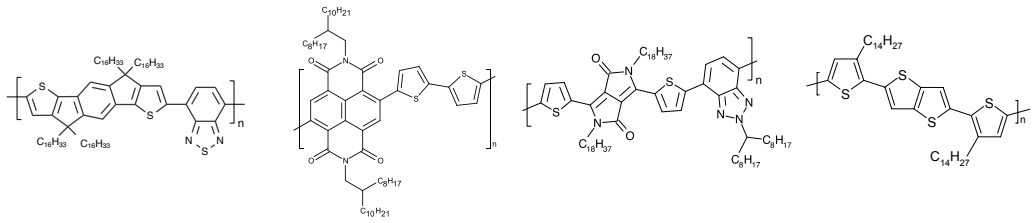

Figure 7.1: Molecular structures of investigated polymers.

Device architecture

The absence of systematic studies of spin relaxation in polymeric semiconductors can be traced back to the experimental challenges posed by FI-ESR measurements: charge carriers are only accumulated within 1–2 nm of the gate dielectric, yielding a very small number of spins in the sample and requiring large-area devices to obtain a satisfactory signal-to-noise ratio (S/N). The microwave field distribution in the cavity on the other hand constrains the substrate dimensions to $3 \times 40\,\mathrm{mm}^2$ for typical X-band cavities, a geometry where spin-coating - the method of choice to deposit high-quality polymer films - reaches its limits. Even at such dimensions, acquiring a single spectrum may take up to one hour and drawing meaningful conclusions about the spin relaxation mechanism from cw-ESR measurements requires temperature, gate-voltage and microwave power dependent data. The resulting days of measurement time demand both an excellent sample stability and a patient experimentalist.

As a result, most published FI-ESR measurements only report spin dephasing times which, unlike spin-lattice relaxation times, can be extracted from a spectrum at a single microwave power, and often do not report either gate voltage or temperature dependences. Especially the missing knowledge of T_1 lifetimes and reporting of ensemble dephasing times T_2^* instead of coherence times T_2 at low temperatures has hindered the identification of spin relaxation mechanisms beyond the motional narrowing regime typically observed for the ESR linewidth at intermediate temperatures[69,142].

To allow for the required integration times and gate voltage as well as microwave power dependent scans, we developed an integrated Python software enabling fully autonomous measurement and temperature cycles (see Appendix C).

We further solve the challenges in sample processing by using quartz glass substrates with grooved back sides that allow for sample fabrication and spin-coating on large and symmetric $40 \times 40\,\mathrm{mm}^2$ substrates which can be subsequently separated into individual $3 \times 40\,\mathrm{mm}^2$ devices. We employ a top-gate bottom-contact architecture with lithographically patterned, interdigitated source-drain electrodes with a channel length of 100 µm and an overall width of 24.3 mm. Each device has an active area of $2.45 \times 20\,\mathrm{mm}^2$ and evaporated contact pads on the far end of the sample allow for electrical contacting outside of the ESR cavity. A schematic of the device architecture is depicted together with a photograph in Fig. 7.2d and details of the manufacturing process can be found in Section 5.5.

7.1 Spin dynamics in IDTBT

With hole mobilities of 1–2 $\mathrm{cm^2\,V^{-1}\,s^{-1}}$, exceptionally low energetic disorder despite its nearly amorphous morphology[36], and a high operational and environmental stability under prolonged bias stress[143], IDTBT is an ideal material to investigate spin dynamics. We will therefore initially establish an understanding of spin relaxation for this model system and will then proceed by discussing to which extent it can be generalized and applied to more complex semi-crystalline films.

Following the work of Nikolka et al.[143], IDTBT films were spin-coated from a 10 mg $\mathrm{mL^{-1}}$ solution of polymer in equal parts of 1,2-dichlorobenzene (DCB) and chloroform (CF) with 7.5 wt% of the small molecule tetracyanoquinodimethane (TCNQ) and annealed at 80 °C for 60 min. The additive TCNQ was shown to passivate the effect of residual water in the polymer film which may otherwise act as polaron traps and degrade the device performance. A 500 nm layer of Cytop (Asahi Glass) was subsequently spin-coated and annealed at 80 °C for 30 min before the shadow-mask evaporation of a 25 nm thick aluminum gate electrode.

The resulting devices show text-book like FET characteristics with a gate voltage (V_G) independent saturation mobility μ_sat down to ~ 170 K and remain operational down to 30 K (see Fig. 7.2a,b). Moreover, any effects of contact resistance

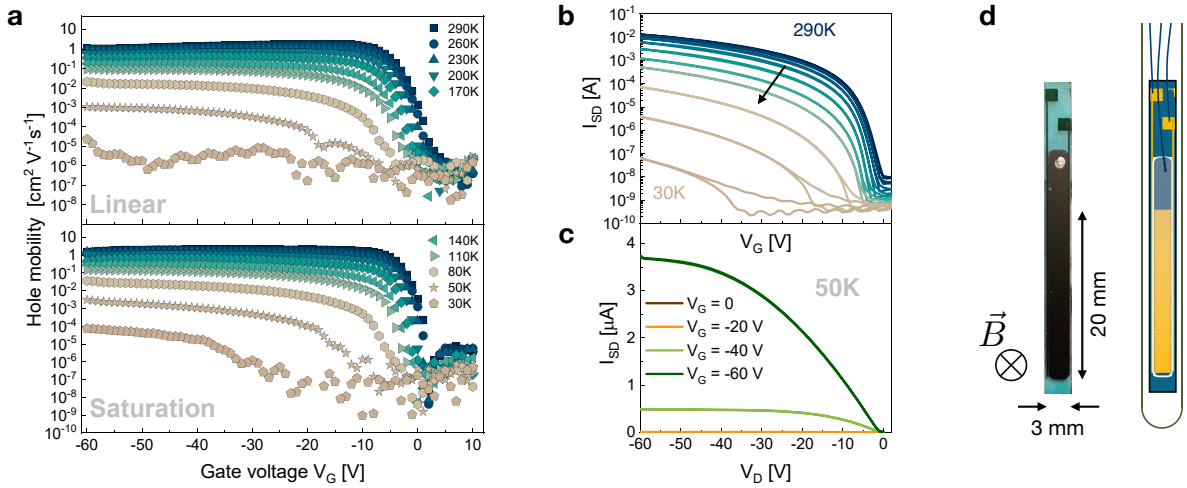

Figure 7.2: Transistor characteristics of IDTBT device for FI-ESR. (**a**) Hole mobilities in the linear and saturation regimes μ_lin and μ_sat with $V_\mathrm{D} = -5$ V and -60 V, respectively, from 290 K to 30 K. The mobility becomes gate voltage independent at 170–200 K. (**b**) Source-drain currents I_SD in the saturation regime of a representative FET from 290 K to 30 K, colour scale same as for mobilities. (**c**) Output curve of the same device at 50 K showing negligible contact resistance at the onset but a visible threshold voltage shift: I_SD vanishes at $V_\mathrm{G} = -20$ V. (**d**) Photograph and schematic of the FET architecture used for FI-ESR.

on the onset of the output curves remains negligible (see Fig. 7.2c) while the eventual shift of the threshold voltage (V_{th}) manifests itself in a vanishing source-drain current I_{SD} for small gate voltages. Charge transport is temperature-activated with μ_{sat} increasing from 10^{-4} at 30 K to 1 $\mathrm{cm^2\,V^{-1}\,s^{-1}}$ at 290 K. Furthermore, both the increase of $V_{\mathrm{th}} \geq 3\,\mathrm{V}$ and a gate voltage dependence of μ_{sat} below 170 K indicate that energetic disorder does manifest itself at lower temperatures and that the hole mobility becomes dependent on the carrier concentration, a phenomenon which we will see reflected in the spin coherence time.

Spin lifetimes in IDTBT

Spin lifetimes have been directly measured by pulsed ESR but can be determined by continuous wave (cw) ESR from the linewidth and power saturation behavior of the resonance line[78,79,100,101,144]. We first verify that the paramagnetic susceptibility $\chi_0 = \mu_0 n_{\mathrm{spin}} \hbar^2 \gamma_{\mathrm{e}}^2/(4k_{\mathrm{B}}T)$ from the ESR spectra (γ_{e}^2, electron gyromagnetic ratio, $2\pi\hbar$, Planck constant, μ_0, vacuum permeability, k_{B}, Boltzmann constant, T, temperature) matches the gate-induced charge concentration calculated from the dielectric capacitance (see Fig. 7.3a,b; Sections 3.3 and 5.3). This confirms that we detect all electronically injected spins.

To determine the spin-lattice relaxation and coherence times T_1 and T_2, respectively, we employ a similar approach to established literature but perform a two-dimensional (2D) surface fit of the microwave power dependent spectra and explicitly account for the effects of field modulation (see Section 5.2 and Fig. 7.3c). This especially reduces the error in T_1 which is otherwise introduced by fitting low S/N spectra at high microwave powers individually.

All spectra above 50 K can be successfully fitted with the saturation behavior of a single Lorentzian resonance, showing that spins experience a *homogeneous* magnetic environment with uniform lifetimes. Below 50 K, spin packets experience an *inhomogeneous* environment with a Gaussian distribution of different HFI and g-tensor fields and the lineshape is well reproduced by a Voigt function: a convolution between this Gaussian distribution with width δB_{rms} and the ever present homogeneous Lorentzian shape of individual spin packets. Assuming similar lifetimes for individual spin packets and only weak spectral diffusion, we may model the saturation behavior as the sum of individual spin packets and determine both δB_{rms} and the intrinsic lifetimes $T_{1,2}$ (see Section 5.2). Note that in this regime, the decay of the longitudinal magnetization takes place within the dephasing time $T_2^* \simeq (\gamma_{\mathrm{e}} \Delta B_{1/2})^{-1}$ which scales with the overall ESR linewidth $\Delta B_{1/2}$. Unlike decoherence, this includes inhomogeneous dephasing which is fully reversible by a π-pulse of resonant microwaves.

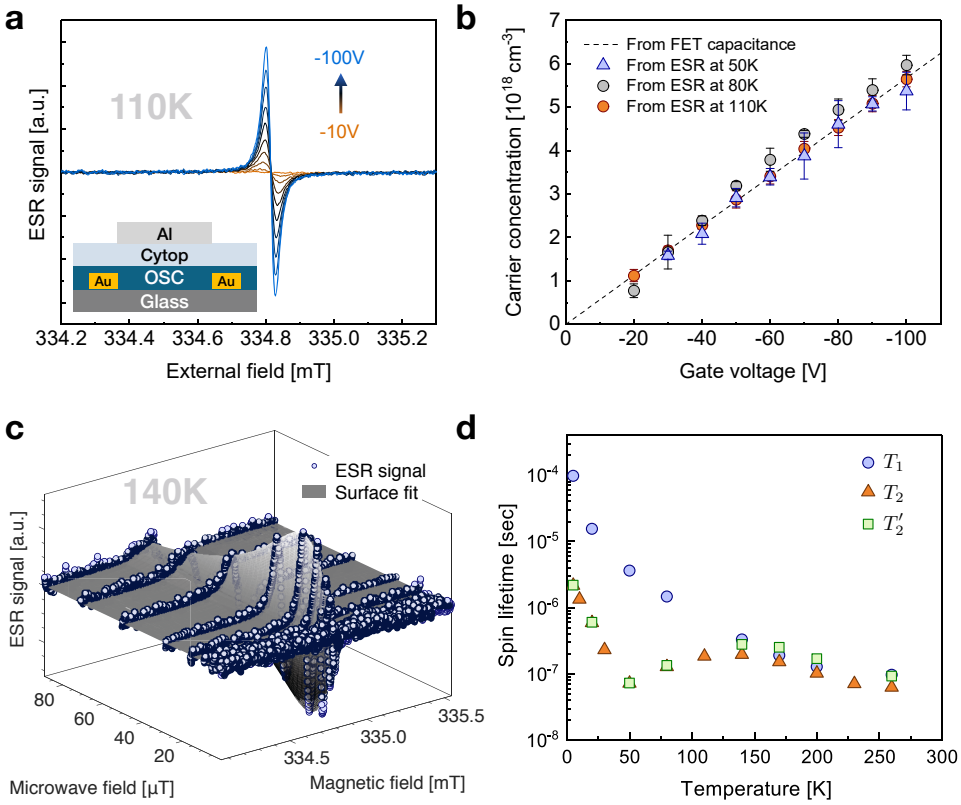

Figure 7.3: FI-ESR in IDTBT. (**a**) FI-ESR spectra of IDTBT at 110 K for gate voltages of 0 V to −100 V in steps of 10 V. Inset shows a cross-section of the FET architecture. (**b**) Gate voltage dependence of the spin concentration n_{spin} determined from the Curie magnetic susceptibility at different temperatures and calculated from the FET capacitance (active area of $2.45 \times 20\,\text{mm}^2$). Surface concentration were converted to volumetric concentrations assuming a 2 nm thick accumulation layer[41]. (**c**) ESR spectra of IDTBT at $V_{\text{G}} = -70\,\text{V}$, 140 K, for increasing microwave powers and 2D fit to determine spin lifetimes. (**d**) Spin lifetimes T_1, T_2 and T_2' for hole polarons in IDTBT at $V_{\text{G}} = -70\,\text{V}$.

The extracted spin lifetimes over the temperature range of 5–290 K are summarized in Fig. 7.3d together with the reduced coherence time $T_2' = (1/T_2 - 1/2T_1)^{-1}$. The latter is determined by subtracting out spin-lattice relaxation effects, which are only half as effective at dephasing a spin, and retaining only the contribution from longitudinal local fields[56]. From Fig. 7.3d, we can identify three distinct regimes of spin dynamics: (1) Below 50 K, the coherence time T_2 gradually decreases with increasing temperatures to reach a minimum of 70 ns while the lineshape remains distinctly inhomogeneous. (2) At intermediate temperatures of 50–150 K, the resonance shape becomes Lorentzian with an increasing coherence time while T_1 and T_2 gradually approach each other up to a maximum coherence time of 200 ns at 140 K where (3) we reach a regime with $T_1 \simeq T_2$ and both lifetimes decrease gradually.

7.2 A motional relaxation picture

Of the above three regimes, the intermediate one has previously been observed and attributed to 'motional narrowing' (for instance by Matsui et al.[80]). Its physics is elegantly captured by the Bloch-Wagness-Refield theory for the spin-density matrix[56,85], which is valid if the amplitude δB_{rms} of the fluctuating fields $B_{\mathrm{eff}}(t)$ that drive relaxation are small compared to their characteristic frequency τ_{c}^{-1}, namely if $\gamma_{\mathrm{e}}\delta B_{\mathrm{rms}}\tau_{\mathrm{c}} \ll 1$. A change of the local field by δB_{rms} then cannot manifest itself as a change in Larmor frequency, since this would require at least the time $t_{\mathrm{d}} = (\gamma_{\mathrm{e}}\delta B_{\mathrm{rms}})^{-1}$, but only causes relaxation. Within this framework, the lifetimes can be expressed in terms of the spectral densities $k_{q=x,y,z}(\omega)$ of field fluctuations which, assuming an exponential decay of field correlations, take the form $k_q(\omega) = (\delta B^q_{\mathrm{rms}})^2\ \tau_{\mathrm{c}}/(1+\omega^2\tau_{\mathrm{c}}^2)$. The spin-lattice relaxation rate scales with the spectral density at the Larmor frequency ω_{L}, as transitions between Zeeman-split levels require an exchange of energy $\hbar\omega_{\mathrm{L}}$ with the lattice, while the decoherence rate includes an additional contribution from $k_q(\omega = 0)$. The lifetimes are therefore given by[48]:

$$T_1^{-1} = \gamma_{\mathrm{e}}^2 \left((\delta B^x_{\mathrm{rms}})^2 + (\delta B^y_{\mathrm{rms}})^2 \right) \frac{\tau_{\mathrm{c}}}{1+\omega_{\mathrm{L}}^2\tau_{\mathrm{c}}^2} \tag{7.1}$$

$$T_2^{-1} = \frac{1}{2T_1} + \gamma_{\mathrm{e}}^2 (\delta B^z_{\mathrm{rms}})^2\ \tau_{\mathrm{c}}\,, \tag{7.2}$$

where the z-axis is defined by the external magnetic field.

Equations (7.1) and (7.2) imply that an increase of the frequency τ_{c}^{-1} always causes an increase in coherence time, therefore resulting in a narrowed resonance line. Spin-lattice relaxation on the other hand is most effective 'on resonance' when $\tau_{\mathrm{c}}\omega_{\mathrm{L}} = 1$. At lower frequencies, the two spin lifetimes gradually approach each other, and at higher frequencies $T_1 \simeq T_2$ both increase with more rapid fluctuations (see Fig. 4.5). Moreover, Eq. (7.2) can be used, if T_1, T_2 and δB_{rms} are known, to determine the characteristic frequency of field fluctuations τ_{c}^{-1}.

The opposite temperature dependence of T_1 and T_2 between 50–150 K shows that we are indeed in such a Redfield regime with $\tau_{\mathrm{c}}\omega_{\mathrm{L}} > 1$ and the slowly converging lifetimes indicate faster field fluctuations at higher temperatures. Decreasing local fields δB_{rms}, for instance due to a reduction of HFI interactions from more delocalized charges[65,129], would increase both T_1 and T_2 concurrently and can therefore be ruled out as the source of longer coherence times.

There are multiple possibilities for a temperature-activated process causing more rapid fluctuations, such as the population of higher frequency vibrational

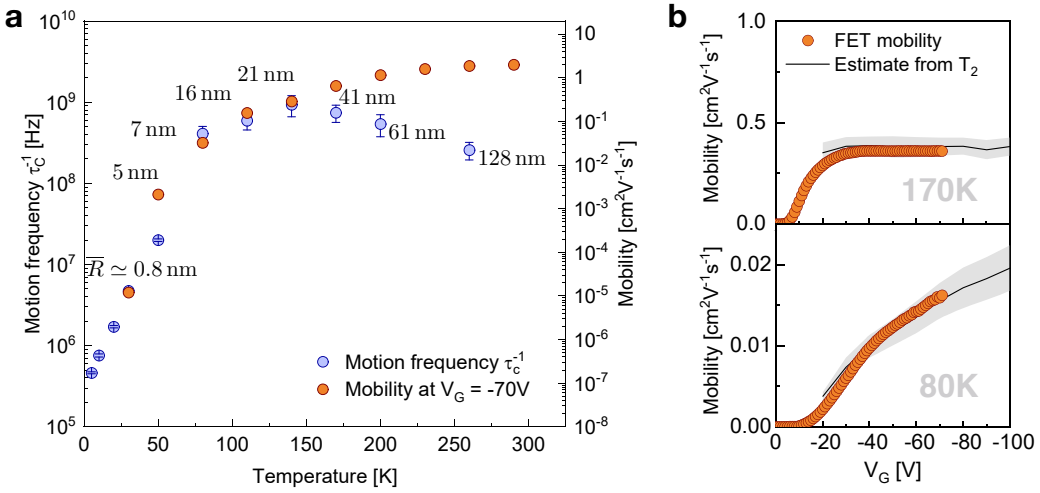

Figure 7.4: Motional relaxation in IDTBT. (**a**) Motion frequency of charges ν determined from T_2' under the assumption of motional relaxation on the left axis and saturation mobilities at $V_G = -70\,\mathrm{V}$ on the right axis. Labels show the extracted hopping distances by relating the two quantities with the Einstein relation. (**b**) V_G dependence of the FET mobility and predicted mobilities form T_2' at 80 K and 170 K by using the Einstein relation with a fixed $\overline{R}$ from (a).

modes. However, the transition from an inhomogeneous to a single Lorentzian line at 50 K indicates that the randomly distributed local fields that broaden the resonance line at low temperatures eventually act as fluctuating fields (with $\gamma_e \delta B_{rms} \tau_c \ll 1$) due to the increasingly rapid charge motion and cause spin relaxation. Direct evidence for this is provided by the matching gate voltage dependences of T_2 and the charge carrier mobility in this regime: the increase of μ_{sat} with V_G, presumably due more rapid charge motion, manifests itself in a narrowing of the resonance line and therefore an increase in T_2. We will quantify this relationship in the following, as shown in Fig. 7.4b.

Incidentally, the onset of motional narrowing at 50 K almost coincides with the onset of macroscopic charge transport in FET measurements. We can therefore identify τ_c^{-1} in this regime as the frequency ν of charge motion between sites and determine $\delta B_{rms}^z \simeq 0.34\,\mathrm{mT}$ from the Gaussian contribution to the linewidth at 5 K where such motion freezes out. In the limit of incoherent charge transport, ν corresponds to the hopping frequency between localized states in the polymer film.

The transition towards longer coherence times below 50 K, when motional narrowing becomes ineffective, has been theoretically predicted[76,90] but to our knowledge not yet experimentally observed. It follows phenomenologically by gener-

alizing the motional relaxation picture to slow hopping rates: decoherence remains driven by charge motion, but the dwell time during which a spin experiences an unchanging local field is sufficiently long to affect its Larmor frequency (thus the Gaussian distribution of resonance positions). In this case, a spin will decohere only after moving to a different environment within $\tau_c = \nu^{-1}$ plus the necessary time $t_d = (\gamma_e \delta B_{rms})^{-1}$ to lose its initial phase such that $T_2' = \tau_c + t_d$[90].

In this picture, the transition to a Redfield regime is modeled by attenuating $t_d \to t_d\,(1 + t_d/\tau_c)$ according to the reduced dwell time at each site and the total coherence time becomes

$$T_2' = \tau_c + \frac{1}{\gamma_e \delta B_{rms}} + \frac{1}{\gamma_e^2 \delta B_{rms}^2 \tau_c}\,. \tag{7.3}$$

Equation (7.3) interpolates between regimes (1) and (2) and enables us to probe charge motion all the way down to 5 K. This is shown in Fig. 7.4a where the motion frequency ν is plotted together with μ_{sat} from FET measurements, both determined at $V_G = -70$ V. The latter is potentially less susceptible to artifacts from contact resistance compared to μ_{lin} and therefore a better measure of the intrinsic mobility[103]. The temperature dependence of ν is significant, showing an increase by four orders of magnitude from 0.5 MHz, where charge motion is frozen out to an extent where FET operation is no longer possible, to 5 MHz, where we start detecting a macroscopic current, to 1 GHz at 140 K.

We have already established that the motion frequency correlates with the macroscopic mobility. In a diffusive model for charge transport, the two are then coupled via Einstein's relationship as $\mu = e\overline{R}^2/(k_B T)\nu$ where e is the elementary charge and $\overline{R}$ denotes the mean length over which charge motion takes place. Resulting estimates for this characteristic length scale are given as labels in Fig. 7.4a. They range from 0.8 nm at 30 K, half the length of an IDTBT repeat unit[106], to ~20 nm at 140 K. Moreover, Fig. 7.4b shows that, for a fixed temperature, the measured gate voltage dependence of μ_{sat} follows the mobility calculated from the gate voltage dependent coherence time T_2' via Eq. (7.3) and Einstein's relationship, using a constant value of $\overline{R}$ form Fig. 7.4a.

This constitutes microscopic evidence for the increase in mobility originating from both faster and longer range charge motion. Such an increase of hopping distances for higher energy states has been theoretically anticipated for instance by Fornari and Troisi[28]. However, one must carefully consider how different states contribute to the macroscopic charge carrier mobility and the coherence time, respectively. The mobility may be dominated by charge carriers occupying states

higher up in the DOS which allow for longer-range hopping. This will be the case for instance for percolation transport in a DOS with variable hopping ranges[39]. On the other hand, we determine the average hopping frequency from T_2' – which is an ensemble value. If τ_c^{-1} is significantly smaller for certain states, this may cause subtle tails in the ESR lineshape that are not captured by a single Lorentzian model with Eq. (7.3)[83]. (The decay of field correlations will no longer be purely exponential with a single characteristic time τ_c.) Such tails are difficult to pick up experimentally, especially with the signal-to-noise ratios achievable in FI-ESR measurements. Spin lifetimes will be dominated by the narrowest feature and the experimentally determined T_2' may be equally skewed towards more mobile charge carriers.

The exceptionally long length scale of ~ 13 repeat units at 140 K may also be somewhat overestimated, since neglecting relaxation pathways other than charge motion may lead to an underestimation of ν. We will revisit this later when discussing spin relaxation above 140 K. On the other hand, a possibly smaller value of $\delta B_{\mathrm{rms}}^z$ from the occupation of more delocalized states would cause an overestimation of ν and an underestimation of $\overline{R}$. Nevertheless, our estimate lies within theoretically predicted values on the order of 10 repeat units for hopping along along a model polymer chain with low energetic disorder[28]. The low amount of backbone torsion[36] and the expected large persistence length in IDTBT[145] corroborate that charge motion indeed takes places over such long length scales. A similar analyses for pBTTT and p(NDI2OD–T2) in Section 7.4 reveals that their lower mobilities are reflected by significantly shorter values for $\overline{R}$.

7.3 High-temperature spin relaxation

We now turn to discussing spin dynamics in the high temperature regime > 140 K. Extending the previously established motional relaxation model to this domain fails for multiple reasons. First, the now decreasing coherence time stands in contrast to the continuously temperature-activated mobility, leading to extracted motion distances of up to 130 nm at room temperature. Such length scales, on the order of the total polymer chain length, are exceedingly unlikely. Second, if the motion frequency were indeed decreasing again below 1 GHz, this should be reflected by an increase of T_1 with temperature, contrary to observations.

We must conclude that spin lifetimes are determined by an alternative relaxation pathway. Remaining within the Redfield model, as supported by the single

Lorentzian resonance, the dominant mechanism above 140 K must be driven by a process faster than $\omega_L = 9.4\,\text{GHz}$, since $T_1 \simeq T_2$, and must either exhibit a decreasing frequency or an increasing amplitude δB_{rms} with higher temperatures.

It is worth noting that the correspondence between the gate voltage dependences of T_2 and μ_{sat} still exists, in the sense that both become independent of V_G. However, while the constant μ_{sat} is a result of low energetic disorder in IDTBT, we will see in Section 7.4 that T_2 in this regime also remains constant for polymers with gate voltage dependent mobilities.

At this point, we would like to highlight the recent work by Tsurumi et al.[78] who report temperature dependent spin lifetimes on single crystalline 3,11-didecyldinaphtho[2,3-d:2',3'-d']benzo[1,2-b:4,5-b']dithiophene (C10–DNBDT–NW) films and see a similar turnaround in the temperature dependence of T_2 above 100 K. They correlate the spin lifetimes with momentum scattering rates estimated from independent Hall effect measurements and a decreasing mobility at higher temperatures, concluding that conventional Elliott-Yafet (EY) spin relaxation of charges in a band structure provides the main relaxation pathway. In contrast, the hole mobility in IDTBT remains temperature-activated up to 300 K and no signs of coherent charge transport such as a Hall effect have been observed. A conventional EY mechanism therefore cannot be applied here.

An Elliott-Yafet type model

However, EY relaxation has been recently adapted by Yu to systems with incoherent hopping transport where spatial scattering, i.e., hopping, replaces momentum scattering in driving spin relaxation[16,75]. Yu recognizes that SOC in organic semiconductors mixes up- and down-spin states of π- and σ-orbitals and quantifies this with the dimensionless spin admixture parameter $\gamma^2 \sim \xi^2/(2\Delta)^2$ where ξ is the atomic SOC and Δ the energy difference between mixed orbitals. As a result, transfer integrals become spin-dependent and the electron-phonon couplings which drive hopping events[25,32] may also cause spin relaxation. The resulting spin-lattice and decoherence rates consequently scale with the hopping rate as $T_1^{-1} = T_2^{-1} = (3/8)\,\gamma^2 \nu$[75]. Unlike the established EY mechanism invoked in ref.[78], such incoherent EY-like relaxation becomes more effective at higher mobilities since spatial scattering enhances charge transport whereas momentum scattering hinders it. Note that the autocorrelation time of the electron-phonon couplings which drive charge hopping and typically fulfills $\tau_c^{-1} > \omega_L$, leading to equal lifetimes T_1 and T_2. Qualitatively, such an EY-like mechanism reproduces the temperature dependence of spin lifetimes in IDTBT.

To a first order approximation, γ^2 is independent of the external magnetic field and fully determined by the electronic structure of the polymer film. We can calculate γ^2 from density functional theory (DFT) for a representative IDTBT morphology to quantitatively assess possible EY-like relaxation. To this end, we use a crystalline morphology based on the most stable (thermodynamic) supramolecular organization and a disordered morphology from ref.[36], determined from molecular dynamics simulations and verified against 2D grazing-incidence wide-angle X-ray scattering (GIWAXS) measurements. Details regarding the DFT calculations are summarized in Appendix F.

The resulting spin admixture of $\gamma^2 = 1.5 \times 10^{-7}$ for a crystalline unit cell increases to an average 1.6×10^{-6} for the disordered morphology due to larger backbone torsion. These values are comparatively small for polymeric semiconductors but consistent with the small g-shift of 110 ppm ($g = 2.00243$) in IDTBT.

The total spin relaxation rates are then given by

$$\frac{1}{T_{1,2}^{\text{tot}}} = \frac{1}{T_{1,2}^{\text{M}}} + \frac{1}{T_{1,2}^{\text{EY}}} \tag{7.4}$$

where $T_{1,2}^{\text{M}}$ and $T_{1,2}^{\text{EY}}$ denote the contribution from motional and EY-like relaxation, respectively. They are plotted in Fig. 7.5a as a function of motion frequency, showing that EY-like relaxation should only contribute significantly in IDTBT for hopping rates above 200 GHz and requires a rate of 20–30 THz to reproduce experimental spin lifetimes at 260 K. The latter is on the order of the vibrational relaxation time $\lesssim 1$ ps in organic semiconductors, meaning that a treatment of charge dynamics in terms of incoherent hopping breaks down[28].

Moreover, the experimental lifetimes indicate that EY-like relaxation should set in around 140 K. We can determine the required motion frequencies throughout this transition from the experimental coherence times with Eq. (7.4). As evident from Fig. 7.5a, there are always two possible values of ν, to the right and left of the crossover point, giving the same coherence times. Unique values can still be determined with the condition of increasing motion frequencies with higher temperatures, and the results are shown in Fig. 7.5b. Those values demonstrate that an onset of EY-like relaxation at 140 K requires a sudden jump in motion frequency from 10^9 Hz to 10^{13} Hz. A smooth increase on the other hand can only be achieved with a significantly higher spin admixture of $\gamma^2 \simeq 5 \times 10^{-3}$ since motion frequencies below 140 K are only lightly affected by a larger γ^2. Such an increase lies beyond what we might expect from outliers in the morphology (compare histogram in Fig. 7.9).

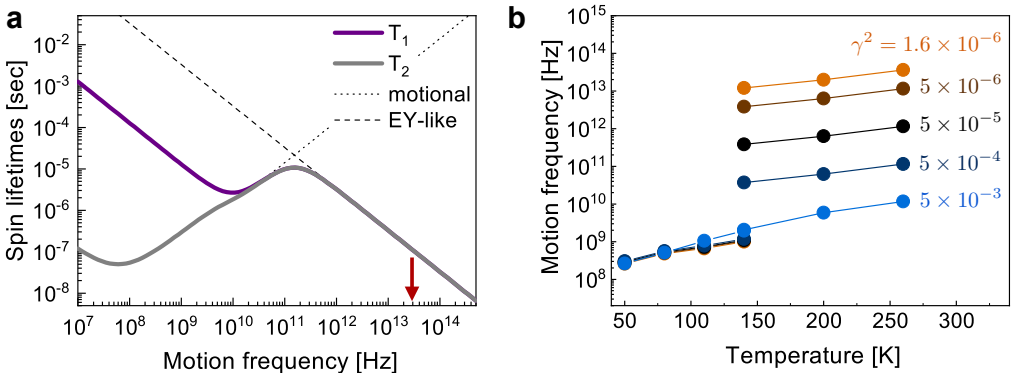

Figure 7.5: EY-like relaxation. (**a**) Expected spin lifetimes as a function of motion frequency ν for an experimental value of $\delta B_{\mathrm{rms}} = 0.34\,\mathrm{mT}$ and a spin admixture of $\gamma^2 = 1.6 \times 10^{-6}$ from DFT. Dashed and dotted lines extrapolate motional relaxation to higher temperatures and EY-like relaxation to lower temperatures, respectively. The red arrow indicates the required motion frequency to reach the measured coherence time at 260 K. (**b**) Required motion frequencies for Eq. (7.4) to reach the experimental coherence times in IDTBT. Plots for different values of γ^2 show that a smooth transition between the two regimes of dominant EY-like and motional relaxation can only be achieved for $\gamma^2 \simeq 5 \times 10^{-3}$.

This leaves us to conclude that EY-like spin relaxation during incoherent hopping events cannot quantitatively explain either the transition away from motional relaxation or the absolute magnitude of achieved lifetimes. Instead, this high temperature relaxation regime must be caused by a type of dynamics that is not directly related to the macroscopic charge carrier mobility.

Intra-site vibrational relaxation

We turn to an alternative temperature-activated process which may couple to the spin and exhibits frequencies exceeding ω_{L}: vibrational modes of the polymer backbone and the accompanying fluctuations of HFI- and g-tensors. From Eqs. (7.1) and (7.2), it is clear that only low frequency modes strongly couple to the spin while higher frequency vibrations are only effective through multi-vibron Raman-like processes. Moreover, translational modes do not change the coupling tensors in the spin's rest frame. We consequently focus on the lowest frequency torsional modes, which also affect the largest spatial displacements of the backbone.

Such modes typically set in at 0.1–1 THz and are challenging to probe experimentally with low frequency Raman or THz spectroscopy. Furthermore, while their frequencies may be experimentally accessible, the corresponding amplitudes (displacements) remain elusive.[1] We again turn to molecular dynamics calculations for a temperature dependent, microscopic picture of torsional modes. The following work has been carried out together with Anton Melnyk and Denis Andrienko at

[1] Pioneering work on measuring such amplitudes in small molecules has been carried out by Illig et al.[47].

the Max Planck Institute of Polymer Research, Mainz, and David Beljonne, Yoann Olivier, and Vincent Lemaur at the University of Mons.

To simulate torsional dynamics, we first constructed a unit cell and built a super cell of 8 lamellae × 16 chains, i.e., 128 tetramers in total. The supercell was equilibrated for 1 ns in the isothermal–isobaric (NTP) ensemble at 100 K. Morphologies were then simulated in the 100 K to 300 K temperature range, at a 10 K step. These trajectories, 1000 snapshots each, were used for further analysis. Details regarding the calculations are given in Appendix G.

To quantify backbone ordering, we evaluated the dynamic order parameter S for the backbone fragments[146,147],

$$S = \left\langle \frac{1}{N} \sum_{i=1}^{N} \left[\frac{3}{2} \left(\mathbf{U}^{(i)} \cdot \mathbf{u}^{(i)} \right)^2 - \frac{1}{2} \right] \right\rangle , \tag{7.5}$$

where the sum is over N equivalent fragments, and $\langle ... \rangle$ indicates time averaging. $\mathbf{u}^{(i)}$ are normal vectors to conjugated fragments, as shown in Fig. 7.6a, while $\mathbf{U}^{(i)} = \left\langle \mathbf{u}^{(i)} \right\rangle$ is the time average of $\mathbf{u}^{(i)}$. The order parameter is close to one, $S \approx 1$, if a fragment retains its orientation through time and an increasing range of motions will result in lower values of S. $S = 0$ indicates a uniformly rotating fragment. The dynamic order parameters of IDT and BT fragments are directly related to the dynamics of the connecting dihedrals, ϕ.

Calculated order parameters are shown in Fig. 7.6b. Note that the dependencies are rescaled to effectively account for quantum effects, which become noticeable at low temperatures, as described in Appendix G. The magnitude of S is dominated by the lowest frequency modes which have the largest amplitudes and start around 0.2 THz for an isolated monomer and 0.3 THz for a chain segment of five monomers, taken from the disordered morphology (see Fig. 7.6a).

Below 170 K, IDT and BT fragments exhibit similar dynamics. Upon further heating, the motion of IDTs gradually increases, while the motion of BT units is subjected to a number of transitions, with the first one at $T = 170$ K. They are a combined effect of the thermal activation of modes and subtle changes in the polymer's morphology which result in a larger free volume for rotations (the melting of side-chains indeed takes place at a much higher temperature of $T_{\mathrm{m}}^{(\mathrm{sc})} \approx 250$ K). The predicted onset of backbone dynamics takes place at temperatures comparable to the experimentally measured $T_{\mathrm{exp}} = 140$ K, at which the coherence time starts to decrease.

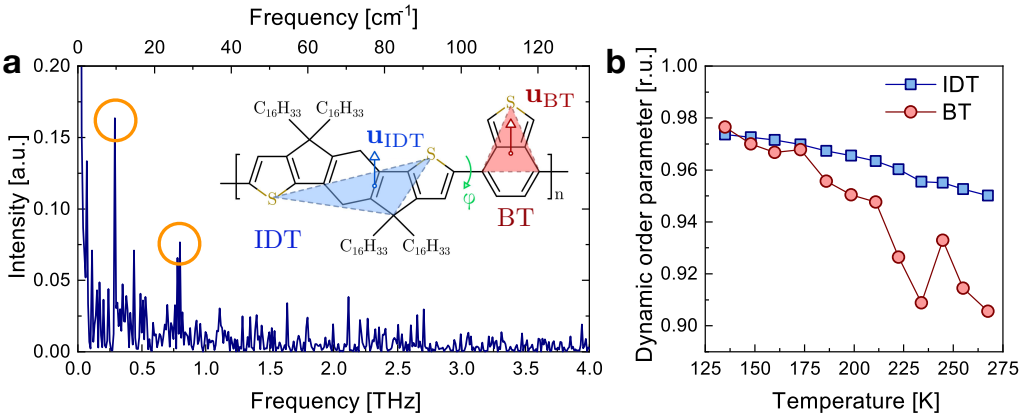

Figure 7.6: Torsional dynamics in IDTBT. (**a**) Fourier transform of the torsion angle autocorrelation function for an IDTBT segment of 5 repeat units, taken from a disordered morphology. It shows the typical frequencies responsible for the fluctuations in torsion angle with two distinct peaks at 3.0×10^{11} Hz and 6.7×10^{11} Hz (orange circles). Inset shows the chemical structure of an IDTBT repeat unit. Vectors $\mathbf{u}_{\mathrm{IDT}}$ and $\mathbf{u}_{\mathrm{BT}}$ define orientations of respective conjugated fragments, which are used to calculate the order parameter S. The dihedral angle ϕ, connecting IDT and BTZ units, is shown in green. (**b**) Dynamic order parameter of IDT and BT fragments as a function of temperature.

From the largest dynamic order parameter of $S \approx 0.9$ and lowest frequencies torsional modes we can estimate the vibrational spin relaxation rate. The expected δB_{rms} from g-tensor fluctuations can be estimated as $2(1-S)\Delta g B_0$ where Δg is the measured g-shift along the external field B_0. This gives in fact an upper bound since the actual change in g-tensor field by a π rotation of the backbone is given by the smaller deviation of the measured Δg from the isotropic value: $2(\Delta g - \Delta g_{\mathrm{iso}})$. With $\Delta g = 120\,\mathrm{ppm}$, this gives a total g-tensor field $\leq 0.04\,\mathrm{mT}$ and a fluctuation amplitude of $\delta B_{\mathrm{rms}}^{\Delta g} \leq 8\,\mu\mathrm{T}$. This indicates that the broadening of the resonance line at 5 K is dominated by HFIs. The larger isotropic HFIs will not be modulated by torsional modes, and a conservative estimate for the dipolar HFIs yields $\delta B_{\mathrm{rms}}^{\mathrm{HFI}} = 0.17\,\mathrm{mT}$.

With the above considerations, the relaxation time from the lowest frequency torsional modes can then be estimated from Eqs. (7.1) and (7.2) to be $T_1^{\mathrm{vib}} = T_2^{\mathrm{vib}} = 150\,\mu\mathrm{s}$, significantly exceeding experimental values. Of course, higher energy modes will become populated at higher temperatures, but they will be less effective at coupling to the spin due to both their higher frequencies and lower amplitudes. We must therefore conclude that torsional modes, despite exhibiting the correct temperature activation, only weakly couple to the spin and cannot explain the observed relaxation times.

Rapid intra-chain dynamics

Despite having ruled out EY-like and vibrational relaxation, the above simulations demonstrate that torsional dynamics show a temperature activation which matches the observed decrease in coherence times. Such dynamic changes in the backbone conformation take place on timescales which are sufficiently slow for the charge density distribution to adapt. The resulting intra-chain displacements of the charge density take place on similar timescales as the vibrational modes themselves and may become sufficiently fast to drive EY-like relaxation.

To this end, we take snapshots from the temporal evolution of an IDTBT chain segment, used to generate the autocorrelation spectrum in Fig. 7.6a, and determine the spin density distribution of an unpaired charge in intervals of 0.8 ps. In our simplified model, the spin density always remains confined to 5 monomers and we neglect any inter-chain effects on the spin density distribution (beyond taking the backbone confirmation from a full morphology). Inter-chain effects however should be small in the amorphous IDTBT, and limiting the simulations to a truncated chain segment should not significantly distort the timescales of spin density fluctuations.

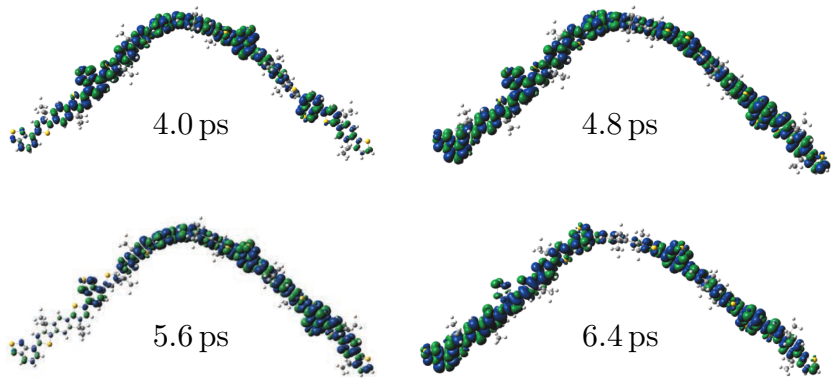

Figure 7.7: Plots of the spin density (CAM-B3LYP/6-31G**) along an IDTBT chain of 5 monomers, extracted from the disordered phase. Representative snapshots in intervals of 0.8 ps, from a total simulated time evolution of 80 ps.

Figure 7.7 shows the resulting spin density contour plots with significant displacements visible on the order of the snapshot intervals themselves. We can therefore conclude that fluctuations of the charge density along the polymer backbone indeed take place at frequencies of 1–10 THz, sufficiently fast to drive the observed spin relaxation even for a spin admixture of $\gamma^2 = 1.6 \times 10^{-6}$.

Furthermore, not only can the lowest frequency torsional modes be effective at displacing the charge density along the backbone. Anderson et al.[148] recently

showed that higher frequency carbon-stretching modes starting around 1000 cm^{-1} (30 THz), observable as intense peaks in the infrared (IR) absorption spectrum of doped polymer films, can displace the charge density at an unusually low frequency. As the temperature increases beyond 140 K, such modes will gradually become populated, potentially further driving spin density fluctuations and relaxation. We therefore attribute spin relaxation at high temperatures to a rapid, intra-chain shuttling motion of the spin density in combination with a finite spin admixture from SOC. Simulations of the dynamic order parameter suggest that this is partially owed to torsional modes which become more pronounced at 170 K. We would like to emphasize however that such an onset does not need to be immediate since spin lifetimes are determined by a competition of relaxation processes and motional relaxation becomes less effective at high temperatures. The gradual onset of adiabatic intra-chain charge motion will eventually cause EY-like relaxation to dominate the spin lifetimes – this thermal activation also becomes evident in the further decreasing spin lifetimes when approaching room temperature.

On the other hand, EY-like relaxation theory has been developed for incoherent hopping events and therefore reaches its limit in this regime. While we expect γ^2 to remain a good parameter to quantify the potential for spin relaxation, a microscopic theory for such adiabatic charge dynamics is needed.

To experimentally confirm that spin relaxation is indeed caused by an intra-chain process, we isolate highly diluted IDTBT chains in an inert polystyrene (PS) matrix of comparable molecular weight and introduce a small number of charge carriers by p-type doping the film with the small molecule 2,3,5,6-Tetrafluoro-7,7,8,8-tetracyanoquinodimethane (F4–TCNQ).[1]

[1] Doping with Mo(TFD-$COCF_3)_3$, the radialene-based dopant CN6-CP, or the closed shell anion bis(trifluoromethylsulfonyl)-imide (TFSI) all proved too unstable over the course of a full temperature cycle.

The films were spin-coated at 1200 rpm from a 30 mg mL^{-1} solution of PS in DCB with an added 0.33 wt% of IDTBT. Similar to the FI-ESR sample processing, films were deposited on $40 \times 40\,mm^2$ pre-grooved glass-slides and then separated into $3 \times 40\,mm^2$ large samples. Charge carriers were introduced by thermally evaporating 100 nm of F4–TCNQ on top of the films and we confirmed with van der Pauw measurements that no macroscopic current can be measured. This is consistent with similar results on pBTTT:PS films where macroscopic charge transport breaks down at pBTTT concentrations below 2 wt%[149]. Moreover, owed to the weak interactions between polymer chains, IDTBT is unlikely to aggregate either in the PS solution or the resulting thin film.

The ESR spectra at 260 K are shown in Fig. 7.8a and are successfully fit over the full range of microwave powers by two distinct resonances at $g = 2.0034$

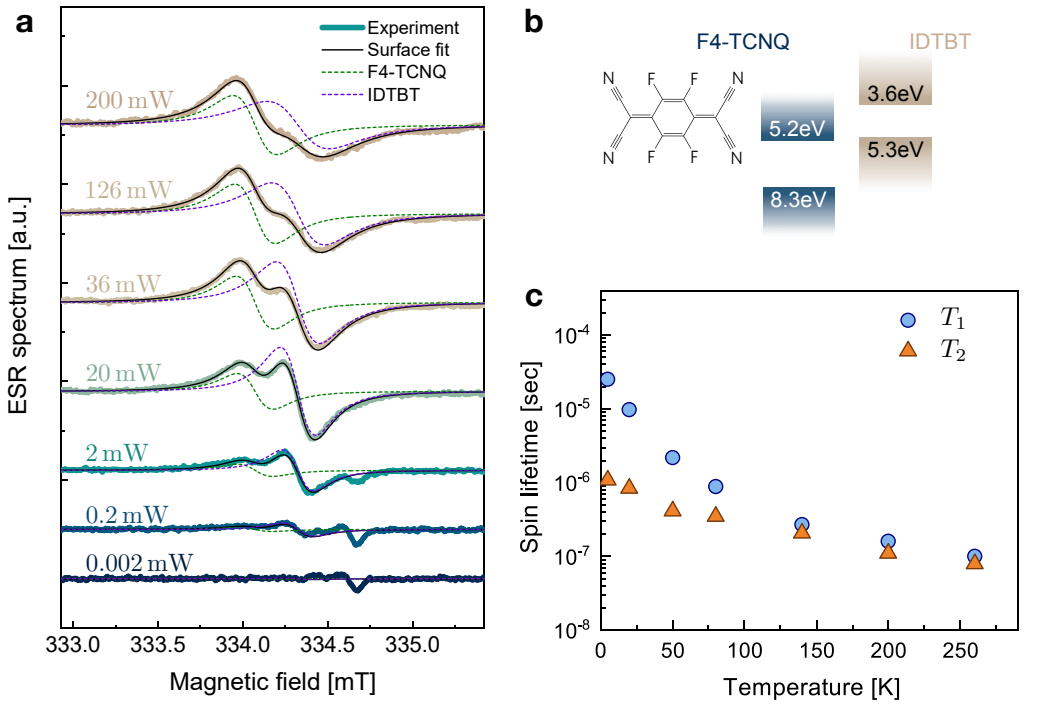

Figure 7.8: Intra-chain relaxation in IDTBT. (**a**) Slices from a ESR power saturation scan of doped IDTBT in a polystyrene matrix (260 K). The surface fit of two resonances (solid black lines) is shown together with separate contributions from F4–TCNQ and IDTBT at $g = 2.00395$ and $g = 2.00243$, respectively (dashed lines). The small signal at 334.7 mT, visible at low microwave powers, comes from a known paramagnetic impurity in the quartz substrate. (**b**) HOMO and LUMO levels of IDTBT and F4–TCNQ. (**c**) Temperature-dependent spin lifetimes of the IDTBT resonance.

and $g = 2.00243$. The lower-field resonance can be attributed to F4–TCNQ$^-$, which has a reported g-factor of ~ 2.003[81,150], while the higher-field resonance matches exactly with the previously determined g-factor of IDTBT. Furthermore, each of the resonances at 260 K corresponds to $(1.9 \pm 0.1) \times 10^{11}$ spins, confirming equal numbers of dopant ions and polarons. The resulting carrier concentration of $\sim 5 \times 10^{17}\,\mathrm{cm}^{-3}$ (per volume of IDTBT, assuming similar weight-to-volume ratios for IDTBT and PS) is lower than in FI-ESR devices, likely due to the weak energetic driving force for electron transfer from IDTBT to F4–TCNQ (see Fig. 7.8, ref.[143]). Indeed, both dopant and polaron spin concentrations show a temperature-activated behavior and decrease by almost one order of magnitude down to 5 K.

The extracted spin lifetimes are shown in Fig. 7.8c and exhibit a remarkable similarity to those determined from FI-ESR above 140 K. The quantitative agreement is not exact, with somewhat longer lifetimes for IDTBT in PS. This difference

may be caused by a number of factors, such as a different backbone conformation in PS or preferential doping of more localized IDTBT sites with a higher HOMO level. Nevertheless, the close resemblance demonstrates that polarons confined to a single IDTBT chain exhibit similar high temperature spin dynamics as in a continuous film, suggesting that intra-chain relaxation is indeed dominant. At lower temperatures, the IDTBT:PS samples show consistently longer coherence times, together with a larger Gaussian contribution to the lineshape, indicating possibly weakly pronounced motional narrowing together with reduced intra-chain charge dynamics.

Such a suppression of motional narrowing for isolated IDTBT chains may be a consequence of preferentially doping (trap) states close-to or within the band gap, but it may also indicate that incoherent hopping between IDTBT chain segments (e.g., separated by kinks in the polymer chain) mostly takes place through an inter-chain process when neighboring backbones come sufficiently close to each other.

7.4 Spin dynamics in semi-crystalline polymers

With our understanding of the relaxation processes in IDTBT, we now turn to the more crystalline polymers pBTTT, DPP–BTz, and p(NDI2O–T2), with the aim to establish a general picture of spin dynamics in high mobility polymers. pBTTT and p(NDI2O–T2) are both widely studied p-type and n-type conjugated polymers, respectively, with field effect mobilities of 0.1–0.5 $\mathrm{cm^2\,V^{-1}\,s^{-1}}$[139,151] while DPP–BTz with a hole mobility of 1–2 $\mathrm{cm^2\,V^{-1}\,s^{-1}}$ belongs to an emerging class of high-performance ambipolar copolymers[140].

Sample processing

FI-ESR devices were again fabricated as outlined in Section 5.5. pBTTT was spin-coated at 1500 rpm from a 10 $\mathrm{mg\,mL^{-1}}$ solution in DCB, DPP–BTz was spin-coated from a 10 $\mathrm{mg\,mL^{-1}}$ solution in CB, and p(NDI2O–T2) was spin-coated at 2000 rpm from a 5 $\mathrm{mg\,mL^{-1}}$ solution in toluene. We used CYTOP as a gate dialectic for pBTTT and poly(methyl methacrylate) (PMMA) for DPP–BTz and p(NDI2O–T2). pBTTT and DPP–BTz films were respectively annealed at 180 °C and 110 °C after spin-coating.

It is known that one can tune the size of the crystalline domains in p(NDI2O–T2) films while keeping other properties such as cumulative positional disorder, energetic disorder and polymer chain orientation in the crystalline domains largly

unaffected[58,152]. Here, we selectively dry the spin-coated films in vacuum ('as-cast') or anneal them at 200 °C ('annealed'). We observe an estimated increase of the crystallite volume by a factor 4 upon annealing, together with a more pronounced face-on orientation (see Fig. 7.9 and Table 7.1). p(NDI2O–T2) therefore is an ideal system to investigate the impact of crystallinity on spin dynamics while keeping other parameters mostly constant.

Results

Figure 7.9 gives an overview of determined spin lifetimes, revealing common motional and inverted relaxation regimes but striking qualitative and quantitative differences in onset and magnitude. All three polymers exhibit a motional relaxation regime with the transition from Voigtian to Lorentzian resonances, i.e., the onset of motional narrowing, taking place at the low temperature minimum in T_2. This onset was observed at 50 K for IDTBT but shifts up to 80 K and 110 K for as-cast p(NDI2O–T2) and pBTTT, respectively, already indicating lower motion frequencies. Only DPP–BTz stands out by exhibiting Lorentzian lineshapes down to 5 K, showing that charge motion at all temperature remains sufficiently fast to average over HFI and g-tensor fields. We are therefore unable to estimate δB_{rms} and determine exact motion frequencies. Nevertheless, from the onset of motional narrowing in other polymers, frequencies likely exceed 10^7 Hz at 5 K, reflecting the exceptional charge carrier mobilities measured in this system[141]. As shown for IDTBT, the gate voltage dependences of the charge mobilities consistently correlate with the coherence times in this regime.

The determined motion frequencies and distances for pBTTT and as-cast p(NDI2O–T2) are given in Fig. 7.9e,f and reach values of 0.2–0.3 GHz around 200 K before a high temperature relaxation mechanism becomes dominant. Comparing charge dynamics at 140 K to IDTBT, we see that the lower mobilities of pBTTT and p(NDI2O–T2) are reflected by 5 to 10 times slower charge motion with $\nu \simeq 0.1$–0.2 GHz and significantly shorter length scales of 1–3 nm. Consistent with previous reports[36], we can confirm that IDTBT stands out by supporting efficient, long range charge transport along highly planar polymer backbones.

All polymers also exhibit a similar high temperature regime of spin relaxation, with an inverted temperature dependence of coherence times and $T_1 \simeq T_2$, as observed for IDTBT. However, the onset of the latter varies significantly: It takes place at 200 K in as-cast p(NDI2O–T2), somewhat earlier compared to 230 K for pBTTT, and notably shifts all the way down to 110 K for annealed p(NDI2O–T2) and DPP–BTz films. Indeed, coherence lifetimes in annealed p(NDI2O–T2) both

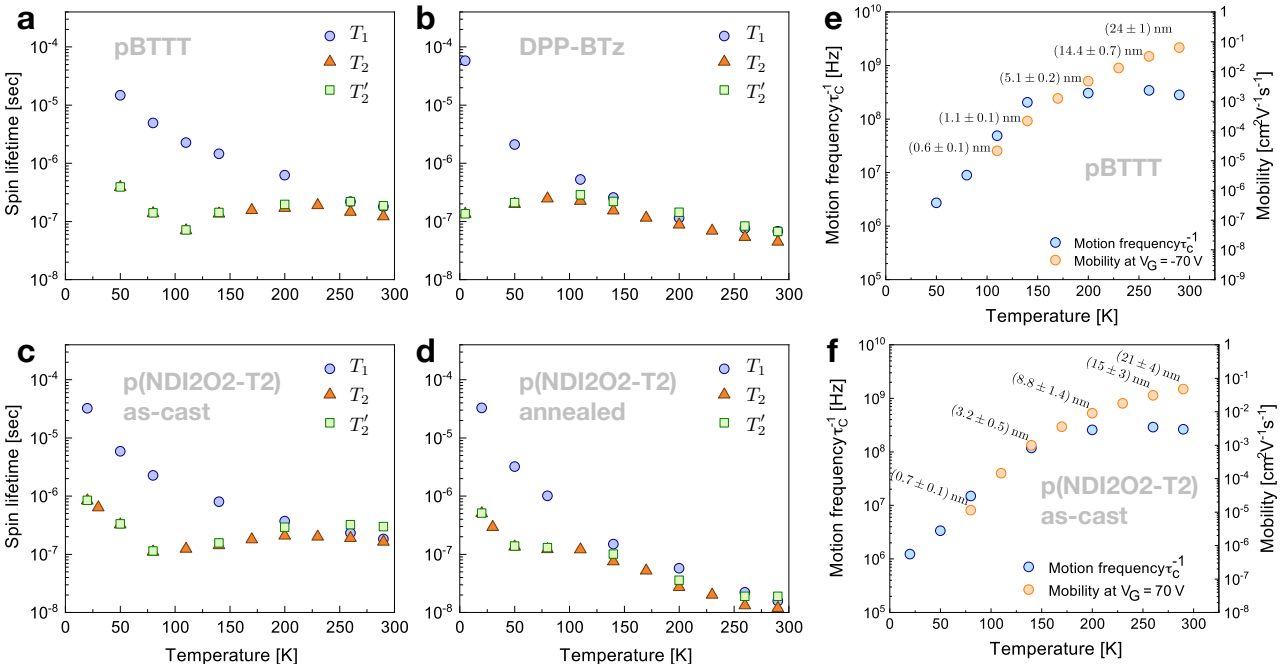

Figure 7.9: Spin lifetimes of field-induced charges in (**a**) pBTTT, (**b**, **c**) as-cast and annealed p(NDI2O–T2), and (**d**) DPP–BTz, determined by power saturation measurements at gate voltages of −70 V for p-type and 70 V n-type materials. The low temperature minima of T_2 coincide with transitions from Voigtian to Lorentzian lineshapes, except for DPP–BTz which shows a Lorentzian resonance down to 5 K. (**e**, **f**) Charge carrier mobilities from FET characteristics, motion frequencies determined from T_2' (assuming motional relaxation), and resulting distances $\overline{R}$ for pBTTT and as-cast p(NDI2O–T2).

decrease considerably earlier and are overall reduced by an order of magnitude at room temperature. We can therefore dramatically change spin dynamics for the same polymer by tuning its morphology, providing us with a unique opportunity to isolate the underlying mechanism.

Spin relaxation and morphology in p(NDI2O–T2)

We characterized the microstructure of annealed and as-cast polymer films by GIWAXS measurements (Fig. 7.10). The lattice spacing from both lamellar and backbone directions are slightly expanded upon annealing, while the π-π stacking distance is marginally reduced. Thermal annealing also effectively increases the coherence length of stacking along all three crystallographic directions, with an increase of in-plane (IP) coherence lengths from 16.5 to 20.7 nm along the backbone direction and from 20.1 to 38.1 nm along the lamellar stacking direction. Stacking distances and coherence lengths are summarized in Table 7.1. Moreover, the GIWAXS pattern of the annealed film in Fig. 7.10b shows emerging cross peaks indicative of an enhanced periodicity in backbone stacking (e.g., NDI units

stacking next to NDI units). From a radial slice along the (100) diffraction, we can determine the fraction of crystallites at different backbone tilt angles, revealing a more pronounced face-on orientation of backbones (Fig. 7.10c).

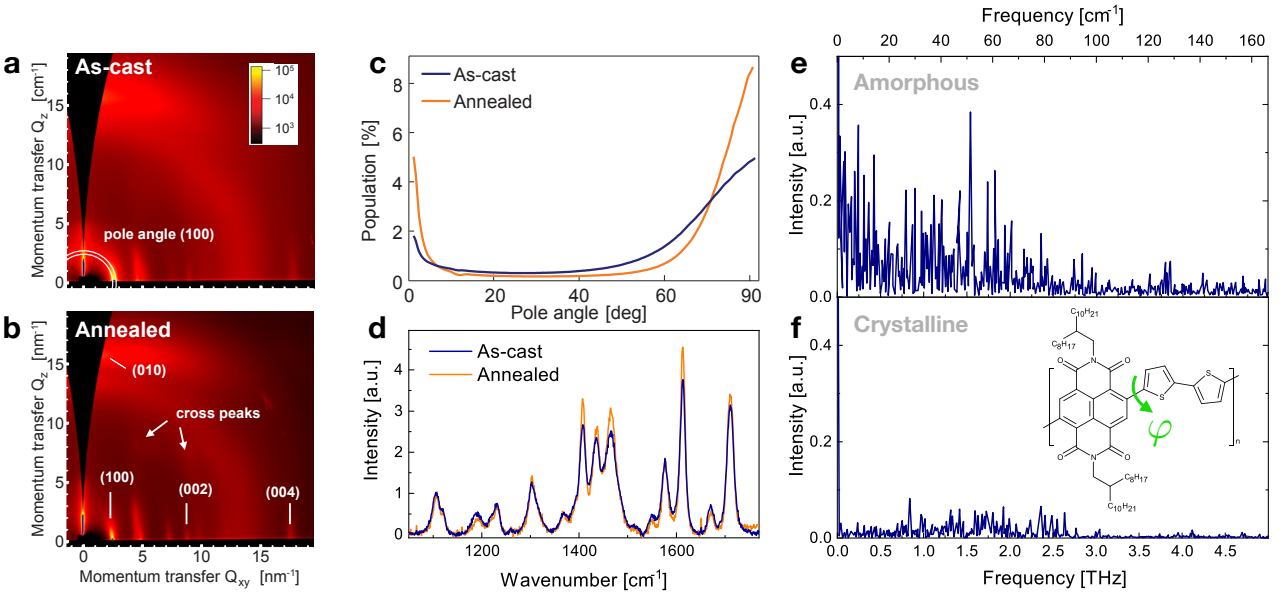

Figure 7.10: Structural characterization of p(NDI2O–T2). (**a**, **b**) GIWAXS patterns of as-cast and annealed p(NDI2OD–T2) films. Peak assignments are based on previous reports[153,154] and respective stacking distances and coherence lengths are given in Table 7.1. (**c**) Crystallite orientation distribution profiles (COD) extracted from the circular line cut across the (100) diffraction indicated in (a). 0° denotes the direction perpendicular to the substrate. Annealed p(NDI2OD–T2) forms more face-on crystallites, as evidenced by the higher population for pole angles $> 70°$ (data close to 0° is affected by 'specular spray' and may not reflect scattering from crystallites). (**d**) Normalized Raman spectra of as-cast and annealed p(NDI2O–T2) films (532 nm excitation). The difference in relative peak amplitudes can be traced back to a narrowing of the carbon-carbon stretching resonances at 1400–1500 cm^{-1} for the annealed film while relative peak areas remain unaffected. Peak assignments are based on ref.[155]. (**e**, **f**) Simulated autocorrelation functions of the NDI–T torsional angle φ (see inset) for amorphous and crystalline phases from ref.[156]. The crystalline phase shows reduced amplitudes as well as a narrowing and shift of modes to higher frequencies.

The GIWAXS measurements therefore mainly show an enlargement of crystallites and a reduction in orientational disorder, neither of which is expected to cause an increase in spin admixture. Furthermore, Di Pietro et al. have shown that all charge carriers detectable by charge accumulation spectroscopy (CAS) reside within the crystalline domains of the film[152], regardless of the degree of crystallinity, and are therefore likely to experience a similar local environment.

Furthermore, from the subtle changes in stacking distances upon annealing, we do not anticipate a significant increase in torsional dynamics. In fact, simulated autocorrelation spectra of the torsion angle between the naphthalene diimide (NDI)

	Lamellar (IP)		Backbone (IP)		π-π stacking (OOP)	
	Spacing [nm]	Coh. length [nm]	Spacing [nm]	Coh. length [nm]	Spacing [nm]	Coh. length [nm]
As-cast	2.45	20.13	1.40	16.48	0.387	2.12
Annealed	2.53	38.06	1.42	20.73	0.382	3.49

Table 7.1: In-plane (IP) and out-of-plane (OOP) stacking distances and coherence lengths for as-cast and annealed p(NDI2O–T2) films. Lamellar spacing is determined from the (100), backbone spacing from the (002), and π-spacing from the (010) peak position. Coherence lengths are determined from the respective peak widths by the Scherrer equation. The narrowing of diffraction peaks upon annealing indicates an increase in the average crystallite volume by a factor of 4 and the average lamellar area by a factor of 2.

and thiophene (T) units for amorphous and crystalline phases indicate a shift of modes to higher frequencies and a decrease of amplitudes for the more ordered structure (Fig. 7.10e,f). For either processing condition, charges predominantly reside in crystalline areas and should only be weakly affected. In the higher frequency range of 1000–1800 cm^{-1} (30–54 THz), Raman measurements on as-cast and annealed films only reveal a narrowing of the collective carbon-carbon stretching modes at 1400–1500 cm^{-1} (Fig. 7.10d), but no shift of frequencies.

A further effect of annealing, the emergence of a gate voltage dependent mobility at room temperature, has recently been linked to a small fraction of charge carriers which exhibit enhanced mobilities due to Coulomb repulsion in multiply occupied crystallites[58,152]. We observe a similar, albeit less pronounced, gate voltage dependence of μ_{sat} in our FI-ESR devices at 290 K but note that the coherence time remains gate voltage independent (Fig. 7.11). As previously concluded for IDTBT, high temperature spin relaxation therefore cannot be correlated with the macroscopic mobility.

Crystallinity and spin dynamics

The apparent relationship between in-plane crystallite size and the onset of the EY-like regime extends beyond p(NDI2O–T2) to the other two polymer systems. DPP–BTz exhibits IP spacing coherence lengths of 30 nm[141], approaching those of annealed p(NDI2O–T2), while the ribbon phase of pBTTT exhibits much smaller coherence on the scale of ∼7 nm (despite showing micrometer-sized topographic features)[157–159]. IDTBT, as a point of reference, is the least crystalline of the above systems, with coherence lengths of 4.9 nm and 3.3 nm for lamellar and π-π spacing, respectively.

We therefore speculate that for the above systems, rapid intra-crystallite dynamics of the charge density and scattering by translational and vibrational modes

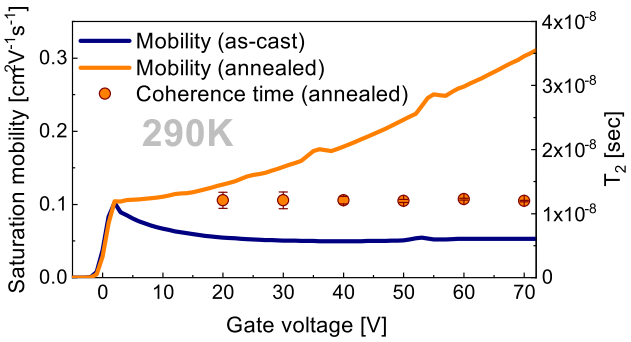

Figure 7.11: Gate voltage dependence of the electron mobility in FI-ESR devices with as-cast and annealed p(NDI2O–T2) at room temperature (left axis) and gate voltage dependence of the coherence time for annealed p(NDI2O–T2) (right axis).

replaces the intra-chain charge dynamics in IDTBT in driving an EY-like relaxation process. In fact, ab initio calculations and CAS measurements indicate that polarons in highly crystalline polymers such as pBTTT[27] and p3HT[35] are delocalization over several π-stacks. This has recently been quantified systematically by Chew et al. from CAS spectra of p3HT[160]: they demonstrate that an in increase in molecular weight reduces the energetic disorder along the intra-chain direction in crystallites and leads to polaron coherence lengths of up to five π-stacks, i.e., fully 2D polarons. Interestingly, they show that the macroscopic mobility is limited by transport between crystallites for molecular weights exceeding $13\,\mathrm{kg\,mol^{-1}}$, as opposed to the local extent of polarons. This is consistent with previous results by Statz, Di Pietro et al. who attribute the increase in mobility for annealed p(NDIO2–T2) to more efficient transport between crystallites[58,152].

We therefore expect an increased 2D character of polarons due to the reduced disorder along the inter-chain direction in annealed p(NDIO2–T2). This will simultaneously expose polarons to bulk and inter-chain vibrational modes which may transiently localize wave functions, analogous to the transient localization picture recently established for small molecules[22]. Such intra-crystallite charge dynamics will only become more pronounced with increased crystallite sizes.

Spin admixtures in pBTTT and p(NDI2O–T2)

Relaxation in this picture remains a consequence of the finite admixture between spin-up and -down states from SOC. This admixture γ^2 is expected to be larger for p(NDI2O–T2) with a typical torsion angle of $\sim 41°$ between NDI and T units[156]. We therefore carried out similar DFT calculations for crystalline morphologies of pBTTT and p(NDI2O–T2), determining the distribution of γ^2 across different sites in the morphologies.Figure 7.12 shows the resulting histograms and reveals a

shift of the γ^2 distribution to values of $1–3 \times 10^{-6}$ for p(NDI2O–T2) compared to $0.2–1.0 \times 10^{-6}$ for pBTTT.

The larger SOC in p(NDI2O–T2) also manifests itself in a g-shift of 1070 ppm for the as-cast sample which increases by 60% to 1670 ppm for the annealed film, contrary to expectations from the more pronounced face-on orientation of backbones. This may result from larger torsion angles due to an enhanced periodicity in backbone stacking, or from a slight redistribution of local spin densities towards the sulfur atoms[110]. In either case, the dramatic decrease of spin lifetimes upon annealing is likely driven by a combination of enhanced intra-crystallite charge dynamics and larger SOC.

In addition, a notable difference between IDTBT and the more crystalline polymers lies with the distribution of γ^2 across sites. pBTTT and p(NDIO2–T2) consistently show a number of outliers up to $\gamma^2 \sim 7 \times 10^{-6}$ while IDTBT exhibits a very narrow distribution around an average of $\gamma^2 = 1.6 \times 10^{-6}$. We attribute the larger distribution of spin admixtures to a wider variety of local backbone geometries and are currently in the processes of identifying the nature of those sites and their contribution to charge transport. Increasing the size of crystallites will allow polarons to sample a larger part of the γ^2 distribution and should therefore contribute to more pronounced spin-flip relaxation, likely contributing the dramatic effects upon annealing of p(NDIO2–T2) films.

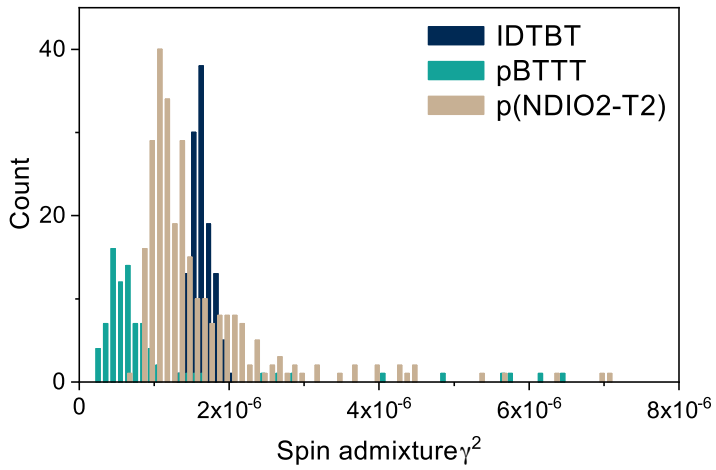

Figure 7.12: Spin admixtures γ^2 calculated for an amorphous IDTBT morphology and crystalline morphologies of pBTTT and p(NDI2O–T2). The histograms contain a total of 120, 90 and 275 segments for IDTBT, pBTTT and p(NDI2O–T2), respectively, and outliers can be traced back to sites with larger backbone torsion. Details regarding the DFT calculations are given in Appendix F.

DFT calculations for DPP–BTz are currently still in progress. Nevertheless, from the g-shift of 1480 ppm we expect a similarly high spin admixture which again, combined with the large crystallite size, is consistent with the pronounced EY-like relaxation.

7.5 Discussion

We have demonstrated that polaron spin dynamics at low and intermediate temperatures are driven by charge motion through static local HFI fields and g-tensor anisotropies. The coherence time undergoes a distinct transition at the onset of motional narrowing and we can quantify the charge's motion frequency throughout this transition and down to temperatures where electrical measurements are no longer possible. Spin coherence times therefore serve as a probe for hopping frequencies which form the basis of charge transport simulations but often remain elusive to the experimentalist.

Comparing motion frequencies with macroscopic mobilities, we show that the temperature-activated mobility stems from both faster and longer range motion and identify polymers such as IDTBT and DPP–BTz that support exceptionally long range charge displacements or rapid charge motion.

At higher temperatures an EY-like process becomes the dominant relaxation pathway, which however must take place on significantly faster timescales than the motion which determines the macroscopic mobility. For IDTBT, we can isolate this to be an intra-chain process and DFT calculations suggest that temperature-activated torsional modes indeed cause sufficiently rapid adiabatic charge density displacements.

In more crystalline systems, spin lifetimes become highly sensitive to the crystallite size. This indicated that intra-crystallite motion replaces the intra-chain motion in driving EY-like relaxation and is consistent with the expected 2D nature of polarons in such systems. Moreover, such semi-crystalline systems exhibit a larger distribution of spin admixtures with a tail of outliers up to $\gamma^2 \sim 7 \times 10^{-6}$ and likely allow a polarons to sample large larger admixtures with increased crystallite sizes.

The presented measurements and simulations also provide first guidelines for the targeted development of systems that support both efficient charge transport and long spin lifetimes. By tuning the polymer morphology to achieve low torsional disorder and to suppress vibrational modes which transiently localize the spin density,

we anticipate that microsecond room temperature spin lifetimes should be achievable in high mobility polymers. Recently reported spin diffusion lengths of 1 µm in pBTTT are possible despite comparatively short spin lifetimes[7], demonstrating the potential impact of the right molecular design. Our work will ideally provide the starting point for more elaborate structure property relationship studies.

Chapter 8

Conclusions

We have seen in the previous chapters that both SOC and HFIs in organic semiconductors highly depend not only on the elemental composition but also the molecular geometry and thin film morphology of a material. We have developed clear design guidelines for tuning the effective SOC in a series of isolated molecules, which in principle should extend to thin films when accounting for the inter-molecular spread of spin densities. In a second step, we turned to probing spin dynamics in polymer thin films by FI-ESR, revealing an interplay of competing motional and EY-like relaxation processes – the former driven by longer range hopping events and the latter determined by sub-picosecond microscopic dynamics of the spin density. The investigated molecular and polymeric semiconductors were deliberately chosen from classes of state-of-the-art charge transport materials that are currently being investigated for thermoelectric and thin film transistor applications.

Especially the ESR measurements on solid state devices reveal a complex dependence of spin lifetimes on vibrational modes which can displace the spin density on microscopic intra-chain or intra-crystallite length scales. From the thermal activation of the resulting EY-like relaxation and the DFT calculations of spin density dynamics, it is likely that the lowest frequency torsional modes already contribute to such displacements. However, higher frequency carbon-carbon stretching modes or acoustic phonons in crystallites may also contribute to relaxation. Probing such processes directly can be challenging, especially due to low $\geq 100\,\mathrm{ns}$ resolution of time-resolved ESR measurements and the failure of typical magneto-optic detection schemes (e.g., Kerr and Faraday rotation spectroscopy) for polaron spins in OSCs.

A more promising route may lie in suppressing or enhancing certain modes, for example by physical strain on thin films deposited on flexible or piezoelectric substrates[161,162] and probing the resulting effects on charge transport and spin relaxation. The latter may well be combined with the excitation of specific modes through surface acoustic waves.

Our results also suggest that coherence times exceeding $10\,\mu\mathrm{s}$ should be possible at room temperature if charge motion is suppressed and the polaron wave function

remains sufficiently confined to a single molecule. This will require the careful selection and isolation of molecules in a suitable host system and may lead to a realization of molecular quantum bits.

Finally, while spin relaxation is increasingly better understood, there remain a number of fundamental question about the nature of spin transport in organic materials. Notably, the ability to detect ESR signals from polaronic charge carriers provides unambiguous proof for the expected spin precession at $\omega_\mathrm{L} = \gamma_\mathrm{e} B_0$ but there has been to date no reliable observation of the Hanle effect in such materials[121,163]. This may be the result of artifacts inherent to certain device architectures such as organic spin valves[136,137], or the ac-microwave drive in spin-pumping based injection schemes[164,165]. Nevertheless, the lack of any Hanle signature casts doubt on the suitability of organic materials for spintronics applications. Pulsed ESR may provide a way to directly probe spin diffusion in multi-layer samples with materials of varying g-factors. Creating an in-plane magnetization with a $\pi/2$-pulse tuned to one g-factor and rephasing it with a π-pulse tuned to a second material's g-factor may enable the time resolved detection of spin diffusion between layers.

Another such question regards the contribution of exchange coupling to spin transport at carrier concentrations of $> 10^{20}\,\mathrm{cm}^{-3}$, achievable by molecular doping. It is hard to explain the micrometer spin-diffusion lengths $\lambda_\mathrm{s} = \sqrt{D_\mathrm{s} T_1}$ in pBTTT and p3HT merely by rapid charge diffusion, indicating a larger spin diffusion constant D_s. Current models include contributions from exchange-driven mutual spin-flips and consider a very simplified morphology with resulting exchange couplings of $J \simeq 10\,\mathrm{meV}$, estimated from spherical wave functions[77]. Such couplings should manifest themselves in the temperature dependence of the magnetic susceptibility and in signatures of dipolar interactions in the ESR lineshape. Neither has been observed to date[81]. Quantifying spin-spin interactions in highly doped systems will be essential to understanding the origin of such long range spin transport and ESR techniques may provide unique insights.

The young field of organic spintronics therefore offers unique spin-transport and relaxation physics but still poses several unanswered questions. Addressing them will require the combination of established methods for the structural, optical and electronic characterization of such materials with spin-sensitive techniques. Once we understand this physics, the knowledge of organic chemistry and optoelectronics materials design can be applied to the development of spintronics materials.

Appendix A

The density matrix

The density matrix operator of a quantum mechanical ensemble is defined as

$$\sigma = \sum_i p_i \left|\psi_i\right\rangle \left\langle\psi_i\right| \tag{A.1}$$

where p_i are the occupation probabilities of the states $|\psi_i\rangle$. Any such state can be developed in a set of orthogonal eigenstates $|n\rangle$ such that $|\psi_i\rangle = \sum_n c_n^i |n\rangle$. The matrix elements of σ can then be expressed in terms of the coefficients c_n by inserting this expansion into Eq. (A.1):

$$\sigma_{mm'} = \langle m| \sigma \left|m'\right\rangle = \sum_i p_i c_m^i (c_{m'}^i)^* = \overline{c_m {c_{m'}}^*} \tag{A.2}$$

where the overline denotes the ensemble average. It is clear that the diagonal elements $\overline{c_m c_m{}^*}$ denote the populations of eigenstates while the off-diagonal elements describe coherences between the latter.

The expectation value of any operator $\mathbf{Q}$ over an ensemble described by σ can then conveniently be expressed as

$$\langle \mathbf{Q} \rangle = \sum_i p_i \left\langle\psi_i\right| \mathbf{Q} \left|\psi_i\right\rangle = \sum_i \mathrm{Tr}(p_i \left|\psi_i\right\rangle \left\langle\psi_i\right| \mathbf{Q}) \tag{A.3}$$

$$= \mathrm{Tr} \sum_i p_i \left|\psi_i\right\rangle \left\langle\psi_i\right| \mathbf{Q}) = \mathrm{Tr}(\sigma \mathbf{Q}) \,. \tag{A.4}$$

The time evolution of the density matrix can be determined by taking the partial derivative of Eq. (A.1) with respect to time and substituting the derivatives of $|\psi_i\rangle$ and $\langle\psi_i|$ with the Schrödinger equation

$$i\hbar \frac{\partial}{\partial t} \left|\psi_i\right\rangle = \mathcal{H} \left|\psi_i\right\rangle \,. \tag{A.5}$$

This gives the von-Neumann equation, which describes the full dynamics of populations and coherences in the system:

$$\frac{\partial \sigma}{\partial t} = -\frac{i}{\hbar} [\mathcal{H}, \sigma] \,. \tag{A.6}$$

Equation (A.6) is the quantum mechanical equivalent to the Liouville equation in classical mechanics. If the Hamilton $\mathcal{H}$ is time independent, the solution is easily given by

$$\sigma(t) = e^{-i\mathcal{H}t/\hbar}\sigma(0)e^{i\mathcal{H}t/\hbar} \tag{A.7}$$

but either perturbative or numerical methods must be used in the general case.

Appendix B

An energy level picture of motional narrowing

We have seen in Section 4.5 that EY-like relaxation in organics can be intuitively described in terms of the admixture between up- and down-spin states and resulting finite transition rates between the latter. We will discuss in this Appendix that relaxation by hyperfine interactions can similarly be discussed in terms of spin-admixture and spin-dependent hopping rates. The onset of motional narrowing, i.e., the turnaround from decreasing to increasing spin lifetimes, can be universally understood as the point where the states between which relaxation takes place are broadened beyond their energy splitting, for instance by sufficiently fast charge hopping. This picture has been invoked by Boross et al. to visualize a unified description of D'yakonov-Perel' and EY relaxation in inorganic semiconductors[166].

We have seen in Section 3.4 that the hyperfine interaction Hamiltonian $\mathcal{H}_{\mathrm{HFI}}$ has off-diagonal matrix elements in the basis of $|m_S, m_I\rangle$ and therefore causes a mixing of spin-up and -down states of the electron spin. The nominally up state reads $|+\rangle = |\uparrow\rangle + \chi\,|\downarrow\rangle$ and $\chi = \Omega/\omega_{\mathrm{L}}$ is the spin admixture. Here, $\hbar\Omega$ is the HFI matrix element between up and down states and $\hbar\omega_{\mathrm{L}}$ is their energy separation.[1]

As a result, there is a small but finite hopping rate between up and down states at different sites. Faster charge hopping will then cause more rapid spin relaxation and the 'spin-flip' hopping rate can be shown to scale linearly with χ^2[76] such that

$$\frac{1}{T_1} \simeq \chi^2 k \sim \chi^2 \tau_{\mathrm{c}}^{-1} \ . \tag{B.1}$$

At the turnaround point of the spin-lattice relaxation time T_1, the condition $\omega_{\mathrm{L}} \leq \tau_{\mathrm{c}}^{-1}$ means that the Zeeman-split states are broadened beyond distinguishability by hopping and relaxation is caused by two quasi-degenerate states. T_1 starts to increase again.

[1] At high fields, the spin admixture from HFIs decreases since the off-diagonal elements of $\mathcal{H}_{\mathrm{HFI}}$ become small compared to the diagonal spin-Zeeman energy.

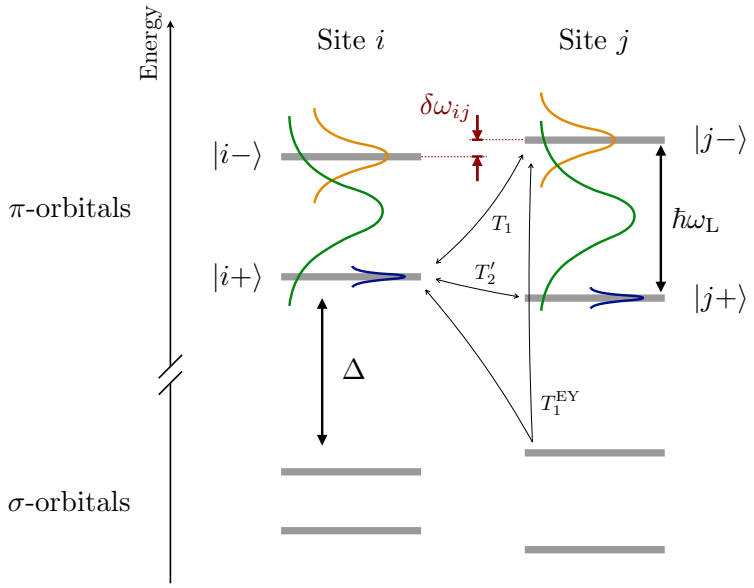

Figure B.1: Energy level diagram of spin relaxation. Motional T_1 relaxation takes place between spin-up and -down states $|i\pm\rangle$ and $|j\mp\rangle$ from neighboring sites and becomes 'motionally narrowed' when those are broadened beyond distinguishability with $\tau_{\mathrm{c}}^{-1} > \omega_{\mathrm{L}}$ (green curve). Motional decoherence T_2' does not involve spin flips and takes place between states of the same spin $|i\pm\rangle$ and $|j\pm\rangle$. Here, the onset of motional narrowing takes place earlier when $\tau_{\mathrm{c}}^{-1} > \delta\omega_{ij}$ (orange curve), which is the condition for the Redfield theory to apply. Finally, EY-like relaxation involves transitions between π- and σ-orbitals and therefore does not exhibit motional narrowing unless $\tau_{\mathrm{c}}^{-1} > \Delta/\hbar$, which is beyond the limit of incoherent hopping.

A similar argument holds for the coherence time T_2: decoherence in the slow motion limit is caused by the difference in resonance frequencies between sites $\delta\omega$. It is therefore a relaxation process between spin-up (or -down) states on neighboring sites. The onset of motional narrowing takes place at $\delta\omega \leq \tau_{\mathrm{c}}^{-1}$ when the broadening of those states exceeds their energy difference $\delta\omega$ and T_2 increases with faster hopping rates.

In principle, such a turnaround should take place for Elliott-Yafet type relaxation as well, when the lifetime broadening from hopping exceeds the energy separation Δ between the mixed σ- and π-orbitals, in analogy to similar predictions for inorganic conductors[166]. This would however require hopping rates in excess of what can be considered within an incoherent transport model.

Appendix C

Automation of ESR experiments

Performing the ESR measurements presented in this thesis would have been challenging without automation. This is particularly true for field-induced measurements where the charge carriers are only accumulated within 1–2 nm of the film. A sufficiently high signal-to-noise ratio often requires averaging for up to one hour for a single spectrum, and in most cases spectra at different microwave powers and gate voltages are required.

Such measurements only become feasible in the desired quality by automating the acquisition process. Over the course of my PhD, I have therefore developed the Python software suite 'CustomXepr' for Linux and macOSX which interfaces with all instruments involved in the measurements: the Bruker E500 spectrometer, through Bruker's Xepr Application Programming Interface (API), the Oxford Instruments MercuryiTC temperature controller, and the Keithley 2602b source measurement units (SMUs). This Appendix gives an introduction to CustomXepr's functionality; the full source code is published on GitHub.

Job-scheduling

The aim of CustomXepr is twofold: First and foremost, it enables the user to automate and schedule full measurement plans which may run for days without user input. Second, it complements the functionality of Bruker's Xepr control software. This includes for instance powerful logging capabilities for all key events, a more accurate determination of the cavity's Q-value from its frequency response (mode picture), more precise tuning of the cavity, the ability to re-tune during long-running measurements, logging of the cryostat temperature during measurements, and many more. On the other hand, low level functionality and communication with the spectrometer remains with Xepr.

CustomXepr's core consists of functions for preconfigured tasks, such as changing the cryostat temperature, recording a transfer curve, or performing a preconfigured ESR measurement. For instance, `setTemperature(110)` tells the MercuryiTC to change its temperature set-point to 110 K and waits until the latter is reached

and maintained with the desired stability (default: ±0.1 K for 120 sec). It also adjusts the helium flow if necessary and warns the user if the target temperature cannot be reached within the expected time. `runXeprExperiment(PowerSat)` will run the preconfigured ESR measurement 'PowerSat' while tuning the cavity between scans and monitoring the temperature stability during the measurement.

Such built-in jobs are not performed immediately but are queued and executed in the background after the successful completion of the previous jobs. Any data returned by a job, such as ESR spectra, FET transfer curves, or cavity mode pictures, will be kept in a result queue and saved to a specified file if requested. CustomXepr functions that are expected to run for longer than 1 sec can gracefully abort upon user request without leaving the setup in an inconsistent state.

In addition, the queuing system can be used to manually schedule any user-specified function, related or unrelated to the ESR setup and its ancillary equipment.

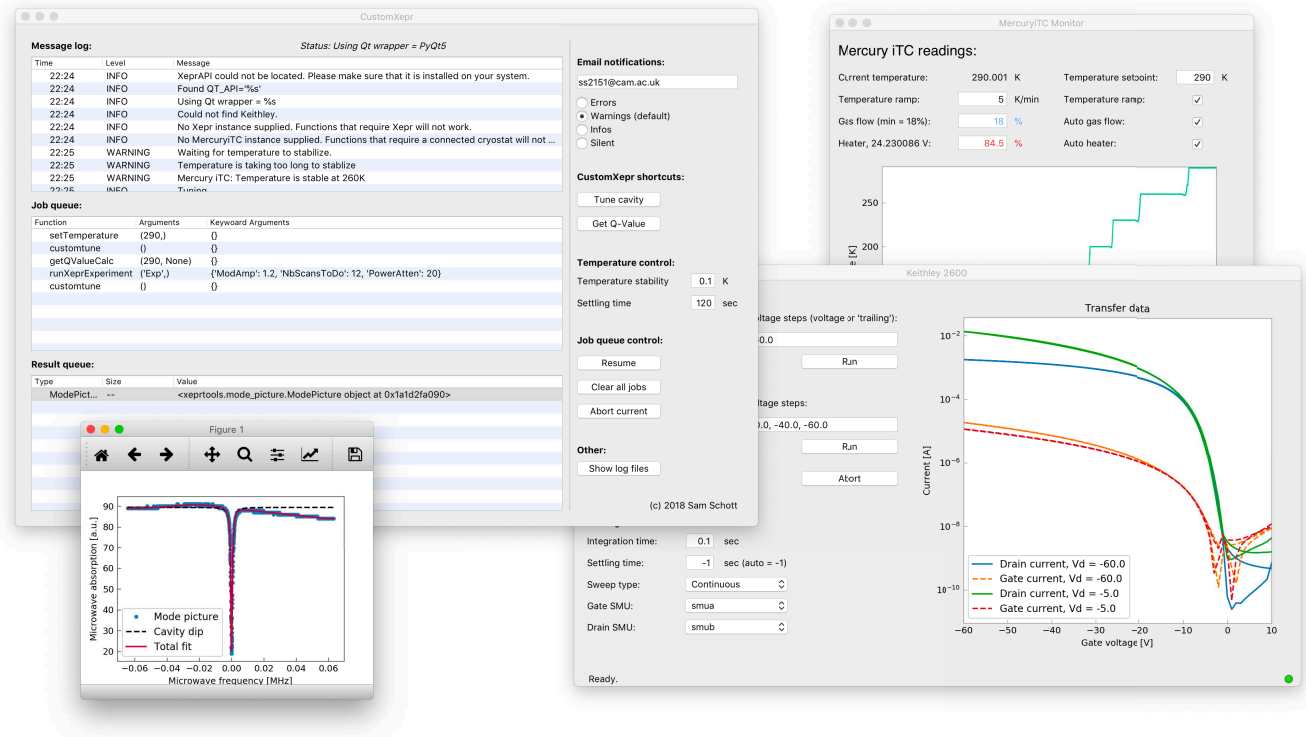

Figure C.1: Screenshot of the CustomXepr user interface on macOSX. The main panel in the top-left corner shows logs from previous jobs, pending experiments, and a list of results. It also allows the user to adjust basic settings such as the temperature settling time, etc.

Logging and error handling

All CustomXper functions release logging messages of the levels *status*, *info*, *warning*, and *error* during their execution. Status notifications will only be shown in the user interface and typically contain information about the progress of a job (number of completed scans in an ESR measurement, countdown until the temperature is stable, etc). Info notifications typically contain information about the beginning or completion of a job (e.g., 'Waiting for temperature to stabilize.', 'All scans complete.'), and potentially useful information about how the job was completed (e.g., 'Temperature stable at 120.01 ± 0.02 K during scans.').

Warning notifications are only logged when CustomXepr believes that there may be a problem which requires user intervention, for instance if a measurement is taking significantly longer than expected, or if the gas flow required to maintain a certain temperature is unusually high. Finally, error messages are only released if CustomXepr is unable to proceed with a job, in which case it will abort and pause all pending jobs. Such errors may include for instance loss of communication with an instrument or repeated strong temperature fluctuations during an ESR measurement.

By default, all messages of level *info* and higher are logged to a file in the user's home directory and messages of level *warning* and higher are sent as an email to the specified addresses. In addition, temperature readings are saved in regular intervals, allowing the user to retrospectively confirm the temperature stability during measurements.

Such detection and escalation of possible problems is key to enabling unattended measurements. Otherwise the user may come back after two days expecting a completed measurement cycle, only to see that the helium dewar was emptied a day ago or that the program got stuck asking the user if it should really override a data file.

Example usage and code

CustomXepr has a user interface (see Fig. C.1) which displays all jobs waiting in the queue, all results returned from previous jobs, and all logging messages. Common tasks such as pausing, aborting and clearing jobs, plotting and saving returned data, and setting temperature stability tolerances can be performed through the interface itself. However, apart from tuning the cavity and reading a Q factor, all jobs must be scheduled programmatically through the console. For example, a FI-ESR measurement script which cycles through different temperatures and records ESR spectra and transfer curves at each step reads as follows:

```
from customxepr import run
customXepr, xepr = run()
# get preconfigured experiment from Xepr
exp = xepr.XeprExperiment('Experiment')
# specify path to save data
path = '/path/to/folder/my_sample_'
# set-up modulation amplitudes in Gauss for different temperatures
mod = {5: 3, 50: 2, 100: 1, 150: 1, 200: 1, 250: 1.5, 300: 2}

for T in [5, 50, 100, 150, 200, 250, 300]:
    # ================================================================
    # Prepare temperature
    # ================================================================
    customXepr.setTemperature(T)        # set desired temperature
    customXepr.customtune()             # tune the cavity
    customXepr.getQValueCalc(path, T)   # measure the Q factor

    # ================================================================
    # Perform FET measurements
    # ================================================================
    # generate file name for transfer curve
    transferFile = path + str(T) + 'K_transfer.txt'
    # record default transfer curve and save to file
    customXepr.transferMeasurement(filePath=transferFile)

    # ================================================================
    # Perform ESR measurements at Vg = -70V and Vg = 0V
    # ================================================================
    for Vg in [0, -70]:
        customXepr.setGateVoltage(Vg)  # bias gate
        customXepr.runXeprExperiment(exp, ModAmp=mod[T])  # run exp
        customXepr.setGateVoltage(0)  # set gate voltage to zero

        # save ESR spectrum to file
        esrDataFile = path + str(T) + 'K_Vg_' + str(Vg)
        customXepr.saveCurrentData(esrDataFile)

customXepr.setStandby()  # ramp down field and turn off MWs
```

In this code, all functions belonging to CustomXepr will be added to the job queue and will be carried out successively such that, for instance, ESR measurements will not start while the temperature is still being ramped.

Mercury controls

CustomXepr includes a Python driver for the MercuryiTC temperature controller and starts a worker thread which regularly queries the MercuryiTC for its sensor readings and provides a live stream to other parts of the software. This prevents individual functions from querying the MercuryiTC directly and causing unnecessary overhead.

The user interface for the cryostat plots historic temperature readings going back up to 24 h and provides access to relevant temperature control settings such as gas flow, heater power, and ramping speed while lower-level configurations such as calibration tables must be changed programatically.

Keithley controls

As with the cryostat, CustomXepr includes a Python driver for Keithley 2600 series instruments and a high-level user interface which allows the user to configure, record and save voltage sweeps such as transfer and output measurements. Since there typically is no need to provide a live stream of readings from the Keithley, the data from an IV-curve is buffered locally on the instrument and only transferred to CustomXepr after completion of a measurement.

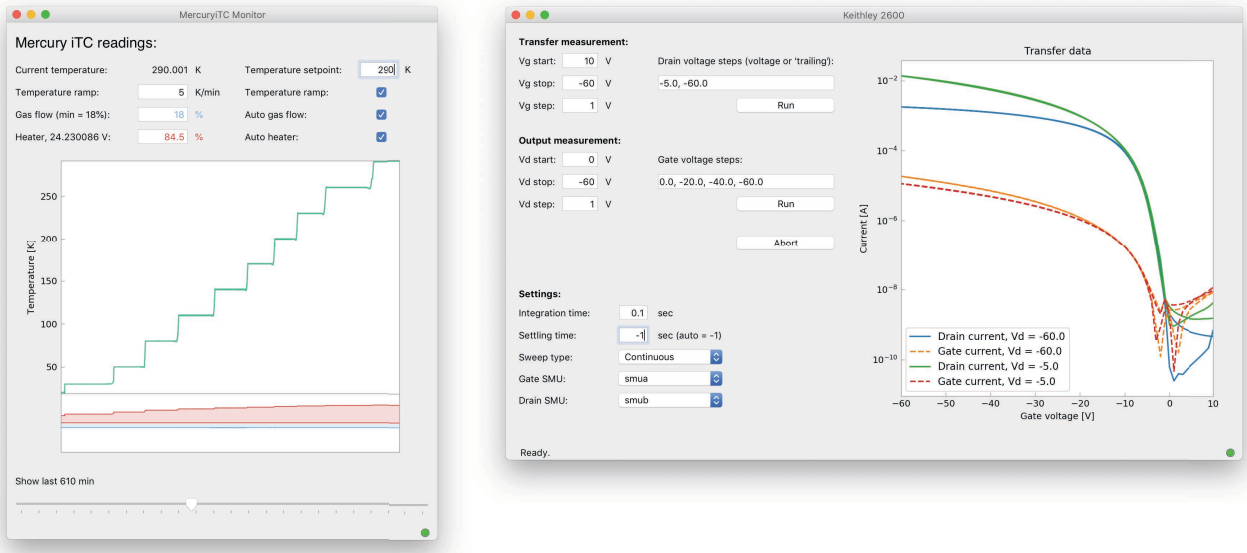

Figure C.2: Screenshots of the MercuryiTC and Keithley 2600 user interfaces.

Appendix D

DFT calculations of g-shifts

This appendix provides additional detail on the theoretical calculations performed. As stated in the main text, the theoretical work is intended to support the key message that g-shifts in the studied class of molecules may be understood in terms of the effective spin-orbit coupling, or equivalently, the degree of overlap between the orbital and spin angular momentum distributions.

We argue that, given simple geometries and/or weak spin-orbit coupling (SOC), we may predict the dominant $\Delta g^{OZ/SOC}$ term of the g-tensor shifts from a linear model of atomically localized SOC interactions. The latter amounts to a linear fit of atomically localized spin populations to the $\Delta g^{OZ/SOC}$ terms, on the form of Eq. (6.3). In other words, if a linear model with the distribution of atomic spin population as the only independent variable is predictive, we consider our hypothesis confirmed. We validate the model by studying the correlation between the fitted $\Delta g^{OZ/SOC}$ values, and those calculated from first-principles.

The theoretical methodology follows three steps: i) DFT calculations of molecular geometries, cation spin densities, and g-tensors; ii) calculations of atomic spin populations using an atom-in-molecule (AIM) decomposition method; and iii) a multivariate linear regression of the calculated dominant $\Delta g^{OZ/SOC}$ g-shift term versus atomic spin populations.

DFT Calculations

We use DFT to predict g-tensor shifts from first-principles theory. These shifts depend on SOC, which ranges from weak and nearly insignificant in the pure hydrocarbons studied, to significant in the Se-substituted molecules. We therefore require an accurate and transferable level of theory able to describe a wide range of SOC strengths on a consistent footing.

Consequently, we opted for an all-electron DFT method, with nuclear relativistic effects described by the zeroth-order regular approximation (ZORA[116]) using the standard point-charge approximation for the atomic nuclei. g-tensors were

calculated using the method[67] developed by Neese et al. and related techniques[117] as implemented in the ORCA software package[115], version 3.0.3.

Tests showed hybrid exchange-correlation functionals in general, and the PBE0[167] parametrization in particular, to perform very well for the prediction of the experimentally measured g-tensor shifts, in agreement with previous findings[67]. Exhaustive tests of the SARC basis set family[168] revealed that no qualitative features improved past the triple-zeta level (a.k.a. the 'ma-zora-def2-tzvp' basis set). The benchmark level quadruple-zeta 'ma-zora-def2-qzvp' basis set gives slightly larger (on the order of hundreds of ppm) g-shifts. Therefore, while the 'ma-zora-def2-tzvp' basis set, with linear dependencies eliminated by removing the diffuse (a.k.a. 'minimal augmentation') functions on the carbon atoms represents the optimal balance between accuracy of predictions and computational cost, the accuracy of predicted g-shifts is partially due to error cancellation between the basis set and other, over-estimating factors.

All molecules were fully geometry-optimized in a charge-neutral state and the above-described level of theory including all-electron spin-orbit coupling using the NWChem quantum chemistry software package[114], version 6.5. Compared to a non-relativistic, spin-orbit free level of theory, the influence of the ZORA on the geometry is significant, but SOC effects are negligible. Geometry differences between molecules optimized in a neutral and charged state were small, allowing for greater comparability by obtaining all geometries in the neutral state. The neglect of these geometry effects implies that our model describes a charge state short-lived on the timescale of structural relaxation because of the charge.

While experimental measurements were performed on molecules of varying alkyl chain lengths, e.g. 'C10-X', 'C12-X' etc., all molecules in the theoretical calculations were given 8-membered alkyl chains. Tests showed the alkyl chain influence to be well-converged at this length, meaning that the theoretical results presented here are comparable to experimental measurements at chains equal to or longer than 8 methylene units.timescale For each optimized geometry, a single-point calculation with a total charge of +1 and multiplicity 2 was performed, with a subsequent calculation of the g-tensor and dumping of the DFT spin density onto a dense regular grid. The resulting calculated g-tensor shifts are shown in Table 6.2 in ppm. Evidently, the total g-tensor shift Δg is strongly dominated by the orbital Zeeman / SOC-dependent term $\Delta g^{OZ/SOC}$ in the studied class of molecules. That is, as mentioned in the main text, the gauge correction and relativistic mass correction terms add up to a very small, mostly positive term (67 ppm on average in Table 6.2).

In the main text we show that g-tensor shifts in the studied class of molecules can be understood in terms of a linear relationship between the dominant $\Delta g^{OZ/SOC}$ term, and the spin density distribution among the nuclei in the molecule. More specifically, $\Delta g^{OZ/SOC}$ is approximated as a sum over fitted proportionality constants representing the effective orbital angular momentum coupling for a given element, multiplied with sums of atomic spin populations at that element.

This requires calculating atomic spin populations from the molecular spin density; in other words, finding an appropriate solution to the atoms-in-molecules (AIM) problem. The AIM problem is commonly solved using methods partitioning either a) wave-functions based on projections of basis functions, or b) charge- or spin-densities based on their spatial distribution.

The first option, exemplified by the Mulliken and Löwdin[169] population analysis methods, is conceptually simpler and readily implemented, but suffers from significant basis set effects[119,170]. Tests using the arguably more rigorous Löwdin method confirmed significant variations in calculated atomic spin populations with basis set type and size. The basis set dependence also manifested in a sensitive dependence on relative nuclear coordinates, appearing as an unexplained scatter in correlation plots of data fitted according to the procedure below.

The second option, exemplified by the Bader method[171], does not depend on the basis-set used in the calculation of the molecular spin density. However, for the current set of molecules, the Bader method did not prove significantly more stable with respect to small variations in molecular structure than the above-mentioned Löwdin method, nor did using the alternative weighting method proposed by Yu and Trinkle[172] alleviate the problem. The Voronoi Deformation Density (VDD) method[119] proved significantly more stable and consistent, however, and is the method used in all fits of $\Delta g^{OZ/SOC}$ presented in this manuscript. All density-based partitioning methods were applied using the 'bader' program developed by Henkelman et al.[120], version 0.95a.

DOSY–NMR of BSBS

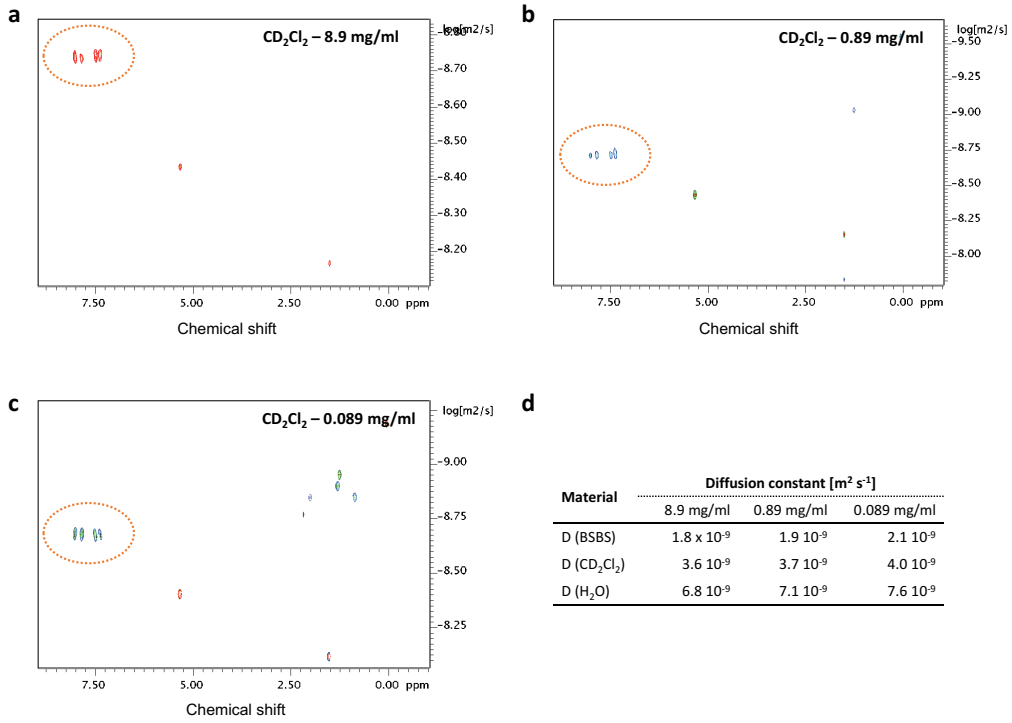

d

Material	Diffusion constant [$m^2\ s^{-1}$]		
	8.9 mg/ml	0.89 mg/ml	0.089 mg/ml
D (BSBS)	1.8×10^{-9}	$1.9\ 10^{-9}$	$2.1\ 10^{-9}$
D (CD_2Cl_2)	$3.6\ 10^{-9}$	$3.7\ 10^{-9}$	$4.0\ 10^{-9}$
D (H_2O)	$6.8\ 10^{-9}$	$7.1\ 10^{-9}$	$7.6\ 10^{-9}$

Figure E.1: (**a** – **c**) DOSY NMR spectra for solutions of BSBS of different concentrations in deuterated dichloromethane (DCM). (**d**) Diffusion constants of all species in solution for different concentrations of BSBS.

Appendix F

DFT calculation of spin admixtures

Calculations for the dimensionless spin admixture parameter γ^2 have been carried out in collaboration with Jairo Sinova, Erik McNellis, and Uday Chopra at the Johannes Gutenberg University Mainz. They are based on the approach suggested by Yu in ref.[77] but with two main improvements. While γ^2 was originally derived within the restricted open-shell Hartree-Fock (ROHF) approximation to the density functional theory (DFT) wave-function, we generalize its formulation to the unrestricted HF (UHF) approximation. This significant reduction in variational constraints on the wave-function used to obtain γ^2 correspondingly raises its predictive quality.

We further improve the quality of γ^2 by calculating SOC matrix elements from first-principles, within the Zeroth Order Regular Approximation (ZORA)[173] as implemented in the NWChem computational chemistry package[114]. The original formulation of γ^2 uses SOC constants (SOC matrix element prefactors) from experimental literature, i.e., observable 'orbitals'. Since this set of elements is only complete for the same number of orbitals in the theoretical treatment, the DFT calculations are restricted to very poor, minimal basis sets. Using SOC matrix elements from first-principles theory allows us to use basis sets of any quality. The single-zeta, polarized SARC basis set (ma-zora-def2-svp), which has been recontracted for ZORA, was found sufficient for the properties studied here. In order to remove linear dependencies, carbon diffuse (minimal augmentation) functions were removed from the basis set, which was otherwise unmodified.

Finally, we choose a hybrid exchange-correlation functional specifically designed to improve the description of magnetic properties, PBE0[167]. Our estimates of γ^2 are presented in Chapter 7.

Appendix G

Dynamical disorder in IDTBT

Dihedral frequencies

Using the DFT method (B3LYP functional and 6-311+g(d,p) basis set), we optimized an IDTBT monomer in vacuum (see Fig. G.1, side-chains reduced to methyls), and calculated vibrational frequencies in its respective geometry.

Since IDTBT is a hole-conducting polymer, we investigate two cases: a neutral state (total charge $q = 0$) and a cationic state ($q = +1$). In a neutral state, the lowest frequency is $\omega_1^{(0)} = 1.9 \times 10^{11}$ Hz and corresponds to oscillations around the dihedral angle ϕ, shown in Fig. 1. The following two modes are $\omega_2^{(0)} = 6.4 \times 10^{11}$ Hz and $\omega_3^{(0)} = 1.4 \times 10^{12}$ Hz, and correspond to the out-of-plane oscillations. Similarly, in a cation state, the frequency of the dihedral mode ϕ is twice the one in a ground state, $\omega_1^{(0)} = 3.5 \times 10^{11}$ Hz, which is consistent with higher planarity of the backbone due to charging. The following two out-of-plane modes have frequencies $\omega_2^{(0)} = 6.1 \times 10^{11}$ Hz and $\omega_3^{(0)} = 1.3 \times 10^{12}$ Hz. In both states, the calculated dihedral frequencies are within the anticipated range.

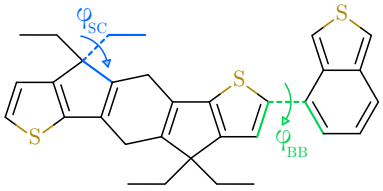

Figure G.1: Structure of the IDTBT force field and re-parameterized dihedrals: ϕ_{BB} connects IDT and BTZ units in a backbone, while ϕ_{SC} connects side-chains to a backbone via a bridging carbon. Respective PES scans are shown in Fig. G.2.

Force field

In order to simulate morphologies of the polymer, we developed an atomistic force field. The chemical structure of an IDTBT monomer used to parametrize the force field is shown in Fig. G.1. A monomer with side-chains reduced to ethyls is optimized using the B3LYP/6- 311g(d,p) as a functional and a basis set. Partial charges are obtained using the Merz-Kollman method[174,175].

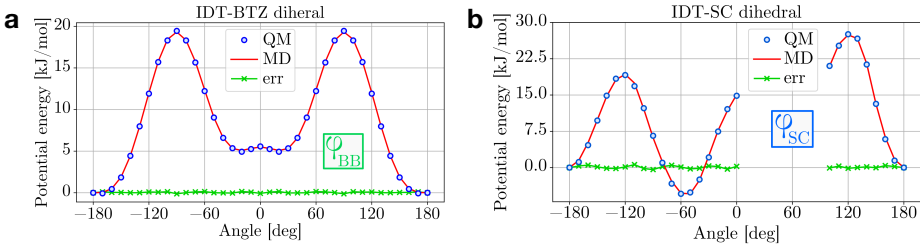

Figure G.2: Re-parametrization of the potential energies for the backbone dihedral angle ϕ_{BB} (**a**) and the dihedral angle ϕ_{SC} (**b**), as defined in Fig. G.1. Blue markers indicate the QM values, the red curve is from MD with an optimized force field, the green curve denotes the difference between the two.

All Lennard-Jones parameters for non-bonded interactions are taken from the OPLS-AA force field[176–179], while differentiating between conjugated fragments and hydrocarbons.

Values for bonds and angles are taken from the DFT-optimized geometry, while most spring and dihedral constants are taken from the OPLS-AA[176–179] force field. Two dihedrals, ϕ_{BB} and ϕ_{SC} (Fig. G.1), were re-parametrized by matching first-principle and molecular dynamics (MD) force field potential energy surfaces (PES). If q is the degree of freedom of interest, constrained geometry optimizations must be performed using both first-principles and the force-field levels, yielding the total energies $U_{\mathrm{DFT}}(q)$ and $U_{\mathrm{FF}}^{\mathrm{initial}}(q)$, respectively. The missing force-field (FF) terms are then fitted to this difference using a prescribed functional form. Finally, the constrained geometry optimizations are repeated on the force-field level including the obtained potential and $U_{\mathrm{FF}}^{\mathrm{final}}(q)$ is compared to the first-principles scan.

For a potential corresponding to the dihedral angle ϕ_{BB} we used the Ryckaert-Belleman form

$$V_{\mathrm{RB}}(\phi_{ijkl}) = \sum_{n=0}^{5} C_n \cos^n(\phi_{ijkl})\,, \tag{G.1}$$

while for a potential corresponding to the dihedral angle ϕ_{SC} we used a truncated Fourier series

$$V_a(\phi_{ijkl}) = \sum_{n=0}^{N} C_n \cos\left(n\phi_{ijkl} - \phi_{ijkl}^{(n)}\right) \tag{G.2}$$

to account for a more complex, asymmetric PES shape, arising from a presence of bridging carbons. An upper cut-off at $N = 6$ was sufficient to reproduce the quantum mechanical (QM) curve. The fits are shown in Fig. G.2.

Details of MD simulations

We used the velocity rescaling thermostat[180], the Berendsen barostat[181], while electrostatics and van der Waals interactions were treated with a cut-off at $r_c = 1.2\,\mathrm{nm}$.

Quantum corrections

Quantum corrections are taken into account by introducing an effective temperature. This is achieved by replacing the classical Boltzmann distribution with a suitable quantum equivalent.

In order to introduce quantum corrections, a vibronic density of states (DOS) is required. To make calculations feasible, we calculated a vibronic DOS for an IDTBT tetramer in vacuum, with side-chains reduced to CH_3 groups. For the same reason, we used a PM3 semi-empirical method to optimize the geometry and to calculate frequencies in this geometry[182]. A vibronic DOS is typically normalized as

$$\int_0^\infty g(\omega)\mathrm{d}\omega = 3N - 6\,, \tag{G.3}$$

where $3N$ is the number of DOFs, $g(\omega)$ is a simulated vibronic density of states. The resulting spectrum is shown in Fig. G.3 and is comparable to measured IR and Raman spectra of similar conjugated polymers[183,184].

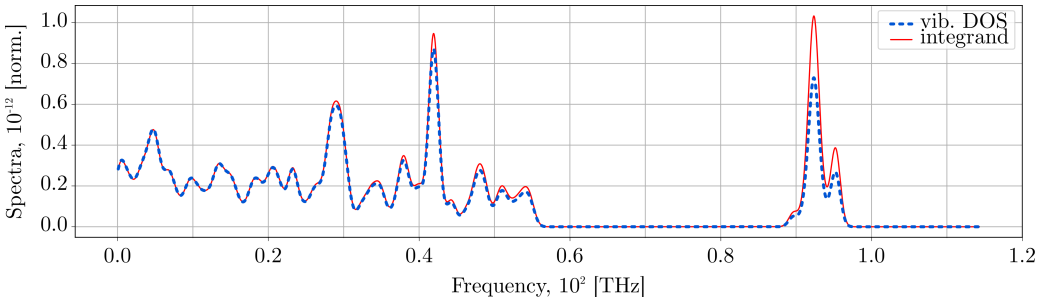

Figure G.3: Simulated vibronic DOS $g(\omega)$ of an IDTBT tetramer and the integrand $g(\omega)W(\omega, T_{\mathrm{QM}})$ used in Eq. (G.4), multiplied by a factor 0.026 for comparison.

Quantum corrections are introduced by re-weighting the system's vibrational DOS. Namely, the following equation holds[185]

$$\int_0^\infty g(\omega)W(\omega, T_{\mathrm{QM}})\hbar\omega\mathrm{d}\omega = 3Nk_{\mathrm{B}}T_{\mathrm{MD}}\,, \tag{G.4}$$

where $W(\omega, T_{\mathrm{QM}})$ is a sum of a Bose-Einstein distribution and a zero-point energy

$$W(\omega, T_{\mathrm{QM}}) = \frac{1}{\exp\left(\frac{\hbar\omega}{k_{\mathrm{B}}T_{\mathrm{QM}}}\right) - 1} + \frac{1}{2}\,, \tag{G.5}$$

as opposed to the Boltzmann distribution. T_{MD} and T_{QM} denote the temperatures from molecular dynamics and the effective "quantum" temperature of the system, respectively. Provided the calculated vibronic DOS above, one can invert Eq. (G.4) and obtain T_{QM}.

Figure G.4 shows the calculated MD-to-QM temperature mapping, and that effective temperatures are notably smaller than the ones used in MD. Within the simulated range, $T_{\mathrm{MD}} = 200\,\mathrm{K}$ corresponds to $T_{\mathrm{QM}} = 150\,\mathrm{K}$, i.e., the reduction factor is close to 3/4. We then fitted the blue curve with a polynomial function, and applied it to the simulated dynamic order parameter curves. This effectively shifted the curves (and the transition temperature) to lower temperatures. The final result is reported in the main text Fig. 7.6a, where T refers to the effective, "quantum" temperature.

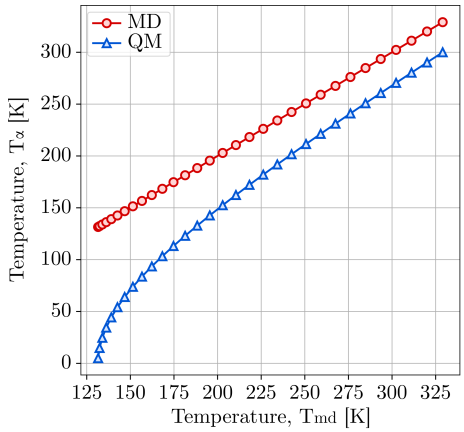

Figure G.4: Relation between MD (classical) and QM (real) temperatures.

Software and analysis tools

Molecular dynamics simulations were performed using the GROMACS simulation package[186], while first-principles calculations were performed in the Gaussian G09 simulations package. Dynamic order parameters S are calculated using in-house python scripts, based on *numpy* and *scipy* python libraries. Figures are produced using *matplotlib* python library and *inskcape* graphics package. Snapshot figures are produced using the VMD program[187].

Appendix H

GIWAXS measurements

Grazing Incidence Wide-Angle X-ray Scattering (GIWAXS) measurements were performed at the SAXS/WAXS beamline at the Australian Synchrotron[188]. 15 keV photons were used with 2-dimensional scattering patterns recorded on a Dectris Pilatus 1M detector. Images shown in Section 7.4 were acquired at an incident angle close to the critical angle. Such images were chosen from a series of images taken with incident X-ray angles varying from 0.02° to 0.15° in steps of 0.01° with the chosen image showing the highest scattering intensity. The X-ray exposure time was 1 sec such that no film damage was identified. The sample-to-detector distance was calibrated using a silver behenate sample. The results were analyzed by an altered version of the NIKA 2D software[189] based on IgorPro.

Crystallite orientation distribution profiles (COD) were extracted from a circular line cut across the (100) diffraction. The angular populations of backbone tilt angles were calculated by normalizing the measured diffraction intensity by the integrated total intensity within the pole angle range of interest, assuming that crystallites from the same crystallographic direction at different pole angles are formed with similar crystallite thickness and lattice disorder.

Bibliography

[1] D. Di et al., "High-performance light-emitting diodes based on carbene-metal-amides", Science **356**, 159–163 (2017) (cit. on p. 1).

[2] M. Tabachnyk, B. Ehrler, S. Gélinas, M. L. Böhm, B. J. Walker, K. P. Musselman, N. C. Greenham, R. H. Friend, and A. Rao, "Resonant energy transfer of triplet excitons from pentacene to PbSe nanocrystals", Nature Materials **13**, 1033–1038 (2014) (cit. on p. 1).

[3] A. Rao and R. H. Friend, "Harnessing singlet exciton fission to break the Shockley–Queisser limit", Nature Reviews Materials **2**, 17063–12 (2017) (cit. on p. 1).

[4] H. Sirringhaus, "25th anniversary article: organic field-effect transistors: the path beyond amorphous silicon", Advanced Materials **26**, 1319–1335 (2014) (cit. on pp. 1, 6, 64).

[5] K. Ando, S. Watanabe, S. Mooser, E. Saitoh, and H. Sirringhaus, "Solution-processed organic spin–charge converter", Nature Materials **12**, 622–627 (2013) (cit. on pp. 1, 72, 96).

[6] D. Sun, K. J. van Schooten, M. Kavand, H. Malissa, C. Zhang, M. Groesbeck, C. Boehme, and Z. Valy Vardeny, "Inverse spin Hall effect from pulsed spin current in organic semiconductors with tunable spin–orbit coupling", Nature Materials **15**, 863–869 (2016) (cit. on pp. 1, 72, 96).

[7] S.-J. Wang et al., "Long-range and fast exchange-enhanced lateral spin transport in doped conjugated polymers", Nature Electronics **submitted** (2018) (cit. on pp. 1, 96, 97, 122).

[8] G. Szulczewski, S. Sanvito, and M. Coey, "A spin of their own", Nature Materials **8**, 693–695 (2009) (cit. on pp. 1, 72, 73).

[9] M. D'yakonov and V. Perel, "Possibility of orienting electron spins with current", Soviet Journal of Experimental and Theoretical Physics Letters **13**, 467 (1971) (cit. on p. 1).

[10] Y. K. Kato, R. C. Myers, A. C. Gossard, and D. D. Awschalom, "Observation of the Spin Hall Effect in Semiconductors", Science **306**, 1910–1913 (2004) (cit. on p. 1).

[11] J. Wunderlich, B. Kaestner, J. Sinova, and T. Jungwirth, "Experimental Observation of the Spin-Hall Effect in a Two-Dimensional Spin-Orbit Coupled Semiconductor System", Phys. Rev. Lett. **94**, 047204 (2005) (cit. on p. 1).

[12] S. O. Valenzuela and M. Tinkham, "Direct electronic measurement of the spin Hall effect", Nature **442**, 176–179 (2006) (cit. on p. 1).

[13] V. Podzorov, E. Menard, J. A. Rogers, and M. E. Gershenson, "Hall effect in the accumulation layers on the surface of organic semiconductors", Physical Review Letters **95**, 226601 (2005) (cit. on pp. 2, 73).

[14] S. R. E. Peierls and R. E. Peierls, *Quantum theory of solids* (Oxford University Press, 1955) (cit. on p. 4).

[15] J. Rybicki and M. Wohlgenannt, "Spin-orbit coupling in singly charged π-conjugated polymers", Phyical Review B **79**, 153202 (2009) (cit. on pp. 4, 31).

[16] Z. G. Yu, "Spin-orbit coupling and its effects in organic solids", Physical Review B **85**, 115201 (2012) (cit. on pp. 4, 33, 34, 50, 96, 106).

[17] Z. Bao and J. Locklin, *Organic field-effect transistors* (CRC Press, May 2007) (cit. on pp. 4, 64).

[18] J.-L. Brédas, D. Beljonne, V. Coropceanu, and J. Cornil, "Charge-transfer and energy-transfer processes in π-conjugated oligomers and polymers: a molecular picture", Chemical reviews **104**, 4971–5004 (2004) (cit. on p. 5).

[19] P. J. Brown, H. Sirringhaus, M. Harrison, M. Shkunov, and R. H. Friend, "Optical spectroscopy of field-induced charge in self-organized high mobility poly(3-hexylthiophene)", Phyical Review B **63**, 125204 (2001) (cit. on p. 5).

[20] H. Sirringhaus, "Device physics of solution-processed organic field-effect transistors", Advanced Materials **17**, 2411–2425 (2005) (cit. on pp. 6, 66).

[21] T. Holstein, "Studies of polaron motion: Part I. The molecular-crystal model", Annals of Physics **8**, 325–342 (1959) (cit. on pp. 6, 7).

[22] S. Fratini, D. Mayou, and S. Ciuchi, "The transient localization scenario for charge transport in crystalline organic materials", Advanced Functional Materials **26**, 2292–2315 (2016) (cit. on pp. 6, 13, 119).

[23] I. G. Lang and Y. A. Firsov, "Kinetic theory of semiconductors with low mobility", Sov. Phys. JETP **16**, 1301 (1963) (cit. on p. 7).

[24] A. Troisi, "Quantum dynamic localization in the Holstein Hamiltonian at finite temperatures", Phyical Review B **82**, 1301–9 (2010) (cit. on p. 7).

[25] C. K. Lee, J. Moix, and J. Cao, "Coherent quantum transport in disordered systems: A unified polaron treatment of hopping and band-like transport", The Journal of Chemical Physics **142**, 164103–8 (2015) (cit. on pp. 7, 9, 11, 106).

[26] H.-T. Chang, P.-P. Zhang, and Y.-C. Cheng, "Criteria for the accuracy of small polaron quantum master equation in simulating excitation energy transfer dynamics", The Journal of Chemical Physics **139**, 224112–12 (2013) (cit. on p. 7).

[27] T. Liu and A. Troisi, "Understanding the microscopic origin of the very high charge mobility in pbttt: tolerance of thermal disorder", Advanced Functional Materials **24**, 925–933 (2013) (cit. on pp. 8, 119).

[28] R. P. Fornari and A. Troisi, "Theory of charge hopping along a disordered polymer chain", Physical Chemistry Chemical Physics **16**, 9997–10007 (2014) (cit. on pp. 8, 104, 105, 107).

[29] R. A. Marcus, "Electron transfer reactions in chemistry. Theory and experiment", Reviews of Modern Physics **65**, 599–610 (1993) (cit. on p. 9).

[30] A. Troisi, A. Nitzan, and M. a Ratner, "A rate constant expression for charge transfer through fluctuating bridges", The Journal of Chemical Physics **119**, 5782–5788 (2003) (cit. on pp. 9, 11).

[31] H. Grabert and U. Weiss, "Quantum tunneling rates for asymmetric double-well systems with Ohmic dissipation", Physical Review Letters **54**, 1605–1608 (1985) (cit. on p. 9).

[32] K. Asadi, A. J. Kronemeijer, T. Cramer, L. Jan Anton Koster, P. W. M. Blom, and D. M. de Leeuw, "Polaron hopping mediated by nuclear tunnelling in semiconducting polymers at high carrier density", Nature Communications **4**, 1710 (2013) (cit. on pp. 10, 106).

[33] J. D. Yuen, R. Menon, N. E. Coates, E. B. Namdas, S. Cho, S. T. Hannahs, D. Moses, and A. J. Heeger, "Nonlinear transport in semiconducting polymers at high carrier densities", Nature Materials **8**, 572–575 (2009) (cit. on p. 10).

[34] A. S. Rodin and M. M. Fogler, "Apparent power-law behavior of conductance in disordered quasi-one-dimensional systems", Physical Review Letters **105**, 106801 (2010) (cit. on p. 10).

[35] D. Beljonne, J. Cornil, H. Sirringhaus, P. J. Brown, M. Shkunov, R. H. Friend, and J.-L. Brédas, "Optical signature of delocalized polarons in conjugated polymers", Advanced Functional Materials **11**, 229–234 (2001) (cit. on pp. 10, 119).

[36] D. Venkateshvaran et al., "Approaching disorder-free transport in high-mobility conjugated polymers", Nature **515**, 384–388 (2014) (cit. on pp. 11, 97, 99, 105, 107, 115).

[37] R. P. Fornari, P. W. M. Blom, and A. Troisi, "How many parameters actually affect the mobility of conjugated polymers?", Physical Review Letters **118**, 086601 (2017) (cit. on p. 11).

[38] N. Tessler, Y. Preezant, N. Rappaport, and Y. Roichman, "Charge transport in disordered organic materials and its relevance to thin-film devices: a tutorial review", Advanced Materials **21**, 2741–2761 (2009) (cit. on p. 12).

[39] M. C. J. M. Vissenberg and M. Matters, "Theory of the field-effect mobility in amorphous organic transistors", Phyical Review B **57**, 12964–12967 (1998) (cit. on pp. 12, 105).

[40] J. J. Brondijk, W. S. C. Roelofs, S. G. J. Mathijssen, A. Shehu, T. Cramer, F. Biscarini, P. W. M. Blom, and D. M. de Leeuw, "Two-dimensional charge transport in disordered organic semiconductors", Physical Review Letters **109**, 056601 (2012) (cit. on p. 12).

[41] A. J. Kronemeijer, V. Pecunia, D. Venkateshvaran, M. Nikolka, A. Sadhanala, J. Moriarty, M. Szumilo, and H. Sirringhaus, "Two-dimensional carrier distribution in top-gate polymer field-effect transistors: correlation between width of density of localized states and Urbach energy.", Advanced Materials **26**, 728–733 (2014) (cit. on pp. 12, 101).

[42] R. Noriega, J. Rivnay, K. Vandewal, F. P. V. Koch, N. Stingelin, P. Smith, M. F. Toney, and A. Salleo, "A general relationship between disorder, aggregation and charge transport in conjugated polymers", Nature Materials **12**, 1038–1044 (2013) (cit. on p. 12).

[43] A. Troisi and G. Orlandi, "Charge-transport regime of crystalline organic semiconductors: diffusion limited by thermal off-diagonal electronic disorder", Physical Review Letters **96**, 086601 (2006) (cit. on p. 13).

[44] J. F. Chang et al., "Hall-effect measurements probing the degree of charge-carrier delocalization in solution-processed crystalline molecular semiconductors", Physical Review Letters **107**, 066601 (2011) (cit. on pp. 13, 37).

[45] T. Sakanoue and H. Sirringhaus, "Band-like temperature dependence of mobility in a solution-processed organic semiconductor", Nature Materials **9**, 736–740 (2010) (cit. on pp. 13, 74).

[46] S. Fratini, S. Ciuchi, and D. Mayou, "Phenomenological model for charge dynamics and optical response of disordered systems: Application to organic semiconductors", Physical Review B - Condensed Matter and Materials Physics **89**, 235201 (2014) (cit. on p. 13).

[47] S. Illig et al., "Reducing dynamic disorder in small-molecule organic semiconductors by suppressing large-amplitude thermal motions", Nature Communications **7**, 10736 (2016) (cit. on pp. 13, 108).

[48] C. P. Slichter, *Principles of magnetic resonance* (Springer Science & Business Media, June 2013) (cit. on pp. 15, 22, 25, 42, 44, 90, 91, 93, 102).

[49] P. A. M. Dirac, *The principles of quantum mechanics* (Oxford University Press, Jan. 1981) (cit. on p. 15).

[50] P. Manninen, *Breit-Pauli Hamiltonian and molecular magnetic resonance properties* (OULU UNIVERSITY PRESS, OULU, 2004) (cit. on pp. 16, 29).

[51] L. L. Foldy and S. A. Wouthuysen, "On the Dirac theory of spin 1/2 particles and its non-relativistic limit", Physical Review B **78**, 29–36 (1950) (cit. on p. 16).

[52] C. Kittel, *Introduction to solid state physics* (John Wiley & Sons, Nov. 2004) (cit. on pp. 17, 26, 27).

[53] S. J. Brodsky, V. A. Franke, J. R. Hiller, G. McCartor, S. A. Paston, and E. V. Prokhvatilov, "A nonperturbative calculation of the electron's magnetic moment", Nuclear Physics B **703**, 333–362 (2004) (cit. on p. 17).

[54] B. Odom, D. Hanneke, B. D'Urso, and G. Gabrielse, "New measurement of the electron magnetic moment using a one-electron quantum cyclotron", Physical Review Letters **97**, 030801 (2006) (cit. on p. 17).

[55] Z. G. Yu, "Spin Hall effect in disordered organic solids", Physical Review Letters **115**, 026601 (2015) (cit. on pp. 18, 73).

[56] A. Abragam, *The principles of nuclear magnetism* (Oxford University Press, 1961) (cit. on pp. 19, 25, 42–45, 93, 101, 102).

[57] G. E. Pake, *Paramagnetic resonance: an introductory monograph*, Vol. 9, Frontiers in Physics (W.A. Benjamin, 1962), 205 pp. (cit. on p. 22).

[58] M. Statz, D. Venkateshvaran, X. Jiao, S. Schott, C. R. McNeill, D. Emin, H. Sirringhaus, and R. Di Pietro, "On the manifestation of electron-electron interactions in the thermoelectric response of semicrystalline conjugated polymers with low energetic disorder", Communications Physics **1**, 1319 (2018) (cit. on pp. 28, 115, 118, 119).

[59] J. A. Weil and J. R. Bolton, *Electron paramagnetic resonance* (John Wiley & Sons, Inc., Hoboken, NJ, USA, 2007) (cit. on pp. 29–31).

[60] F. Neese, "Metal and ligand hyperfine couplings in transition metal complexes: The effect of spin–orbit coupling as studied by coupled perturbed Kohn–Sham theory", The Journal of Chemical Physics **118**, 3939–3948 (2003) (cit. on p. 29).

[61] H. M. McConnell, "Indirect hyperfine interactions in the paramagnetic resonance spectra of aromatic free radicals", The Journal of Chemical Physics **24**, 764 (1956) (cit. on pp. 29, 30).

[62] J. A. Pople, D. L. Beveridge, and P. A. Dobosh, "Molecular orbital theory of the electronic structure of organic compounds. II. Spin densities in paramagnetic species", Journal of the American Chemical Society **90**, 4201–4209 (1968) (cit. on p. 30).

[63] I. C. Lewis and L. S. Singer, "Electron Spin Resonance of Radical Cations Produced by the Oxidation of Aromatic Hydrocarbons with SbCl5", The Journal of Chemical Physics **43**, 2712–2727 (1965) (cit. on p. 30).

[64] G. Breit and I. I. Rabi, "Measurement of nuclear spin", Physical Review B **38**, 2082–2083 (1931) (cit. on p. 30).

[65] A. S. Mishchenko, H. Matsui, and T. Hasegawa, "Distribution of localized states from fine analysis of electron spin resonance spectra of organic semiconductors: Physical meaning and methodology", Phyical Review B **85**, 085211 (2012) (cit. on pp. 30, 102).

[66] T. D. Nguyen, G. Hukic-Markosian, F. Wang, L. Wojcik, X.-G. Li, E. Ehrenfreund, and Z. V. Vardeny, "Isotope effect in spin response of π-conjugated polymer films and devices", Nature Materials **9**, 345–352 (2010) (cit. on pp. 30, 72, 91).

[67] F. Neese, "Prediction of electron paramagnetic resonance g values using coupled perturbed Hartree–Fock and Kohn–Sham theory", The Journal of Chemical Physics **115**, 11080–11096 (2001) (cit. on pp. 32–34, 79, 81, 83, 136).

[68] A. J. Stone, "Gauge invariance of the g tensor", Proceedings of the Royal Society A: Mathematical, Physical and Engineering Sciences **271**, 424–434 (1963) (cit. on pp. 32, 51).

[69] H. Matsui, D. Kumaki, E. Takahashi, K. Takimiya, S. Tokito, and T. Hasegawa, "Correlation between interdomain carrier hopping and apparent mobility in polycrystalline organic transistors as investigated by electron spin resonance", Phyical Review B **85**, 035308 (2012) (cit. on pp. 34, 48, 98).

[70] M. I. Dyakonov and V. I. Perel, "Spin orientation of electrons associated with the interband absorption of light in semiconductors", Soviet Journal of Experimental and Theoretical Physics **33**, 1053 (1971) (cit. on p. 36).

[71] R. J. Elliott, "Theory of the effect of spin-orbit coupling on magnetic resonance in some semiconductors", Physical Review B **96**, 266–279 (1954) (cit. on p. 36).

[72] Y. Yafet, "G Factors and Spin-Lattice Relaxation of Conduction Electrons", in *Solid State Physics*, Vol. 14, edited by F. Seitz and D. Turnbull (Academic Press, Jan. 1, 1963), pp. 1–98 (cit. on p. 36).

[73] P. A. Bobbert, W. Wagemans, F. W. A. Van Oost, B. Koopmans, and M. Wohlgenannt, "Theory for spin diffusion in disordered organic semiconductors", Physical Review Letters **102**, 156604 (2009) (cit. on pp. 36, 72).

[74] N. J. Harmon and M. E. Flatté, "Distinguishing spin relaxation mechanisms in organic semiconductors", Physical Review Letters **110**, 176602 (2013) (cit. on pp. 36, 52, 96).

[75] Z. G. Yu, "Spin-Orbit Coupling, Spin Relaxation, and Spin Diffusion in Organic Solids", Physical Review Letters **106**, 106602 (2011) (cit. on pp. 36, 50, 52, 96, 106).

[76] Z. G. Yu, F. Ding, and H. Wang, "Hyperfine interaction and its effects on spin dynamics in organic solids", Phyical Review B **87**, 205446 (2013) (cit. on pp. 36, 49, 96, 103, 127).

[77] Z. G. Yu, "Suppression of the Hanle effect in organic spintronic devices", Physical Review Letters **111**, 016601 (2013) (cit. on pp. 36, 72, 124, 141).

[78] J. Tsurumi, H. Matsui, T. Kubo, R. Häusermann, C. Mitsui, T. Okamoto, S. Watanabe, and J. Takeya, "Coexistence of ultra-long spin relaxation time and coherent charge transport in organic single-crystal semiconductors", Nature Physics, 1–6 (2017) (cit. on pp. 37, 60, 67, 100, 106).

[79] H. Matsui, A. S. Mishchenko, and T. Hasegawa, "Distribution of localized states from fine analysis of electron spin resonance spectra in organic transistors", Physical Review Letters **104**, 056602 (2010) (cit. on pp. 37, 60, 100).

[80] H. Matsui, T. Hasegawa, Y. Tokura, M. Hiraoka, and T. Yamada, "Polaron motional narrowing of electron spin resonance in organic field-effect transistors", Physical Review Letters **100**, 126601 (2008) (cit. on pp. 37, 48, 102).

[81] K. Kang et al., "2D coherent charge transport in highly ordered conducting polymers doped by solid state diffusion", Nature Materials **15**, 896–902 (2016) (cit. on pp. 37, 96, 113, 124).

[82] R. Kubo, "The fluctuation-dissipation theorem", Reports on Progress in Physics **29**, 255–284 (1966) (cit. on p. 38).

[83] R. Kubo and K. Tomita, "A general theory of magnetic resonance absorption", Journal of the Physical Society of Japan **9**, 888–919 (1954) (cit. on pp. 38, 105).

[84] I. J. Lowe and R. E. Norberg, "Free-induction decays in solids", Physical Review **107**, 46–61 (1957) (cit. on p. 38).

[85] A. G. Redfield, "On the theory of relaxation processes", IBM Journal of Research and Development **1**, 19–31 (1957) (cit. on pp. 39, 42, 44, 45, 90, 102).

[86] S. Stoll, "Spectral simulations in solid-state electron paramagnetic resonance", PhD Thesis (Eidgenössische Technische Hochschule Zürich, 2003) (cit. on pp. 41, 59).

[87] M. Goldman, "Formal theory of spin–lattice relaxation", Journal of Magnetic Resonance **149**, 160–187 (2001) (cit. on pp. 42, 44).

[88] H. Tanaka, M. Kozuka, S. I. Watanabe, H. Ito, Y. Shimoi, K. Takimiya, and S.-i. Kuroda, "Observation of field-induced charge carriers in high-mobility organic transistors of a thienothiophene-based small molecule: Electron spin resonance measurements", Phyical Review B **84**, 081306 (2011) (cit. on p. 48).

[89] M. I. Dyakonov, *Spin physics in semiconductors* (Springer Science & Business Media, July 2008) (cit. on p. 48).

[90] W. J. Baker, T. L. Keevers, J. M. Lupton, D. R. McCamey, and C. Boehme, "Slow hopping and spin dephasing of coulombically bound polaron pairs in an organic semiconductor at room temperature", Physical Review Letters **108**, 267601 (2012) (cit. on pp. 49, 50, 94, 103, 104).

[91] Z. G. Yu, "Microscopic theory of electron spin relaxation in N@ C60", Phyical Review B **77**, 821–6 (2008) (cit. on p. 53).

[92] J. Tatchen, N. Gilka, and C. M. Marian, "Intersystem crossing driven by vibronic spin–orbit coupling: a case study on psoralen", Physical Chemistry Chemical Physics **9**, 5209–13 (2007) (cit. on p. 53).

[93] V. A. Abalmassov and F. Marquardt, "Electron-nuclei spin relaxation through phonon-assisted hyperfine interaction in a quantum dot", Phyical Review B **70**, 16–8 (2004) (cit. on p. 53).

[94] L. Nuccio, L. Schulz, M. Willis, F. L. Pratt, M. Heeney, N. Stingelin, C. Bernhard, and A. J. Drew, "Electron spin relaxation in organic semiconductors probed through μSR", Journal of Physics: Conference Series **292**, 012004 (2011) (cit. on p. 54).

[95] L. Schulz et al., "Importance of intramolecular electron spin relaxation in small molecule semiconductors", Phyical Review B **84**, 1053 (2011) (cit. on p. 54).

[96] L. Nuccio et al., "Importance of spin-orbit interaction for the electron spin relaxation in organic semiconductors", Physical Review Letters **110**, 216602 (2013) (cit. on p. 54).

[97] J. S. Hyde, M. Pasenkiewicz-Gierula, A. Jesmanowicz, and W. E. Antholine, "Pseudo field modulation in EPR spectroscopy", Applied Magnetic Resonance **1**, 483–496 (1990) (cit. on pp. 58, 59).

[98] M. Kälin, I. Gromov, and A. Schweiger, "The continuous wave electron paramagnetic resonance experiment revisited", Journal of Magnetic Resonance **160**, 166–182 (2003) (cit. on p. 60).

[99] A. P. Saiko, R. Fedaruk, and S. A. Markevich, "Multi-photon transitions and Rabi resonance in continuous wave EPR", Journal of Magnetic Resonance **259**, 47–55 (2015) (cit. on p. 60).

[100] J. P. Korb and J. Maruani, "Measurement of spin-spin and spin-lattice relaxation rates for inhomogeneously broadened lines. I. Rapid spectral diffusion case", Journal of Magnetic Resonance **37**, 331–348 (1980) (cit. on pp. 61, 100).

[101] A. M. Portis, "Electronic Structure of F Centers: Saturation of the Electron Spin Resonance", Physical Review **91**, 1071–1078 (1953) (cit. on pp. 61, 100).

[102] W. Brütting and C. Adachi, *Physics of organic semiconductors* (John Wiley & Sons, Oct. 2012) (cit. on p. 64).

[103] R. Di Pietro, D. Venkateshvaran, A. Klug, E. J. W. List-Kratochvil, A. Facchetti, H. Sirringhaus, and D. Neher, "Simultaneous extraction of charge density dependent mobility and variable contact resistance from thin film transistors", Applied Physics Letters **104**, 193501 (2014) (cit. on pp. 66, 104).

[104] Z. H. Xiong, D. Wu, Z. Valy Vardeny, and J. Shi, "Giant magnetoresistance in organic spin-valves", Nature **427**, 821–824 (2004) (cit. on pp. 72, 96).

[105] A. J. Drew et al., "Direct measurement of the electronic spin diffusion length in a fully functional organic spin valve by low-energy muon spin rotation.", Nature Materials **8**, 109–114 (2008) (cit. on p. 72).

[106] X. Zhang et al., "Molecular origin of high field-effect mobility in an indacenodithiophene–benzothiadiazole copolymer", Nature Communications **4**, 2238 (2013) (cit. on pp. 72, 104).

[107] R. Göckeritz, N. Homonnay, A. Müller, T. Richter, B. Fuhrmann, and G. Schmidt, "Nanosized perpendicular organic spin-valves", Applied Physics Letters **106**, 102403 (2015) (cit. on p. 72).

[108] O. Wid, J. Bauer, A. Müller, O. Breitenstein, S. S. P. Parkin, and G. Schmidt, "Investigation of the unidirectional spin heat conveyer effect in a 200 nm thin Yttrium Iron Garnet film", Scientific Reports **6**, 28233 (2016) (cit. on p. 72).

[109] N. A. Minder, S. Lu, S. Fratini, S. Ciuchi, A. Facchetti, and A. F. Morpurgo, "Tailoring the molecular structure to suppress extrinsic disorder in organic transistors.", Advanced Materials **26**, 1254–1260 (2014) (cit. on p. 73).

[110] S. Schott et al., "Tuning the effective spin-orbit coupling in molecular semiconductors.", Nature Communications **8**, 15200 (2017) (cit. on pp. 74, 96, 120).

[111] A. Lund, E. Sagstuen, A. Sanderud, and J. Maruani, "Relaxation-time determination from continuous-microwave saturation of EPR spectra", Radiation research **172**, 753–760 (2009) (cit. on p. 74).

[112] T. Izawa, E. Miyazaki, and K. Takimiya, "Solution-processible organic semiconductors based on selenophene-containing heteroarenes, 2,7-dialkyl[1]benzoselenopheno[3,2- b][1]benzo-selenophenes (c n-bsbss): syntheses, properties, molecular arrangements, and field-effect transistor characteristics", Chemistry of Materials **21**, 903–912 (2009) (cit. on p. 78).

[113] S. Stoll and A. Schweiger, "EasySpin, a comprehensive software package for spectral simulation and analysis in EPR", Journal of Magnetic Resonance **178**, 42–55 (2006) (cit. on p. 78).

[114] M. Valiev et al., "NWChem: A comprehensive and scalable open-source solution for large scale molecular simulations", Computer Physics Communications **181**, 1477–1489 (2010) (cit. on pp. 79, 136, 141).

[115] F. Neese, "The ORCA program system", Wiley Interdisciplinary Reviews: Computational Molecular Science **2**, 73–78 (2012) (cit. on pp. 79, 136).

[116] E. van Lenthe, E. J. Baerends, and J. G. Snijders, "Relativistic regular two-component Hamiltonians", The Journal of Chemical Physics **99**, 4597–4610 (1993) (cit. on pp. 79, 135).

[117] F. Neese, "Efficient and accurate approximations to the molecular spin-orbit coupling operator and their use in molecular g-tensor calculations", The Journal of Chemical Physics **122**, 034107 (2005) (cit. on pp. 79, 136).

[118] E. R. McNellis, S. Schott, H. Sirringhaus, and J. Sinova, "Molecular tuning of the magnetic response in organic semiconductors", Physical Review Materials **2**, 074405 (2018) (cit. on pp. 79, 84, 96).

[119] C. lia Fonseca Guerra, J.-W. Handgraaf, E. J. Baerends, and F. M. Bickelhaupt, "Voronoi deformation density (VDD) charges: Assessment of the Mulliken, Bader, Hirshfeld, Weinhold, and VDD methods for charge analysis.", Journal of Computational Chemistry **25**, 189–210 (2004) (cit. on pp. 85, 137).

[120] W. Tang, E. Sanville, and G. Henkelman, "A grid-based Bader analysis algorithm without lattice bias.", Journal of Physics: Condensed Matter **21**, 084204 (2009) (cit. on pp. 85, 137).

[121] S. W. Jiang, S. Liu, P. Wang, Z. Z. Luan, X. D. Tao, H. F. Ding, and D. Wu, "Exchange-dominated pure spin current transport in Alq3 molecules", Physical Review Letters **115**, 086601 (2015) (cit. on pp. 89, 96, 124).

[122] S. Watanabe, K. Ando, K. Kang, S. Mooser, Y. Vaynzof, H. Kurebayashi, E. Saitoh, and H. Sirringhaus, "Polaron spin current transport in organic semiconductors", Nature Physics **10**, 308–313 (2014) (cit. on pp. 89, 96, 97).

[123] W. Xie, K. A. McGarry, F. Liu, Y. Wu, P. P. Ruden, C. J. Douglas, and C. D. Frisbie, "High-mobility transistors based on single crystals of isotopically substituted rubrene- d28", The Journal of Physical Chemistry C **117**, 11522–11529 (2013) (cit. on p. 91).

[124] T. Fujita, S. Atahan-Evrenk, N. P. D. Sawaya, and A. Aspuru-Guzik, "Coherent dynamics of mixed frenkel and charge-transfer excitons in dinaphtho[2,3-b:2´3´- f]thieno[3,2- b]-thiophene thin films: the importance of hole delocalization", The Journal of Physical Chemistry Letters **7**, 1374–1380 (2016) (cit. on p. 92).

[125] K. J. van Schooten, D. L. Baird, M. E. Limes, J. M. Lupton, and C. Boehme, "Probing long-range carrier-pair spin–spin interactions in a conjugated polymer by detuning of electrically detected spin beating", Nature Communications **6**, 6688 (2015) (cit. on p. 94).

[126] Y. Olivier, V. Lemaur, J. L. Brédas, and J. Cornil, "Charge hopping in organic semiconductors: influence of molecular parameters on macroscopic mobilities in model one-dimensional stacks", The Journal of Physical Chemistry A **110**, 6356–6364 (2006) (cit. on p. 94).

[127] C. Motta and S. Sanvito, "Charge transport properties of durene crystals from first-principles", Journal of Chemical Theory and Computation **10**, 4624–4632 (2014) (cit. on p. 94).

[128] D. L. Cheung and A. Troisi, "Modelling charge transport in organic semiconductors: from quantum dynamics to soft matter", Physical Chemistry Chemical Physics **10**, 5941 (2008) (cit. on p. 94).

[129] M. Shao et al., "The isotopic effects of deuteration on optoelectronic properties of conducting polymers.", Nature Communications **5**, 3180 (2014) (cit. on pp. 96, 102).

[130] R. Steyrleuthner, Y. Zhang, L. Zhang, F. Kraffert, B. P. Cherniawski, R. Bittl, A. L. Briseno, J.-L. Brédas, and J. Behrends, "Impact of morphology on polaron delocalization in a semicrystalline conjugated polymer", Physical Chemistry Chemical Physics **19**, 3627–3639 (2017) (cit. on p. 96).

[131] S. Pramanik, C.-G. Stefanita, S. Patibandla, S. Bandyopadhyay, K. Garre, N. Harth, and M. Cahay, "Observation of extremely long spin relaxation times in an organic nanowire spin valve", Nature Nanotechnology **2**, 216–219 (2007) (cit. on p. 96).

[132] J. H. Shim, K. V. Raman, Y. J. Park, T. S. Santos, G. X. Miao, B. Satpati, and J. S. Moodera, "Large spin diffusion length in an amorphous organic semiconductor", Physical Review Letters **100**, 226603 (2008) (cit. on p. 96).

[133] S. Mooser, J. F. K. Cooper, K. K. Banger, J. Wunderlich, and H. Sirringhaus, "Spin injection and transport in a solution-processed organic semiconductor at room temperature", Physical Review B **85**, 235202 (2012) (cit. on p. 96).

[134] D. R. McCamey, K. J. van Schooten, W. J. Baker, S. Y. Lee, S. Y. Paik, J. M. Lupton, and C. Boehme, "Hyperfine-field-mediated spin beating in electrostatically bound charge carrier pairs", Physical Review Letters **104**, 13–4 (2010) (cit. on p. 96).

[135] T. D. Nguyen, B. R. Gautam, E. Ehrenfreund, and Z. V. Vardeny, "Magnetoconductance Response in Unipolar and Bipolar Organic Diodes at Ultrasmall Fields", Physical Review Letters **105**, 166804 (2010) (cit. on p. 96).

[136] M. Grünewald, M. Wahler, F. Schumann, M. Michelfeit, C. Gould, R. Schmidt, F. Würthner, G. Schmidt, and L. W. Molenkamp, "Tunneling anisotropic magnetoresistance in organic spin valves", Physical Review B **84**, 125208 (2011) (cit. on pp. 96, 124).

[137] M. Grünewald, R. Göckeritz, N. Homonnay, F. Würthner, L. W. Molenkamp, and G. Schmidt, "Vertical organic spin valves in perpendicular magnetic fields", Physical Review B **88** (2013) (cit. on pp. 96, 124).

[138] P. Pingel, M. Arvind, L. Kölln, R. Steyrleuthner, F. Kraffert, J. Behrends, S. Janietz, and D. Neher, "P-Type Doping of Poly(3-hexylthiophene) with the Strong Lewis Acid Tris(pentafluorophenyl)borane", Advanced Electronic Materials, 1600204–7 (2016) (cit. on p. 96).

[139] H. Yan, Z. Chen, Y. Zheng, C. Newman, J. R. Quinn, F. Dötz, M. Kastler, and A. Facchetti, "A high-mobility electron-transporting polymer for printed transistors", Nature **457**, 679–686 (2009) (cit. on pp. 97, 114).

[140] M. Gruber et al., "Enabling high-mobility, ambipolar charge-transport in a DPP-benzotriazole copolymer by side-chain engineering", Chemical Science **6**, 6949–6960 (2015) (cit. on pp. 97, 114).

[141] S. Schott, E. Gann, L. Thomsen, S.-H. Jung, J.-K. Lee, C. R. McNeill, and H. Sirringhaus, "Charge-transport anisotropy in a uniaxially aligned diketopyrrolopyrrole-based copolymer", Advanced Materials **27**, 7356–7364 (2015) (cit. on pp. 97, 115, 118).

[142] H. Matsui and T. Hasegawa, "Direct observation of field-induced carrier dynamics in pentacene thin-film transistors by electron spin resonance spectroscopy", Japanese Journal of Applied Physics **48**, 04C175 (2009) (cit. on p. 98).

[143] M. Nikolka et al., "High operational and environmental stability of high-mobility conjugated polymer field-effect transistors through the use of molecular additives", Nature Materials **16**, 356–362 (2016) (cit. on pp. 99, 113).

[144] R. Alger, *Electron paramagnetic resonance: techniques and applications* (Interscience Publishers, 1968) (cit. on p. 100).

[145] M. S. Vezie et al., "Exploring the origin of high optical absorption in conjugated polymers.", Nature Materials **15**, 746–753 (2016) (cit. on p. 105).

[146] V. Marcon, D. W. Breiby, W. Pisula, J. Dahl, J. Kirkpatrick, S. Patwardhan, F. Grozema, and D. Andrienko, "Understanding Structure-Mobility Relations for Perylene Tetracarboxydiimide Derivatives", J. Am. Chem. Soc. **131**, 11426–11432 (2009) (cit. on p. 109).

[147] F. May, V. Marcon, M. R. Hansen, F. Grozema, and D. Andrienko, "Relationship between supramolecular assembly and charge-carrier mobility in perylenediimide derivatives: The impact of side chains", J. Mater. Chem. **21**, 9538–9545 (2011) (cit. on p. 109).

[148] M. Anderson et al., "Displacement of polarons by vibrational modes in doped conjugated polymers", Physical Review Materials **1**, 055604–9 (2017) (cit. on p. 111).

[149] G. Lu et al., "Moderate doping leads to high performance of semiconductor/insulator polymer blend transistors.", Nature Communications **4**, 1588 (2013) (cit. on p. 112).

[150] R. Fujimoto, Y. Yamashita, S. Kumagai, J. Tsurumi, A. Hinderhofer, K. Broch, F. Schreiber, S. Watanabe, and J. Takeya, "Molecular doping in organic semiconductors: fully solution-processed, vacuum-free doping with metal–organic complexes in an orthogonal solvent", J. Mater. Chem. C **5**, 12023–12030 (2017) (cit. on p. 113).

[151] I. McCulloch et al., "Liquid-crystalline semiconducting polymers with high charge-carrier mobility", Nature Materials **5**, 328–333 (2006) (cit. on p. 114).

[152] R. Di Pietro et al., "Coulomb enhanced charge transport in semicrystalline polymer semiconductors", Advanced Functional Materials **26**, 8011–8022 (2016) (cit. on pp. 115, 117–119).

[153] J. Rivnay, M. F. Toney, Y. Zheng, I. V. Kauvar, Z. Chen, V. Wagner, A. Facchetti, and A. Salleo, "Unconventional face-on texture and exceptional in-plane order of a high mobility n-type polymer", Advanced Materials **22**, 4359–4363 (2010) (cit. on p. 117).

[154] J. Rivnay, R. Noriega, R. J. Kline, A. Salleo, and M. F. Toney, "Quantitative analysis of lattice disorder and crystallite size in organic semiconductor thin films", Phyical Review B **84**, 045203 (2011) (cit. on p. 117).

[155] E. Giussani, D. Fazzi, L. Brambilla, M. Caironi, and C. Castiglioni, "Molecular level investigation of the film structure of a high electron mobility copolymer via vibrational spectroscopy", Macromolecules **46**, 2658–2670 (2013) (cit. on p. 117).

[156] V. Lemaur, L. Muccioli, C. Zannoni, D. Beljonne, R. Lazzaroni, J. Cornil, and Y. Olivier, "On the supramolecular packing of high electron mobility naphthalene diimide copolymers: the perfect registry of asymmetric branched alkyl side chains", Macromolecules **46**, 8171–8178 (2013) (cit. on pp. 117, 119).

[157] D. M. DeLongchamp et al., "Controlling the Orientation of Terraced Nanoscale "Ribbons" of a Poly(thiophene) Semiconductor", ACS Nano **3**, 780–787 (2009) (cit. on p. 118).

[158] C. Wang, L. H. Jimison, L. Goris, I. McCulloch, M. Heeney, A. Ziegler, and A. Salleo, "Microstructural Origin of High Mobility in High-Performance Poly(thieno-thiophene) Thin-Film Transistors", Advanced Materials **22**, 697–701 (2010) (cit. on p. 118).

[159] T. Schuettfort, B. Watts, L. Thomsen, M. Lee, H. Sirringhaus, and C. R. McNeill, "Microstructure of polycrystalline pbttt films: domain mapping and structure formation", ACS Nano **6**, 1849–1864 (2012) (cit. on p. 118).

[160] A. R. Chew, R. Ghosh, V. Pakhnyuk, J. Onorato, E. C. Davidson, R. A. Segalman, C. K. Luscombe, F. C. Spano, and A. Salleo, "Unraveling the Effect of Conformational and Electronic Disorder in the Charge Transport Processes of Semiconducting Polymers", Advanced Functional Materials, 1804142 (2018) (cit. on p. 119).

[161] J. P. Schmidtke, J.-S. Kim, J. Gierschner, C. Silva, and R. H. Friend, "Optical spectroscopy of a polyfluorene copolymer at high pressure: intra- and intermolecular interactions", Physical Review Letters **99**, 167401 (2007) (cit. on p. 123).

[162] H. T. Yi, M. M. Payne, J. E. Anthony, and V. Podzorov, "Ultra-flexible solution-processed organic field-effect transistors", Nature Communications **3**, 1259 (2012) (cit. on p. 123).

[163] A. Riminucci, M. Prezioso, C. Pernechele, P. Graziosi, I. Bergenti, R. Cecchini, M. Calbucci, M. Solzi, and V. Alek Dediu, "Hanle effect missing in a prototypical organic spintronic device", Applied Physics Letters **102**, 092407 (2013) (cit. on p. 124).

[164] H. Sakimura, T. Matsumoto, and K. Ando, "Spin rectification induced by dynamical Hanle effect", Applied Physics Letters **103**, 132402 (2013) (cit. on p. 124).

[165] R. C. Roundy, M. C. Prestgard, A. Tiwari, and M. E. Raikh, "Shape of the Hanle curve in spin-transport structures in the presence of an ac drive", Phyical Review B **90**, 2372 (2014) (cit. on p. 124).

[166] P. Boross, B. Dóra, A. Kiss, and F. Simon, "A unified theory of spin-relaxation due to spin-orbit coupling in metals and semiconductors", Scientific Reports **3**, 3233 (2013) (cit. on pp. 127, 128).

[167] C. Adamo and V. Barone, "Toward chemical accuracy in the computation of NMR shieldings: the PBE0 model", Chemical Physics Letters **298**, 113–119 (1998) (cit. on pp. 136, 141).

[168] D. A. Pantazis, X.-Y. Chen, C. R. Landis, and F. Neese, "All-electron scalar relativistic basis sets for third-row transition metal atoms", Journal of Chemical Theory and Computation **4**, 908–919 (2008) (cit. on p. 136).

[169] P.-O. Löwdin, "On the non-orthogonality problem connected with the use of atomic wave functions in the theory of molecules and crystals", The Journal of Chemical Physics **18**, 365–375 (1950) (cit. on p. 137).

[170] J. J. Philips, M. A. Hudspeth, P. M. Browne, and J. E. Peralta, "Basis set dependence of atomic spin populations", Chemical Physics Letters **495**, 146–150 (2010) (cit. on p. 137).

[171] R. F. W. Bader, "Atoms in molecules", Accounts of Chemical Research **18**, 9–15 (1985) (cit. on p. 137).

[172] M. Yu and D. R. Trinkle, "Accurate and efficient algorithm for Bader charge integration", The Journal of Chemical Physics **134**, 064111 (2011) (cit. on p. 137).

[173] P. Nichols, N. Govind, E. J. Bylaska, and W. A. de Jong, "Gaussian Basis Set and Planewave Relativistic Spin-Orbit Methods in NWChem", J. Chem. Theory Comput. **5**, 491–499 (2009) (cit. on p. 141).

[174] U. C. Singh and P. A. Kollman, "An approach to computing electrostatic charges for molecules", Journal of Computational Chemistry **5**, 129–145 (1984) (cit. on p. 143).

[175] B. H. Besler, K. M. Merz, and P. A. Kollman, "Atomic charges derived from semiempirical methods", Journal of Computational Chemistry **11**, 431–439 (1990) (cit. on p. 143).

[176] N. A. McDonald and W. L. Jorgensen, "Development of an All-Atom Force Field for Heterocycles. Properties of Liquid Pyrrole, Furan, Diazoles, and Oxazoles", J. Phys. Chem. B **102**, 8049–8059 (1998) (cit. on p. 144).

[177] W. L. Jorgensen and N. A. McDonald, "Development of an all-atom force field for heterocycles. Properties of liquid pyridine and diazenes", Journal of Molecular Structure: THEOCHEM, A Faithful Couple: Qualitative and Quantitative Understanding of Chemistry **424**, 145–155 (1998) (cit. on p. 144).

[178] W. L. Jorgensen, D. S. Maxwell, and J. Tirado-Rives, "Development and Testing of the OPLS All-Atom Force Field on Conformational Energetics and Properties of Organic Liquids", J. Am. Chem. Soc. **118**, 11225–11236 (1996) (cit. on p. 144).

[179] W. L. Jorgensen and J. Tirado-Rives, "The OPLS [optimized potentials for liquid simulations] potential functions for proteins, energy minimizations for crystals of cyclic peptides and crambin", J. Am. Chem. Soc. **110**, 1657–1666 (1988) (cit. on p. 144).

[180] G. Bussi, D. Donadio, and M. Parrinello, "Canonical sampling through velocity rescaling", The Journal of Chemical Physics **126**, 014101 (2007) (cit. on p. 145).

[181] H. J. C. Berendsen, J. P. M. Postma, W. F. van Gunsteren, A. DiNola, and J. R. Haak, "Molecular dynamics with coupling to an external bath", The Journal of Chemical Physics **81**, 3684–3690 (1984) (cit. on p. 145).

[182] J. J. P. Stewart, "Optimization of parameters for semiempirical methods I. Method", Journal of Computational Chemistry **10**, 209–220 (1989) (cit. on p. 145).

[183] D. M. DeLongchamp, R. J. Kline, D. A. Fischer, L. J. Richter, and M. F. Toney, "Molecular characterization of organic electronic films", Advanced Materials **23**, 319–337 (2011) (cit. on p. 145).

[184] J. Gao, A. K. Thomas, R. Johnson, H. Guo, and J. K. Grey, "Spatially Resolving Ordered and Disordered Conformers and Photocurrent Generation in Intercalated Conjugated Polymer/Fullerene Blend Solar Cells", Chem. Mater. **26**, 4395–4404 (2014) (cit. on p. 145).

[185] A. I. Khan, I. A. Navid, M. Noshin, H. M. A. Uddin, F. F. Hossain, and S. Subrina, "Equilibrium Molecular Dynamics (MD) Simulation Study of Thermal Conductivity of Graphene Nanoribbon: A Comparative Study on MD Potentials", Electronics **4**, 1109–1124 (2015) (cit. on p. 145).

[186] S. Pronk et al., "GROMACS 4.5: a high-throughput and highly parallel open source molecular simulation toolkit", Bioinformatics **29**, 845–854 (2013) (cit. on p. 146).

[187] W. Humphrey, A. Dalke, and K. Schulten, "VMD: Visual molecular dynamics", Journal of Molecular Graphics **14**, 33–38 (1996) (cit. on p. 146).

[188] N. M. Kirby, S. T. Mudie, A. M. Hawley, D. J. Cookson, H. D. T. Mertens, N. Cowieson, and V. Samardzic-Boban, "A low-background-intensity focusing small-angle X-ray scattering undulator beamline", Journal of Applied Crystallography **46**, 1670–1680 (2013) (cit. on p. 147).

[189] J. Ilavsky, "Nika: software for two-dimensional data reduction", Journal of Applied Crystallography **45**, 324–328 (2012) (cit. on p. 147).